PUMMA

Research and Innovation Action (RIA)

This project has received funding from the Euratom research and innovation programme 2019-2020 under Grant Agreement No 945022

Start date : 2020-10-01 Duration : 54 Months

PuMMA
Plutonium Management for More Agility

New MOX fuel and PuO2 properties catalogue (20 – 70 % Pu range)

Authors : Laura Geisler, Bertrand Baurens (Framatome), Nathalie Chauvin, Philippe Martin, Marie-Margaux Desagulier, Julien Martinez, Christine Guéneau, Mathilde Pons, Maxime Duchateau, Thomas Barral, Hugo François, Bruno Michel, Adrien Socie, Salomon Elbez, Jean-Christophe Dumas, P. Fouquet-Métivier (CEA), Dragos Staicu, Luka Vlahovic, Davide Robba, E. Dahms, G. Montagnier, C. Nourry (JRC), Laureline Argeles (EDF), Nicolas Clavier (CNRS), Zoltán Hózer (MTA EK), G. Nicodemo, D. Pizzocri, L. Luzzi (Polimi)

PUMMA - Contract Number: 945022

Project officer: Renata BACHORCZYK-NAGY

Document title	New MOX fuel and PuO2 properties catalogue (20 – 70 % Pu range)
Author(s)	Laura Geisler, Bertrand Baurens (Framatome), Nathalie Chauvin, Philippe Martin, Marie-Margaux Desagulier, Julien Martinez, Christine Guéneau, Mathilde Pons, Maxime Duchateau, Thomas Barral, Hugo François, Bruno Michel, Adrien Socie, Salomon Elbez, Jean-Christophe Dumas, P. Fouquet-Métivier (CEA), Dragos Staicu, Luka Vlahovic, Davide Robba, E. Dahms, G. Montagnier, C. Nourry (JRC), Laureline Argeles (EDF), Nicolas Clavier (CNRS), Zoltán Hózer (MTA EK), G. Nicodemo, D. Pizzocri, L. Luzzi (Polimi)
Number of pages	224
Document type	Deliverable
Work Package	WP3
Document number	D3.9
Issued by	Framatome
Date of completion	2025-12-16 18:30:35
Dissemination level	Public

Summary

During the ESFR-SMART project and then the PuMMA project, new experimental measurements of properties have been performed on both fresh and irradiated MOX fuels. The aim of this deliverable is to provide updated versions of several chapters of the 2017 catalogue, based on the new experimental results collected in the frame of both ESFR-SMART and PuMMA projects. The properties concerned are lattice parameter, thermal conductivity, melting point, specific heat and thermal expansion. In particular, a new law is recommended regarding melting point.

Approval

Date	By
2025-10-28 06:56:06	HÓzer ZOLTáN (MTA EK)
2025-10-28 11:15:06	Nathalie CHAUVIN (CEA)

PuMMA
Plutonium Management for More Agility

Research & Innovation Action

NFRP-2019-2020

New MOX fuel and PuO_2 properties catalogue (20 – 70 % Pu range)

D3.9

Authors:

Laura Geisler, Bertrand Baurens (Framatome),
Nathalie Chauvin, Philippe Martin, Marie-Margaux Desagulier,
Julien Martinez, Christine Guéneau, Mathilde Pons,
Maxime Duchateau, Thomas Barral, Hugo François,
Bruno Michel, Adrien Socie, Salomon Elbez,
Jean-Christophe Dumas, P. Fouquet-Métivier (CEA),
Dragos Staicu, Luka Vlahovic, Davide Robba, E. Dahms,
G. Montagnier, C. Nourry (JRC),
Laureline Argeles (EDF),
Nicolas Clavier (CNRS),
Zoltán Hózer (MTA EK),
G. Nicodemo, D. Pizzocri, L. Luzzi (Polimi).

Disclaimer

Table of contents

This project has received funding from the Euratom research and training programme 2019-2020 under grant agreement No 945022.

This project has received funding from the Euratom research and training programme 2019-2020 under grant agreement No 945022.

This project has received funding from the Euratom research and training programme 2019-2020 under grant agreement No 945022.

This project has received funding from the Euratom research and training programme 2019-2020 under grant agreement No 945022.

List of figures

This project has received funding from the Euratom research and training programme 2019-2020 under grant agreement No 945022.

This project has received funding from the Euratom research and training programme 2019-2020 under grant agreement No 945022.

This project has received funding from the Euratom research and training programme 2019-2020 under grant agreement No 945022.

This project has received funding from the Euratom research and training programme 2019-2020 under grant agreement No 945022.

This project has received funding from the Euratom research and training programme 2019-2020 under grant agreement No 945022.

This project has received funding from the Euratom research and training programme 2019-2020 under grant agreement No 945022.

List of tables

This project has received funding from the Euratom research and training programme 2019-2020 under grant agreement No 945022.

This project has received funding from the Euratom research and training programme 2019-2020 under grant agreement No 945022.

1. Introduction

In the frame of the European project ESNII+, an update of the European catalogue of properties of (U,Pu)O2 mixed oxide fuel was published in 2017. For each property, recommendations and validity ranges were given and the knowledge gaps were also highlighted.

During the ESFR-SMART project and then the PuMMA project, new experimental measurements of properties have been performed on both fresh and irradiated MOX fuels. The aim of this deliverable is to provide updated versions of several chapters of the 2017 catalogue, based on the new experimental results collected in the frame of both ESFR-SMART and PuMMA projects. The properties concerned are lattice parameter, thermal conductivity, melting point, specific heat and thermal expansion. In particular, a new law is recommended regarding melting point.

In the meantime, an international report on recommendations on oxide fuels and fuels for Fast Reactor has been published by experts in the field (https://www.oecd-nea.org/jcms/pl_107583/recommendations-on-fuel-properties-for-fuel-performance-codes?details=true).

So in our new European catalog we have tried to compare, when it was possible, our European recent measurements with these recommendations.

This project has received funding from the Euratom research and training programme 2019-2020 under grant agreement No 945022.

2. Lattice parameter

This chapter was originally provided by J.P. Ottaviani (CEA).

2.1 Literature data

2.1.1 Effect of plutonium content

The law originally recommended in the European catalogue is based on the assumption that the lattice parameter of stoichiometric mixed oxide $(U_{1-y}Pu_y)O_2$ may be calculated by applying the Vegard's law from the commonly accepted values of 5.470 Å, and 5.396 Å as lattice parameters of $UO_{2.00}$ and $PuO_{2.00}$ respectively. This means that lattice parameter changes in a straight line with increasing Pu content.

2.1.2 Effect of deviation from stoichiometry

For hypo-stoichiometric mixed oxide $(U_{1-y}Pu_y)O_{2-x}$, considering a linear variation of the lattice parameter as a function of deviation from stoichiometry and Pu content, Vegard's law is extended between $UO_{2.00}$ and $PuO_{2.00}$ poles by adding a term featuring the effect of the O/M ratio, depending on both the deviation from stoichiometry and the Pu content. The evolution of the lattice parameter is given by Eq. 2.1:

$$a\,(\mathrm{pm}) = 547.0 - 7.4\,y + (30.1 + 11.0\,y)\,x \qquad \text{Eq. 2.1}$$

This recommendation has been implemented from the review of the CEA internal catalogue dating back to 1977, data published in the open literature [Ben69, Jav72, Mar67], as well as other measurements carried out at CEA [Phi90].

It is applicable to a single phase domain for Pu contents limited to $0 < y < 0.30$. Moreover, it is worth noting that, due to the observed experimental dispersion, the slope $\Delta a/\Delta x$ is given with substantial uncertainty, in the order of 20%, or approximately ± 6 pm.

The above correlation recommended by Philipponneau was established from experimental data strongly scattered, particularly for the lowest Pu contents. The dispersion was explained by poor Pu homogeneity of the samples.

An additional study was achieved by Duriez et al. in 2000 [Dur00] on $(U_{1-y}Pu_y)O_{2-x}$ fuel samples thermally treated in order to promote plutonium homogenization, and finely characterized. The results obtained from this study were less scattered than those that had conducted to the previous recommendation. The revaluation was suggested as given per Eq. 2.2:

This project has received funding from the Euratom research and training programme 2019-2020 under grant agreement No 945022.

$$a\,(\mathrm{pm}) = 547.0 - 7.4\,y + 32\,x \qquad \text{Eq. 2.2}$$

Accordingly, the effect of deviation from stoichiometry appeared again independent from the Pu content .

The range of applicability of Philipponneau's recommendation is limited to Pu contents lower than 30%, as a single-phase solid solution in this range was considered. However, due to the complexity of the U-Pu-O system, this range of applicability still remains open to discussion. Indeed, for low Pu contents all literature data [Mar67, Sar70] show the existence of a single phase $(U,Pu)O_{2-x}$ solid solution until complete reduction of Pu to trivalent state, then transition to a two-phase domain MO_{2-x} + metal. For higher Pu contents, a phase separation is observable when reducing Pu, leading to two FCC phases in the miscibility gap of the hypo-stoichiometric region. The lowest value of Pu content for which this phenomenon has been observed at room temperature is variable according to the authors. It was proposed at 35% by Markin et al. in 1967 [Mar67]. Later the phenomenon was observed between 15 and 20% by Sari et al. [Sar70] and Koizumi et al.[Koi69]. Sari et al. indicated that samples of the same composition exhibited sometimes a single phase, and sometimes two phases. The kinetics of formation of the second FCC phase, very slow at room temperature in this range of Pu content, could explain the disparity in the results. The lowest value of Pu content at which the second phase appears increasing as temperature increases [Koi69, Sar70, Mar67] single phase solid solutions observed at room temperature for Pu contents higher than 20% may correspond to equilibriums at high temperature.

So, in a large hypo-stoichiometric region, the limit of applicability of 30% Pu should be considered cautiously.

Furthermore, it is important to mention that Sari et al. observed the existence of single phase solid solutions containing between 17% and 100% Pu and O/M ratios exceeding 1.985. In this narrow hypo-stoichiometric region, the lattice parameter varies linearly with the Pu content.

In 2009, Kato et al. [Kat09a] and Morimoto et al. [Mor09] determined the lattice parameters at room temperature of hypo-stoichiometric uranium-plutonium mixed oxide fuels doped with americium and neptunium, of type $(U_{1-z-y'-y''}Pu_zAm_{y'}Np_{y''})O_{2-x}$ with (z = 0 - 1, y'= 0 - 0.02, y'' = 0 - 0.12). Figure 2.1 shows a linear variation of lattice parameter as a function of the O/M ratio for each type of fuel, in accordance with the recommendation ofPhilipponneau. However, as well as Sari et al, Kato et al. observed single phase solid solutions on fuels with O/M ratio lower than 2.00, even for Pu contents greater than 30%.

This project has received funding from the Euratom research and training programme 2019-2020 under grant agreement No 945022.

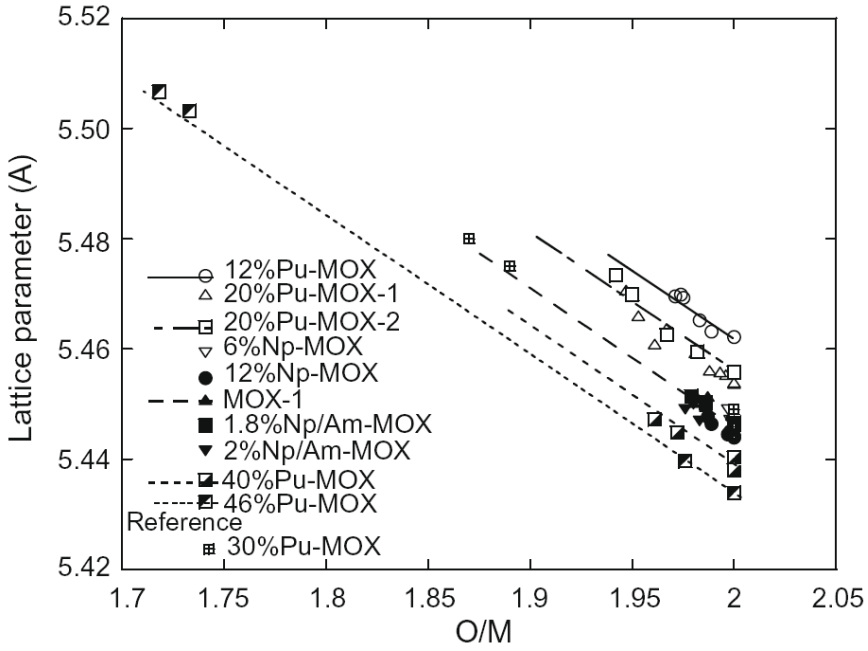

Figure 2.1: Effect of the O/M ratio on the lattice parameter of hypo-stoichiometric oxides of type $(U,Pu,Am,Np)O_{2-x}$ [Kat09a].

These recent results added to those of Sari et al. tend to demonstrate that a new recommendation could be extended to higher Pu contents but in a reduced hypo-stoichiometric area (1.985 < O/M < 2).

2.1.3 Effect of addition of minor actinides

Any Japanese studies tend to demonstrate that the addition of minor actinides is likely to change the limit of phase separation [Kom10, Kat06]. In 2006, Kato et al. studied the effect of addition of minor actinides Am and Np on the lattice parameter of $U_{0.7}Pu_{0.3}O_{2-x}$ mixed oxide [Kat06]. Figure 2.2a shows that the lattice parameter linearly decreases according to the Vegard's law for stoichiometric material. Figure 2.2b shows that the evolution of the lattice parameter as a function of the deviation from the stoichiometry in oxygen is linear, with a slope similar to that of the material without minor actinides. The lattice parameter was described by the correlation given in Eq. 2.3:

$$\mathrm{a\ (pm)} = \mathrm{a}(MO_2) + 24.8\,\mathrm{x} \qquad \text{Eq. 2.3}$$

where x is the deviation from the stoichiometry and $a(MO_2)$ is the lattice parameter of the stoichiometric mixed oxide calculated from Vegard's law as per Eq. 2.4:

$$\mathrm{a}(MO_2) = \sum a_i\, c_i \qquad \text{Eq. 2.4}$$

where a_i (pm) is the lattice parameter of the i^{th} AnO_2 end-member, and c_i is its concentration, defined as per Eq. 2.5

This project has received funding from the Euratom research and training programme 2019-2020 under grant agreement No 945022.

$$\sum c_i = c_{UO_2} + c_{PuO_2} + c_{AmO_2} + c_{NpO_2} = 1 \qquad \text{Eq. 2.5}$$

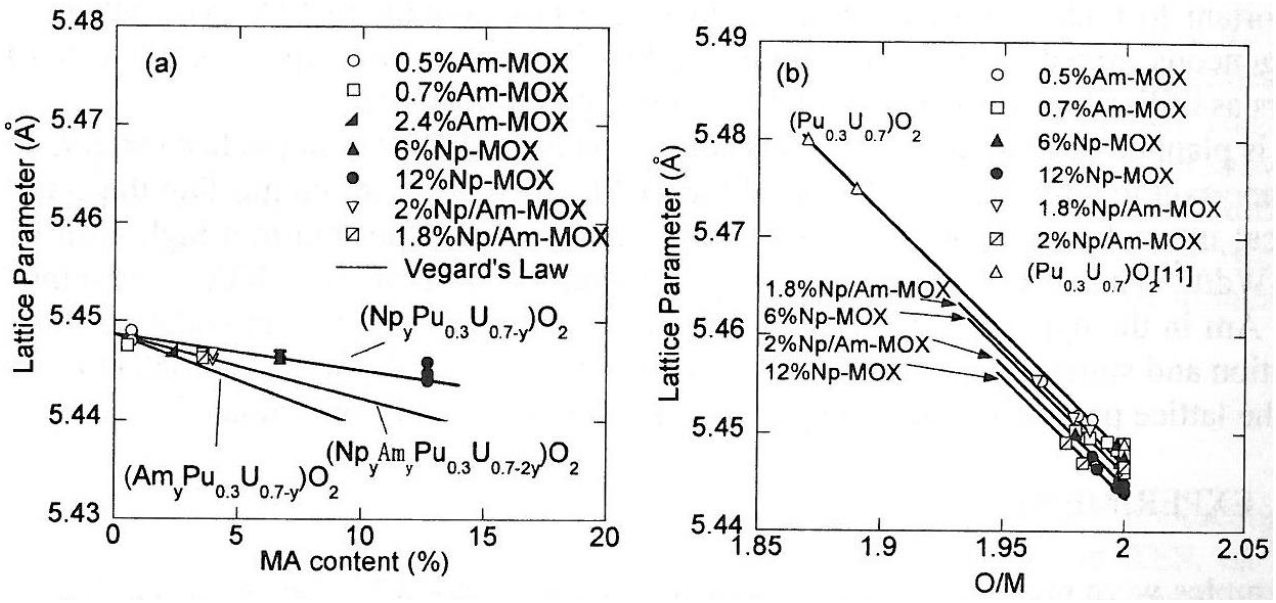

Figure 2.2: Lattice parameter of MOX doped with minor actinides (a) as a function of minor actinide content, (b) as a function of the O/M ratio [Kat06].

The previously mentioned study from Kato et al. [Kat09a] also analyzes the effect of addition of minor actinides on the lattice parameter of stoichiometric or hypo-stoichiometric uranium-plutonium mixed oxide fuels (Figure 2.1 & Figure 2.3). From the compilation of a significant number of experimental and bibliographic data, the authors offer a new expression of the lattice parameter (Eq. 2.6) as a function of U, Pu, Am, and Np contents, their respective ionic radii (see Table 2.1 and Table 2.2), the deviation from the stoichiometry in oxygen, and ionic radius of the oxygen anion r_a.

$$\mathrm{a} = 4/\sqrt{3}[(r_U(1-z-y'-y'') + r_{Pu}\,z + r_{Am}\,y' + r_{Nb}\,y'')(1+0.112\,x) + r_a] \qquad \text{Eq. 2.6}$$

where a is expressed in the same unit as ionic radii.

Table 2.1: Ionic radii from [Kat09a].

Ionic species	Ionic radius (Å)
U^{4+} (CN=8)	0.9972
Pu^{4+} (CN=8)	0.9642
Am^{4+} (CN=8)	0.9539
Np^{4+} (CN=8)	0.9805
O^{2-} (CN=4)	1.372

This project has received funding from the Euratom research and training programme 2019-2020 under grant agreement No 945022.

Table 2.2: Ionic radii from [Sha76].

Ionic species	Ionic radius (Å)
U^{5+} (CN=8)	0.840
Pu^{3+} (CN=6)	1.00
Am^{3+} (CN=8)	1.090
Am^{3+} (CN=6)	0.975

The previous correlation represents the experimental data very well, within a standard deviation of σ = ±0.025%. The correlation suggested by Kato et al. [Kat09a] may also be written according to Eq. 2.7 which highlights the fact that the effect of deviation from stoichiometry proves to be weakly dependent on the Pu or MA content:

$$a\,(\mathrm{pm}) = 547.1 - 7.6\,z - 10.0\,y' - 3.8\,y'' + (25.8 - 0.9\,z - 1.1\,y' - 0.4\,y'')\,x \qquad \text{Eq. 2.7}$$

This correlation, based on a significant number of experimental data represented with great precision, could be considered as a new recommendation for the calculation of the lattice parameter of stoichiometric or hypo-stoichiometric uranium-plutonium-minor actinides mixed oxides within the following limits:

$0 \le Pu/M \le 100\%,\ 0 \le Am/M \le 2\%,\ 0 \le Np/M \le 12\%,\ 1.985 \le O/M \le 2.$

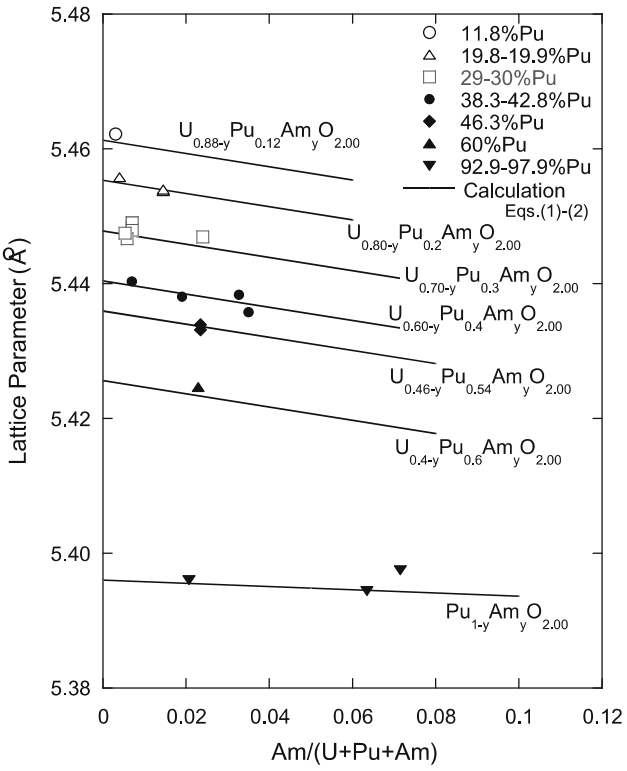

Figure 2.3: Effect of Am content on the lattice parameter of oxide $(U,Pu,Am)O_{2.00}$ [Kat09a].

This project has received funding from the Euratom research and training programme 2019-2020 under grant agreement No 945022.

Kurosaki et al. [Kur04] have directed molecular dynamics calculations aimed at studying the effect of addition of americium on the lattice parameter of MOX fuel of type $U_{0.7-x}Pu_{0.3}Am_xO_2$ (with x = 0; 0.016; 0.03; 0.05; 0.1 and 0.15) as a function of temperature (Figure 2.4). The lattice parameter of $U_{0.7-x}Pu_{0.3}Am_xO_2$ decreases with the addition of americium. Their calculation is consistent with the limited data available in the literature.

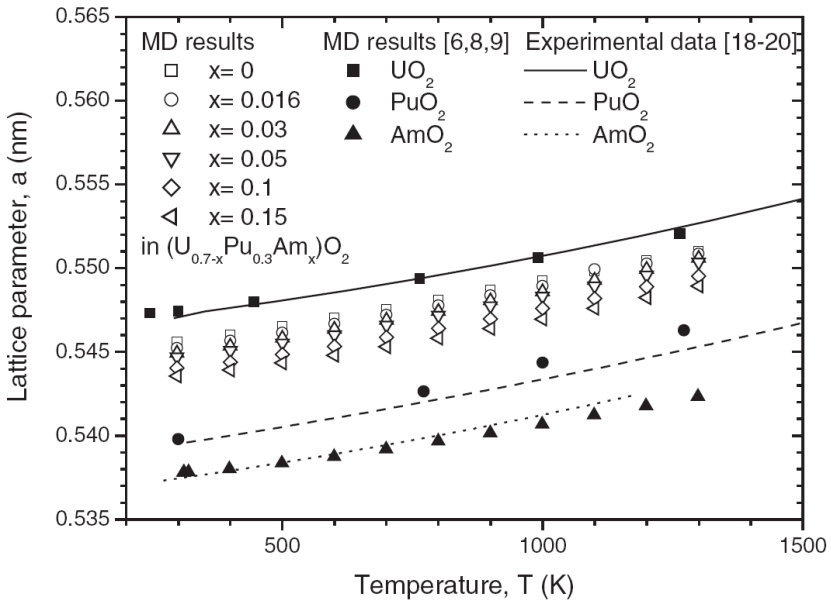

Figure 2.4: Variation of the lattice parameter of MOX fuel of type $U_{0.7-x}Pu_{0.3}Am_xO_2$ as a function of temperature [Kur04].

2.1.4 Effect of self-irradiation

Self-irradiation α induces an increase of the lattice parameter as a function of time. The given recommendation (Eq. 2.8) is independent of the fuel composition, taking as parameter not the plutonium content but the dose absorbed by the material d, expressed in $\alpha.m^{-3}$ (one α-decay by m^3).

$$\Delta a\ (\mathrm{pm}) = 4.453\ 10^{-25}\ \mathrm{d}\ (\alpha.m^{-3}) \qquad \text{Eq. 2.8}$$

The change can be considered linear up to a dose of about 5 10^{24} $\alpha.m^{-3}$.

In 1994, Philipponneau conducted an in-depth study of the effect of α self-irradiation on the lattice parameter of uranium-plutonium mixed oxides [Phi94]. Taking account of the evolution of the O/M ratio over time helped to significantly reduce the dispersion of the experimental results and to suggest a new recommendation (Eq. 2.9) giving the variation of the lattice parameter as a function of the d dose absorbed by the material, expressed in $\alpha.m^{-3}$.

$$\Delta a\ (\mathrm{pm}) = 3.954\ 10^{-25}\ \mathrm{d}\ (\alpha.m^{-3}) \qquad \text{Eq. 2.9}$$

As previously, it applies up to a dose level of about 5 10^{24} $\alpha.m^{-3}$.

This project has received funding from the Euratom research and training programme 2019-2020 under grant agreement No 945022.

In 2009, Kato et al. [Kat09b] published a study on the effect of α self-irradiation in mixed oxides with Pu content between 17% and 49%. They proposed the following law of evolution for the lattice parameter (Eq. 2.10):

$$\Delta a/a_0 = 2.9\ 10^{-3}(1 - \exp(-12000\ \lambda' t)) \qquad \text{Eq. 2.10}$$

Where λ' is the average alpha decay constant of plutonium weighted by its isotopy taking into account ^{241}Am nuclides as given per Eq. 2.11. Relative expansion $\Delta a/a_0$ reached saturation to 0.29% after a sufficiently long storage time.

$$\lambda' = c_{Pu} \sum \lambda_i C_i \qquad \text{Eq. 2.11}$$

Where c_{Pu} is plutonium content, λ_i is decay constant (of α-decay) of plutonium isotope as given in Table 2.3 and C_i is plutonium isotopic composition.

Table 2.3: decay constant of Plutonium isotopes.

Isotope	Decay constant (s^{-1})
Pu^{238}	2.505×10^{-10}
Pu^{239}	9.116×10^{-13}
Pu^{240}	3.349×10^{-12}
Pu^{241}	6.869×10^{-14}
Pu^{242}	5.888×10^{-14}
Am^{241}	5.086×10^{-11}

2.1.5 Effect of Burn-up

Change of lattice parameter as a function of burn up (τ) has been established from experimental results obtained on PHENIX fuels. The recommended correlation for fast fuel is given by Eq. 2.12:

$$\Delta a\ (\mathrm{pm}) = -0.039\ \tau\ (\mathrm{at.\%}) \qquad \text{Eq. 2.12}$$

This correlation, established from experimental results obtained on PHENIX fuels, Is based on a reduced amount of experimental data. Then, it appears difficult to extrapolate this recommendation to all mixed oxide fuels, and therefore it should be used cautiously.

2.2 NEA recommendation

The recommended law in [NEA25] for lattice parameter calculation for solid solution $(U_{1-z-y'-y''}Pu_zAm_{y'}Np_{y''})O_{2-x}$ is the one proposed by Kato in Eq. 2.6, with ionic

This project has received funding from the Euratom research and training programme 2019-2020 under grant agreement No 945022.

radii given in Table 2.1 and Table 2.2. Comparison of this law to experimental data is given in Figure 2.5.

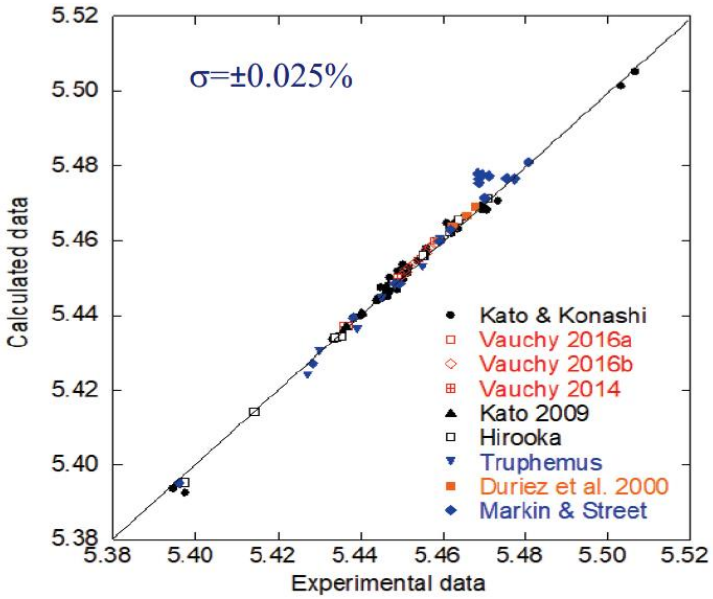

Figure 2.5: Comparison of calculated vs. experimental data of lattice parameter for MOX fuels [NEA25].

The lattice parameter slightly decreases with MA content, and increases with decreasing O/M, as shown in Figure 2.3.

The range of parameters for the validity of the recommendation is:

- O/M from 1.94 to 2.0
- Pu content from 10 to 45%
- Am content from 0 to 5%

Uncertainty is estimated to be σ = ± 0.025%.

2.3 Data obtained in the frame of ESFR-SMART project

In the frame of the ESFR-SMART project, lattice parameter on three fresh MOX samples were measured [ESF23]. Details of the measured samples and obtained results are given in Table 2.4.

As expected with Vegard's law, lattice parameter decreases when Pu content increases.

This project has received funding from the Euratom research and training programme 2019-2020 under grant agreement No 945022.

Table 2.4: Details of the three fresh $(U,Pu)O_2$ samples studied and measured lattice parameter.

Name	Composition	Lattice parameter (Å)
PHENIX29	$U_{0.70}Pu_{0.29}Am_{0.01}O_{1.984}$	5.445 ± 0.003
CAPRA4	$U_{0.70}Pu_{0.28}Am_{0.02}O_{2.004}$	5.446 ± 0.003
TRABANT40	$U_{0.60}Pu_{0.39}Am_{0.01}O_{1.995}$	5.434 ± 0.003

2.4 Data obtained in the frame of the PuMMA project

In the frame of the PuMMA project, lattice parameter was measured at 300 K on one fresh MOX samples (MOX70-F), manufactured by co-milling process, with an O/M ratio of 1.99 ± 0.01 and a Pu content of 69% [PuM25].
Lattice parameter was measured equal to 5.417 ± 0,001 Å. This value is in very good agreement with those calculated using the empirical relations developed by Kato and Konashi [Kat09a] and Duriez et al. [Dur00], respectively 5,416 Å and 5,418 Å (for calculation the considered plutonium content values were those determined by EPMA (0.704 %Pu/(U+Pu)) with an O/M ratio equal to 2.00).

2.5 Conclusions and recommendations

Taking into account the limitations of the law recommended for the calculation of the lattice parameter of $(U,Pu)O_{2-x}$ fuels as well as the limited number of published data, it is possible to propose a work plan as follows:

Verification of applicability limit of the recommendation

For significant values of deviation from the stoichiometry in oxygen, it seems essential to determine more precisely the plutonium content limit beyond which the law recommended for the calculation of the lattice parameter is no longer applicable. This limit must be less than the Pu content corresponding at the beginning of the miscibility gap observed in the phase diagram. However, the limit of the existence of this gap is controversial. Fine characterizations of hypo-stoichiometric samples $U_{1-y}Pu_yO_{2-x}$ (with $0.2 < y < 0.35$) elaborated by controlling the oxygen potential are needed.

Extension of the recommendation to higher Pu contents for minor deviations from stoichiometry in oxygen

Studies are needed in a wide Pu content range (20% – 40%) but for minor deviations from stoichiometry in oxygen ($1.985 < O/M < 2.000$) to validate the work of Sari and Kato tending to reveal the existence of a monophasic area.

Characterizations shall be clearly realized by X-ray diffraction (XRD) - nature of the phases and determination of the lattice parameter - but also by X-ray

This project has received funding from the Euratom research and training programme 2019-2020 under grant agreement No 945022.

absorption spectroscopy (XAS) at beamlines dedicated to radioactive materials [Den16]. This method could be used to quantitatively assess the oxidation state of U or Pu cations, and therefore determine the average value of the O/M ratio.

Extension of the recommendation to high temperature

The given recommendation is applicable only at room temperature. However, knowing the evolution of the lattice parameter as a function of temperature is of major interest for a better understanding of the in-pile fuel behaviour. The high-temperature X-ray diffractometer available at CEA could be used to extend the recommendation up to the melting point. These data could also be used to assess the thermal expansion coefficient depending on the plutonium content and compare the values thus obtained to those determined by dilatometry.

Influence of the Am and Np minor actinides

Finally, given the limited amount of data available in this area, the effect of minor actinides Am and Np on the lattice parameter must be considered. Samples doped to various Am and/or Np contents should be developed and characterized by XRD and XAS. These results will be compared to those published by Kato et al. [Kat09a]. According to the results, an extension of the recommendation taking into account Am and Np could then be proposed.

2.6 References

[Ben69] U. Benedict and C. Sari, Studies on the ternary system UO_2-U_3O_8-PuO_2, presented at the European Atomic Energy Community - Euratom (1969).

[Den16] M.A. Denecke, 19 - X-Ray Spectroscopy in Studies of the Nuclear Fuel Cycle, in: J.A.V. Bokhoven, C. Lamberti (Eds.), X-Ray Absorpt. X-Ray Emiss. Spectrosc., John Wiley & Sons, Ltd, (2016) pp. 523–559.

[Dur00] C. Duriez, J.P. Alessandri, T. Gervais, and Y. Philipponneau, Thermal conductivity of hypostoichiometric low Pu content (U,Pu)O_{2-x} mixed oxide, J. Nucl. Mater. 277 (2000) 143.

[ESF23] D. Staicu, D. Robba, L. Vlahovic, P. Pöml, E. Dahms, P. Fouquet-Metivier, F. Cabezas, M.-M. Desagulier, Ph. Martin, N. Chauvin, I. Viallard and J.-C. Dumas, « New measurements of properties of MOX fuel with associated characterizations », Deliverable D2.5.5, ESFR-SMART European Project (2023).

[Jav72] N. Javed and J. Roberts, Thermodynamic and Defect-Structure Studies in Mixed Oxide Fuels, Argonne National Laboratory, ANL-7901, (1972).

[Kat06] M. Kato, H. Uno, T. Tamura, K. Morimoto, K. Konashi and Y. Kihara, Phase Relation of Mixed Oxide Fuel Containing Np and Am, in Recent Advance in Actinide Science - Actinides 2005, Manchester, 2006, p. 367.

[Kat09a] M. Kato and K. Konashi, Lattice parameters of (U,Pu,Am,Np)O_{2-x}, J. Nucl. Mater. 385 (2009) 117.

This project has received funding from the Euratom research and training programme 2019-2020 under grant agreement No 945022.

[Kat09b] M. Kato, A. Komeno, H. Uno, H. Sugata, N. Nakae, K. Konashi and M. Kashimura, Self-radiation damage in plutonium and uranium mixed dioxide, J. Nucl. Mater. 393(1) (2009) 134.

[Koi69] M. Koizumi and Y. Nakamura, Phase studies and fuel performance in the system Pu-U-O, Am. Ceram. Soc. Bull., 48 (1969) 476.

[Kom10] A. Komeno, M. Kato, H. Uno, K. Takeuchi, K. Morimoto and M. Kashimura, Phase separation behaviour of $(U_{0.7},Pu_{0.3})O_{2-x}$ (1.92<x<2.00) based fuels containing actinides and/or lanthanides, Actinides 2009 IOP Series: Materials Science and Engineering, vol. 9, no. 1 (2010) p. 012016.

[Kur04] K. Kurosaki, M. Imamura, I. Sato, T. Namekawa, M. Uno and S. Yamanaka, Molecular Dynamics Studies of Minor Actinide Dioxides, J. Nucl. Sci. and Tech. 41 (2004) 827.

[Mar67] T.L. Markin and R.S. Street, The Uranium-Plutonium-Oxygen ternary phase diagram, J. Inorganical Nucl. Chem. 29 (1967) 2265.

[Mor09] K. Morimoto, M. Kato, M. Ogasawara and M. Kashimura, Thermal conductivity of $(U,Pu,Np)O_2$ solid solutions, J. Nucl. Mater. 389 (2009) 179.

[NEA25] N. Chauvin et al., Recommendations on Fuel Properties for Fuel Performance Codes, NEA/NSC/R(2024)1, July 2025

[Phi90] Y. Philipponneau, Private communication (1990)

[Phi94] Y. Philipponneau, Private communication (1994)

[Sar70] C. Sari, U. Benedict and H. Blank, A study of the ternary system UO_2-PuO_2-Pu_2O_3, J. Nucl. Mater. 35 (1970) 267.

[Sha76] R.D. Shannon, Revised Effective Ionic Radii and Systematic Studies of Interactomic Distances in Halides and Chalcogenides, Acta Cryst. A32 (1976) 751.

This project has received funding from the Euratom research and training programme 2019-2020 under grant agreement No 945022.

3. Thermal conductivity

This chapter was originally provided by D. Staicu (JRC-Karlsruhe).

3.1 Literature data

In 1990, Philipponneau recommended equation Eq. 3.1 to calculate the thermal conductivity of mixed oxide fuel.

$$\lambda = \left[\frac{1}{A + BT} + CT^3\right]\alpha \qquad \text{Eq. 3.1}$$

Where:
T = temperature (K)
A = coefficient depending on the deviation from stoichiometry x = 2-O/M and on the fractional burn-up τ calculated by Eq. 3.2:

$$A = 1.320\sqrt{x + 0.00931} - 0.0911 + 0.38\tau \quad [\text{m.W}^{-1}.\text{K}^{-1}] \qquad \text{Eq. 3.2}$$

B = 2.493 10^{-4} $m.W^{-1}$ (constant)
C = 88.40 10^{-12} $W.m^{-1}.K^{-4}$ (constant)
α = porosity correction factor calculated with Eq. 3.3

$$\alpha = \frac{1 - p}{1 + 2p} \qquad \text{Eq. 3.3}$$

The ranges of applicability are:

- 500K < T < melting point
- O/M ≤ 2.00
- Pu content limits 0 < y < 0.30
- Porosity limits 0 ≤ p ≤ 0.4

The thermal conductivity is considered as independent of the plutonium content, which was clearly shown for fresh fuels in the range 0.15 < y < 0.30, and would need be checked below 0.15.

The influence of non-stoichiometry was quantified using fresh fuels measurements results.

The effect of burn-up is introduced using results for simulated irradiated fuels [Har73] or models. The influence of burn-up considers only the effect of some solid fission products and was deduced from only a small number of results, with a large uncertainty due to the O/M correction. The available results correspond to doped samples where the O/M ratio is expected to have decreased and to a model by Martin.

This project has received funding from the Euratom research and training programme 2019-2020 under grant agreement No 945022.

3.1.1 Effect of the Plutonium content and stoichiometry

A slightly revised recommendation was published in the open literature by Philipponneau for FBR MOX in 1992 [Phi92]. Inoue [Ino00] proposed a formula for fast reactors fuels giving similar results as the formula of Philipponneau for stoichiometric fuel but predicting a weaker effect of non-stoichiometry. He has validated his law on measurements made in JOYO facility, on hypo-stoichiometric fuel (O/M ratio of 1.95 and 1.96), illustrated on Figure 3.1.

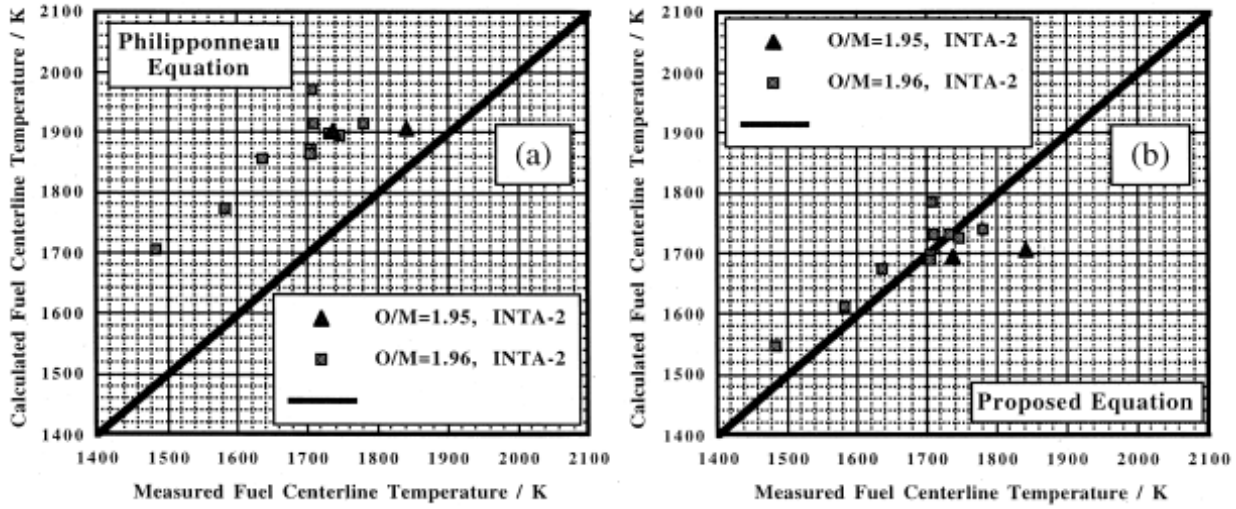

Figure 3.1: Thermal conductivity for hypo-stoichiometric MOX proposed by Inoue [Ino00]

Duriez et al. [Dur00] has measured the thermal diffusivity and deduced the thermal conductivity for unirradiated LWR MOX with Pu contents between 3 and 15 wt.%. They have shown that the conductivity of stoichiometric LWR MOX is lower than for UO_2 and in the same range as the recommendation of Philipponneau for FBR MOX (Figure 3.2). A significant difference in thermal conductivity is observed between LWR and FBR MOX for hypo-stoichiometric fuels, the impact of non-stoichiometry is stronger in FBR fuel.

This project has received funding from the Euratom research and training programme 2019-2020 under grant agreement No 945022.

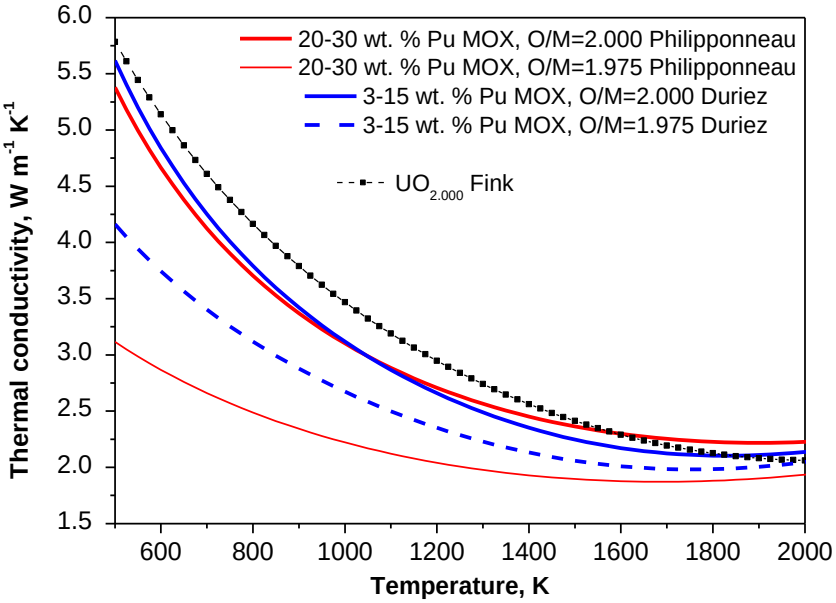

Figure 3.2: Conductivity of MOX at 95% TD obtained with the correlations of Duriez and Philipponneau, and thermal conductivity of UO_2 recommended by Fink [Fin00].

Kato [Kat11] and Morimoto [Mor08a, Mor08b] have measured the thermal conductivity of FBR MOX with 30% Pu and proposed a correlation for the effect on non-stoichiometry. The conductivities of Kato and Philipponneau are compared in Figure 3.3. For stoichiometric fuel, the conductivity of Kato is higher than UO_2 in the low temperatures range. The conductivity of Kato is higher than the recommendation of Philipponneau, both for stoichiometric and hypo-stoichiometric fuels. The conductivity of FBR MOX obtained with the recommendation of Kato is compared to the results of Duriez for LWR MOX in Figure 3.4. The conductivity of Kato for stoichiometric fuel is higher, but a relatively good agreement is observed for hypo-stoichiometric fuel.

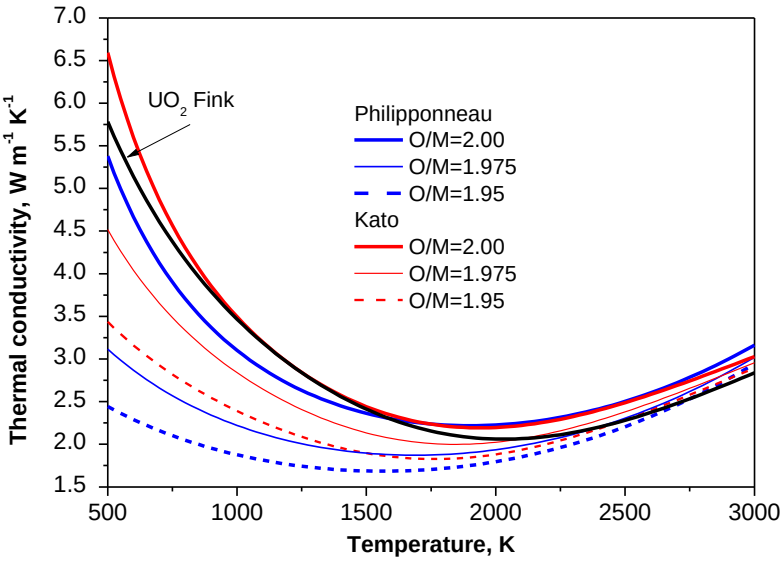

Figure 3.3: Conductivity of FBR MOX at 95% TD obtained with the recommendation of Philipponneau compared to the results of Kato [Kat11].

This project has received funding from the Euratom research and training programme 2019-2020 under grant agreement No 945022.

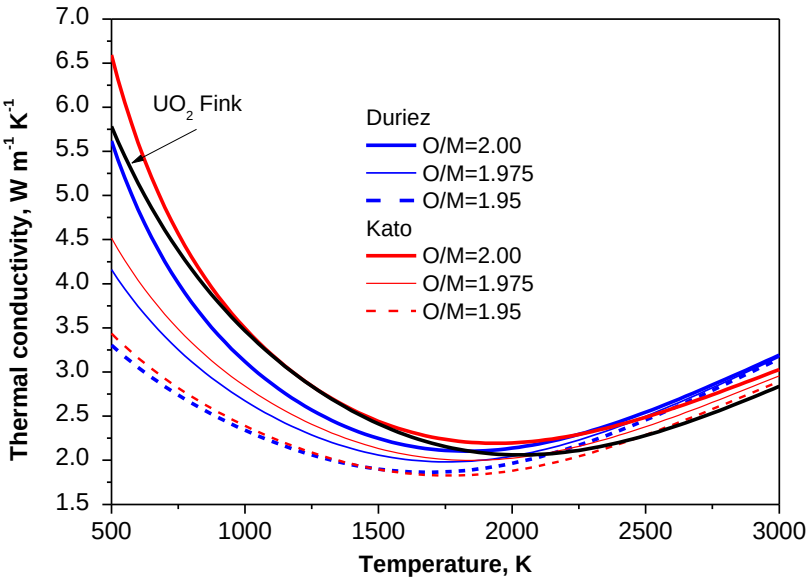

Figure 3.4: Conductivity of FBR MOX at 95% TD obtained with the recommendation of Kato compared to the results of Duriez for LWR MOX.

Sengupta [Sen09] measured the thermal diffusivity and deduced the thermal conductivity of stoichiometric FBR MOX with 44% Pu and a density of 82% TD. The obtained thermal conductivity was converted to 95% TD (Figure 3.5) and is significantly below the recommendation of Philipponneau for FBR fuel, which was interpreted as due to the high Pu content.

Vasudeva Rao [Vas06] measured the thermal diffusivity and deduced the thermal conductivity of stoichiometric FBR MOX with 21, 28 and 40 % Pu and a density of about 96% TD (Figure 3.5). Vasudeva Rao observed that the thermal conductivity decreases with the increase of the plutonium content. The uncertainty on these results is probably high, as suggested by the crossing of the curves.

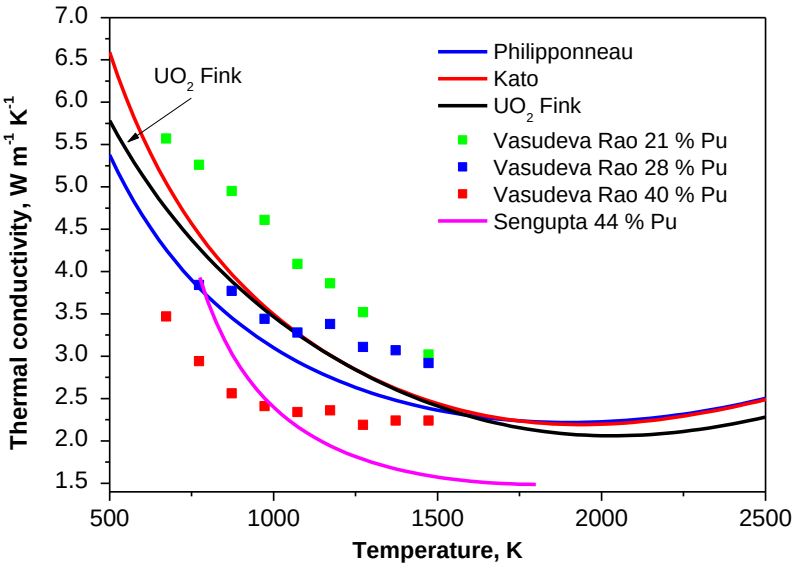

Figure 3.5: Conductivity of FBR MOX determined by Vasudeva Rao and Sengupta, and comparison to the recommendation of Philipponneau and to the results of Kato [Kat12].

This project has received funding from the Euratom research and training programme 2019-2020 under grant agreement No 945022.

The effect of the Plutonium content in LWR MOX fuels was investigated by Staicu et al. [Sta13] and it was concluded that the difference in thermal conductivity between LWR UO_2 and MOX fuels with Pu contents up to 11% is not linked to the Pu content but can mainly be attributed to the stoichiometry fluctuations in heterogeneous MOX. The study included homogeneous and heterogeneous MOX samples with Pu contents up to 11% and can therefore not be extrapolated to FBR MOX.

Recently, Magni et al. [Mag20] has considered a slight effect of the plutonium content for the thermal conductivity of MOX fuel, in the range between 0 and 45wt.%, supported by literature works [Dur00, Phi92], and by the recent measurements on TRABANT fresh MOX fuel performed in the framework of the ESNII+ European Project [Sta17b].

The correlation for fresh MOX thermal conductivity obtained by Magni et al is given as per Eq. 3.4:

$$k_0(T,x,[Pu],p) = \left(\frac{1}{A_0 + A_x \cdot x + A_{Pu} \cdot [Pu] + (B_0 + B_{Pu}[Pu])T} + \frac{D}{T^2} e^{-\frac{E}{T}}\right)(1-p)^{2.5} \qquad \text{Eq. 3.4}$$

Where :

$A_0 = 0.01926$
$A_x = 1.06 \cdot 10^{-6}$
$A_{Pu} = 2.63 \cdot 10^{-8}$
$B_0 = 2.39 \cdot 10^{-4}$
$B_{Pu} = 1.37 \cdot 10^{-13}$
$D = 5.27 \cdot 10^{+9}$
$E = 17109.5$

Other than from experimental approach, Molecular Dynamic calculations were performed to estimate the evolution of fresh fuel thermal conductivity with Pu content. Cooper et al. [Coo15] investigated Pu content impact by molecular dynamic using non-equilibrium method from 300 to 2000 K. Figure 3.6 from [Coo15] evidences a sensible effect of Pu content up to about ~1600 K, as expected. Most interesting point is that Pu degrades thermal conductivity in $(U,Pu)O_2$ up to 25% content roughly, but then lead to an increase of the thermal conductivity. This work also indicates that, from temperature of interest in Fast Reactor (at least 800 K and more) it seems reasonable not to account of Pu content in thermal conductivity, at least for stoichiometric fuel. Indeed, the deviation from 0 Pu to 100 % Pu is very limited above this temperature.

This project has received funding from the Euratom research and training programme 2019-2020 under grant agreement No 945022.

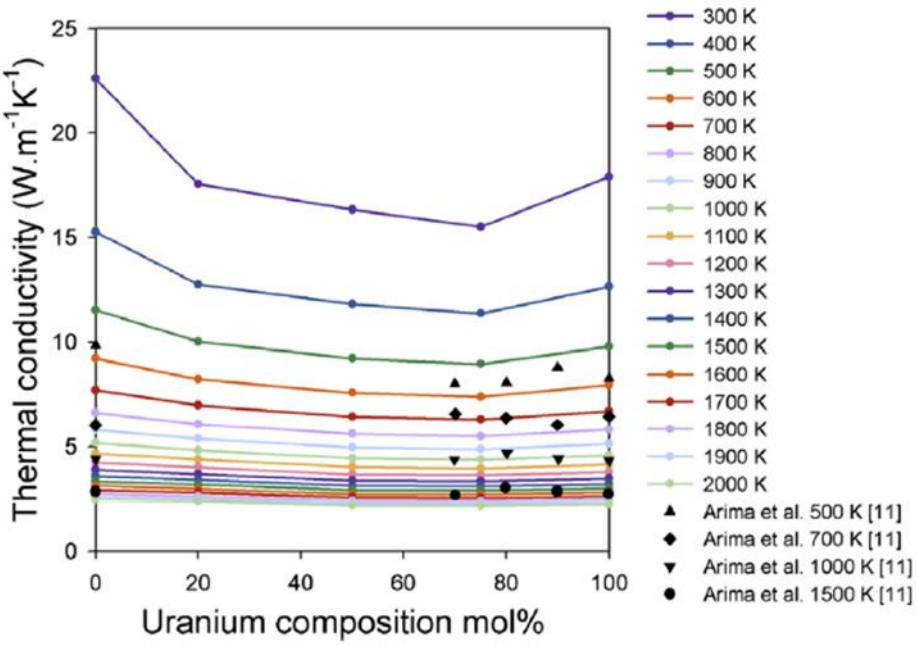

Figure 3.6: The variation of thermal conductivity as a function of uranium composition for $(U_xPu_{1-x})O_2$ at a range of temperatures obtained in [Coo15].

3.1.2 Effect of porosity

The effect of porosity on fuel thermal conductivity is hard to experimentally investigate as the samples porosity value varies and a correction is applied in order to compare results obtained by different authors. Usually, the thermal conductivity data are converted to 95% or 100% TD.

Philipponneau recommended the formula given per Eq. 3.5:

$$\alpha = \frac{1-p}{1+2p} \qquad \text{Eq. 3.5}$$

Kato used the correction factor given by Eq. 3.6:

$$\alpha = \frac{1-p}{1+0.5p} \qquad \text{Eq. 3.6}$$

Brandt and Neuer [Bra76] proposed a formula which was later recommended by Fink [Fin00] for the normalisation of the LWR UO_2 conductivity to 95% TD as given per Eq. 3.7.

$$\alpha_{95} = \frac{1-0.05\ f(T)}{1-p\ f(T)} \qquad \text{Eq. 3.7}$$

where $f(T)$=2.6-0.5 T/1000 and T is in °C.

This project has received funding from the Euratom research and training programme 2019-2020 under grant agreement No 945022.

The formula of Brandt and Neuer takes into account the radiative heat transfer in the pores, which results in the temperature dependence of this correction.

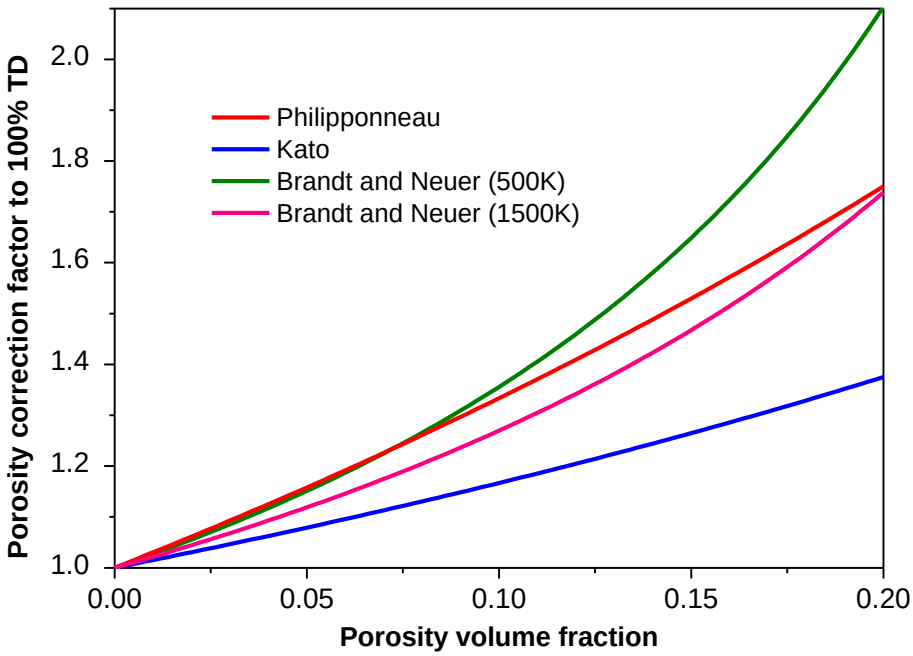

Figure 3.7: Porosity correction factor (from a given porosity to 100%TD) for the thermal conductivity evaluated by three correlations.

The porosity correction factor (from a given porosity to 100%TD) for the thermal conductivity evaluated by these three correlations is shown in Figure 3.7 for porosity volume fractions between 0 and 0.2. The formula of Kato gives the smallest correction factor. At the temperature of 500K and up to a porosity volume fraction of 0.1, the formulas of Philipponneau and Brandt and Neuer [Bra76] give identical correction factors. At the temperature of 1500K, the Brandt and Neuer formula gives a correction which is intermediary between the corrections of Philipponneau and Kato.

Finally, Magni [Mag20] used another factor as given per Eq. 3.8:

$$\alpha = (1-p)^{2.5} \qquad \text{Eq. 3.8}$$

3.1.3 Effect of burn-up

New out-of-pile thermal diffusivity measurements for irradiated LWR fuels were obtained since 1990, mostly for UO_2 fuels, a few for MOX fuels. These were used to obtain new correlations for the effects of burn-up and irradiation temperature on the thermal conductivity. For irradiated LWR MOX fuels, most of the in-pile central temperature measurements and out-of-pile thermal diffusivity results show that the thermal conductivity of irradiated UO_2 and LWR MOX can be supposed to be equal, within the uncertainties.

A relatively large number of out-of-pile thermal diffusivity measurements for irradiated LWR fuels were obtained [Ama02, Yag00, Coz08, Hir97, Min01, Nak98, Sta07, Sta14 as examples]. Only one publication is available for FBR MOX with

This project has received funding from the Euratom research and training programme 2019-2020 under grant agreement No 945022.

17.7 % Pu and burn-ups of 8, 19 and 35 GWD/t [Yam93], but surprisingly no burn-up degradation of the thermal conductivity was observed.

- **Correlation of NFI (1997-2005)**

Ohira [Ohi97] proposed the 'NFI' model (Eq. 3.9, Table 3.1) for the thermal conductivity, based on experimental results for an UO_2 fuel with about 61 MWd·kgHM^{-1}. A linear dependence of the parameter A on burn-up was assumed for the effect of fission products in solution, *f(bu)*, and the effect of radiation damage was modelled as increasing slowly with burn-up (proportional to $bu^{0.28}$) and to be progressively annealed when temperature increases, as described by h(T).

$$\lambda_{95} = \frac{1}{A + B \cdot T + f(bu) + g(bu)h(T)} + C \cdot T^2 + D \cdot T^4 \qquad \text{Eq. 3.9}$$

Lanning [Lan05] modified this model (Eq. 3.10, Table 3.1) and verified it against the experimental results of Carroll [Car94] and Ronchi [Ron04].

$$\lambda_{95} = \frac{1}{A + a \cdot gad + B \cdot T + f(bu) + (1 - 0.9e^{-0.04 \cdot bu})g(bu)h(T)} + \frac{E}{T^2} e^{\frac{-F}{T}} \qquad \text{Eq. 3.10}$$

The Duriez-Modified NFI model (Eq. 3.11, Table 3.1) was proposed for MOX fuels [Lan05]. It is a combination of the fresh MOX fuel model of Duriez [Dur00] and the modified NFI model for irradiated UO_2, incorporating a modification of the high temperatures term of Duriez (C_{mod}). The constants A(x), B(x) and D are those proposed by Duriez for fresh MOX and x is the deviation from stoichiometry (i.e. x=2-O/M). This model was verified by PNNL using in-pile fuel central temperature measurements.

$$\lambda_{95} = \frac{1}{A(x) + B(x) \cdot T + f(bu) + (1 - 0.9e^{-0.04 \cdot bu})g(bu)h(T)} + \frac{C_{mod}}{T^2} e^{\frac{-D_1}{T}} \qquad \text{Eq. 3.11}$$

Table 3.1: Constants of the NFI and NFI based models.

a = 1.1599	A = 0.0452 m·K·W^{-1}
gad : weight fraction of gadolinia	B = 2.46·10^{-4} m·K·W^{-1}·K^{-1}
f(bu) = 0.00187·bu : effect of fission products in solution in the matrix	C=-5.47·10^{-9} W·m^{-1}·K^{3}
g(bu) = 0.038·$bu^{0.28}$ effect of irradiation defects	D=2.29·10^{14} W·m^{-1}·K^{-5}
h(T)=1/(1+396 exp(-6380/T)) : annealing of irradiation defects	D_1 = 13520 K
x = 2.00 – O/M (O/M is the oxygen-to-metal ratio)	E = 3.5·10^{9} W·K·m^{-1}
A(x) = 2.85x + 0.035 m·K·W^{-1}	F = 16361 K
B(x) = (2.86 - 7.15x)·10^{-4} m·W^{-1}	C_{mod}=1.5·10^{9} W·K·m^{-1}

This project has received funding from the Euratom research and training programme 2019-2020 under grant agreement No 945022.

- **Correlation of Baron and NFIR (1998-2004)**

Using NFIR experimental results for UO_2 up to a burn-up of 80 MWd·kgHM^{-1}, Baron [Bar98] proposed a correlation where thermal recovery during the out-of-pile annealing is accounted for by using the variation of the lattice parameter as a marker of the matrix damage evolution. Comparison with experimental results shows a good agreement, but the application of the correlation is possible only when the lattice parameter is known. For this reason, approximate formulae for A_0 and B_0 for the conductivity before recovery were deduced from the original plots. The correlation includes the effect of Pu and Gd. The effects of these two additives were obtained from fresh fuel measurements and from NFIR results for irradiated gadolinia fuel [Bar98].

An updated correlation for UO_2 and $(U,Gd)O_2$ (Eq. 3.12) was derived by Yagnik et al. from the NFIR thermal conductivity results obtained on samples irradiated below 800°C [Yag04] . This correlation takes into account the thermal recovery observed during laboratory measurements. The lattice thermal conductivity before and after thermal recovery is given by λ_{start} and λ_{end}, respectively, and the temperature dependence of the fission products redistribution and radiation damage recovery is given by the coefficient F. The burn-up, Bu, is in MWd·kgHM^{-1} and T is in °C.

$$\lambda_{95}(Bu) = (1-F)\cdot\lambda_{start} + F\cdot\lambda_{end} + \lambda_{el} \qquad \text{Eq. 3.12}$$

with:

$$\lambda_{start} = \frac{1}{A_1 + A_2\cdot Bu + A_3\cdot Bu^2 + (B_1 - B_2\cdot Bu)\cdot T(°C)}$$

$$\lambda_{end} = \frac{1}{A_1 + A_4\cdot Bu + (B_1 - B_3\cdot Bu)\cdot T(°C)}$$

$$\lambda_{el} = C\cdot e^{D\cdot T(°C)}$$

$$F = 0.5\left(1 - tanh\left(\frac{T(°C) - 900}{150}\right)\right)$$

For $(U,Gd)O_2$ the same formula is used, replacing the coefficients A_1 and B_1 by:

$$A'(Gd) = \left(A_5 + A_6\cdot Gd + A_7\cdot Gd^2 + A_8\cdot Gd^3\right)\cdot 0.26\cdot e^{\frac{28.5875}{bu + 19.8085}} \quad \text{and} \quad B'(Gd) = B_1 e^{B_4\cdot Gd}$$

In this correlation, no information on the irradiation temperature or on the out-of-pile auto-irradiation is explicitly taken into account.

- **HBRP (2004)**

UO_2 and $(U,Gd)O_2$ samples were irradiated in the framework of the High Burn-up Rim Project (HBRP) which comprised a matrix of four burn-ups (from 34 to 96 MWd·kgHM^{-1}) and four irradiation temperatures (~750 to ~ 1500 K) [Ron04].

Kinoshita [Kin04] derived a first correlation (Eq. 3.13) summarizing the HBRP thermal conductivity results and including the effect of the HBS structure formation (Table 3.2). A slight increase of the conductivity normalized to 100% TD was observed after its formation.

This project has received funding from the Euratom research and training programme 2019-2020 under grant agreement No 945022.

$$\lambda = \frac{1}{A + B \cdot T} + \lambda_e \qquad \text{Eq. 3.13}$$

λ_e is the electronic contribution to the conductivity.

Table 3.2: Parameters of the thermal conductivity model of Kinoshita [Kin04].

$T < 1273K$ $A = (40 + 4.12 \cdot bu) \cdot 10^{-3}$ $bu < 50$ $B = 0.22 \cdot 10^{-3}$ $50 \le bu \le 80$ $B = (0.447 - 0.00453 \cdot bu) \cdot 10^{-3}$ $80 < bu$ $B = 0.084 \cdot 10^{-3}$	$T > 1473K$ $A = (40 + 1.74 \cdot bu) \cdot 10^{-3}$ $B = (0.22 + 0.0003 \cdot bu) \cdot 10^{-3}$	$1273 \le T \le 1473K$ linear interpolation between the conductivities in the two temperature regions

Ronchi obtained a second model based on the HBRP results [Ron04], taking explicitly into account the irradiation temperature. The model considers the effects of radiation damage, soluble and volatile fission products, and of the HBS formation.

- **Thermal conductivity determined from in-pile measurements**

The fuel thermal conductivity can be deduced from a measurement of the temperature history at the pellet centre during irradiation with a thermocouple. The main result was obtained by the Halden Reactor Project.

The thermal conductivity of irradiated UO_2 (Eq. 3.14) is given by Wiesenack [Wie97]. A recent adaptation was cited by Lanning [Lan05], including the effect of gadolinia.

$$k_{95} = \frac{1}{0.1148 + 3.05 \cdot 10^{-3} \cdot BU + 2.475 \cdot 10^{-4}(1 - 3.3 \cdot 10^{-3} \cdot BU)T_C} + 0.0132\, e^{0.00188 \cdot T_C} \qquad \text{Eq. 3.14}$$

The Halden Reactor Project also developed an adaptation of their correlation for MOX fuel, based on fuel central temperature measurements. As cited and adapted by Lanning et al. [Lan05], this formula is obtained by multiplying the phonon term of the formula for UO_2 by the factor 0.92, corresponding to the ratio of the conductivities of fresh UO_2 and LWR MOX.

Magni et al [Mag20] proposed recently a correlation for irradiated fuel in function of the burn-up bu in GWd/tHM, based on Yamamoto [Yam93] and ESNII+ results [Sta17b] as given per

$$k_{irr}(T, x, [Pu], p, bu) = k_{inf} + (k_0(T, x, [Pu], p) - k_{inf}) \cdot e^{-\frac{bu}{\varphi}} \qquad \text{Eq. 3.15}$$

Where: $k_{inf} = 1.755$ $\varphi = 128.75$

This project has received funding from the Euratom research and training programme 2019-2020 under grant agreement No 945022.

- **PhD Thesis of P. Bonev: assessing thermal conductivity of irradiated fuel using thermal mechanical and thermal chemistry approach to interpret NESTOR-3 measurements**

An interesting approach on MOX fast reactor fuel thermal conductivity modelling in the recent year has been done by P. Bonev in his PhD work [Bon23]. He worked on the impact of irradiation on thermal conductivity of SFR fuels, adapting Lucuta's model [Luc94] based on LWR SIMFUEL to SFR irradiated fuel pins characteristics. Lucuta's model assess thermal conductivity degradation with burnup using hypothesis on dissolved and precipitates fission product contribution to thermal conductivity of irradiated fuel. Thermal conductivity is then given as per Eq. 3.16.

$$\lambda(BU) = \lambda_0 \times F_{porosity} \times F_{FP_{precipitates}} \times F_{FP_{dissolved}} \times F_{Irradiation\ damage} \qquad \text{Eq. 3.16}$$

With : λ the thermal conductivity of irradiated fuel;

λ_0 the thermal conductivity of fresh 100% dense fuel;

$F_{porosity}$ the impact of porosity on thermal conductivity;

$F_{FP_{precipitates}}$ the impact of Fission Products (FP) precipitates on thermal conductivity;

$F_{FP_{dissolved}}$ the impact of FP in (U,Pu,PF)$O_{2\pm x}$ solid solution on thermal conductivity;

$F_{Irradiation\ damage}$ the impact of irradiation on fuel thermal conductivity.

His work identified in particular $F_{FP_{precipitates}}$ and $F_{FP_{dissolved}}$ using representative elements or compounds concentration:

- $F_{FP_{precipitates}}$: based on Maxwell-Eucken's formula for two dispersed phases representing the Grey Phase (i.e. $BaZrO_3$) which lower the fuel thermal conductivity and the Metallic precipitates (i.e. Mo, Ru, Tc, Rh, Pd) which is increasing the thermal conductivity. Impact depends on estimation of each phase thermal conductivity and and their own volume fraction;
- $F_{FP_{dissolved}}$: Using Nd impact on MOX fuel thermal conductivity (from dedicated experiments) as representative of dissolved FP, based on dissolved FP molar concentration higher than 0.1%.

Access to FP concentration in each phase or in solid solution depends on:

- Local burnup, temperature, stoichiometry, FP concentration and matter transport (U, Pu, PF), accessible from fuel performance code GERMINAL V2 (in his work);
- Thermal-chemistry calculation of phase equilibrium, accessible from ThermoCalc + TAF-ID database (in his work).

Applying his methodology to NESTOR-3 irradiation, he greatly improved thermal conductivity predictions of measurements performed from the maximum power elevation of the fuel pin, see Figure 3.8, MFP=Max Flux Plan data. However, his modelling, even if giving reasonable results for measurements on the Top of Fissile Column (TFC) at temperature above 1000 K, failed in predicting lower temperature, probably related to a missing parameter in the modelling at low temperature. Nevertheless, it shows the capability of this approach to adapt to different irradiation case better than traditional model (Philipponneau, Lucuta from PWR fuel).

This project has received funding from the Euratom research and training programme 2019-2020 under grant agreement No 945022.

The approach coupling thermal mechanical and thermal chemistry calculations to interpret irradiated fuel thermal conductivity measurements allow to better understand each phase contribution. The model derived appears to lead to better predictions and improved capability of adaptation to fuel irradiation specificity but requires including in fuel performance codes a thermal chemistry model to predict the chemical phases formation in the fuel.

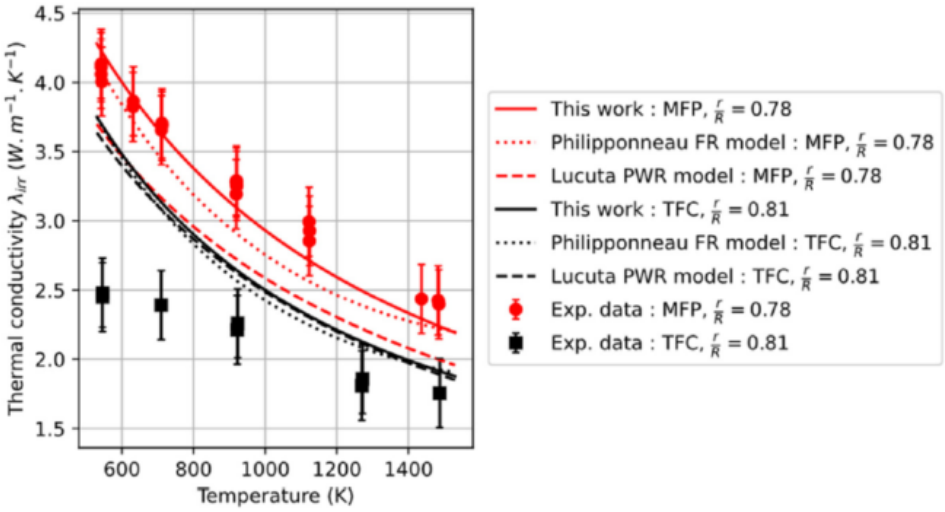

Figure 3.8: Bonev et al [Bon23] prediction of NESTOR-3 fuel thermal conductivity measurements

3.1.4 Relevance of LWR MOX results for FBR fuel

The thermal conductivities of irradiated LWR [Ron04] and FBR fuels (European Catalogue of 1990) with a burn-up of 13 at.% are compared in Figure 3.9. The thermal conductivity of irradiated LWR fuel evaluated with the recommendation of Ronchi [Ron04] is based on experimental results obtained up to 1500K both on as irradiated and annealed LWR fuel. The irradiated FBR fuel thermal conductivity recommended in the European Catalogue of 1990 results from fresh fuel measurements and a burn-up effect determined from fresh fuels with simulated burn-up effects. The thermal conductivity of LWR fuel was both evaluated at end of life (EOL) and annealed at 1500K, which is the maximum temperature for the correlation of Ronchi. The conductivity of the annealed LWR fuel is considered in order to have values corresponding to the high irradiation temperatures relevant for FBR fuels. It appears that the thermal conductivity of LWR fuel is much lower that the recommendation of Philipponneau, even if annealed LWR fuel is considered.

This project has received funding from the Euratom research and training programme 2019-2020 under grant agreement No 945022.

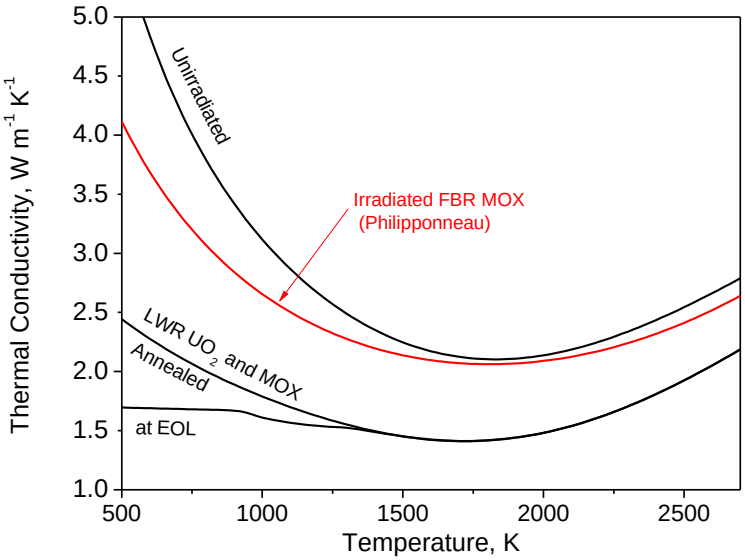

Figure 3.9: Recommendation of thermal conductivities of irradiated LWR fuel [Ron04] (determined from measurements on irradiated fuels up to 1500K and extrapolated up to 2700K using a standard high temperature contribution) and FBR fuel (European Catalogue of 1990, determined from simulated irradiated fuels) at the burn-up of 13 at.%.

3.2 NEA recommendation

The recommended law in [NEA25] for thermal conductivity is the one proposed by Kato [Kat11] and given in Eq. 3.17 as it is in good agreement with the most recent experimental results obtained by JAEA and JRC. Thermal conductivity is defined as a function of density, temperature, Np content, Am content and deviation to stoichiometry.

$$\lambda = \frac{(1-p)}{(1+0.5p)}\left[\frac{1}{(2.713x + 3.583\times10^{-1}\times z_1 + 6.317\times10^{-2}\times z_2 + 1.595\times10^{-2}) + (2.493 - 2.625x)\times10^{-4}T} + \frac{1.541\times10^{11}}{T^{5}/_{2}}exp\left(-\frac{1.522\times10^{4}}{T}\right)\right] \quad \text{Eq. 3.17}$$

With:
λ : thermal conductivity
p : porosity
x : deviation to stoichiometry in $MO_{2.00-x}$
z_1 : Am content
z_2 : Np content

Effect of porosity is taken into account via the recommended porosity correction factor (1-p)/(1=0.5p).

It was shown that Np and Am addition to MOX caused the data to decrease slightly in the lower temperature range of less than 1000K and the change was negligibly small in the operation temperature range of fast reactor MOX fuels. It was

This project has received funding from the Euratom research and training programme 2019-2020 under grant agreement No 945022.

estimated that the addition of 1.6% Am and 1.6% Np caused the thermal conductivity to decrease by 2.0–2.5%.

The range of parameters for the validity of the recommendation is:

- Temperature from 500 to 1800 K for fresh, stoichiometric fuels
- Temperature from 500 to 2270 K for fresh, hypostoichiometric fuels
- Temperature from 500 to 1600 K for irradiated fuels
- O/M from 1.92 to 2.00
- Pu content from 19 to 45%
- Porosity volume fraction from 0 to 15%

Uncertainty is estimated to be about 10% for fresh and irradiated fuels.

3.3 Measurements obtained in the framework of the ESNII+ Project

Measurements of thermal diffusivity on fresh and irradiated FBR MOX were obtained in the framework of the ESNII+ Project. Measurements on unirradiated PHENIX (24%Pu) and TRABANT2 (40 and 45% Pu) were obtained in order to investigate the effect of the plutonium content. The burn-up effect was investigated with irradiated Nestor 3 fuel (19.82% Pu, 12.5 at.%).

3.3.1 Fresh FBR MOX fuel

The thermal diffusivity of a fresh stoichiometric PHENIX MOX with a Pu content of 24 % and a density of about 95 % TD was measured and the thermal conductivity was deduced. In the temperature range from 500 to 1600 K, the thermal conductivity was interpolated with the 1/(A+BT) equation, with $A=2.135 \cdot 10^{-2}$ $K \cdot m \cdot W^{-1}$ and $B=2.493 \cdot 10^{-4}$ $m \cdot W^{-1}$. Thermal conductivity was found higher than the recommendations of Philipponneau and slightly higher than the recommendations of Kato (Figure 3.10).

TRABANT stoichiometric fuels obtained by mechanical milling with 40% Pu and TRABANT stoichiometric fuels obtained by sol-gel with 45% Pu were also measured in the framework of the ESNII+ Project. The thermal conductivities for the Pu contents of 40 and 45% are very close and significantly lower than the conductivity of the PHENIX fuel with 24% Pu but remain higher than the recommendation of Philipponneau for Pu contents from 15 to 30%. An effect of the Pu content on the thermal conductivity, as suggested by the measurements of Sengupta [Sen09] and Vasudeva Rao [Vas06] is therefore observed and is still present in the higher temperature range, as shown in Figure 3.11, where the uncertainties linked to the measurements of thermal diffusivity and density are taken into account (the specific heat was obtained using the same formula for all samples and does not introduce supplementary uncertainties in the comparison of the different Pu contents).

This project has received funding from the Euratom research and training programme 2019-2020 under grant agreement No 945022.

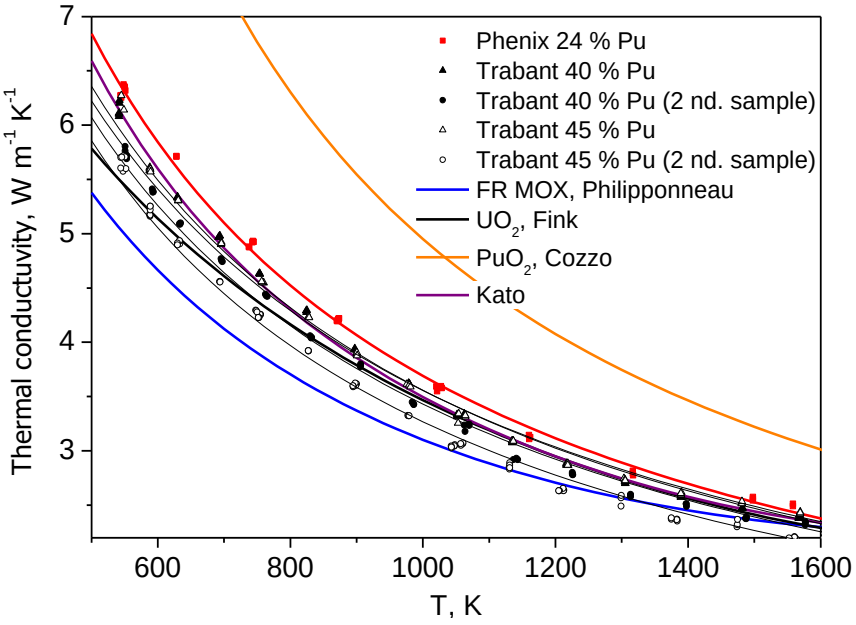

Figure 3.10: Thermal conductivity of fresh MOX with Pu contents of 24% (PHENIX), 40 and 45% (TRABANT) measured within the ESNII+ Project and comparison to literature data.

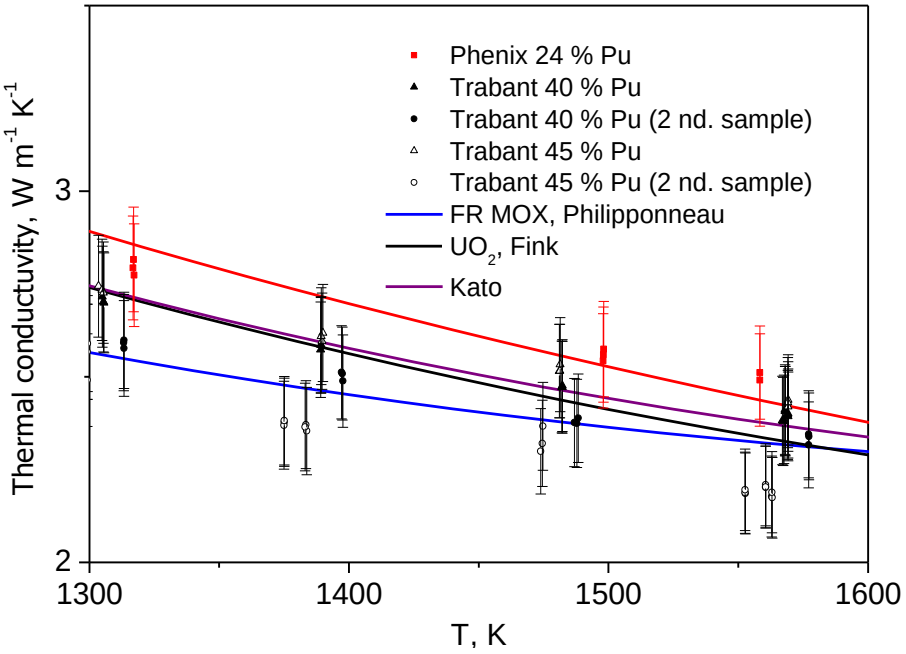

Figure 3.11: Thermal conductivity in the temperature range 1300 to 1600K of fresh MOX with Pu contents of 24% (PHENIX), 40 and 45% (TRABANT) measured within the ESNII+ Project and comparison to literature data

3.3.2 Irradiated FBR MOX fuel

The thermal diffusivity and specific heat were characterised for irradiated NESTOR 3 samples with burn-ups of 8.4 and 13 at.%. The results are presented in the ESNII+ deliverable D7.4.2 [Sta17a]. The two samples were obtained from

This project has received funding from the Euratom research and training programme 2019-2020 under grant agreement No 945022.

the same fuel pin, but from different axial positions. The sample with burn-up of 8.4 at % was irradiated near the top position of the fuel pin, where irradiation temperatures are lower than in the medium flux plane. The sample with a burn-up of 13 at % was irradiated near the medium flux plane, where the irradiation temperatures are the highest.

The thermal conductivity results have shown a non-trivial variation with burn-up, with the sample at 8.4 at.% burn-up having a lower thermal conductivity than the sample at 13 at.% burn-up (Figure 3.12). As shown in Figure 3.12, the sample with 13 at.% burn-up had higher local irradiation temperatures compared to the sample at 8.4 at.% burn-up.

The experimental results are compared to two correlations:

- The recommendation of Philipponneau for FBR MOX from the European Catalogue on FBR MOX fuel properties from 1990, also published in [Phi92], which was obtained from results on fresh FBR MOX fuels with a burn-up effect determined from simulated irradiated fuel (simfuel). As not all the burn-up effects are present in simfuel samples, the burn-up effect is underestimated in this kind of recommendation, as shown in [Wal06] for LWR simfuel.
- The recommendation of Ronchi [Ron04] for LWR UO_2 or MOX fuels, which was obtained from a large number of measurements up to 1500K on real irradiated LWR fuels. The advantage of this recommendation is that all the burn-up effects are taken into account, but the plutonium content and the irradiation temperatures are not in the range relevant for FBR fuels. As a consequence, the typical microstructure of FBR fuel and the extensive restructuring and diffusion processes are not taken into account.

For the sample at 13 at.% burn-up, the thermal conductivity was found to be significantly higher than observed experimentally for LWR UO_2 or MOX fuels [Ron04] at a similar burn-up. This can only be achieved by supposing a lower than expected effect of the non-volatile fission products, part of which are present in the JOG and therefore do not contribute anymore to the fuel thermal conductivity degradation. The thermal conductivity was found to be in good agreement with the recommendation of Philipponneau for FBR MOX. This fact can be a coincidence resulting from the fact that part of the fission products have diffused out of the fuel matrix, resulting in an attenuation of the expected burn-up effects and in a conductivity as high as for a simfuel.

At the burn-up of 8.4 at.%, the thermal conductivity was found to be in the range of that observed experimentally for LWR UO_2 or MOX fuels with similar burn-up, and significantly lower than the recommendation of Philipponneau for FBR MOX. This is probably due to the lower temperature during irradiation, resulting in less diffusion of fission products from the fuel matrix. This hypothesis is sustained by the reduced JOG thickness observed at this position, compared to the fuel irradiated at the burn-up of 13 at%. Differences in the fuel microstructure, in the recovery of irradiation defect, and a higher gas retention can also explain the observed differences in the thermal conductivity degradation.

The differences in the concentration of fission products dissolved in the fuel matrix, in their diffusion and the resulting variations in the extent of JOG and in the presence of metallic precipitates are proposed as major parameters for the estimation of the FBR fuel thermal conductivity. Therefore, simple correlations

This project has received funding from the Euratom research and training programme 2019-2020 under grant agreement No 945022.

based on temperature and burn-up, which give satisfactory results for LWR fuel, are not sufficient in order to predict the thermal conductivity of FBR fuel, and further measurements on irradiated FBR fuels are necessary.

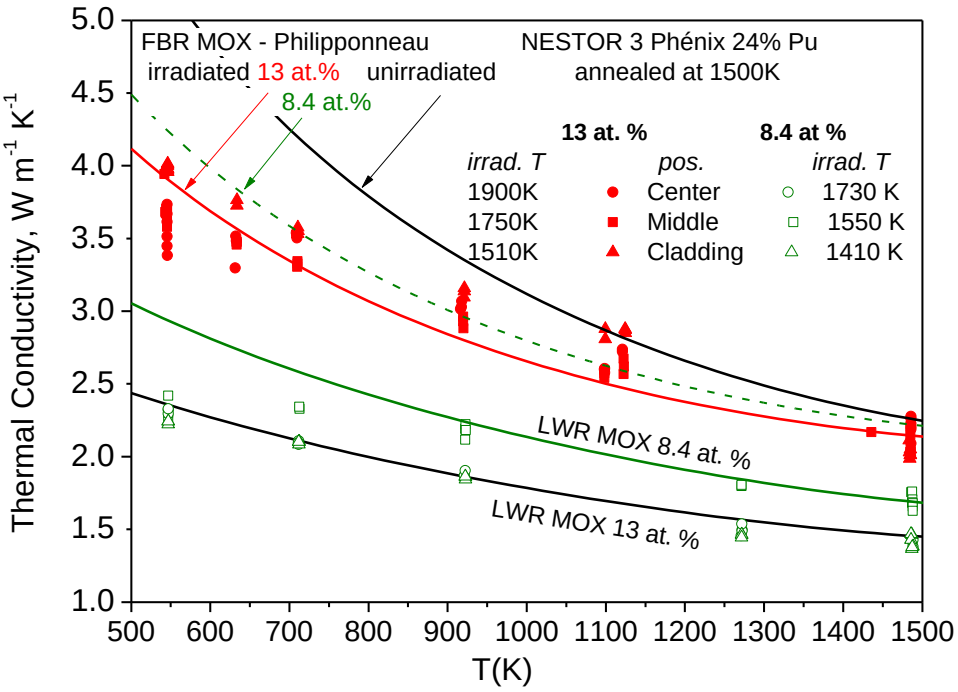

Figure 3.12: Comparison of the measurements for NESTOR 3 fuels at 8.4 and 13 at.% burn-up annealed at 1500 K with unirradiated MOX [Phi92] and irradiated fuels at the same burn-up:
LWR MOX [Sta11] and the recommendation of Philipponneau for FBR MOX [Phi92]. For each NESTOR 3 fuel, the conductivity was measured in 3 radial positions (Center, Middle, Cladding) characterized by different irradiation temperatures.

3.4 Data obtained in the frame of the ESFR-SMART project

3.4.1 Fresh fuel

In the framework of the ESFR-SMART project, the thermal diffusivity was measured, and the thermal conductivity was calculated on several fresh MOX samples, as described in [ESF23]. The names and chemical compositions of these samples are summarized in Table 3.3. The new measurements included thermal diffusivity and specific heat measurements on all the samples in the temperature range 1800-2800K, and thermal diffusivity measurements in the temperature range 550-1500K for the PHENIX29-OM and CAPRA4 samples which were not measured in the ESNII+ Project. The thermal conductivity results are plotted in Figure 3.13. In the low temperature range (550-1600K), the scatter in the data is low but no trend for the effect of the plutonium content could be observed. In the high temperature range (1600-2800K), the scatter in the data is high and here also no trend for the effect of the plutonium content could be recognized.

This project has received funding from the Euratom research and training programme 2019-2020 under grant agreement No 945022.

Table 3.3: Details of the fresh $(U,Pu)O_2$ studied samples.

Samples	Compositions
PHENIX24	$U_{0.76}Pu_{0.235}Am_{0.005}O_{1.983}$
PHENIX29	$U_{0.70}Pu_{0.29}Am_{0.01}O_{1.984}$
PHENIX29-OM	$U_{0.70}Pu_{0.29}Am_{0.01}O_{1.998}$
CAPRA4	$U_{0.70}Pu_{0.28}Am_{0.02}O_{2.004}$
TRABANT40-A	$U_{0.60}Pu_{0.39}Am_{0.01}O_{1.995}$
TRABANT40-B	$U_{0.60}Pu_{0.39}Am_{0.01}O_{1.978}$
TRABANT40-OM	$U_{0.60}Pu_{0.39}Am_{0.01}O_{1.999}$
RV45	$U_{0.55}Pu_{0.45}O_{1.987}$
TRABANT45	$U_{0.55}Pu_{0.44}Am_{0.01}O_{2.00}$

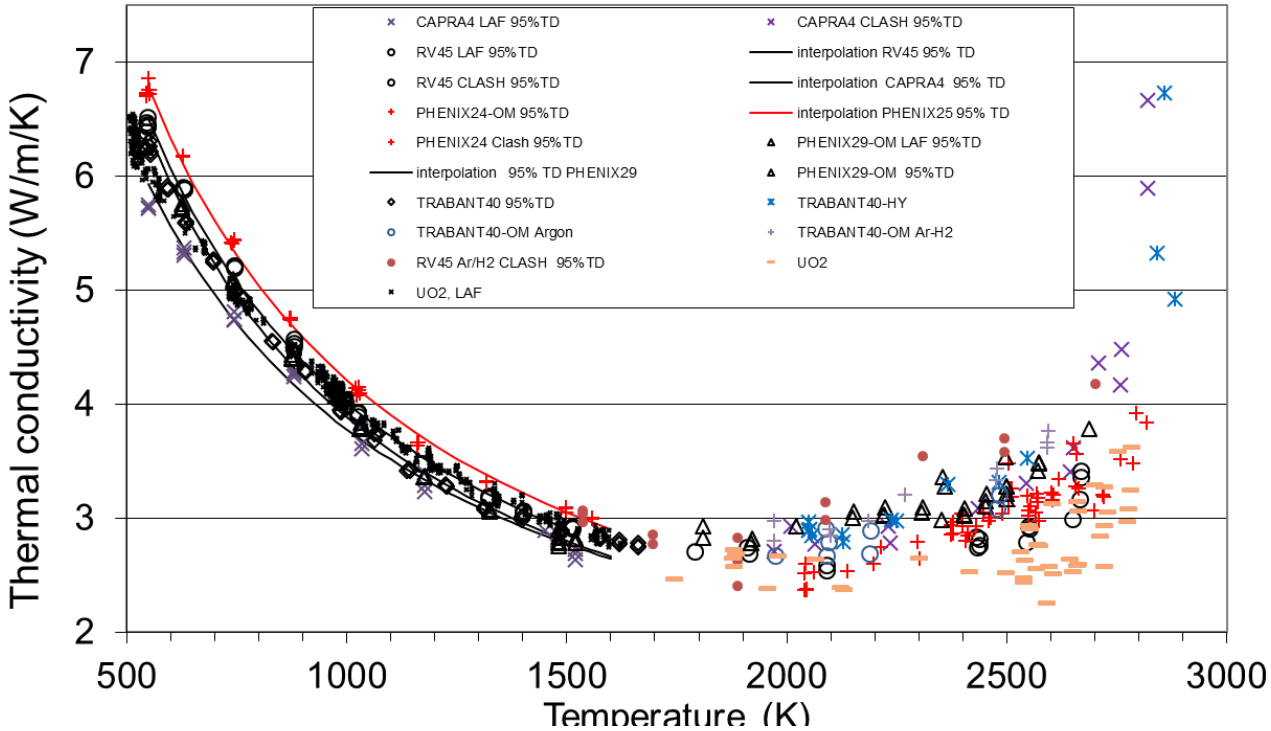

Figure 3.13: Thermal conductivity of the fresh MOX samples over the entire temperature range and comparison with UO_2.

The review and comparison of the literature data has shown that a clear difference is observed between a previous correlation [Phi92] and the most recent JAEA and JRC results presented in this report (Philipponneau recommendation for stoichiometric MOX being significantly below the recent results), but this difference decreases with increasing temperature as shown in Figure 3.14.

This project has received funding from the Euratom research and training programme 2019-2020 under grant agreement No 945022.

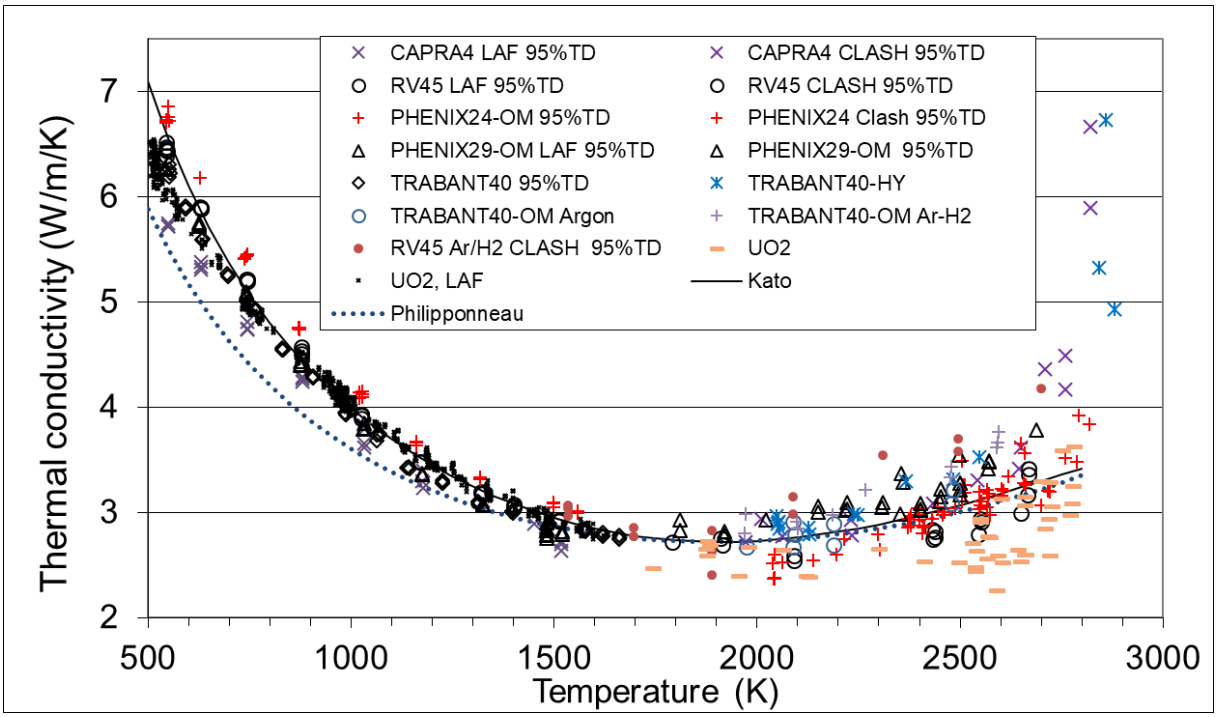

Figure 3.14: Thermal conductivity of the fresh MOX samples over the entire temperature range and comparison with UO_2.

JAEA and JRC obtained measurement results which are in very good agreement for stoichiometric fuels with various Pu contents. A clear trend with the Pu content was not observed. Only JAEA has obtained results for hypostoichiometric fuels and for different Am and Np contents, and has proposed a correlation based on these (see Eq. 3.17). Because the very good agreement with the data obtained at JRC for stoichiometric fuels, this correlation is recommended.

3.4.2 Irradiated fuel

In the framework of the ESFR-SMART project, thermal diffusivity was measured, and the thermal conductivity was calculated on two irradiated MOX fuels [ESF23]:

- PAVIX-8 pin: fresh fuel Pu content of 23.3%, initial O/M = 1.975 and burn-up = 13.0% FIMA.
- MYOSOTIS-12 pin: fresh fuel Pu content of 28.3%, initial O/M = 1.971 and burn-up = 15.2% FIMA.

The thermal conductivity was deduced from the measured thermal diffusivity, the density predicted by a fuel performance code and the specific heat of the fresh fuel. The results are shown in Figure 3.15.

This project has received funding from the Euratom research and training programme 2019-2020 under grant agreement No 945022.

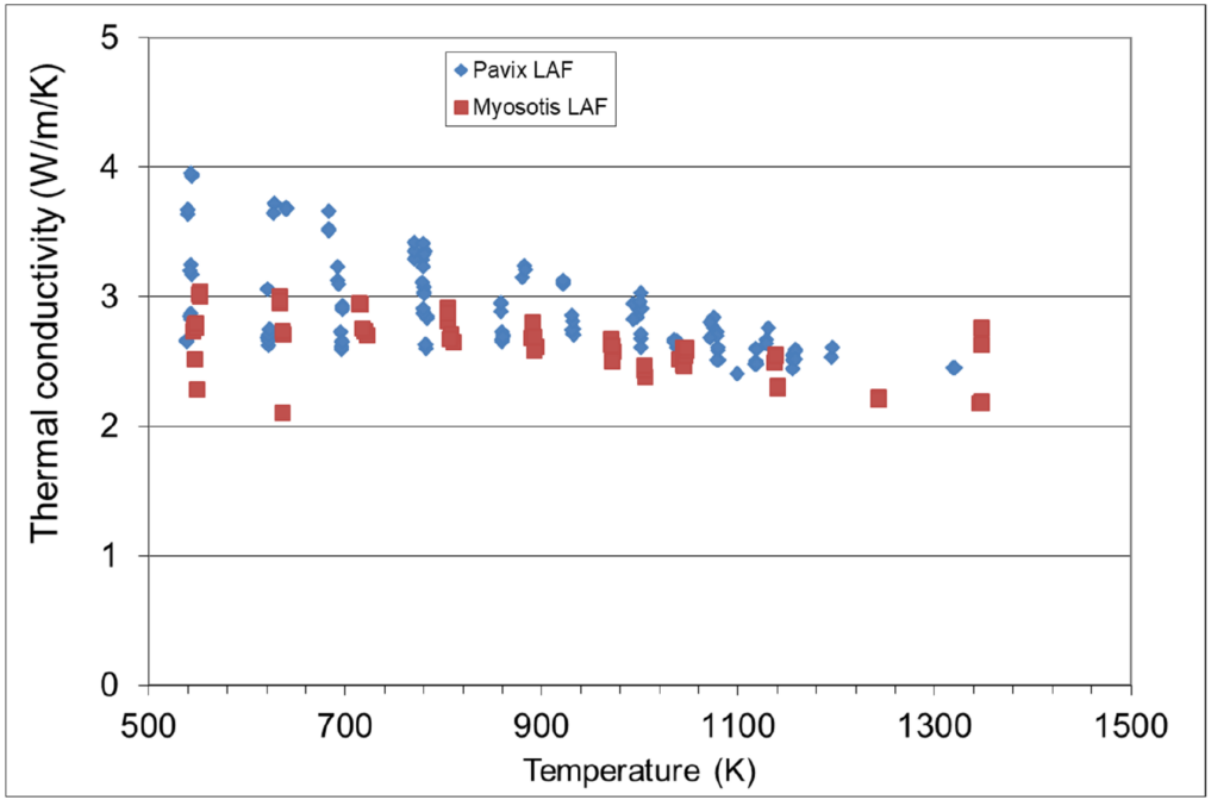

Figure 3.15: Thermal conductivity of irradiated PAVIX and MYOSOTIS MOX samples.

Thermal conductivity before recovery is in the same range for the two fuels, but after recovery PAVIX sample has a higher thermal conductivity. The lower thermal conductivity of the MYOSOTIS sample can be explained by the damage of the sample which took place during the measurement of the thermal diffusivity and was recognized by an increase scatter in the values.

3.5 Data obtained in the frame of the PuMMA project

3.5.1 Fresh fuel

In the frame of the PuMMA project, thermal diffusivity was measured on PuO_2 samples and 6 fresh MOX samples [PuM25a] :

- PuO_2 samples with an initial O/M = 2.00.
- Three stoichiometric samples (O/M = 1.99 ± 0.01) with Pu content of 59, 63 and 69% named MOX60-F, MOX65-F and MOX70-F respectively.
- Three annealed hypostoichiometric samples (O/M = 1.98) with Pu content of 59, 63 and 69% named MOX60-A, MOX65-A and MOX70-A respectively.

Thermal diffusivity was measured with laser-flash device (LAF) between 500 and 1500K for F batch only. No data were collected for the A batch as hypostoichiometry of the samples cannot be preserved within the LAF experimental setup. Uncertainty of measured thermal diffusivity is about 2%. The

This project has received funding from the Euratom research and training programme 2019-2020 under grant agreement No 945022.

same values were obtained for MOX60-F and MOX65-F on the whole temperature range. Concerning the MOX70-F sample, higher values were systematically measured up to 1400K. These experimental data were also compared with empirical law determined for 28 and 45% Pu/(U+Pu) in the frame of the ESFR-SMART project (see §3.4). The results obtained for MOX60-F and MOX65-F are in good agreement with the law as shown in Figure 3.16.

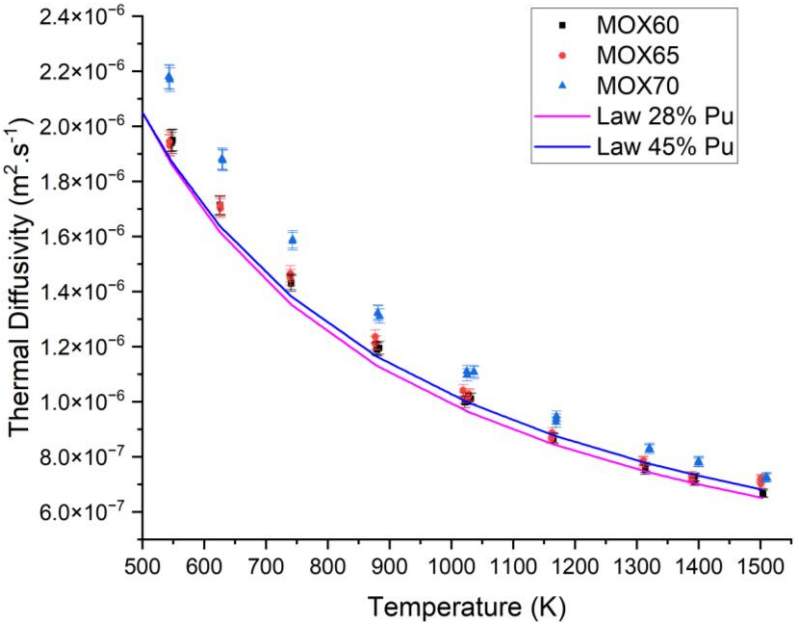

Figure 3.16: Thermal diffusivity measured by LAF compared to law obtained for 28 and 45% Pu/(U+Pu) in frame of the ESFR-SMART project [ESF23].

Measurements between ~ 1500K and ~ 2800K were done on all the 6 samples with the CLASH setup at JRC, under Ar and Ar + 6.5 H_2. Oxygen partial pressure was monitored and controlled inside the chamber, allowing the determination of O/M ratio of the samples after measurement. Although the scatter of the results is rather high, a tendency can be suggested with slightly lower values obtained with the A batch in both atmospheres, meaning a reduction of the samples (lower O/M ratio) would induce a decrease of the thermal conductivity above 1500 K.

All data acquisitions (LAF and CLASH) are shown in Figure 3.17 for each sample. One can see that thermal diffusivity decreases between 500 and 1500 K, then experimental values stabilise up to 3000 K. This pattern is consistent across the three plutonium contents studied, and there is a notable continuity in the measurements obtained from the two techniques employed. However, a higher dispersion can also be observed for measurements at high temperatures (T > 1500K), which corresponds to greater instability of the thermograms at elevated temperatures due to the experimental method: laser surface heating, non-isothermal conditions and low signal to noise ratio. The O/M characterizations performed after thermal diffusivity measurement, either with HERFD-XANES (High Energy Resolution Fluorescence Detected X-rays Absorption Near-Edge Spectroscopy) or with oxygen partial pressure follow-up in the experimental chamber during the experiment, show that O/M ratio remains constant over the whole temperature range, for all samples.

This project has received funding from the Euratom research and training programme 2019-2020 under grant agreement No 945022.

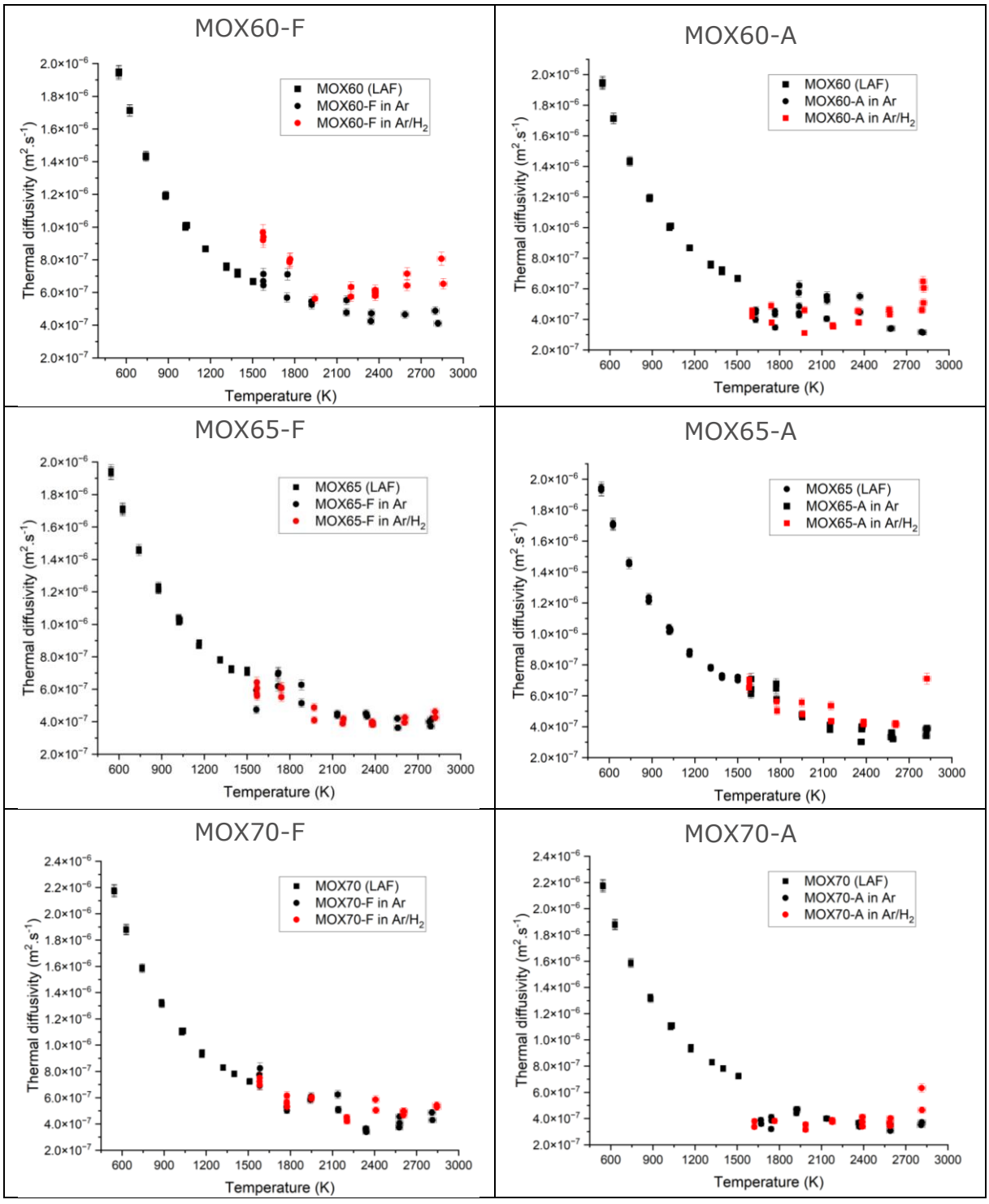

Figure 3.17: Thermal diffusivity of the fresh MOX samples over the entire temperature range.

The thermal diffusivity of PuO_2 was also measured with both facilities LAF and CLASH. The results are presented in Figure 3.18. The CLASH results under Ar are fitting well with results of LAF, performed under vacuum. The measured diffusivity under Ar + H_2 is lower than under Ar atmosphere up to 2000 K. Above 2200 K, the diffusivity seems to stabilise and slightly increasing at higher temperatures.

This project has received funding from the Euratom research and training programme 2019-2020 under grant agreement No 945022.

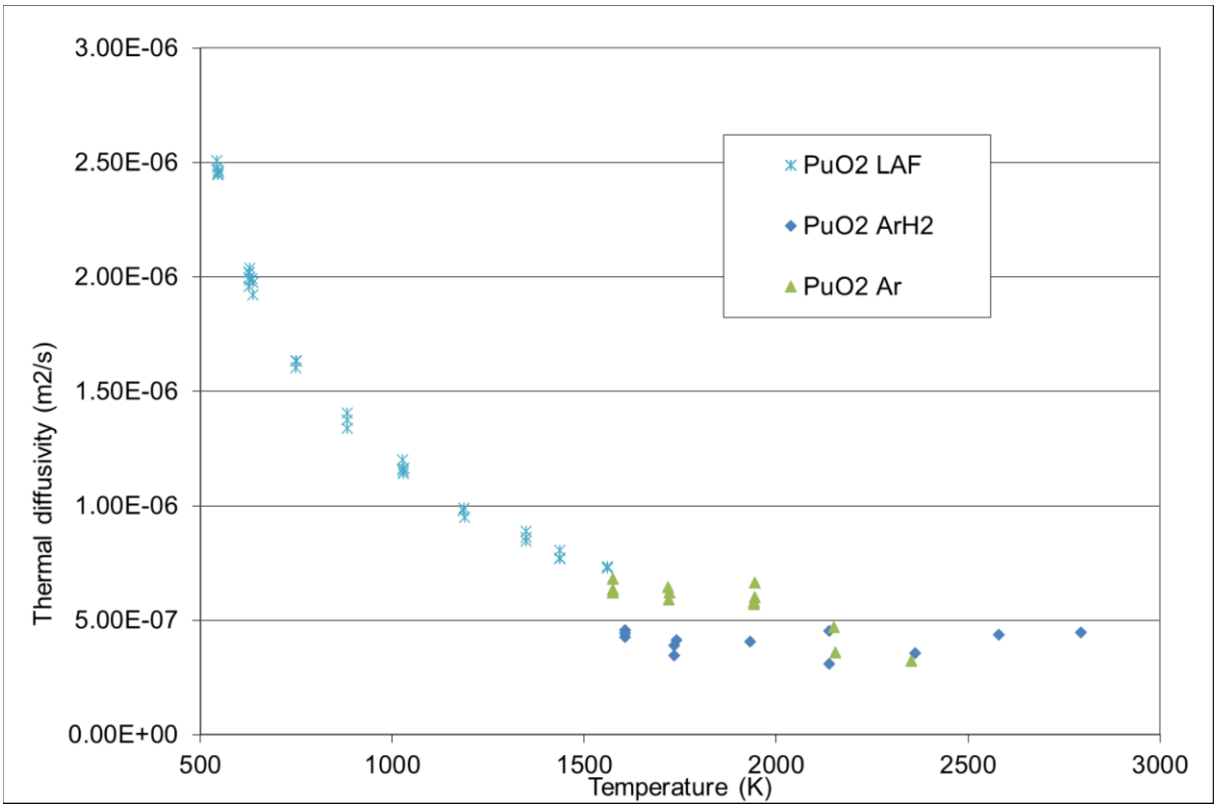

Figure 3.18: Thermal diffusivity of PuO_2 over the entire temperature range.

3.5.2 Irradiated fuel

Still in the frame of the PuMMA project, thermal diffusivity was also measured by the laser-flash method using the LAF set-up in the temperature range 550-1600 K for various irradiated samples [PuM25b]:

- two samples coming from TRABANT 1-1 pin: 45% Pu in fresh fuel, burnup 9.5%at. Samples were taken from the bottom of the fuel pin, supposed less affected by the pin failure (presence of sodium in the pin at the top of fuel column).
- two samples coming from CAPRIX pin, from the Maximum Flux Plane (MFP) (B-271 segment): 45% Pu in fresh fuel, burnup 12.2%at.
- One sample coming from CAPRIX pin, from the top of the fissile column (HCF) (B-267 segment): 45% Pu in fresh fuel, burnup 7.8%at.

Due to the very small size of the CAPRIX and TRABANT 1.1 samples, it was not possible to measure more than one position per sample, the samples size being just sufficient to provide one measurement point.
The precision of the individual measurements is better than 1% for the thermal diffusivity. The accuracy of the measured thermal diffusivity is, however, worse than the precision of the method, being principally determined by sample thickness variations.
Thermal conductivity was calculated assuming a density of 95% TD and the specific heat of the fresh fuel. Results are shown in Figure 3.19 and compared to other experimental results (PAVIX and MYOSOTIS samples) in Figure 3.20.

This project has received funding from the Euratom research and training programme 2019-2020 under grant agreement No 945022.

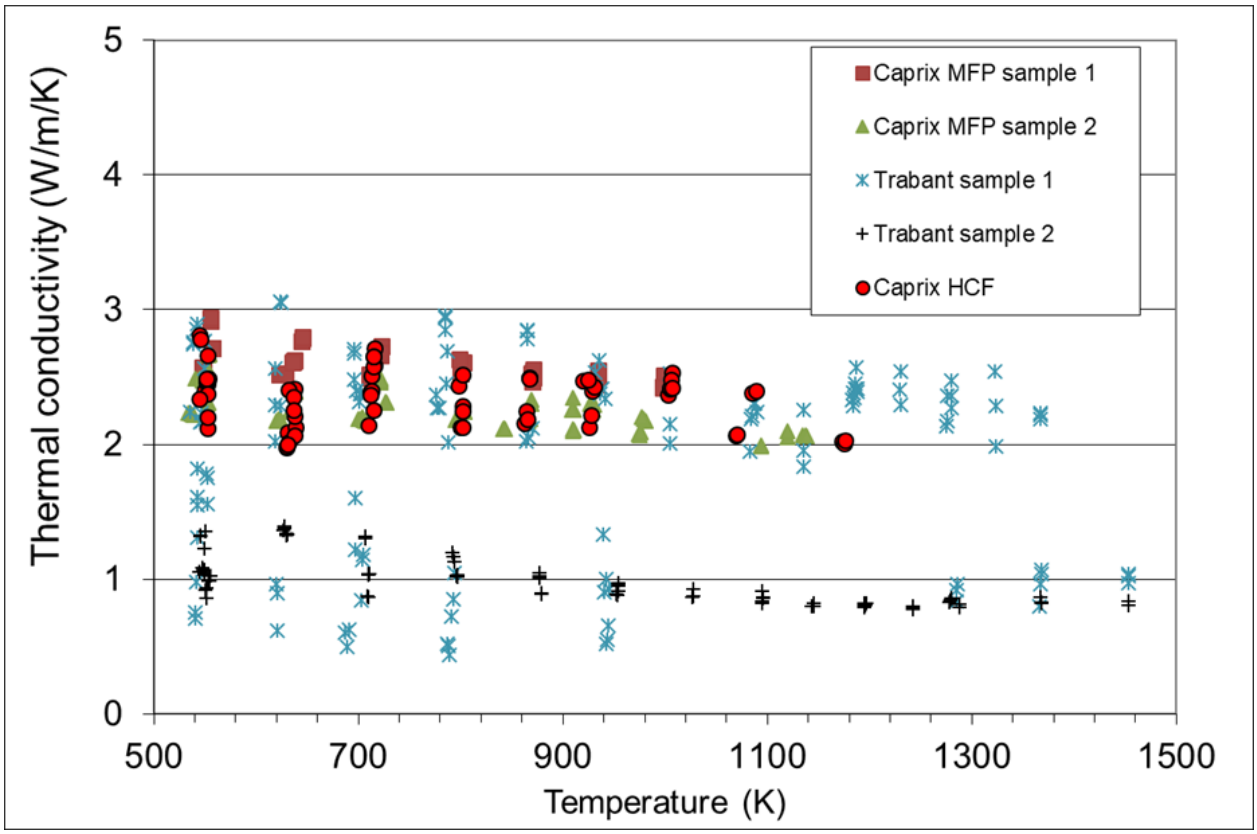

Figure 3.19: Thermal conductivity of irradiated TRABANT and CAPRIX samples.

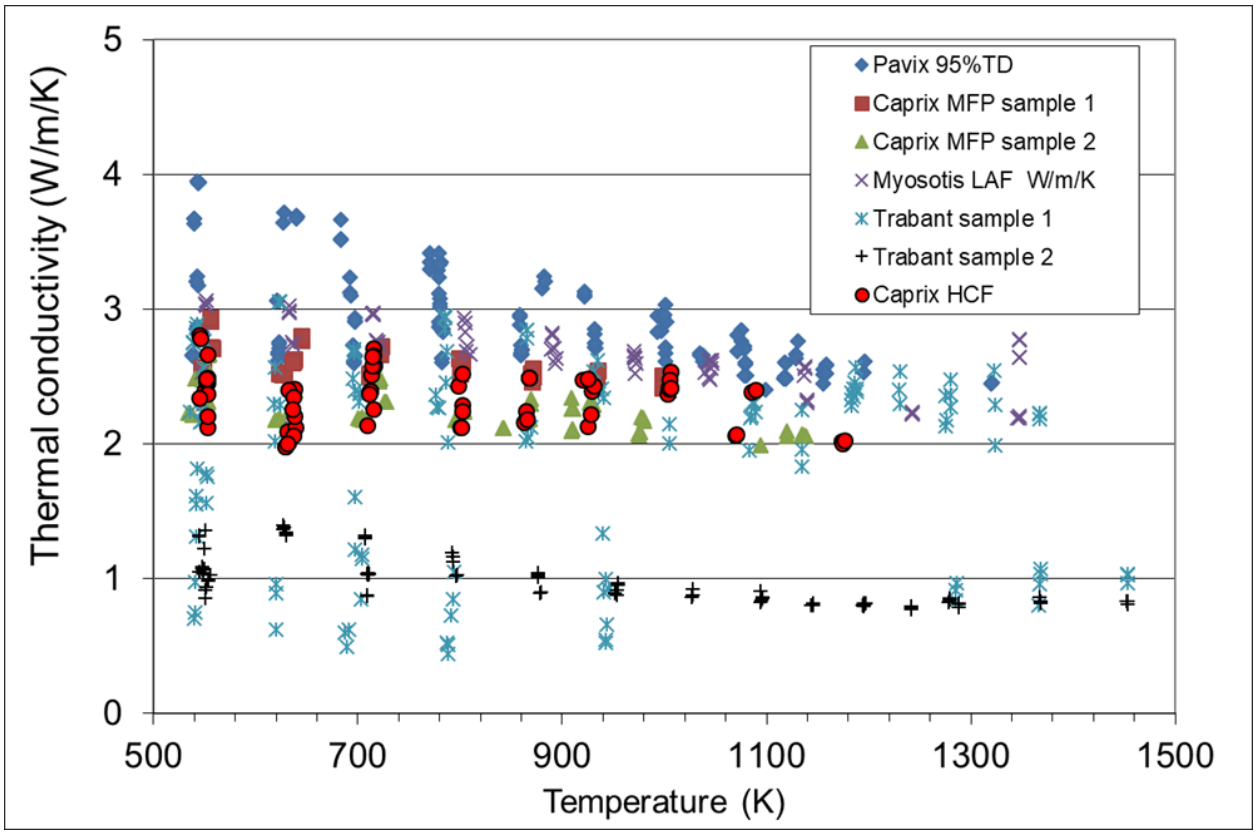

Figure 3.20: Thermal conductivity of irradiated TRABANT and CAPRIX samples compared to PAVIX and MYOSOTIS samples.

This project has received funding from the Euratom research and training programme 2019-2020 under grant agreement No 945022.

Measurements obtained on the CAPRIX pin were in the same range for all the three samples leading to the conclusion that no clear effect of the axial position in the pin was observed between the two axial positions measured (MFP and HCF).

Regarding TRABANT 1.1 samples, thermal diffusivity measurements were significantly scattered and both samples show unexpected low results although no obvious signs of sample damage were observed.

3.6 Conclusions and recommendations

New results obtained in the frame of the PuMMA project on fresh samples are consistent with the conclusions drawn from previous project ESFR-SMART which will therefore renewed here. Although recent measurements are in very good agreement for stoichiometric fuels with various Pu contents, a clear trend with the Pu content is not observed at low temperature. For high temperature (>2000K) the MOX thermal conductivity values are more much higher than for UO_2. If the Cp deduced for CLASH thermograms is taken into account the conductivity increases with Pu content. The stoechiometry after the test is not completely confirmed and the dispersion among the results don't allow any definitive conclusion on the effect of Pu%. Furthermore, a lack of data for low O/M is noticed whereas the effect of Pu content is linked to O/M.

Based on these recent results, JAEA correlation (Eq. 3.17) should then be recommended.

Even with 5 sets of measurements (NESTOR, PAVIX, MYOSOTIS, CAPRIX, TRABANT) a complete understanding of the effect of irradiation on thermal properties is still pending. Indeed, a recommendation for the thermal conductivity of irradiated FBR fuel is currently not possible, taking into account the dependence not only on burn-up, but also on the irradiation temperature range and resulting fuel composition.

3.7 References

[Ama02] M. Amaya, M. Hirai, H. Sakurai, K. Ito, M. Sasaki, T. Nomata, K. Kamimura, R. Iwasaki, Thermal conductivities of irradiated UO_2 and $(U,Gd)O_2$ pellets, J. Nucl. Mater. 300 (2002) 57.

[Bar98] D. Baron. Fuel thermal conductivity: A review of the modeling available for UO_2, $(U,Gd)O_2$ and MOX fuel. in Proc. Seminar on Thermal Perf. of High Burn-up LWR Fuel. 1998. Cadarache, France: OECD/NEA.

[Bon23] P. Bonev, Thermal conductivity of mixed oxide fuel (MOX): effect of temperature, elementary chemical composition, microstructure and burn-up in reactor, PhD Thesis, Université de Lorraine, 2023

This project has received funding from the Euratom research and training programme 2019-2020 under grant agreement No 945022.

[Car94] J. Carrol, R. Gomme and N.A. Leech, Thermal diffusivity measurements on unirradiated archive fuel, and fuel irradiated in the Halden IFA-558 experiment, in Enlarged Halden Programme Mtg. 1994. Bolkesjo, Norway.

[Coo15] M.W.D. Cooper et al, Modelling the thermal conductivity of $(U_xTh_{1-x})O_2$ and $(U_xPu_{1-x})O_2$, J. Nucl. Mater. 466, (2015), 29

[Coz08] C. Cozzo, D. Staicu, G. Pagliosa, D. Papaioannou, S. Bremier, et al. Thermal conductivity of homogeneous and heterogeneous MOX fuel with up to 44 MWd/kgHM burnup. in Proc. Int. LWR Fuel Perf. Mtg. 2008, Seoul, Korea.

[Coz11] C. Cozzo, D. Staicu, J. Somers, A. Fernandez and R.J.M. Konings, Thermal diffusivity and conductivity of thorium–plutonium mixed oxides, J. Nucl. Mater. 416 (2011) 135.

[Dur00] C. Duriez, J.-P. Alessandri, T. Gervais and Y. Philipponneau, Thermal conductivity of hypostoichiometric low Pu content $(U,Pu)O_{2-x}$ mixed oxide, J. Nucl. Mater. 277 (2000) 143.

[ESF23] D. Staicu, D. Robba, L. Vlahovic, P. Pöml, E. Dahms, P. Fouquet-Metivier, F. Cabezas, M.-M. Desagulier, Ph. Martin, N. Chauvin, I. Viallard and J.-C. Dumas, « New measurements of properties of MOX fuel with associated characterizations », Deliverable D2.5.5, ESFR-SMART European Project (2023).

[Fin00] J. K. Fink, Thermophysical properties of uranium dioxide, J. Nucl. Mater. 279 (2000) 1.

[Gom98] R.A. Gomme, J.C. Carrol and T.L. Shaw, Thermal conductivity determinations for irradiated fuel. High Temp - High Press. 30 (1998) 135.

[Har73] S.M. Hartlib, A. Hough, M.P. Waite, and A.R. Hall, Report AERE-R 7325, 1973.

[Hir97] M. Hirai, Thermal diffusivity measurements of irradiated UO_2 pellets, in IAEA TCM on advances in Pellet Technology for Improved performance at High Burn-up. 1996. Tokyo, Japan: IAEA-TECDOC-1036.

[Ino00] M. Inoue, Thermal conductivity of uranium–plutonium oxide fuel for fast reactors, J. Nucl. Mater. 282 (2000) 186.

[Kat11] M. Kato, K. Maeda, T. Ozawa, M. Kashimura and Y. Kihara, Physical Properties and Irradiation Behavior Analysis of Np- and Am-Bearing MOX Fuels, J. Nucl. Sci. Technol. 48 (2011) 646.

[Kin04] M. Kinoshita, T. Sonoda, S. Kitajima, A. Sasahara, T. Kameyama et al., High burnup rim project: (III) properties of rim-structured fuel., in Proc. Int. Mtg. on LWR Fuel Perf. 2004. Orlando, Florida.

[Lan05] D.D. Lanning, C.E. Beyer, and K.J. Geelhood, FRAPCON-3: Modifications to Fuel Rod Material Properties and Performance Models for High Burn-up Application, Report NUREG/CR-6534, Vol. 4, PNNL-11513, 2005.

[Luc94] P.G. Lucuta et al, Modelling of UO_2-based SIMFUEL thermal conductivity The effect of burnup, J. Nucl. Mater 217 (1994), 279

This project has received funding from the Euratom research and training programme 2019-2020 under grant agreement No 945022.

[Mag20] A. Magni, T. Barani, A. Del Nevo, D. Pizzocri, D. Staicu, P. Van Uffelen and L. Luzzi, Modelling and assessment of thermal conductivity and melting behaviour of MOX fuel for fast reactor applications. *J. Nucl. Mater. 541* (2020)

[Mor08a] K. Morimoto, M. Kato, M. Ogasawara and M. Kashimura, Thermal conductivities of hypostoichiometric (U, Pu, Am)O_{2-x} oxide, J. Nucl. Mater. 374 (2008) 378.

[Mor08b] K. Morimoto, M. Kato, M. Ogasawara, M. Kashimura and T. Abe, Thermal conductivities of (U, Pu, Am)O_2 solid solutions, J. All. Comp. 452 (2008) 54.

[Min01] K. Minato, T. Shiratori, H. Serizawa, K. Hayashi, K. Une, K. Nogita, M. Hirai and M. Amaya, Thermal conductivities of irradiated UO_2 and (U,Gd)O_2, J. Nucl. Mater. 288 (2001) 57.

[Nak98] J. Nakamura, Thermal diffusivity of high burn-up UO_2 pellet irradiated at HBWR, in Proc. Seminar on Thermal Perf. of High Burn-up LWR Fuel. 1998. Cadarache, France: OECD/NEA

[NEA25] N. Chauvin et al., Recommendations on Fuel Properties for Fuel Performance Codes, NEA/NSC/R(2024)1, July 2025

[Ohi97] K. Ohira and N. Itagaki, Thermal conductivity measurements of high burn-up UO_2 pellet and a benchmark calculation of fuel temperature, in Proc. Int. Topical Mtg. on LWR Fuel Perf. 1997. Portland, Oregon: ANS.

[Phi92] Y. Philipponneau, Thermal conductivity of (U,Pu)O_{2-x} mixed oxide fuel, J. Nucl. Mater. 188 (1992) 194.

[PuM25a] P. Martin, M.-M. Desagulier, J. Martinez, C. Guéneau, M. Pons, M. Duchateau, T. Barral, D. Staicu, L. Vlahovic, D. Robba and N. Clavier, « Measurements of thermal properties on fresh fuels », Deliverable D3.7, PuMMA European Project (2025).

[PuM25b] D. Staicu, E. Dahms, G. Montagnier, C. Nourry, N. Chauvin, P. Martin, « Results of measurements of irradiated MOX fuel », Deliverable D3.8, PuMMA European Project (2025).

[Ron04] C. Ronchi, M. Sheindlin, D. Staicu and M. Kinoshita, Effect of burn-up on the thermal conductivity of uranium dioxide up to 100.000 $MWdt^{-1}$, J. Nucl. Mater. 327 (2004) 58.

[Sen09] A.K. Sengupta, K.B. Khan, J. Panakkal, H.S. Kamath and S. nerjee, Evaluation of high plutonia (44% PuO_2) MOX as a fuel for fast breeder test reactor, J. Nucl. Mater. 385 (2009) 173.

[Sih92] A.H. Sihvola, I.V. Lindell, Effective permeability of mixtures. In Dielectric Properties of Heterogeneous Materials, Edited by A. PRIOU, New York: Elsevier, 1992, p.101.

[Son07] T. Sonoda, T. Kameyama, A. Sasahara, S. Kitajima, Y. Nauchi, et al., Clarification of Rim Structure Effects on Properties and Behaviour of LWR UO_2 Fuels and Gadolinia Doped Fuels, in Proc. Int. LWR Fuel Perf. Mtg. 2007. San Francisco, California: ANS (CD-ROM).

This project has received funding from the Euratom research and training programme 2019-2020 under grant agreement No 945022.

[Sta00] D. Staicu, Conductivité thermique des combustibles nucléaires héterogènes, Thesis INSA Lyon (2000) N° 2000 ISAL 0018

[Sta01] D. Staicu, D. Jeulin, M. Beauvy, M. Laurent, C. Berlanga, N. Negrello, D. Gosset, Effective thermal conductivity of heterogeneous materials: calculation methods and application to different microstructures, High Temp. - High Press. 33 (2001) 293.

[Sta07] D. Staicu, G. Pagliosa, D. Papaioannou, V.V. Rondinella, C. Cozzo, et al., Thermal Diffusivity of Homogeneous SBR MOX Fuel with a Burn-up of 35 MWd/kgHM, in Proc. Int. LWR Fuel Perf. Mtg. 2007. San Francisco, California: ANS (CD-ROM).

[Sta13] D. Staicu and M. Barker, Thermal conductivity of heterogeneous LWR MOX fuels, J. Nucl. Mater. 442 (2013) 46.

[Sta14] D. Staicu, V.V. Rondinella, C.T. Walker, D. Papaioannou, R.J.M. Konings, C. Ronchi, M. Sheindlin, A. Sasahara, T. Sonoda and M. Kinoshita, Effect of burn-up on the thermal conductivity of uranium–gadolinium dioxide up to 100GWd/tHM, J. Nucl. Mater. 453 (2014) 259.

[Sta17a] D. Staicu, E. Dahms, T. Wiss, O. Benes, J.-Y. Colle, N. Chauvin, P. M. Martin, Properties measurements on irradiated fuels (NESTOR 3), European Commission, ESNII+ project, Deliverable D.7.4.2 (2017).

[Sta17b] D. Staicu, E. Dahms, D. Manara, J.-Y. Colle, O. Benes, M. Marchetti and P.M. Martin, Measurements of properties of fresh PHENIX fuel, ESNII+ project, Deliverable D7.4.1. (2017)

[Vas06] P.R. Vasudeva Rao, S. Anthonysamy, M.V. Krishnaiah and V. Chandramouli, Oxygen potential and thermal conductivity of (U,Pu) mixed oxides, J. Nucl. Mater. 348 (2006) 329.

[Wal06] C.T. Walker, D. Staicu, M. Sheindlin, D. Papaioannou, W. Goll and F. Sontheimer, On the thermal conductivity of UO_2 nuclear fuel at a high burn-up of around 100MWd/kgHM, J. Nucl. Mater. 350 (2006) 19.

[Wie97] W. Wiesenack, Assessment of UO_2 conductivity degradation based on in-pile temperature data, in Proc. Int. Topical Mtg. on LWR Fuel Perf. 1997. Portland, Oregon: ANS.

[Yag00] S. Yagnik, Thermal Conductivity Recovery Phenomenon in Irradiated UO_2 and $(U,Gd)O_2$, in Proc. Topical Mtg. on LWR Fuel Perf. 2000. Park City, Utah: ANS.

[Yag04] S. Yagnik, Y. Rashid, R. Dunham, and R. Montgomery, Fuel Analysis and Licensing Code: FALCON MOD01: Volume 1: Theoretical and Numerical Bases, EPRI, Palo Alto, CA, Report 1011307. 2004.

[Yam93] K. Yamamoto, T. Hirosawa, K. Yoshikawa, K. Morozumi and S. Nomura, Melting temperature and thermal conductivity of irradiated mixed oxide fuel, J. Nucl. Mater. 204 (1993) p. 85.

This project has received funding from the Euratom research and training programme 2019-2020 under grant agreement No 945022.

4. Melting point

This chapter was originally provided by D. Staicu (JRC-Karlsruhe).

4.1 Literature data

In the early version of this European Catalogue (1990), recommendations were made for unirradiated stochiometric UO_2 (Eq. 4.1) and PuO_2 (Eq. 4.2), and the law for $(U,Pu)O_2$ was obtained via a mixture law depending on the Pu molar fraction Y ($0 < Y < 1$) (Eq. 4.3 and Eq. 4.4) as illustrated on Figure 4.1.

$$T_m(UO_{2.00}) = 3120 \pm 30K \quad \text{Eq. 4.1}$$

$$T_m(PuO_{2.00}) = 2701 \pm 35K \quad \text{Eq. 4.2}$$

$$Solidus: T_S((U,Pu)O_{2.00}) = 3120 - 540\,Y + 121\,Y^2 \quad \text{Eq. 4.3}$$

$$Liquidus: T_L((U,Pu)O_{2.00}) = 3120 - 290\,Y - 129\,Y^2 \quad \text{Eq. 4.4}$$

With Y the Pu molar fraction ($0 < Y < 1$)

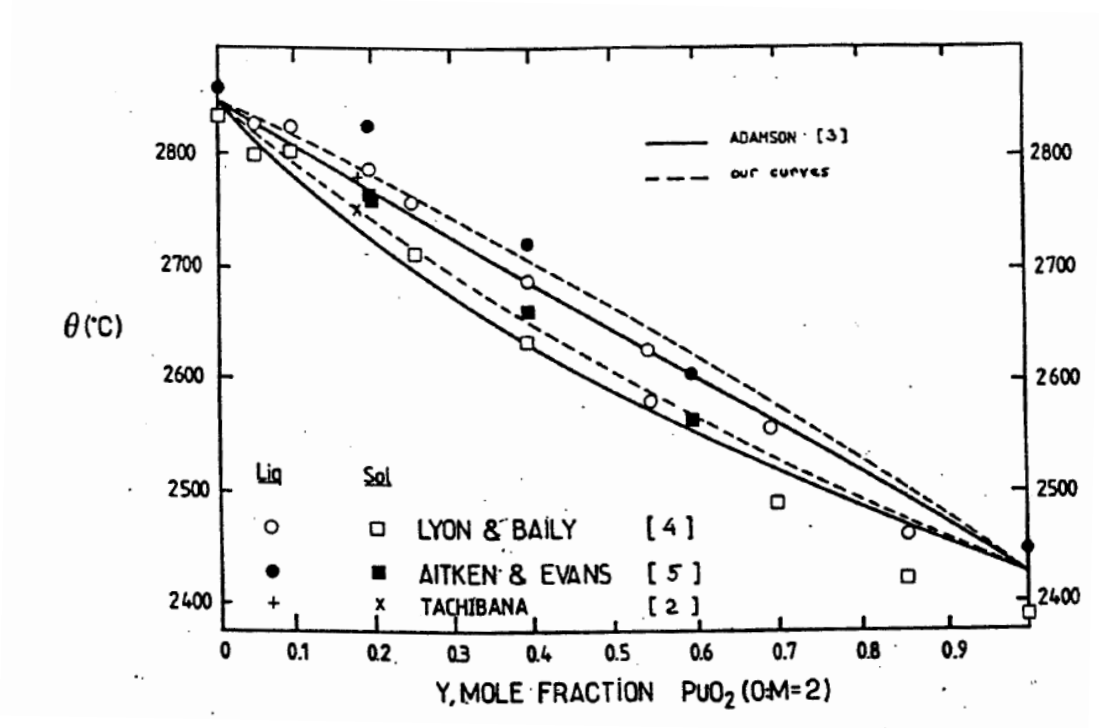

Figure 4.1: Solidus and Liquidus temperature for unirradiated $(U,Pu)O_2$

The decrease in melting temperature due to hypo-stoichiometry was calculated as per Eq. 4.5 and Eq. 4.6.

This project has received funding from the Euratom research and training programme 2019-2020 under grant agreement No 945022.

$$T_S(x) = 10^3\, x \qquad \text{Eq. 4.5}$$

$$T_L(x) = 300\, x \qquad \text{Eq. 4.6}$$

where $x = 2 - O/M$ in the interval between the hypo-stoichiometry limit and 2.00 and 0 < Y < 0.3

For the effect of burn-up, it was recommended that the solidus temperature should be decreased by 34K at 10at% burn-up. It was also stated that the experiments with simulated irradiated fuel give a decrease between 22K and 75K at this burn-up.

The melting behaviour of $(U,Pu)O_{2\pm x}$ has been extensively studied over the past decades by Lyon and Baily [Lyo67], Aitken and Evans [Ait68], Reavis *et al.* [Rea73], Konno and Hirosawa [Kon98], Kato *et al.* [Kat08a, b and c] by classical thermal analysis and later by De Bruycker *et al.* [DeB11], Böhler *et al.* [Böh14] and Strach *et al.* [Str16] by laser heating. Reviews of the literature data for $(U,Pu)O_2$ were performed by M. Kato in 2009 [Kat09] and Guéneau *et al.* in 2011 [Gué11]. The composition range and the methods of the available measurements are given in Table 4.1.

Table 4.1: Experimental solidus/liquidus data on fresh $(U,Pu)O_2$ available in the literature.

Reference	Composition	Experimental technique
Lyon and Baily [Lyo67]	0 < y ≤ 0.85 O/M = 2.00	Thermal arrest using a sealed W crucible
Aitken and Evans [Ait68]	0.20 ≤ y ≤ 0.60 1.76 ≤ O/M ≤ 2.00	Thermal arrest using a sealed W crucible
Reavis *et al.* [Rea73]	y = 0.25 O/M = 1.97 and 1.98	Differential Thermal Analysis using W crucible
Konno and Hirosawa [Kon98]	y = 0.29 O/M=1.95 and 1.99	Thermal arrest technique a sealed W crucible
Kato *et al.* [Kat08a, b and c]	0.117 ≤ y ≤ 0.60 1.922 ≤ O/M ≤ 2.00	Thermal arrest using sealed W or Re crucible
De Bruycker *et al.* [DeB11]	0.75 ≤ y ≤ 0.90 O/M=2.00	Laser heating under Ar and air
Böhler *et al.* [Böh14]	0.037 ≤ y ≤ 0.90 O/M=2.00	Laser heating under Ar (y < 0.50) and air (y > 0.50)
Strach *et al.* [Str16]	0.14 ≤ y ≤ 0.62 O/M = 2.00	Laser heating technique under Ar and air

The available experimental solidus/liquidus data for $(U,Pu)O_{2.00}$ are plotted in Figure 4.2, where only the data for stoichiometric dioxides are represented for sake of clarity. Large discrepancies can be noticed for both solidus/liquidus temperatures. Lyon and Baily (0 < y ≤ 0.85, O/M = 2.00), followed by Aitken and

This project has received funding from the Euratom research and training programme 2019-2020 under grant agreement No 945022.

Evans ($0.20 \leq y \leq 0.60$), used first a thermal arrest technique with stoichiometric $(U,Pu)O_{2.00}$ samples encapsulated in W crucibles [Lyo67 , Ait68]. Their study depicted an ideal solution model between UO_2 and PuO_2, with a melting point of PuO_2 around 2700 K and a decrease of the solidus temperatures when increasing the PuO_2 content. In the study of Aitken and Evans, hypo-stoichiometric $U_{1-y}Pu_yO_{2-x}$ were also studied, with $1.76 \leq O/M \leq 2.00$ [Ait68].

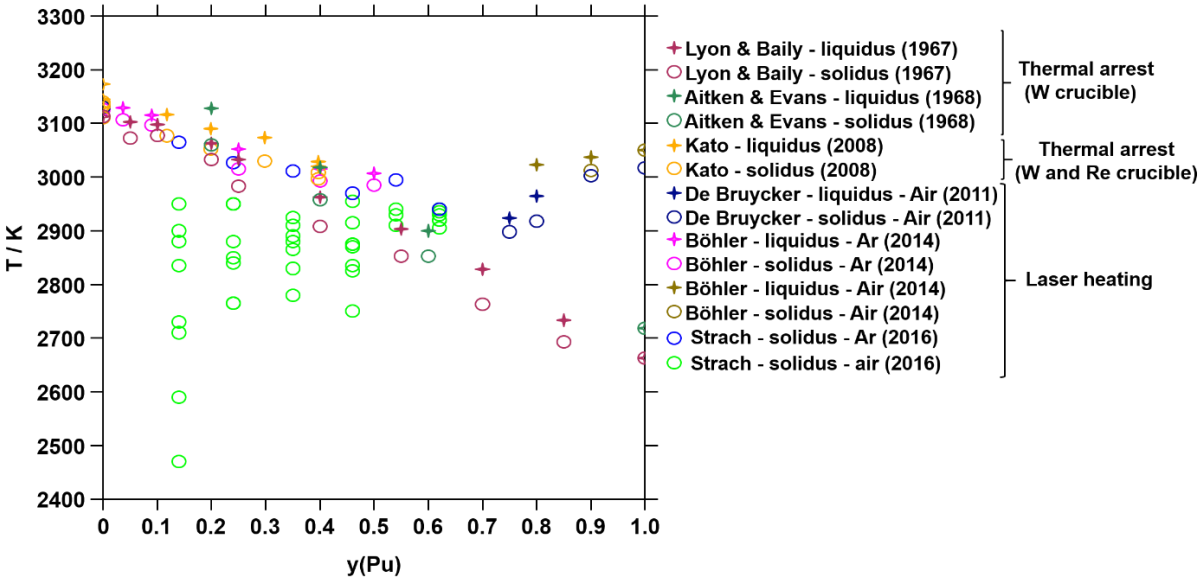

Figure 4.2: Experimental melting data available for $U_{1-y}Pu_yO_{2.00}$
Lyon and Baily [Lyo67], Aitken and Evans [Ait68], Kato *et al.* [Kat08b], De Bruycker *et al.* [DeB11], Böhler *et al.* [Böh14] and Strach *et al.* [Str16].

In 2008, Kato *et al.* performed further investigations on the solidus/liquidus temperatures using also the thermal arrest method with W crucibles, and comparison between the available correlations in the literature for the solidus temperatures for $U_{1-y}Pu_yO_{2.00}$ as a function of Pu content.[Kat08c]. However, for Pu content higher than 20% Pu(/U+Pu), interactions between the samples and the W containers were observed [Kat08c]. Another study was conducted by Kato *et al.* using rhenium capsules to overcome this interaction [Kat08b]. Solidus/liquidus temperatures higher of 100 K were obtained compared to the ones with W crucibles. However, interactions between the material and its capsule were also occurring with Re crucibles for Pu content higher than 50% Pu(/U+Pu) [Kat08a and b]. For hypo-stoichiometric samples, an increase of the solidus/liquidus temperatures was evidenced when decreasing the O/M ratio.

In order to eliminate possible interactions, solidus/liquidus temperatures were measured using a laser heating technique by De Bruycker *et al.* whose results were found to be significantly higher than the ones obtained by thermal arrest [DeB11]. This study was not consistent with the ideal solution model mentioned previously described and a minimum in the melting temperatures was found for $0.50 < Pu/(U+Pu) < 0.80$. Böhler *et al.* with the same laser heating technique observed also a minimum for $0.40 < Pu(U+Pu) < 0.70$ [Böh14]. The results obtained for $y < 0.50$ were found to be in agreement with the ones of Kato *et al.* using thermal arrest [Kat08c]. Strach *et al.* also performed measurements of solidus/liquidus temperatures using laser heating [Str16], with values in agreement with the ones of De Bruycker *et al.* and Böhler *et al.*. In the work of

This project has received funding from the Euratom research and training programme 2019-2020 under grant agreement No 945022.

Strach *et al.*, the influence of the atmosphere of melting was also studied. Indeed, uranium-rich samples tend to oxidize under air, leading to a progressive decrease of the melting temperature [Str16]. In case of Pu-rich samples, air was used to maintain the O/M ratio at 2.00. Moreover, Strach *et al.* performed experimental campaigns under argon and air, and significantly lower solidus temperatures were obtained in the case of air (2470 K) as comparted to argon (3065 K) for $U_{0.86}Pu_{0.14}O_{2.00}$ [Str16].

In the thermodynamic modelling of the U-Pu-O system developed by Guéneau *et al.* [Gué11], the solidus/liquidus temperatures obtained by De Bruycker *et al.* [DeB11] and Kato *et al.* [Kat09] were selected. The obtained model is shown in Figure 4.3 where the discarded data obtained by Lyon and Baily are represented for comparison [Lyo67].

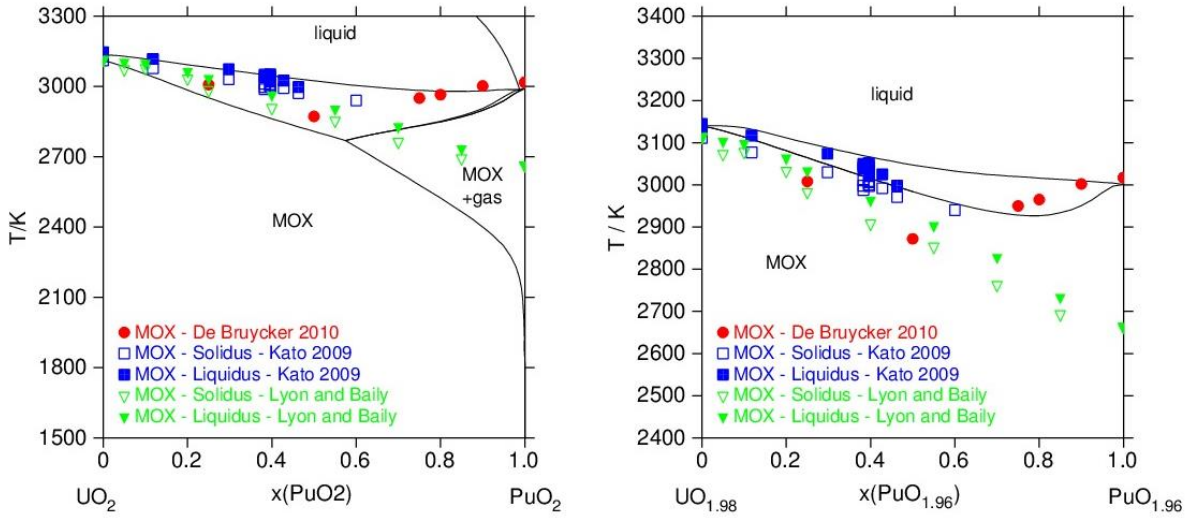

Figure 4.3: Solidus/liquidus temperatures of $U_{1-y}Pu_yO_{2\pm x}$ calculated using the CALPHAD model of Guéneau et al. [Gué11], compared to the experimental values of De Bruycker et al. [DeB11], Kato et al. [Kat09] and Lyon and Baily [Lyo67].

In 2023, Fouquet-Métivier *et al.* [Fou23] proposed a re-evaluation of the thermodynamic model of the U-Pu-O and more especially the liquid/solid transition. This reassessment is based on a critical review of the available data in the literature and the inclusion of experimental data published after 2011 by Böhler *et al.* [Böh14]. The new representation of the solid/liquidus temperatures is given in Figure 4.4. A good agreement between the calculated solidus-liquidus curves and the selected experimental data can be observed.

This project has received funding from the Euratom research and training programme 2019-2020 under grant agreement No 945022.

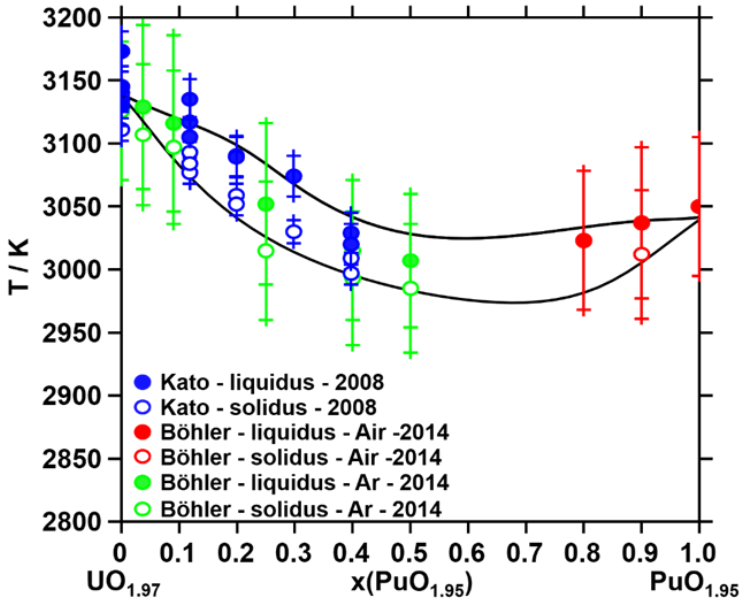

Figure 4.4: $UO_{1.97}$-$PuO_{1.95}$ phase diagram compared with the selected experimental data of Kato *et al.* [Kat08b] and Böhler *et al.* [Böh14] (figure from [Fou23]).

In addition to the CALPHAD models, several authors established empirical correlations between the solidus and liquidus temperatures and different variables such as the oxygen stoichiometry or the plutonium content. Unless stated, the temperature assessed by these equations corresponds to the solidus temperature. For all the correlations, it was evidenced that both the plutonium content and the deviation from the stoichiometry in oxygen decrease the solidus and liquidus temperatures of MOX fuels with respect to UO_2. In agreement with the approach used by Fouquet-Metivier *et al.* [Fou23], only the correlations obtained by Konno et Hirosawa [Kon02a, Kon02b] and by Magni *et al.* [Mag20] are considered. The equations and their validity ranges are given in Table 4.2 and are compared to the experimental solidus temperatures [Böh14, Kat09] selected by Fouquet-Métivier *et al.* in Figure 4.5. These two correlations are in rather good agreement with the experimental data in their validity ranges.

Table 4.2: Correlations for the solidus temperature as a function of the plutonium content (y) and deviation to oxygen stoichiometry (x) for $U_{1-y}Pu_yO_{2-x}$.

References	Equation	Validity ranges	
Konno et Hirosawa [Kon02a]	$T_{solidus} = 3838 - 497y + 60y^2 - x(1000 - 2850y)$	0<y<0.4 0.06<x<0.0	Eq. 4.7
Magni *et al.* [Mag20]	$T_{solidus} = 3147 - 364.85y - 1014.15x$	0<y<0.5 0.06<x<0.0	Eq. 4.8

This project has received funding from the Euratom research and training programme 2019-2020 under grant agreement No 945022.

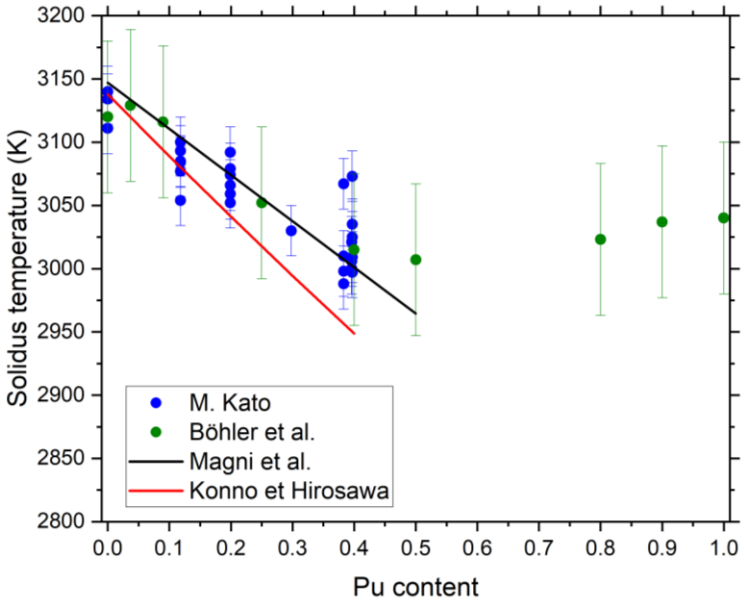

Figure 4.5: Comparison between the correlations available in the literature [Kon02a ,Mag20] for the solidus temperatures for $(U,Pu)O_{2.00}$ as a function of Pu content and the experimental solidus values [Böh14, Kat09] selected by Fouquet-Metivier *et al.* [Fou23] for their model.

In 2001, Carbajo *et al.* [Car01] reviewed the effect of burn-up on the melting point of LWR MOX, and recommended a decrease of 0.5 K for each MWd/tHM burn-up. In 2011, the impact of burn-up on melting point was also studied by Hirosawa et Sato [Hir11] on a 29% Pu/(U+Pu) fuel up to 112.5 $GWd.t^{-1}$. These data obtained using the thermal arrest method with Re crucible are compared to the values obtained by Konno et Hirosawa on 18 and 29% $(U,Pu)O_2$ up to 124 $GWd.t^{-1}$ [Kon02a] in Figure 4.6.

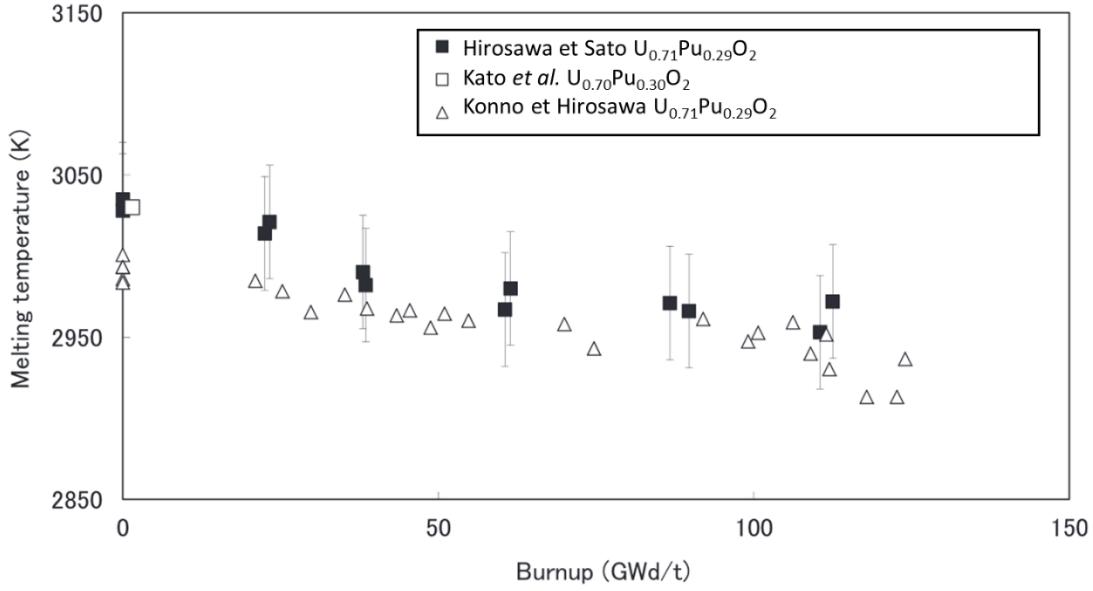

Figure 4.6: Burn-up dependence of melting temperature for $(U,Pu)O_2$ using data of Hirosawa et Sato [Hir11], Konno et Hirosawa [Kon02a] and Kato *et al.* [Kat09]. (figure adapted from [Hir11]).

This project has received funding from the Euratom research and training programme 2019-2020 under grant agreement No 945022.

From these experimental data, Hirosawa et Sato [Hir11] proposed an updated version of the correlation for $(U_{1-y-z}Pu_yAm_z)O_2$ of the correlation between melting temperature and the burn-up determined by Konno and Hirosawa [Kon02a]. This correlation is given by Eq. 4.9.

$$T_{melting} = 30 + T_{sol.MOX} + \Delta T_{sol.O/M} + \Delta T_{sol.Am} + \Delta T_{sol.FP} \quad \text{Eq. 4.9}$$

With :

$$T_{sol.MOX} = 3138 - 497Pu + 60Pu^2 \quad \text{Eq. 4.10}$$

$$\Delta T_{sol.O/M} = -(1000 - 2850y)(2.00 - OM) \quad \text{Eq. 4.11}$$

$$\Delta T_{sol.Am} = -(1206 - 782y)Am \quad \text{Eq. 4.12}$$

$$\Delta T_{sol.FP} = -(1.06 - 1.43y)BU + 0.0008\big((1.06 - 1.43y)/0.66\big)^{1.5} BU^2 \quad \text{Eq. 4.13}$$

With $T_{melting}$ the melting temperature in K, OM the O/M ratio, Pu the Pu fraction (Pu/(U+Pu)) and Am the Am fraction (Am/(Pu+U+Am)) and BU the burn-up in $MWd.kg^{-1}$.

In Figure 4.7, the correlation (Eq. 4.9) and the Hirosawa et Sato experimental data are plotted. A Linear decrease can be observed with a decrease of 0.6 K each $GWd.t^{-1}$.

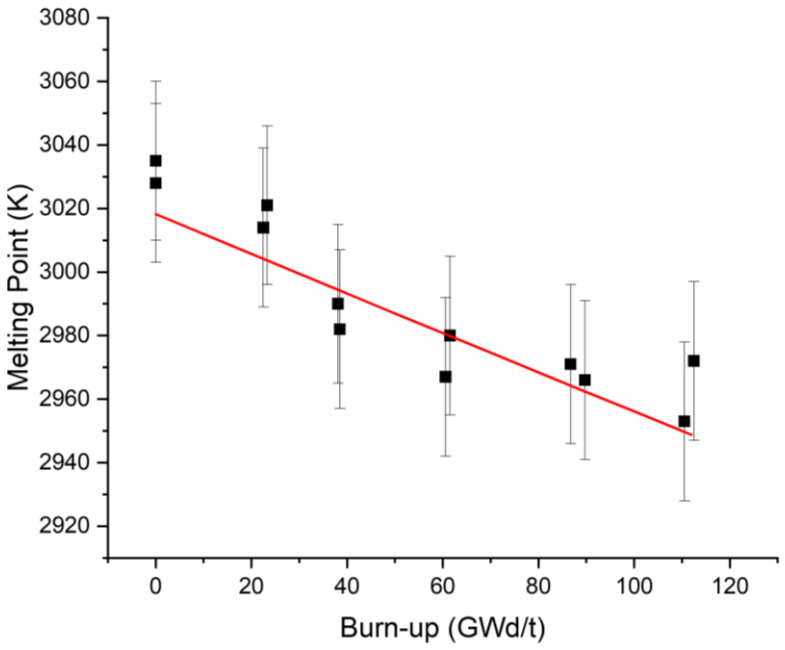

Figure 4.7: Correlation (red curve) and experimental data from Hirosawa et Sato [Hir11] for a 29% Pu/(U+Pu) fuel.

Based on these results, Hirosawa et Sato proposed. A Linear decrease can be observed with a decrease of 0.6 K each $GWd.t^{-1}$ as illustrated

This project has received funding from the Euratom research and training programme 2019-2020 under grant agreement No 945022.

4.2 NEA recommendation

The recommended law in [NEA25] for solidus temperature is given in Eq. 4.14, considering the most recent results obtained by JAEA and JRC.

$$T_{melting} = 3143 - 521\,x + 416\,x^2 \qquad \text{Eq. 4.14}$$

With x is the Pu fraction and $x < 50\%$

This recommendation for the solidus temperature of stoichiometric unirradiated MOX is in good agreement with experimental results for Pu contents up to 40%. At higher Pu contents, a deviation is observed for stoichiometric fuels, the results of JRC showing higher solidus temperatures. The discrepancies could be due to difficulties in the sample's stoichiometry control at high temperatures and require further investigations.

To consider the effect of stoichiometry and minor actinides, the results of Kato [Kat08b] are recommended.
The effect of burn-up is recommended to be of 0.5K per MWd/kgHM, as recommended by Carbajo [Car01].

The range of parameters for the validity of the recommendation is:

- O/M from 1.93 to 2.0
- Pu content from 0 to 50%
- Burn-up from 0 to 112 GWd/t

Uncertainty is estimated to be σ = ± 35 K.

4.3 Data obtained in the frame of the ESFR-SMART project

Measurements using the laser-heating technique were performed at JRC-Karlsruhe in framework of ESFR-SMART [ESF23] to determine the solidus temperature on height samples listed in the Table 4.3.

Table 4.3: Details of the eight fresh $(U,Pu)O_2$ samples studied.

Name	Composition
PHENIX24	$U_{0.760}Pu_{0.235}Am_{0.005}O_{1.983}$
PHENIX29-brut	$U_{0.70}Pu_{0.29}Am_{0.01}O_{1.984}$
PHENIX29-OM	$U_{0.70}Pu_{0.29}Am_{0.01}O_{1.998}$
CAPRA4	$U_{0.70}Pu_{0.28}Am_{0.02}O_{2.004}$
TRABANT40-brut	$U_{0.60}Pu_{0.39}Am_{0.01}O_{1.978}$
TRABANT40-OM	$U_{0.60}Pu_{0.39}Am_{0.01}O_{1.999}$
TRABANT45	$U_{0.55}Pu_{0.44}Am_{0.01}O_{2.00}$
RV45	$U_{0.55}Pu_{0.45}O_{1.987}$

This project has received funding from the Euratom research and training programme 2019-2020 under grant agreement No 945022.

Since the measurements of Strach *et al.* [Str16], the setup was improved by the implementation of oxygen gauges to monitor the oxygen partial pressure during the experiments. Hence, the variation of the oxygen partial pressure inside the chamber during the melting could be assessed and the associated O/M ratio of the samples could be determined. The uncertainty of the O/M ratio value is ±0.005.

The solidus temperatures on the eight samples are shown in Figure 4.8 where they are compared to existing literature on similar plutonium and americium contents. The different values for each sample correspond to the successive measurements performed on the same samples [ESF23]. As it can be seen in, considering the uncertainty (±30 K) the solidus temperatures vary mainly with the plutonium and americium contents. The solidus temperatures are summarized in Table 4.4.

Table 4.4: Solidus temperature values measured for ESFR-SMART.

Sample name	Composition	O/M ratio	Solidus temperature (K)
PHENIX24	$U_{0.760}Pu_{0.235}Am_{0.005}O_2$	1.99	3062 ± 30 K
PHENIX29	$U_{0.70}Pu_{0.29}Am_{0.01}O_2$	2.00 1.99	3050 ± 30 K 3052 ± 30 K
CAPRA4	$U_{0.70}Pu_{0.28}Am_{0.02}O_2$	1.99	3054 ± 30 K
TRABANT40	$U_{0.60}Pu_{0.39}Am_{0.01}O_2$	1.99	3021± 30 K
RV45	$U_{0.55}Pu_{0.45}O_2$	1.99	2994 ± 30 K

This project has received funding from the Euratom research and training programme 2019-2020 under grant agreement No 945022.

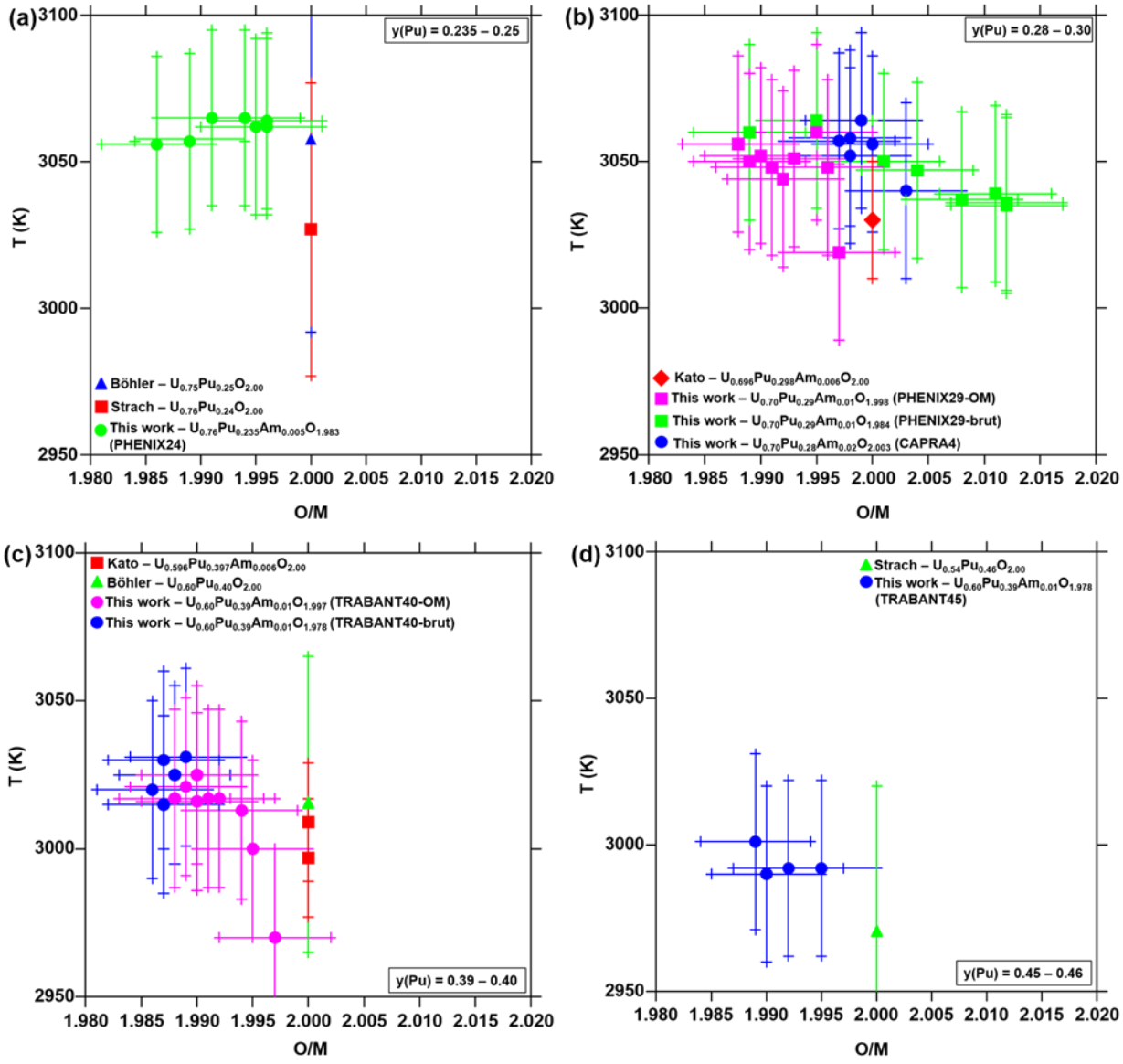

Figure 4.8: Comparison of the new solidus temperatures obtained with the existing literature [Böh14, Str16, Kat09].

The variation of the solidus temperature with the Pu content measured in this work is plotted in Figure 4.9. To this aim, data are selected for samples containing the same americium content (around 1 %, so PHENIX24, PHENIX29, TRABANT40 and TRABANT45) and with the same O/M ratio of about 1.99. As it can be seen, the solidus temperatures decrease linearly when increasing the plutonium content. This observation was already made by Kato *et al.* [Kat08] as well as by Böhler *et al.* [Böh14] and Strach *et al.* [Str16] as illustrated with Figure 4.9. This is in agreement with the fact that the melting point of $UO_{2.00}$ (3147 ± 20 K [Man05]) is higher than the one of $PuO_{2.00}$ (3050 ± 60 K [Böh14]). However, as reported in the works of De Bruycker *et al.* [DeB11] and Böhler *et al.* [Böh14], a minimum in the solidus temperature is expected for $0.50 < y < 0.80$. Thus, the linear decrease of the temperature with the plutonium content can only be stated up to $y = 0.45$.

This project has received funding from the Euratom research and training programme 2019-2020 under grant agreement No 945022.

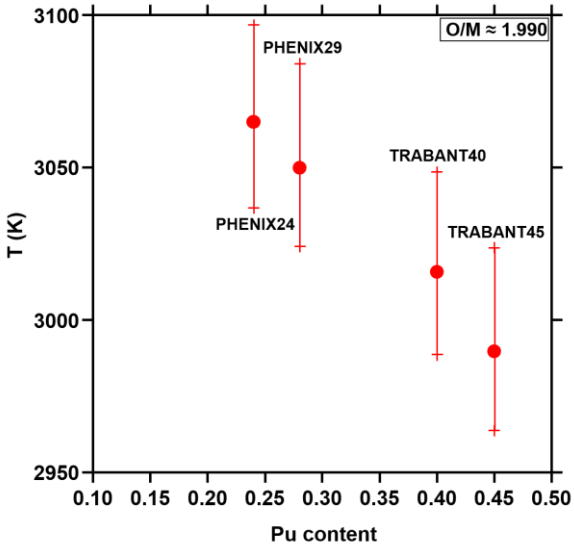

Figure 4.9: Variation of the solidus temperature as a function of the plutonium content (O/M = 1.990).

4.4 Data obtained in the frame of the PuMMA project

In the frame of the PuMMA project, solidus temperature was measured on two PuO_2 samples and on 6 fresh MOX samples [PuM25a] :

- Two PuO_2 samples fabricated at JRC Karlsruhe in 2021, with an initial O/M = 2.00.
- Three stoichiometric MOX samples (O/M = 1.99 ± 0.01) with Pu content of 59, 63 and 69% named MOX60-F, MOX65-F and MOX70-F respectively.
- Three annealed hypostoichiometric MOX samples (O/M = 1.98) with Pu content of 59, 63 and 69% named MOX60-A, MOX65-A and MOX70-A respectively.

For PuO_2 samples, melting point was measured under argon flow and 3.1 bar absolute pressure in the chamber. Results are summarized in Table 4.5. As the samples are reducing shot after shot due to the laser heating, it was not possible to average the results to determine one solidus temperature ; the last result has to be linked to a stoichiometry change.

Table 4.5: Solidus temperatures of $PuO_{2.00}$ measured under Ar.

Shot #	Melting point (± 30 K)	
	Sample 1	Sample 2
1	3046	3055
2	3044	3050
3	3027	3034
4	3022	

This project has received funding from the Euratom research and training programme 2019-2020 under grant agreement No 945022.

Measurements were also performed on $PuO_{2.00}$ Sample 2 (from the same batch as above) under Ar +6.5% H_2. However, the measurements were performed in 2023, two years after fabrication, which implies that the sample was hypostoichiometric. Furthermore, the first transition plateau was seen after the fourth shot, and under a strong reducing atmosphere the sample was well reduced, but with an unknown starting O/M ratio. The results are summarized in Table 4.6.

Table 4.6: Solidus temperatures of $PuO_{1.9x}$ measured under Ar + 6.5% H_2.

Shot #	4	5	6	8	9	10	11
Melting point (± 30 K)	3023	3017	2993	2980	2986	2959	2961

Additionally, measurements were performed also under air flow on a $PuO_{2.00}$ sample from the same batch in the same year as manufactured. Measured solidus temperatures were repeatable (in the uncertainty range), and the average value was to be found 3055 K ± 30 K, which is in accordance with the result of Böhler et al. [Böh14], who reported a solidus temperature of 3050 K ± 59K, but higher than De Bruycker et al. [DeB11] (3017 ± 28 K).

For each MOX sample, 4 successive shots were performed, and lead to a good repeatability for melting temperature determination (measurement uncertainty of ± 30K). Measurements were performed under argon (pO_2 ~ 10^{-6} atm at 923 K) and under argon + 6.5% H_2 (pO_2 = 10^{-26} atm at 923 K) – results are shown on Figure 4.10.

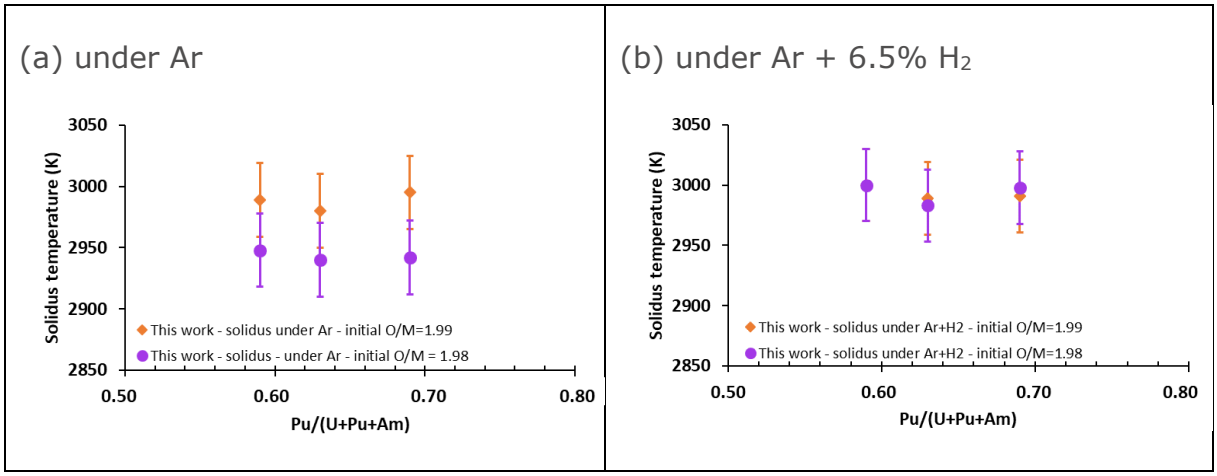

Figure 4.10: Solidus temperature measured for F (♦) and A (•) batches. (a) under Ar ; (b) under Ar + 6.5% H_2

Considering the experimental uncertainty of ± 30 K, no significant variation as a function of plutonium content is observed for both batches F and A and both atmospheres. Under Ar, solidus temperature is lowered by 40-50 K for hypostoichiometric samples. This is in contradiction with the conclusion of Kato et al. [Kat08a] who reported an increase in melting temperature with decreasing O/M ratio although these results correspond to lower plutonium contents (typically % Pu < 0.40) than those studied in the frame of PuMMA project. Under Ar + H_2, the values are the same considering the uncertainty of ± 30 K, which means that no difference is observed between F and B batches.

This project has received funding from the Euratom research and training programme 2019-2020 under grant agreement No 945022.

For each sample, O/M ratio after melting temperature measurement was determined either with the evolution of the oxygen partial pressure in the experimental chamber during the experiment or from the determination of the U, Pu and Am speciation after melting using HERFD-XANES (High Energy Resolution Fluorescence Detected X-rays Absorption Near-Edge Spectroscopy). Both methods give consistent results and show that a final O/M of 1.98 was achieved under all measurement conditions (except for measurements under Ar+H_2 on annealed samples that reached an O/M of 1.99-2.00).

Thermodynamic properties of the fuel were also evaluated in the frame of the PuMMA project [PuM25b]. All available experimental data on fresh $(U,Pu)O_{2\pm x}$ oxides from the literature and measured in frame of the ESNII+, ESFR-SMART and PuMMA projects were reviewed. Data were measured using conventional thermal analysis or advanced laser heating techniques. Based on the analysis of uncertainties, a selection of experimental data is proposed. The data are used as input to derive a new correlation law for fresh fuel as given per Eq. 4.15, to be used in Fuel Performance Codes as it is in very good agreement with most of the data (around 90% lying within the 1% deviation band).

$$T_{m,fresh} = T_{m,UO_2} + A_1 \cdot [Pu] + A_2 \cdot [Pu]^2 + B_1 \cdot |O/M - O/M_{max}| \qquad \text{Eq. 4.15}$$

Where:

$T_{m,UO_2} = 3132\ K$ based on data for UO_2 [Kat09]

$[Pu]$ is the plutonium content between 0 and 1

$$O/M_{max} = \begin{cases} 2 - 0.3077 \cdot [Pu] & if\ [Pu] < 0.65 \\ 1.8 + 1.5214 \cdot [Pu] & if\ [Pu] > 0.65 \end{cases}$$

The best fit for parameters is:

$A_1 = -299.58\ K$

$A_2 = 210.46\ K$

$B_1 = -251.78\ K$

A comparison of the model with experimental data is given on Figure 4.11.

This project has received funding from the Euratom research and training programme 2019-2020 under grant agreement No 945022.

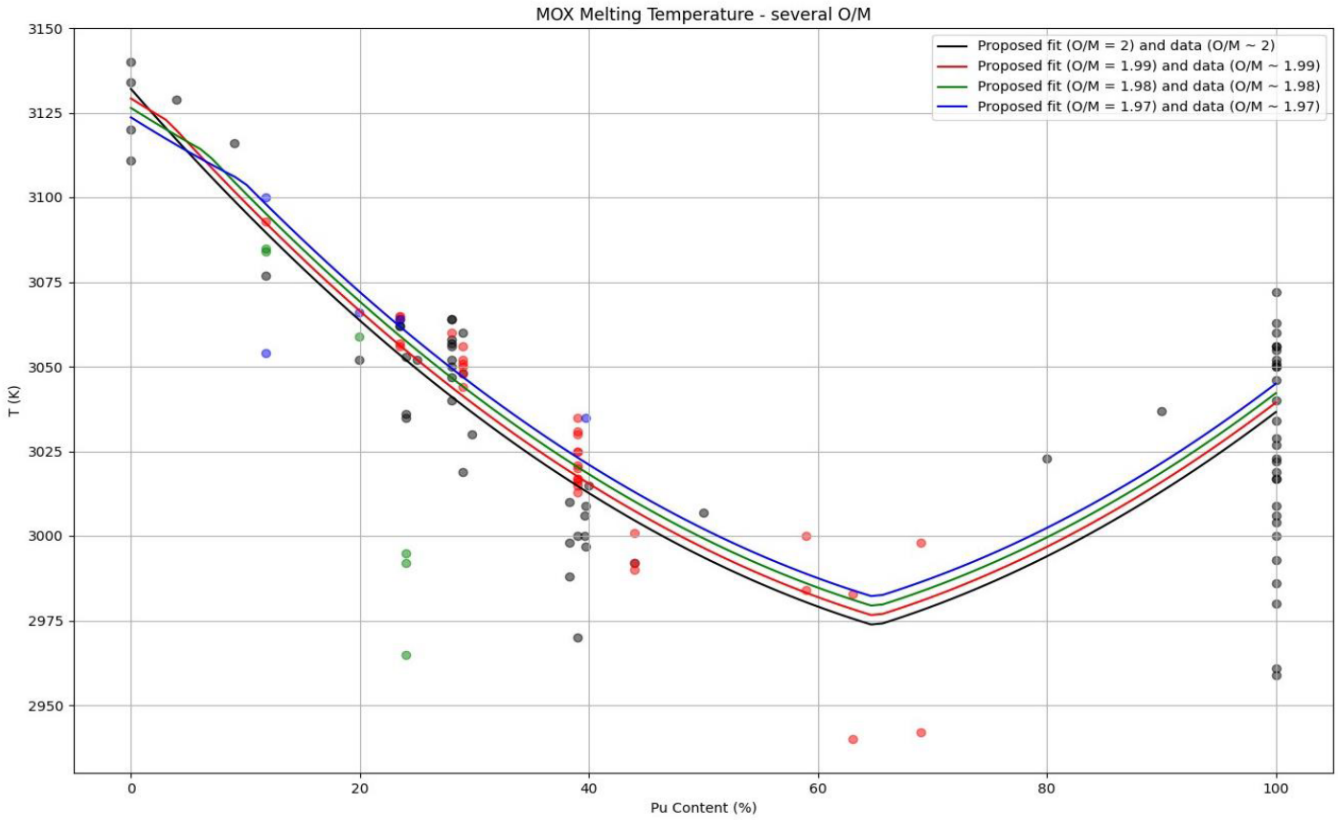

Figure 4.11: Solidus temperature of MOX fuels as a function of the Pu content for various O/M ratios (2 – 1.99 – 1.98 – 1.97) compared to experimental date for each selected O/M.

4.5 Conclusions and recommendations

The new correlation established in the frame of PuMMA project (Eq. 4.15) shall be recommended.

In the future, simulations of thermograms and associated solidification phenomena occurring during cooling would be very useful for a better understanding of melting/solidification processes, and would help to reduce the remaining uncertainties, particularly on the O/M ratio of samples at the measured temperature. Additional melting temperature measurements for lower O/M ratios (below 1.92) would enable a wider range of O/M ratios to be covered, and the exact congruent melting temperature for MOX fuels to be determined

4.6 References

[Ait68] E. A. Aitken and S. K. Evans, « A Thermodynamic Data Program Involving Plutonia and Urania at High Temperatures. Quarterly Report No. 4. », *Quarterly Report No. 4* (1968).

This project has received funding from the Euratom research and training programme 2019-2020 under grant agreement No 945022.

[Böh14] R. Böhler, M. J. Welland, D. Prieur, P. Cakir, T. Vitova, T. Pruessmann, I. Pidchenko, C. Hennig, C. Guéneau, R. J. M. Konings, D. Manara, « Recent advances in the study of the UO_2–PuO_2 phase diagram at high temperatures », *Journal of Nuclear Materials* 448 (2014) 330-339.

[Car01] J. J. Carbajo, G. L. Yoder, S. G. Popov, V. K. Ivanov, « A review of the thermophysical properties of MOX and UO_2 fuels », *Journal of Nuclear Materials* 299 (2001) 181-198.

[DeB11] F. De Bruycker, K. Boboridis, R. J. M. Konings, M. Rini, R. Eloirdi, C. Guéneau, N. Dupin, D. Manara, « On the melting behaviour of uranium/plutonium mixed dioxides with high-Pu content: A laser heating study », *Journal of Nuclear Materials* 419 (2011) 186-193.

[ESF23] D. Staicu, D. Robba, L. Vlahovic, P. Pöml, E. Dahms, P. Fouquet-Metivier, F. Cabezas, M.-M. Desagulier, Ph. Martin, N. Chauvin, I. Viallard and J.-C. Dumas, « New measurements of properties of MOX fuel with associated characterizations », Deliverable D2.5.5, ESFR-SMART European Project (2023)

[Fou23] P. Fouquet-Métivier, P. M. Martin, D. Manara, K. Dardenne, J. Rothe, P. C. M. Fossati, C. Guéneau, « Investigation of the solid/liquid phase transitions in the U–Pu–O system », *Calphad* 80 (2023) 102523.

[Gué11] C. Guéneau, N. Dupin, B. Sundman, C. Martial, J.-C. Dumas, S. Gossé, S. Chatain, F. D. Bruycker, D. Manara, R. J. M. Konings, « Thermodynamic modelling of advanced oxide and carbide nuclear fuels: Description of the U–Pu–O–C systems », *Journal of Nuclear Materials* 419 (2011) 145-167.

[Hir11] T. Hirosawa and I. Sato, « Burnup dependence of melting temperature of FBR mixed oxide fuels irradiated to high burnup », *Journal of Nuclear Materials* 418 (2011) 207-214.

[Kat08a] M. Kato, K. Morimoto, S. Nakamichi, H. Sugata, K. Konashi, M. Kashimura, T. Abe, « Effect of Oxygen-to-Metal Ratio on Melting Temperature of Uranium and Plutonium Mixed Oxide Fuel for Fast Reactor », *Transactions of the Atomic Energy Society of Japan* 7 (2008) 420-428.

[Kat08b] M. Kato, K. Morimoto, H. Sugata, K. Konashi, M. Kashimura, T. Abe, « Solidus and liquidus temperatures in the UO_2–PuO_2 system », *Journal of Nuclear Materials* 373 (2008) 237-245.

[Kat08c] M. Kato, K. Morimoto, H. Sugata, K. Konashi, M. Kashimura, T. Abe, « Solidus and liquidus of plutonium and uranium mixed oxide », *Journal of Alloys and Compounds* 452 (2008) 48-53.

[Kat09] M. Kato, « Melting temperatures of oxide fuel for fast reactors », *Proceedings of 2009 international congress on advances in nuclear power plants, ICAPP 2009*, Japan, 2009, 1940-1947.

[Kon98] K. Konno and T. Hirosawa, Melting Temperature of Irradiated Fast Reactor Mixed Oxide Fuels, J. Nucl. Sci. Technology 35 (1998) 494.

This project has received funding from the Euratom research and training programme 2019-2020 under grant agreement No 945022.

[Kon02a] K. Konno and T. Hirosawa, « Melting Temperature of Mixed Oxide Fuels for Fast Reactors », *Journal of Nuclear Science and Technology* 39 (2002) 771-777.

[Kon02b] K. Konno, « Liquidus Temperature of Irradiated Mixed Oxide Fuels for Fast Reactors », *Journal of Nuclear Science and Technology* 39 (2002) 1299-1302.

[Lyo67] W. L. Lyon and W. E. Baily, « The solid-liquid phase diagram for the UO2-PuO2 system », *Journal of Nuclear Materials* 22 (1967) 332-339.

[Mag20] A. Magni, T. Barani, A. Del Nevo, D. Pizzocri, D. Staicu, P. Van Uffelen, L. Luzzi, « Modelling and assessment of thermal conductivity and melting behaviour of MOX fuel for fast reactor applications », *Journal of Nuclear Materials* 541 (2020) 152410.

[Man05] D. Manara, C. Ronchi, M. Sheindlin, M. Lewis, M. Brykin, « Melting of stoichiometric and hyperstoichiometric uranium dioxide », *Journal of Nuclear Materials* 342 (2005) 148-163.

[NEA25] N. Chauvin et al., Recommendations on Fuel Properties for Fuel Performance Codes, NEA/NSC/R(2024)1, July 2025

[PuM25a] P. Martin, M.-M. Desagulier, J. Martinez, C. Guéneau, M. Pons, M. Duchateau, T. Barral, D. Staicu, L. Vlahovic, D. Robba and N. Clavier, « Measurements of thermal properties on fresh fuels », Deliverable D3.7, PuMMA European Project (2025).

[PuM25b] C. Guéneau et al., New correlation law for melting temperature of MOX fuels, Deliverable D3.6, PuMMA European Project (2025)

[Rea73] J. G. Reavis, R. Basinger, R. D. Baker, « Fuel Property Measurements », Quarterly Progress Report on the Advanced Plutonium Fuels Program LA-5193 Progress Report (1973).

[Str16] M. Strach, D. Manara, R. C. Belin, J. Rogez, « Melting behavior of mixed U–Pu oxides under oxidizing conditions », *Nuclear Instruments and Methods in Physics Research Section B: Beam Interactions with Materials and Atoms* 374 (2016) 125-128.

This project has received funding from the Euratom research and training programme 2019-2020 under grant agreement No 945022.

5. Specific heat / Heat capacity

This chapter was originally provided by D. Staicu (JRC-Karlsruhe).

5.1 Literature data

In 1982, J.K. Fink [Fin82] developed correlations for UO_2, PuO_2 and $(U,Pu)O_2$. The correlation for UO_2 was improved by in 2000 by J.K. Fink [Fink00]. In 1990, Cordfunke et Konings [Cor90] refitted the data of determined by J.K. Fink [Fin82] and proposed new parameters for the correlation for PuO_2.

For mixed oxides, the Neumann-Kopp rule is used to estimate the heat capacity $Cp\left(T, U_{1-y}Pu_yO_2\right)$ [Car01, Dur00]. In such case, the heat capacity of the mixed oxide, considered as an ideal solution, is calculated by a linear combination of the end-members as per Eq. 5.1.

$$Cp\left(T, U_{1-y}Pu_yO_2\right) = (1-y) \times Cp(T, UO_2) + y \times Cp(T, PuO_2) \qquad \text{Eq. 5.1}$$

Where Cp are in $J.kg^{-1}.K^{-1}$ and T in K

In 2001, Carbajo *et al.* [Car01] recommend Eq. 5.2 for $Cp(T, UO_2)$ and $Cp(T, PuO_2)$ using the J.K. Fink [Fin82] and Cordfunke et Konings [Cor90] correlations:

$$Cp = C_2 + 2 \times C_3 \times t + 3 \times C_4 \times t^2 + 4 \times C_5 \times t^3 + 5 \times C_6 \times t^4 - C_7 \times t^{-2} \qquad \text{Eq. 5.2}$$

Where the C_i coefficients for UO_2 and PuO_2 are given in Table 5.1 and $t = T/1000$ with T is the temperature in K.

Table 5.1: Coefficients used in the specific heat correlations recommended by Carbajo *et al.* [Car01].

Constant	UO_2	PuO_2	Units
C_2	193.238	311.7866	$J.Kg^{-1}.K^{-1}$
C_3	162.8647	19.629	$J.Kg^{-1}.K^{-2}$
C_4	-104.0014	-0.752	$J.Kg^{-1}.K^{-3}$
C_5	29.2056	0	$J.Kg^{-1}.K^{-4}$
C_6	-1.9507	0	$J.Kg^{-1}.K^{-5}$
C_7	2.6441	7.0131	$J.K.Kg^{-1}$

In 2000 Duriez *et al.* [Dur00] published a correlation for $(U,Pu)O_2$ based on the same values for UO_2 and PuO_2 used by Carbajo *et al.* [Car01] except for temperatures above 2000 K where they used their PuO_2 data.

This project has received funding from the Euratom research and training programme 2019-2020 under grant agreement No 945022.

The specific heat of unirradiated UO_2, PuO_2 and $(U_{0.75}Pu_{0.25})O_2$ as recommended by Duriez [Dur00] and Carbajo [Car01] is shown in Figure 5.1. The relative uncertainty on the Heat Capacity is 2% from 298 to 1800K and 13% from 1800 K to the melting point.

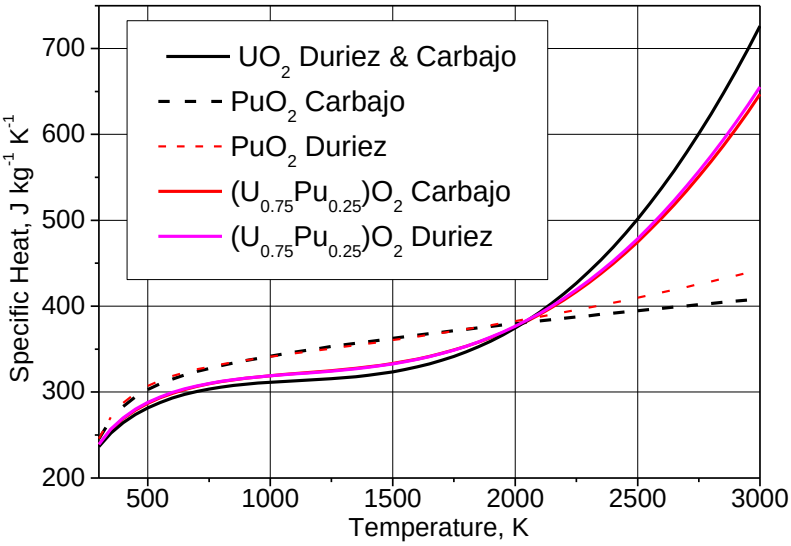

Figure 5.1: Specific heat of unirradiated UO_2, PuO_2 and $(U_{0.75}Pu_{0.25})O_2$ as recommended by Duriez [Dur00] and Carbayo [Car01].

In 2014, Konings et al. [Kon14] published new relations for UO_2 and PuO_2 as given in Eq. 5.3 and Eq. 5.4 respectively.

$$Cp(T, UO_2) = 247.1735 + 1.5976 \times 10^{-1} \times T - 1.3199 \times 10^{-4} \times T^2 + 4.3162 \times 10^{-8} \times T^3 - 4.3278 \times 10^{6} \times T^{-2} \quad \text{Eq. 5.3}$$

$$C_p(T, PuO_2) = 127.8532 + 5.5151 \times 10^{-1} \times T - 4.6097 \times 10^{-4} \times T^2 + 1.3145 \times 10^{-7} \times T^3 - 1.2591 \times 10^{6} \times T^{-2} \quad \text{Eq. 5.4}$$

With Cp in J.kg^{-1}.K^{-1} and T the temperature in K.

Figure 5.2 and Figure 5.3 compare Konings model to the one of Carbajo and to some selected experimental data, for UO_2 and PuO_2 respectively.

This project has received funding from the Euratom research and training programme 2019-2020 under grant agreement No 945022.

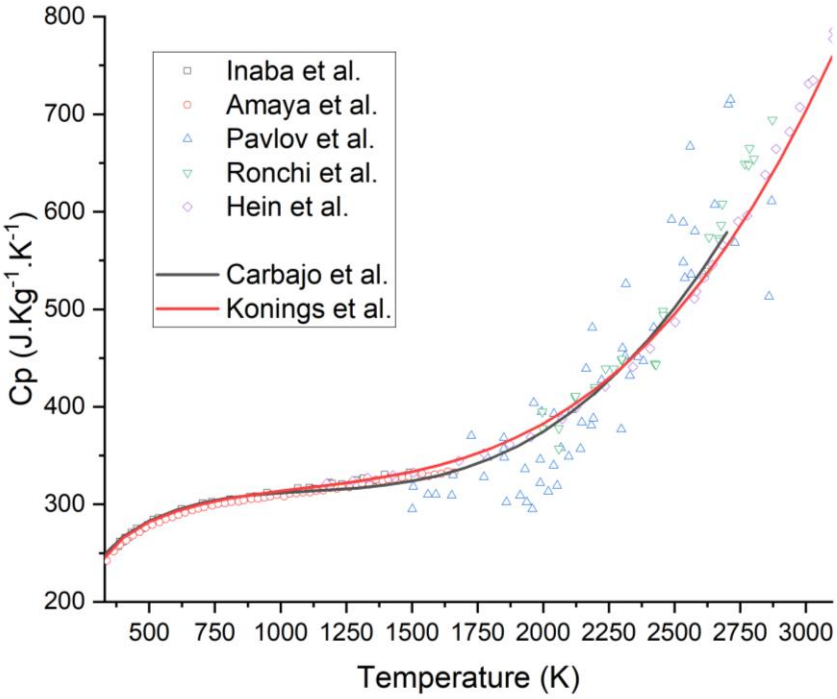

Figure 5.2: Carbajo *et al.* [Car01] and Konings et al. [Kon14] relations compared with selected experimental data for UO_2 heat capacity [Ina87, Ama01, Pav17, Ron99, Hei68].

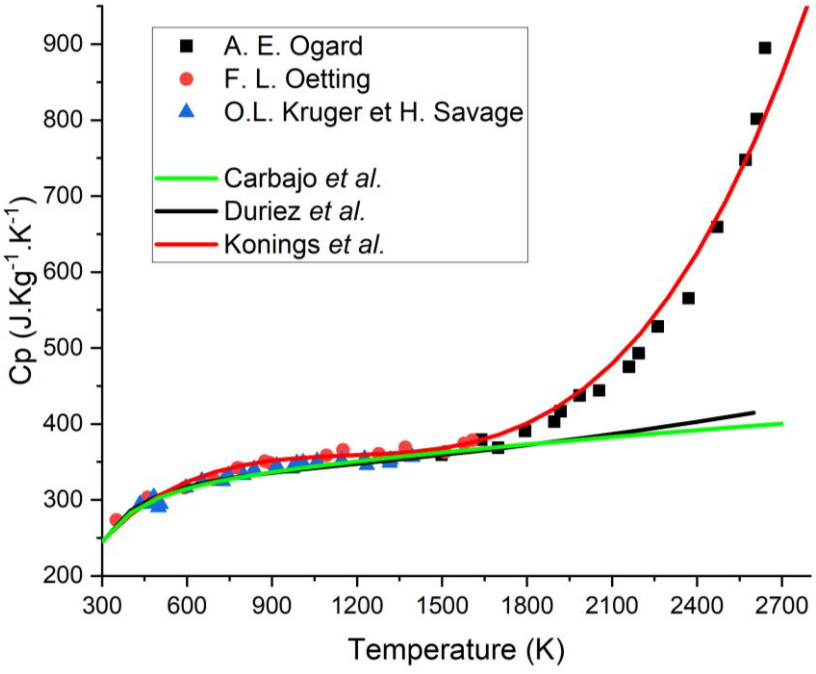

Figure 5.3: Carbajo *et al.* [Car01], Duriez *et al.* [Dur00] and Konings *et al.* [Kon14] relations compared with selected experimental data for PuO_2 heat capacity [Oga70, Oet82, Kru03].

This project has received funding from the Euratom research and training programme 2019-2020 under grant agreement No 945022.

- Effect of stoichiometry

Duriez *et al.* [Dur00] recommended for hypostoichiometric samples the subtraction of a corrective term as per Eq. 5.5:

$$Cp\left(T, U_{1-y}Pu_yO_{2-x}\right) = (1-y) \times Cp(T, UO_2) + y \times Cp(T, PuO_2) - x/2 \times Cp(T, O_2) \quad \text{Eq. 5.5}$$

Where $Cp(T, O_2)$ is given by Eq. 5.6.

$$Cp(T, O_2) = 870.28125 + 0.2665625 \times T - 6.39188 \times 10^{-5} \times T^2 + 6.0375 \times 10^{-9} \times T^3 \quad \text{Eq. 5.6 [1]}$$

With Cp in J.kg^{-1}.K^{-1} and T the temperature in K.

- Molecular Dynamic calculations dedicated to O/M and Pu content influence

With progress in Molecular Dynamic modelling to represent (U,Pu)O_2 system, research work aiming at computing MOX heat capacity has been released in the past years. [Bat21] and [Por24] used the Cooper-Rushton-Grimes interatomic empirical potential [Coo14] to compute the heat capacity of stoichiometric (U,Pu)O_2 on the whole range of Pu content [Bat21] and for O/M ratio from 1.92 to 2.00 [Por24]. Their results are indicating a dependance on O/M ratio and Pu content on the Bredig transition by :

- Moving it to lower temperature range with higher Pu content, see Figure 5.4;
- Reducing its amplitude with decreasing O/M, see Figure 5.4.

A model has been derived from these calculations accounting for Bredig transition, O/M and Pu content. However, for now, no heat capacity model based on experimental data includes Bredig transition, but it is of importance to better assess thermal conductivity from Flash Laser measurements at temperature above 2000 K and better predict temperature transient in irradiated fuel. For the temperature below 2000 K, their work confirms that O/M ratio and Pu content have no impact on heat capacity, which can be considered equivalent to UO_2 law.

[1] Contrary to what is mentioned in [Dur00], $Cp(T, O_2)$ was given in J.mol^{-1}.K^{-1} in the publication. It has been converted here in the mentioned unit J.kg^{-1}.K^{-1}

This project has received funding from the Euratom research and training programme 2019-2020 under grant agreement No 945022.

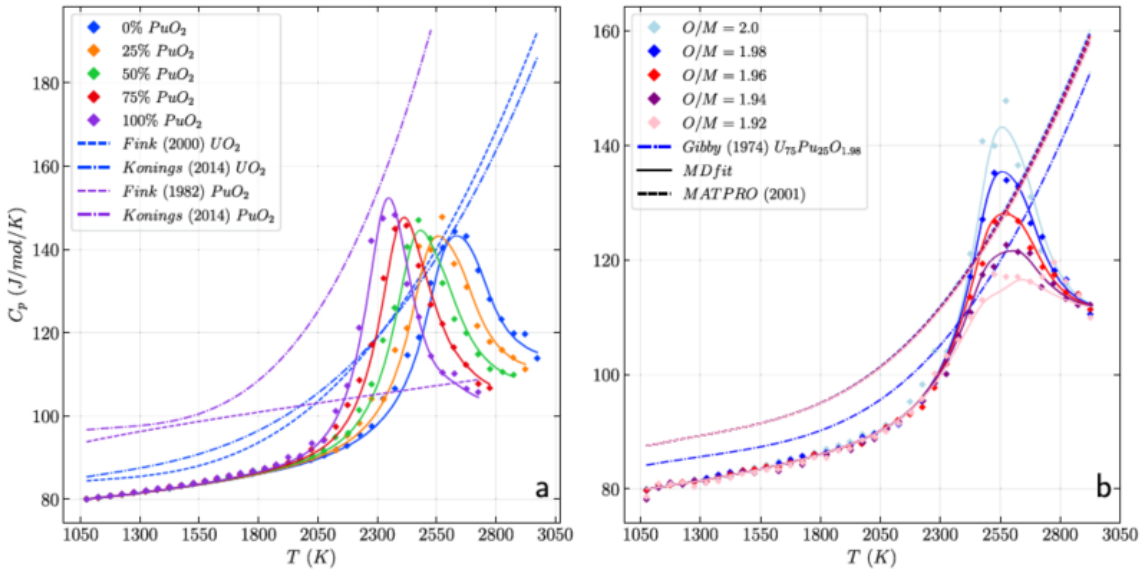

Figure 5.4: Molecular dynamic data evaluating MOX Cp versus temperature for various Pu content on figure a) ([Por24] citing [Bat21]) and for various O/M on figure b) [Por24]

- Effect of burn-up

Only a very limited number of studies is available and the specific heat of irradiated fuel is not yet fully clarified. The effect of soluble FP elements added to fresh UO_2 was quantified for instance by Verall [Ver96], Matzke [Mat97] Matsui [Mat92] or Takahashi [Tak93]. A small (absolutely negligible) effect of burn-up in SIMFUEL was described by Matzke [Mat97]. Carbayo [Car01] recommended the same formula, his equation (21) contains an error compared to the original equation in the paper of Matzke. No large burn-up effect was found because the specific heat obeys the law of mixtures (Neumann-Kopp law) and because only a limited fraction of the fresh fuel heavy metal atoms change nature during irradiation.

Specific heat measurements for irradiated fuel by calorimetric techniques show an exothermic effect during the first heat-up of the sample linked to the recombination of radiation damage and to FP redistribution. The apparent specific heat is lower than for annealed samples because of this heat effect, as observed by Gomme [Gom98] and Yagnik [Yag06]. A similar effect is observed for $(U,Pu)O_2$ samples damaged by auto-irradiation [Sta10]. This means for instance that during fast power increases, the temperature will increase faster than predicted using the fresh fuel specific heat. For the intrinsic specific heat (i.e. measured on annealed samples) no significant difference was found compared with fresh fuel.

In the case of UO_2, a measurement by Amaya [Ama01] has shown that the heat capacity of irradiated UO_2 with 39 GWd/t burn-up is similar to fresh UO_2.

Similar results were obtained by direct measurements of specific heat on irradiated fuels by laser flash, reported by Ronchi for UO_2 [Ron04] and by Sonoda for $(U,Gd)O_2$ [Son07]. Therefore, the specific heat of irradiated fuel is generally assumed to be equal to that of the fresh fuel.

This project has received funding from the Euratom research and training programme 2019-2020 under grant agreement No 945022.

- Measurements on fuel (fresh and irradiated)

Specific heat for fresh and irradiated FBR MOX fuels was determined in the framework of the ESNII+ Project [Sta17a, Sta17b] on:

- two unirradiated PHENIX MOX fuels, with a Pu content of 24% and O/M values of 2.000 and 1.978.
- two unirradiated TRABANT MOX fuels with Pu contents of 40 and 45%.
- two irradiated NESTOR3 fuels, with a fresh fuel Pu content of 24% and burn-ups of 8.4 and 13 at%.

The specific heat of unirradiated fuels obtained during the ESNII+ Project and a comparison to the recommendation of Duriez [Dur00] is shown in Figure 5.5. Taking into account the experimental uncertainties (7%), the new specific heat values can be considered as consistent with the litterature data.

Specific heat of the irradiated NESTOR3 fuels obtained during the ESNII+ Project compared to the fresh fuel value calculated following the recommendation of Duriez [Dur00] is shown in Figure 5.6. The irradiated fuels have a clear tendency to have a higher specific heat when compared to the fresh fuel value. The difference remains however within the experimental uncertainties (10%).

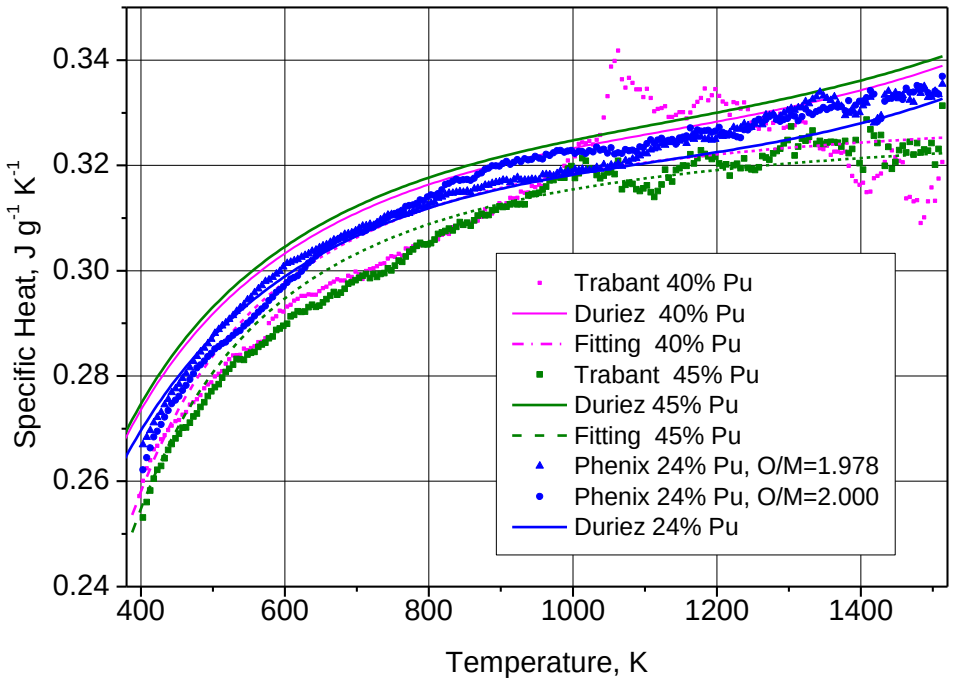

Figure 5.5: Specific heat of unirradiated fuels obtained during the ESNII+ Project and comparison to the recommendation of Duriez [Dur00].

This project has received funding from the Euratom research and training programme 2019-2020 under grant agreement No 945022.

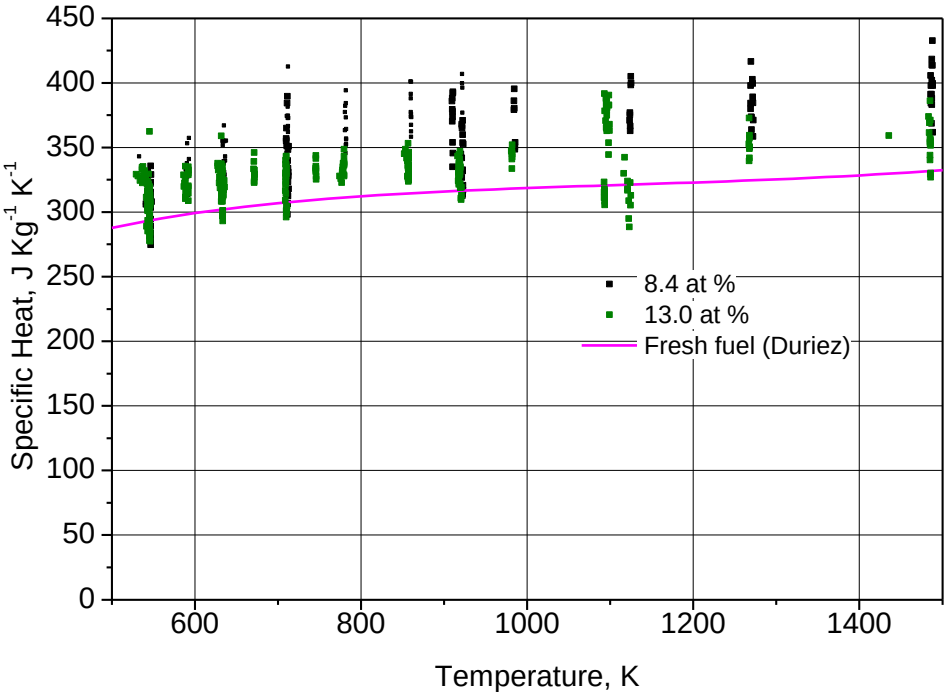

Figure 5.6: Specific heat of the irradiated NESTOR3 fuels obtained during the ESNII+ Project compared to the fresh fuel value calculated following the recommendation of Duriez [Dur00].

[Hir24] performed enthalpy measurements on fresh UO_2, MOX with Pu 18% and 45% Pu and PuO_2 samples. The results obtained are in agreement with literature data below 2000 K. Above, high values of enthalpy are obtained, with a substantial deviation from historical literature data and recent Molecular Dynamic results, see Figure 5.7. From these enthalpy measurements, heat capacity was derived with the same results. Figure 5.8 shows the heat capacity compared to literature and MD results. An important shift is observed in temperature between these results with the increase in Cp evaluated from MD calculations for Bredig transition from Cooper or Pavlov (UO_2), but compared to MD results from [Bat21] reported in Figure 5.4-a), shows an appreciable similarity, at least for onset of Bredig's transition for high Pu content (> 45 %) is similarly observed in measurements and MD calculations. However, maximum values of Cp in [Hir24] are much higher than predicted by MD.

This project has received funding from the Euratom research and training programme 2019-2020 under grant agreement No 945022.

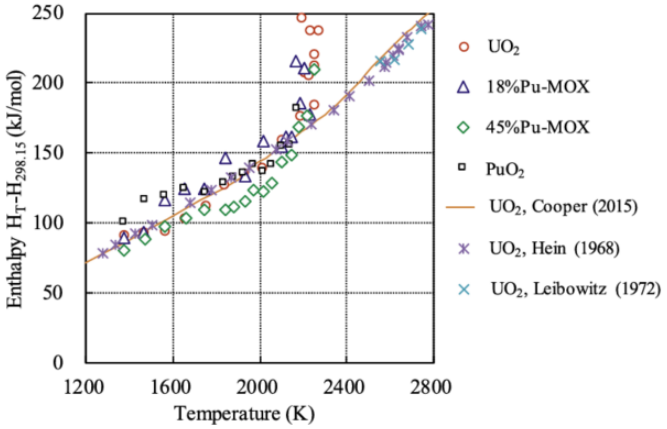

Figure 5.7: Enthalpy increase in UO_2, 18 and 45% Pu MOX and PuO_2 by drop calorimetry [Hir24]. Data are compared with Molecular Dynamic calculations (Cooper) and historical results (Hein, Leibowitz)

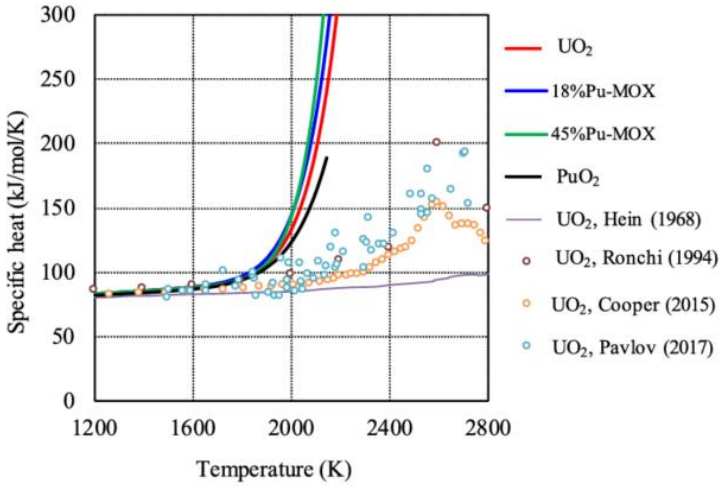

Figure 5.8: Heat Capacity for UO_2, 18 and 45% Pu MOX and PuO_2 derived from enthalpy variation measurements [Hir24] compared to Hein and Ronchi data, and Cooper and Pavlov MD calculations

5.2 NEA recommendation

The recommended law in [NEA25] for heat capacity variation with the plutonium content and the deviation to stoichiometry is based on Neumann-Kopp law (Eq. 5.1) and is given in Eq. 5.7.

$$Cp(MOX) = f_{UO_2}.C_p^{UO_2} + f_{PuO_2}.C_p^{PuO_2} + f_{NpO_2}.C_p^{NpO_2} + f_{AmO_2}.C_p^{AmO_2} + f_{O_2}.C_p^{O_2} \quad \text{Eq. 5.7}$$

Where f_i is the weight fraction of species i,

$C_p^{UO_2}$ and $C_p^{PuO_2}$ are the one recommended by Konings et al. [Kon14] (resp. Eq. 5.3 and Eq. 5.4)

This project has received funding from the Euratom research and training programme 2019-2020 under grant agreement No 945022.

$C_p^{O_2}$ is the one recommended by Duriez *et al.* [Dur00] (Eq. 5.6)

$C_p^{NpO_2}$ and $C_p^{AmO_2}$ are given respectively by Eq. 5.8 (valid up to 2500 K) and Eq. 5.9 (valid up to 1080 K).

$$Cp(NpO_2) = 240.7431 + 1.6301 \times 10^{-1} \times T - 1.3035 \times 10^{-4} \times T^2 + 4.9031 \times 10^{-8} \times T^3 - 2.9338 \times 10^{6} \times T^{-2} \quad \text{Eq. 5.8}$$

$$C_p(AmO_2) = 287.1073 + 1.3948 \times 10^{-2} \times T - 5.1113 \times 10^{6} \times T^{-2} \quad \text{Eq. 5.9}$$

Limited to no heat capacity data exist on irradiated MOX fuel; thus, direct correlations are difficult to assess.

The range of parameters for the validity of the recommendation is:

- O/M from 1.9 to 2.0
- T < 2500 K

Uncertainty is estimated to be ~ 3%.

5.3 Data obtained in the frame of the ESFR-SMART project

5.3.1 Fresh fuel

In the frame of the ESFR-SMART project, heat capacity was measured on various fresh MOX samples for temperatures above 1500K using the CLASH setup at JRC. Details on the measured samples are given in Table 5.2.

Results are shown in Figure 5.9.

Table 5.2: Details of the fresh $(U,Pu)O_2$ studied samples.

Samples	Compositions
PHENIX24	$U_{0.76}Pu_{0.235}Am_{0.005}O_{1.983}$
PHENIX29	$U_{0.70}Pu_{0.29}Am_{0.01}O_{1.984}$
PHENIX29-OM	$U_{0.70}Pu_{0.29}Am_{0.01}O_{1.998}$
CAPRA4	$U_{0.70}Pu_{0.28}Am_{0.02}O_{2.004}$
TRABANT40-A	$U_{0.60}Pu_{0.39}Am_{0.01}O_{1.995}$
TRABANT40-B	$U_{0.60}Pu_{0.39}Am_{0.01}O_{1.978}$
TRABANT40-OM	$U_{0.60}Pu_{0.39}Am_{0.01}O_{1.999}$
RV45	$U_{0.55}Pu_{0.45}O_{1.987}$
TRABANT45	$U_{0.55}Pu_{0.44}Am_{0.01}O_{2.00}$

This project has received funding from the Euratom research and training programme 2019-2020 under grant agreement No 945022.

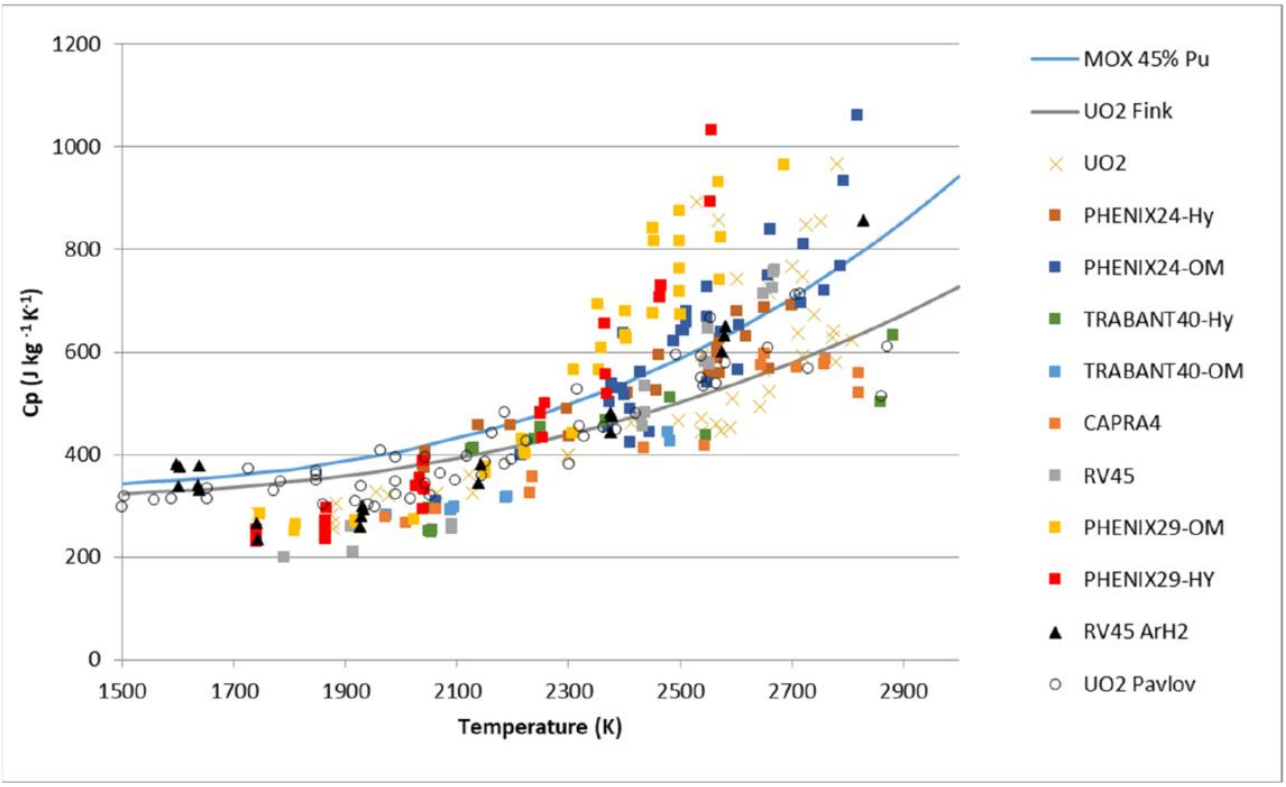

Figure 5.9: Specific heat results for fresh MOX samples obtained with the CLASH set-up
and comparison to UO_2 (Fink) and MOX containing 45 wt. % Pu (based on the Cp of Fink for UO_2 and Konings for PuO_2).

The scatter in the measurement data is typical for this method. No clear trend with the increase in the Pu content or with O/M could be observed, but a clear increase of the specific heat was observed for all samples with increasing temperature.

For comparison purposes, literature data for UO_2 [Fink00] and MOX containing 30 wt. % Pu (based on the Cp of Fink for UO_2 and Konings for PuO_2) are also shown in Figure 5.9. The experimental data are in the expected range. In the low temperature range (below 2200K) the data are below the expectation and tend to be higher in the high temperature range (above 2500K). The results obtained for UO_2 by Pavlov [Pav17] are also shown in Figure 5.9 and show a similar behavior when compared to the values expected from the recommendation of Fink.

5.3.2 Irradiated fuel

In the framework of the ESFR-SMART project, specific heat was determined on two irradiated MOX fuels [ESF23]:

- PAVIX-8 pin: fresh fuel Pu content of 23.3%, initial O/M = 1.975 and burn-up = 13.0% FIMA.
- MYOSOTIS-12 pin: fresh fuel Pu content of 28.3%, initial O/M = 1.971 and burn-up = 15.2% FIMA.

The specific heat of the MYOSOTIS and PAVIX samples was evaluated using the data obtained with the LAF set up and is shown in Figure 5.10.

This project has received funding from the Euratom research and training programme 2019-2020 under grant agreement No 945022.

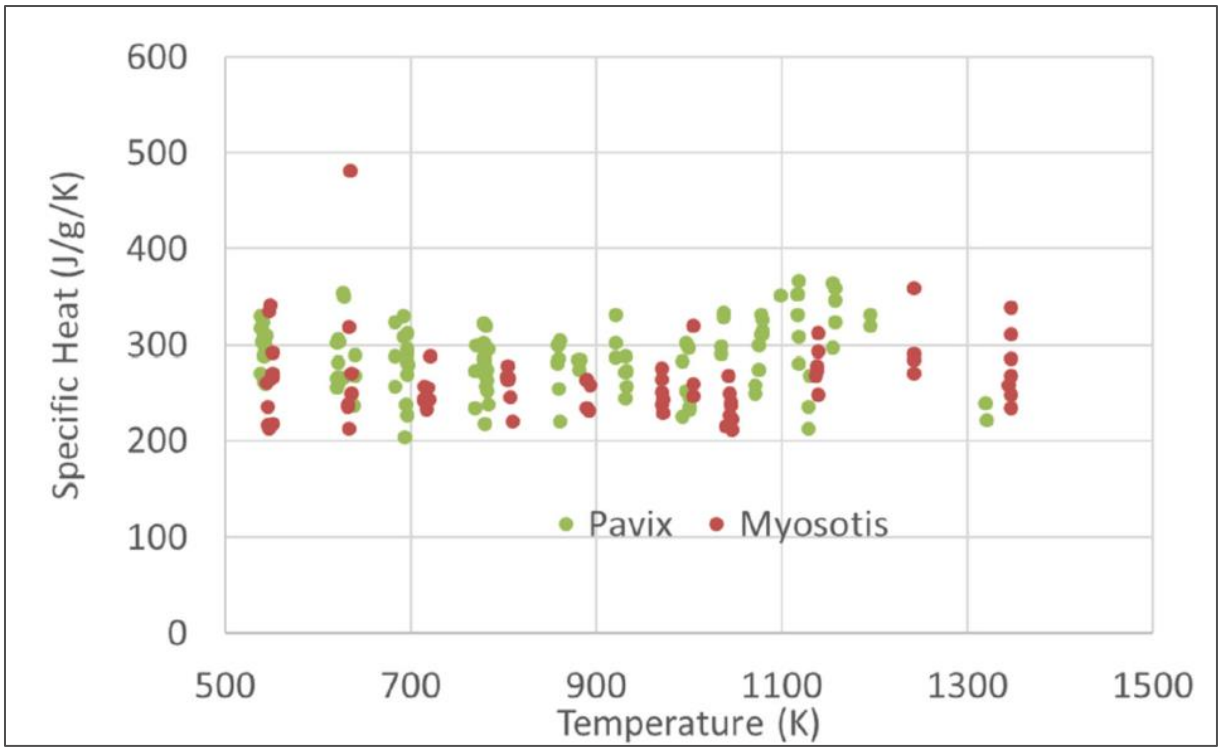

Figure 5.10: Specific heat results for the PAVIX and MYOSOTIS samples obtained with the LAF set-up.

A scatter of about 25% was observed in the data, which is in the usual range and is significantly higher than usual due to the small samples size and complex shape.

5.4 Data obtained in the frame of the PuMMA project

5.4.1 Fresh fuel

In the frame of the PuMMA project, heat capacity was measured on PuO_2 samples and 6 fresh MOX samples for temperatures above 1500K using the CLASH setup at JRC [PuM25a]:

- PuO_2 samples with with an initial O/M = 2.00.
- Three stoichiometric samples (O/M = 1.99 ± 0.01) with Pu content of 59, 63 and 69% called MOX60-F, MOX65-F and MOX70-F respectively.
- Three annealed samples, with an O/M = 1.98, and with Pu content of 59, 63 and 69% called MOX60-A, MOX65-A and MOX70-A respectively.

The results from the measurements on PuO_2 under Ar and Ar + H_2 (CLASH set-up) are plotted in Figure 5.11. Obtained results were scarce due to the low signal to noise ratio, and thus it was not possible to reach a conclusion.

This project has received funding from the Euratom research and training programme 2019-2020 under grant agreement No 945022.

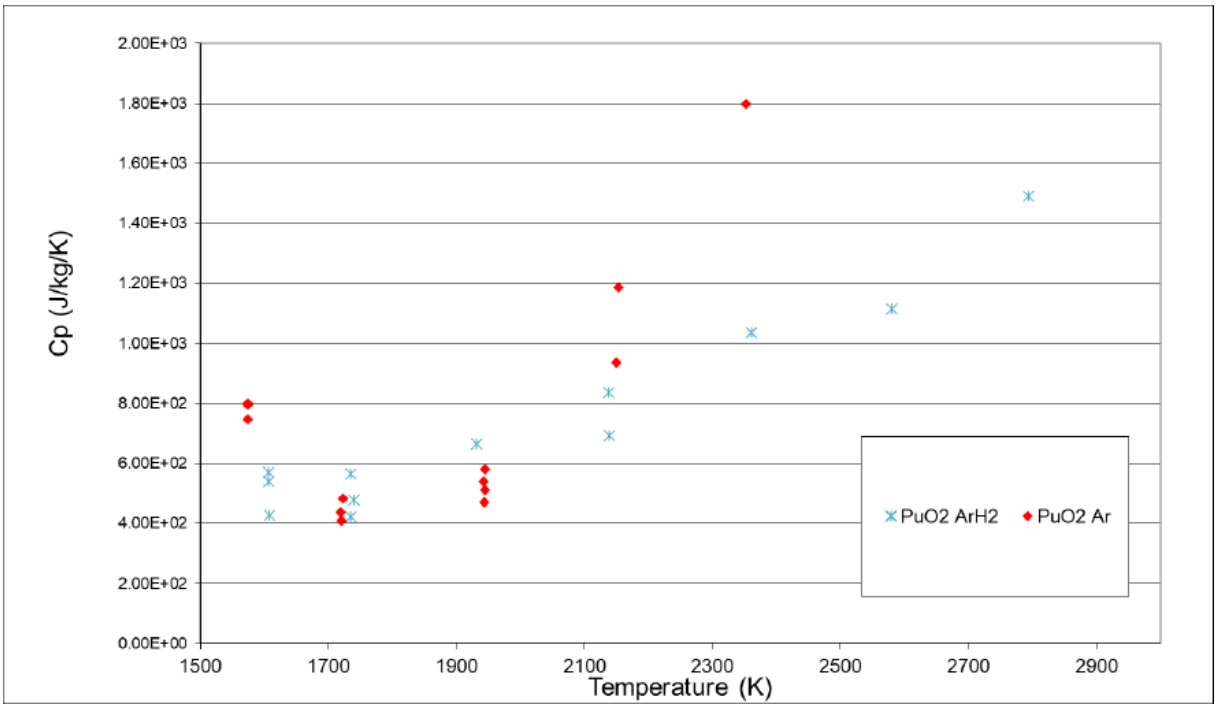

Figure 5.11: Heat capacity results obtained on PuO_2 under Ar and Ar/H_2 atmospheres.

The obtained results are plotted in Figure 5.12 and Figure 5.13 for batches F and A respectively and compared with the empirical laws determined by Konings et al. [Kon14] (Eq. 5.3, Eq. 5.4) for UO_2 and PuO_2.

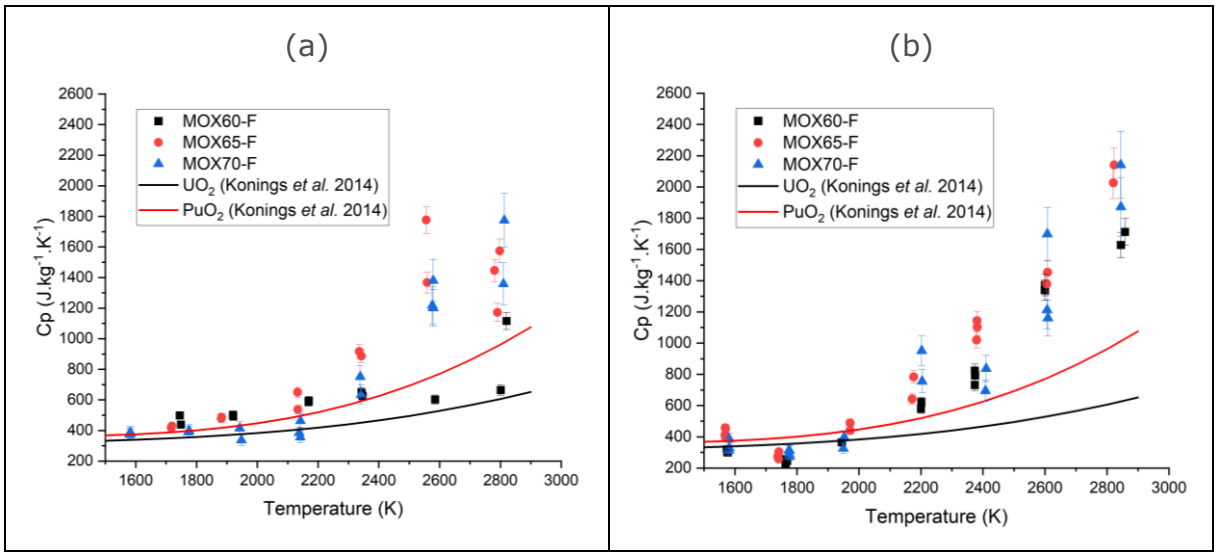

Figure 5.12: Heat capacity results obtained on samples of the F-Batch compared to Konings et al. [Kon14] (a) in Ar, (b) in Ar/H_2.

This project has received funding from the Euratom research and training programme 2019-2020 under grant agreement No 945022.

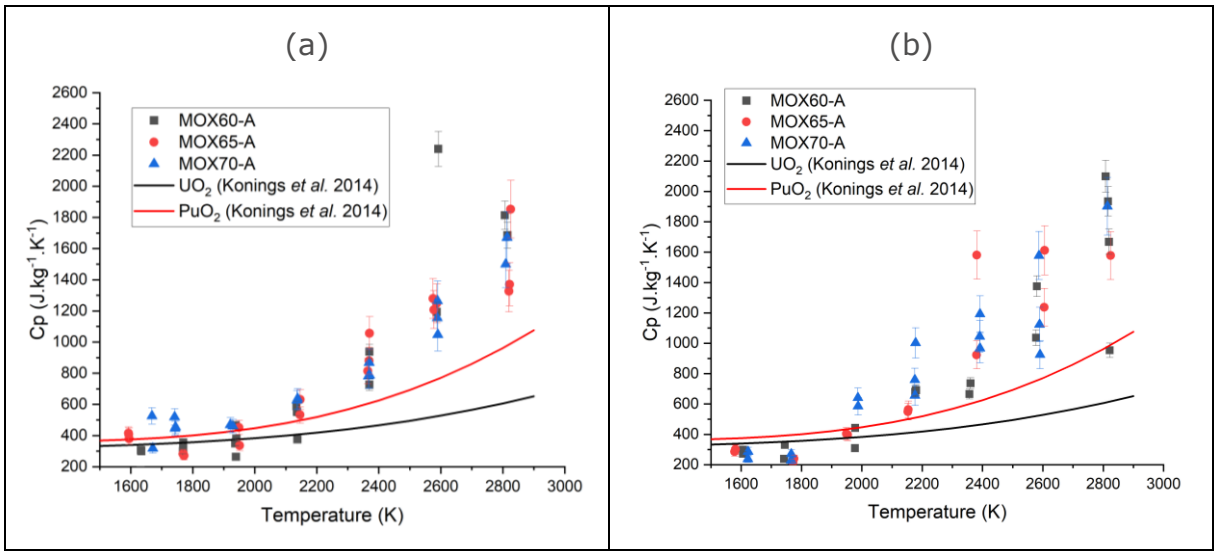

Figure 5.13: Heat capacity results obtained on samples of the A-Batches compared to Konings et al. [Kon14] (a) in Ar, (b) in Ar/H_2.

Typically, values for $(U,Pu)O_2$ compounds are estimated using the Neumann-Kopp rule, which means that the heat capacity for $(U,Pu)O_2$ cannot be higher than that for PuO_2. Nevertheless, as shown in Figure 5.12 and Figure 5.13, all experimental values obtained for temperatures above 2000-2200 K for the tree compositions are systematically above the PuO_2 law. This behavior cannot be attributed to an evolution of the O/M ratio during the measurements, since the latter remains constant over the whole temperature range.

These new experimental results show a significant deviation from the existing law. Nevertheless, as these are the first experimental results for $(U,Pu)O_2$ with such high plutonium content, they have to be taken into account. Furthermore, recent results obtained by Hirooka et al. [Hir24] on 45 % and 18 % Pu/(U+Pu) samples also show a significant increase in the heat capacity above 1800K compared to the literature as previously illustrated in Figure 5.8. Hirooka et al. determined heat capacity values of 1066 $J.Kg^{-1}.K^{-1}$ at 2125 K and 1110 $J.Kg^{-1}.K^{-1}$ at 2160K for samples $(U_{0.516}Pu_{0.453}Am_{0.031})O_{2.000}$ and $(U_{0.816}Pu_{0.179}Am_{0.005})O_{2.000}$ respectively. These values are in good agreement with results show in Figure 5.12 and Figure 5.13.

A dependence of Pu content is not possible to assess considering the large dispersion of the new experimental points. However, the heat capacity increases significantly above 1800 K compared to Konings et al. recommendations.

5.4.2 Irradiated fuel

Still in the frame of the PuMMA project, specific heat was measured simultaneously with the thermal diffusivity by the laser-flash method using the LAF set-up in the temperature range 550-1600 K for various irradiated samples [PuM25b]:

- two samples coming from TRABANT 1-1 pin: 45% Pu in fresh fuel, burnup 9.5%at. Samples were taken from the bottom of the fuel pin, supposed less

This project has received funding from the Euratom research and training programme 2019-2020 under grant agreement No 945022.

affected by the pin failure (presence of sodium in the pin at the top of fuel column).
- two samples coming from CAPRIX pin, from the Maximum Flux Plane (MFP) (B-271 segment): 45% Pu in fresh fuel, burnup 12.2%at.
- One sample coming from CAPRIX pin, from the top of the fissile column (HCF) (B-267 segment): 45% Pu in fresh fuel, burnup 7.8%at.

The specific heat is determined with an uncertainty of 10%, due to the uncertainty on the sample emissivity and to the complex sample shape.

Obtained results on CAPRIX and TRABANT 1.1 samples are shown in Figure 5.14 and compared to other experimental results (PAVIX and MYOSOTIS samples) in Figure 5.15.

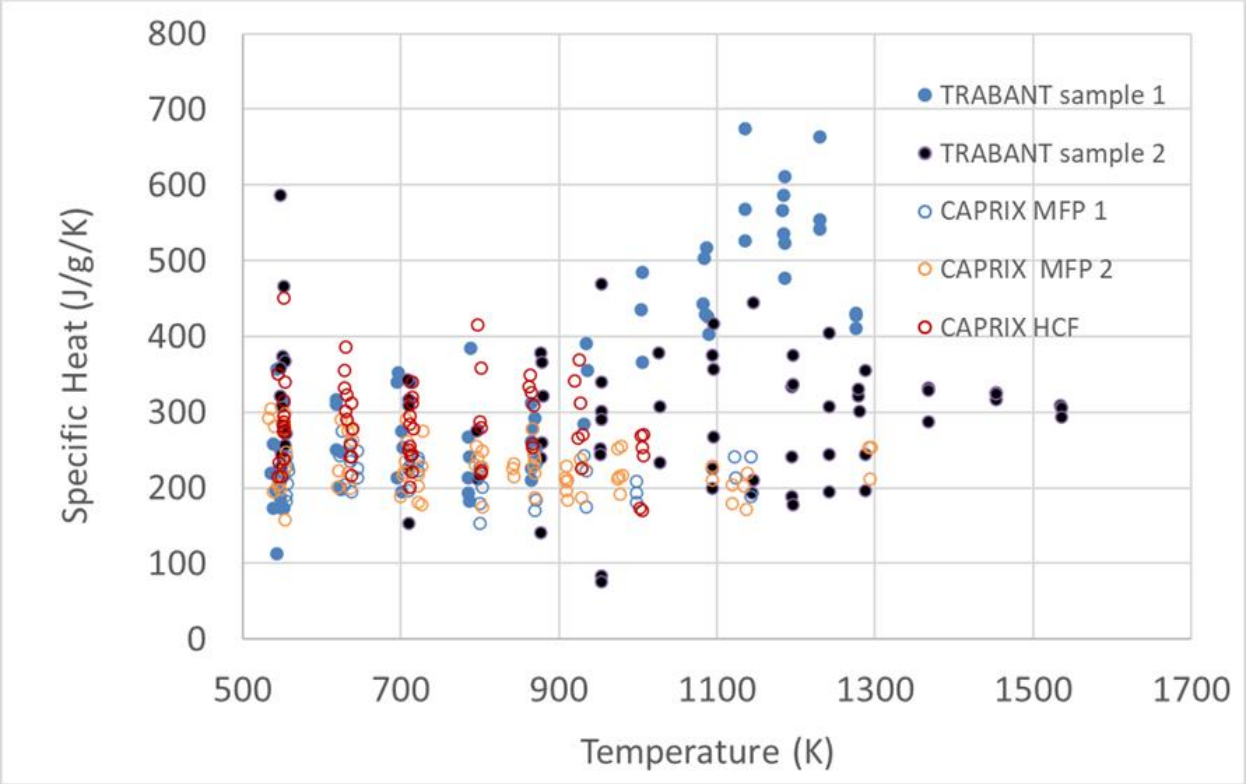

Figure 5.14: Specific heat of irradiated TRABANT and CAPRIX samples.

This project has received funding from the Euratom research and training programme 2019-2020 under grant agreement No 945022.

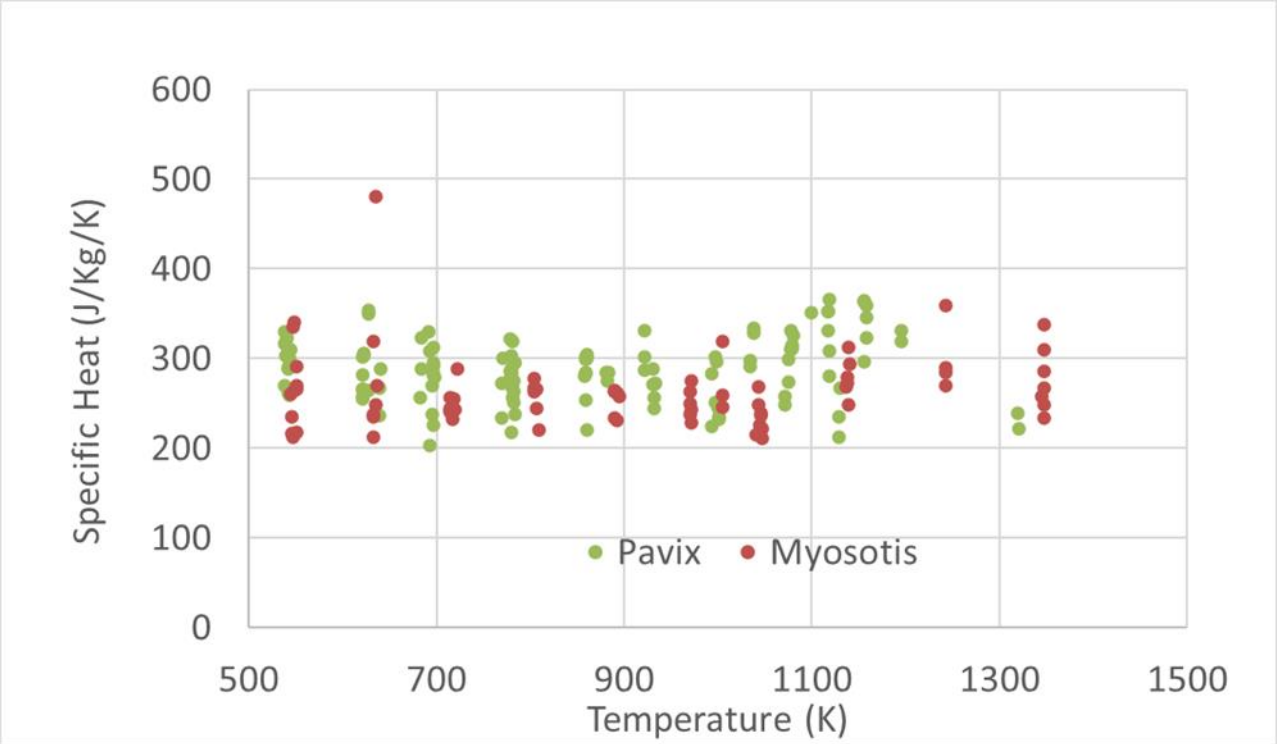

Figure 5.15: Specific heat of irradiated PAVIX and MYOSOTIS samples.

Considering the high scatter on the measurements, it could only be concluded that the specific heats of the different fuels were in the same range, but a more detailed comparison was not possible.

5.5 Conclusions and recommendations

A good consensus exists in the open literature on the specific heat values of unirradiated stoichiometric MOX fuel and the formula of Kopp-Neuman (Eq. 5.1) with Cp-UOX and Cp-PuOX recommended by Konings (resp. Eq. 5.3 and Eq. 5.4) can be recommended. However deviation was highlighted with the measurements for high plutonium content samples performed in the frame of the PuMMA project. For Pu% higher than 45%, Cp was twice the expected values at high temperature (>2000K). These results are consistent with Japanese direct measurements with a drop calorimeter but the interpretation is still on-going.

The effect of stoichiometry should be considered introducing Cp-O_2 in the Kopp-Neuman formula as recommended by Duriez (see Eq. 5.5 and Eq. 5.6). This recommendation will nevertheless need to be subject to experimental validation.

The measurements obtained on irradiated fuels show that the values are very dispersed up to a factor 2 even for the same composition and burn-up conditions. On irradiated fuels all the data provided were obtained between 500 to 1500K.

Effort on modelling high temperature heat capacity should be pursued, as it is a key parameter for thermal conductivity measurements interpretation and transient modelling in fuel performance codes.

This project has received funding from the Euratom research and training programme 2019-2020 under grant agreement No 945022.

5.6 References

[Ama01] M. Amaya, K. Une and K. Minato, Heat capacity measurements on unirradiated and irradiated fuel pellets, J. Nucl. Mater. 294 (2001) 1.

[Bat21] D. Bathellier et al, A new heat capacity law for UO_2, PuO_2 and $(U,Pu)O_2$ derived from molecular dynamics simulations and useable in fuel performance codes, J. Nucl. Mater. 549 (2021), 152877

[Car01] J.J. Carbajo, G.L. Yoder, S.G. Popov and V.K. Ivanov, A review of the thermophysical properties of MOX and UO_2 fuels, J. Nucl. Mater. 299 (2001) 181.

[Coo14] M.W.D Cooper et al, A many-body potential approach to modelling the thermomechanical properties of actinide oxides, J. Phys. Condens. Matter **26** (2014), 10

[Cor90] E.H.P. Cordfunke, R.J.M. Konings, Thermochemical Data for Reactor Materials and Fission Products, North Holland, Amsterdam, 1990.

[Dur00] C. Duriez, J.-P. Alessandri, T. Gervais and Y. Philipponneau, Thermal conductivity of hypostoichiometric low Pu content $(U,Pu)O_{2-x}$ mixed oxide, J. Nucl. Mater. 277 (2000) 143.

[ESF23] D. Staicu, D. Robba, L. Vlahovic, P. Pöml, E. Dahms, P. Fouquet-Metivier, F. Cabezas, M.-M. Desagulier, Ph. Martin, N. Chauvin, I. Viallard and J.-C. Dumas, « New measurements of properties of MOX fuel with associated characterizations », Deliverable D2.5.5, ESFR-SMART European Project (2023).

[Fin82] J.K. Fink, Enthalpy and heat capacity of the actinide oxides, Int. J. Thermophys. 3 (1982) 165.

[Fink00] J.K. Fink, Thermophysical properties of uranium dioxide, J. Nucl. Mater. 279 (2000) 1.

[Gom98] R.A. Gomme, J.C. Carrol, and T.L. Shaw, Thermal conductivity determinations for irradiated fuel. High Temp - High Press. 30 (1998) p. 135-140.

[Hei68] R. A. Hein, L. H. Sjodahl, et R. Szwarc, « Heat content op uranium dioxide from 1200 to 3100 °K », *Journal of Nuclear Materials* 25 (1968) 99-102.

[Hir24] S. Hirooka et al, Enthalpy measurement on $(U_{1-x}Pu_x)O_2$ (x=0, 0.18, 0.45, and 1) and analysis of heat capacity, J. Nucl. Mater **598** (2024), 155188

[Ina87] H. Inaba, K. Naito, et M. Oguma, « Heat capacity measurement of $U_{1-y}Gd_yO_2$ ($0.00 \leqq y \leqq 0.142$) from 310 to 1500 K », *Journal of Nuclear Materials* 149 (1987) 341-348.

[Kon14] R. J. M. Konings, O. Beneš, A. Kovács, D. Manara, D. Sedmidubský, L. Gorokhov, V. S. Iorish, V. Yungman, E. Shenyavskaya, et E. Osina, « The Thermodynamic Properties of the *f* -Elements and their Compounds. Part 2. The Lanthanide and Actinide Oxides », *Journal of Physical and Chemical Reference Data* 43 (2014) 013101

This project has received funding from the Euratom research and training programme 2019-2020 under grant agreement No 945022.

[Kru03] O. L. Kruger et H. Savage, « Heat Capacity and Thermodynamic Properties of Plutonium Dioxide », *The Journal of Chemical Physics* 49 (2003) 4540-4544.

[Mat92] T. Matsui, Y. Arita, and K. Naito, High temperature heat capacities and electrical conductivities of UO_2 doped with yttrium and simulated fission products, J. Nucl. Mater. 188 (1992) 205.

[Mat97] Hj. Matzke, P.G. Lucuta, R.A. Verrall and J. Henderson, Specific heat of UO_2-based SIMFUEL, J. Nucl. Mater. 247 (1997) 121.

[NEA25] N. Chauvin et al., Recommendations on Fuel Properties for Fuel Performance Codes, NEA/NSC/R(2024)1, July 2025

[PuM25a] P. Martin, M.-M. Desagulier, J. Martinez, C. Guéneau, M. Pons, M. Duchateau, T. Barral, D. Staicu, L. Vlahovic, D. Robba and N. Clavier, « Measurements of thermal properties on fresh fuels », Deliverable D3.7, PuMMA European Project (2025).

[PuM25b] D. Staicu, E. Dahms, G. Montagnier, C. Nourry, N. Chauvin, P. Martin, « Results of measurements of irradiated MOX fuel », Deliverable D3.8, PuMMA European Project (2025).

[Oet82] F. L. Oetting, « The chemical thermodynamics of nuclear materials. VII. the high-temperature enthalpy of plutonium dioxide », *Journal of Nuclear Materials* 105 (1982) 257-261.

[Oga70] A. E. Ogard, « High-temperature heat content of plutonium dioxide », *Plutonium 1970 and Other Actinides* (1970).

[Pav17] T. R. Pavlov, M. R. Wenman, L. Vlahovic, D. Robba, R. J. M. Konings, P. Van Uffelen, et R. W. Grimes, « Measurement and interpretation of the thermo-physical properties of UO_2 at high temperatures: The viral effect of oxygen defects », *Acta Materialia* 139 (2017) 138-154.

[Por24] G. Porto et al, Thermodynamic and thermoelastic properties of hypostoichiometric MOX fuels with molecular dynamics simulations, J. Nucl. Mater **598** (2024), 155163

[Ron99] C. Ronchi, M. Sheindlin, M. Musella, et G. J. Hyland, « Thermal conductivity of uranium dioxide up to 2900 K from simultaneous measurement of the heat capacity and thermal diffusivity », *Journal of Applied Physics* 85 (1999) 776-789.

[Ron04] C. Ronchi, M. Sheindlin, D. Staicu and M. Kinoshita, Effect of burn-up on the thermal conductivity of uranium dioxide up to 100.000 $MWd.t^{-1}$, J. Nucl. Mater. 327 (2004) 58.

[Son07] T. Sonoda, T. Kameyama, A. Sasahara, S. Kitajima, Y. Nauchi, et al. Clarification of Rim Structure Effects on Properties and Behaviour of LWR UO_2 Fuels and Gadolinia Doped Fuels. in Proc. Int. LWR Fuel Perf. Mtg. 2007. San Francisco, California.

This project has received funding from the Euratom research and training programme 2019-2020 under grant agreement No 945022.

[Sta10] D. Staicu, T. Wiss, V.V. Rondinella, J.P. Hiernaut, R.J.M. Konings and C. Ronchi, Impact of auto-irradiation on the thermophysical properties of oxide nuclear reactor fuels, J. Nucl. Mater. 397 (2010) 8.

[Sta17a] D. Staicu, E. Dahms, D. Manara, J.-Y. Colle, O. Benes, M. Marchetti, D. Robba, N. Chauvin, P. M. Martin, Measurement of properties of fresh PHENIX fuel, European Commission, ESNII+ Project, Deliverable D.7.4.1 (2017).

[Sta17b] D. Staicu, E. Dahms, T. Wiss, O. Benes, J.-Y. Colle, N. Chauvin, P. M. Martin, Properties measurements on irradiated fuels (NESTOR 3), European Commission, ESNII+ Project, Deliverable D.7.4.2 (2017).

[Tak93] Y. Takahashi and M. Asou, High-temperature heat-capacity measurements on $(U,Gd)O_2$ by drop calorimetry and DSC, J. Nucl. Mater. 201 (1993) 108.

[Ver96] R.A. Verall and P.G. Lucuta, Specific heat measurements of UO_2 and SIMFUEL, J. Nucl. Mater. 228 (1996) 251.

[Yag06] S. Yagnik and J.A. Turnbull. Specific heat and density of high burnup fuel. in Proc. Int. LWR Fuel Perf. Mtg. 2006. Salamanca, Spain.

This project has received funding from the Euratom research and training programme 2019-2020 under grant agreement No 945022.

6. Enthalpy of fusion

This chapter was originally provided by R. Calabrese (ENEA).

6.1 Literature data

The enthalpy of fusion (heat of fusion) of MOX fuel is a thermodynamic property assumed to be small and whose experimental measurement is affected by high uncertainties. The review of the open literature provided a set of values in great part calculated and mostly based on the ideal solution model. The data on MOX fuel is scanty while the determinations of the enthalpy of fusion of UO_2 are more abundant. Recent laser heating measurements have increased the value assumed for the melting temperature of PuO_2 pointing out the need for a re-evaluation of the phase diagram of the UO_2-PuO_2 system at high concentrations of plutonium. Based on these recent measurements, the validity of the ideal solution model was questioned, whereas the description of the entropy of fusion according to the Epstein's proposal has been confirmed in the literature presented here [Eps67].

The study of Epstein is fundamental for the following investigations on the enthalpy of fusion of MOX fuel [Eps67]. The author, relying on the measurements of the phase diagram of the UO_2-PuO_2 system discussed in [Lyo67], calculates the enthalpy of fusion of UO_2 and PuO_2 [Eps67]. His results are based on the hypothesis that UO_2 and PuO_2 form an ideal solution with a continuous series of solid solutions and a lens-shaped phase diagram. In addition, he assumes that the entropy of fusion follows correlation (Eq. 6.1).

$$\Delta S_{fusion\,i} = \Delta H_{fusion\,i} \,/\, T_{melting\,i} \;=\; \alpha_i N_i R \qquad \text{Eq. 6.1}$$

In this correlation, ΔS_{fusion} stands for the entropy of fusion; ΔH_{fusion} for the enthalpy of fusion; $T_{melting}$ is the melting temperature; N_i the number of atoms forming the compound; R the ideal gas constant (8.314 $J.K^{-1}.mol^{-1}$); α_i is a coefficient expressing the deviation from the hypothesis that the entropy of fusion is R multiplied by the number of atoms in the compound (α = 1). The subscript *i* indicates the specific compound under consideration.

His analysis of the enthalpies of fusion and melting points of 56 elements and 46 oxides showed that the departure from ideality is limited. In the case of oxides, the average value of α turned out to be 1.178 [Eps67]. The analysis of the experimental measurements presented in [Lyo67] gave for α_{UO_2} and α_{PuO_2} the values 1.140 and 1.057, respectively [Eps67]. The corresponding enthalpies of fusion were 88.8 and 70.3 $kJ.mol^{-1}$. Under the hypothesis of ideal behaviour (α = 1), the enthalpies of fusion of UO_2 and PuO_2 determined by Epstein are 77.9 and 66.6 $kJ.mol^{-1}$, respectively.

A high-energy laser technique was employed by Ohse et al. to determine the vapour pressure of MOX fuel up to 7000 K [Ohs76]. The heat of fusion of MOX fuel for a PuO_2 concentration of 20 mol.% and 1.96 oxygen-to-metal (O/M) ratio was determined by subtraction of the vapour pressure slopes obtained from measurements performed below and above the melting point (3073 K). Their

This project has received funding from the Euratom research and training programme 2019-2020 under grant agreement No 945022.

measurements gave a value of 82.5 $kJ.mol^{-1}$ in good agreement with the differential thermal analysis (DTA) measurements performed by the authors on MOX fuels with similar composition (83.7 $kJ.mol^{-1}$) [Ohs76]. The authors noted that their evaluation was in good agreement with the value of 81.2 $kJ.mol^{-1}$ presented in [Oga69]. According to their measurements, the enthalpy of UO_2 is 69.1 $kJ.mol^{-1}$ [Ohs76].

Measurements performed by means of a calorimetric technique indicated in the case of UO_2 a value of 74.1 $kJ.mol^{-1}$ with estimated uncertainties of 4.6 $kJ.mol^{-1}$ [Lei71]. This result was in good agreement with the value of 76.2 $kJ.mol^{-1}$ previously published in [Hei68].

In the study by Adamson et al. the experimental phase diagram of the UO_2-PuO_2 system presented in [Lyo67] and [Ait68] was re-analyzed by assuming an ideal solution model [Ada85]. Under the hypothesis that the melting temperature of UO_2 is 3120 K, the authors published a revised value of the PuO_2 melting temperature (2701 K) [Ada85]. Based on these assumptions, the heats of fusion of UO_2 and PuO_2 turned out to be 86.9 and 90.5 $kJ.mol^{-1}$. These results are not consistent with the data presented here where the heat of fusion of UO_2 is generally higher than PuO_2.

In the study by Komatsu et al., the ideal solution model was employed to discuss the phase diagram of the UO_2-PuO_2 system relying on the heats of fusion published in [Eps67] and the melting temperatures resumed in Table 6.1 [Kom88]. The impact of the O/M ratio on the enthalpy of fusion was assumed to be small where the value of $PuO_{1.61}$ was close to that of stoichiometric PuO_2 [Kom88].

Values of the enthalpy of fusion have been reported in [Bak97]. In particular, 78 $kJ.mol^{-1}$ and 67 ± 15 $kJ.mol^{-1}$ have been employed for UO_2 and PuO_2, respectively.

Konno and Hirosawa present a value of the heat of fusion of MOX that is employed in an ideal solution model [Kon98]. It has been obtained from the measurement of the melting temperature of an unirradiated MOX fuel (30 wt.% in plutonium) and under the hypothesis proposed by Epstein (Eq. 6.1).

In the review presented in [Fin00], the author recommends for UO_2 a value of 70 ± 4 $kJ.mol^{-1}$. This value is consistent with the curves of solid and liquid enthalpy also recommended by the author. Fink underlines that this evaluation, lower than the value of 74.83 $kJ.mol^{-1}$ published in [Fin81], is more accurate as based on a comprehensive review of both enthalpy and specific heat this latter not used in his previous determinations [Fin00].

Carbajo et al. confirm the recommendation given for UO_2 in the Fink's review [Car01]. The authors also suggest for MOX the experimental value of 67 ± 3 $kJ.mol^{-1}$ published in [Lei74]. This measurement was obtained by means of a calorimetric technique on a MOX fuel with a concentration in plutonium dioxide of 20 mol.%. In agreement with [Cha74], they affirm that the enthalpy of fusion of MOX, should be not markedly different from UO_2 [Car01]. The authors do not give indications for PuO_2 due to the scatter seen in the published data [Car01].

This project has received funding from the Euratom research and training programme 2019-2020 under grant agreement No 945022.

Under the hypothesis of ideal solution, Konno and Hirosawa determine the enthalpies of fusion of UO_2 (78 kJ.mol^{-1}) and PuO_2 (62 kJ.mol^{-1}) [Kon02].

Kato et al. perform a comprehensive analysis of the conditions applied for the measurement of the solidus and liquidus temperature of MOX fuel [Kat08]. They adopt an ideal solid solution modelling and the hypothesis introduced in the work of Epstein. Their evaluation of the PuO_2 melting temperature was higher by about 200 K than previous determinations. They fitted their experimental measurements suggesting for the enthalpy of fusion of UO_2 and PuO_2 a value of 77.9 and 70.9 kJ.mol^{-1}, respectively [Kat08]. Based on the findings presented in [Kat08], several investigations were performed on the melting temperature of MOX with high plutonium content employing a laser heating method. In the study of De Bruycker et al., this technique gave for the melting temperature of PuO_2 a value much higher (3017 K) than previously assumed [DeB11]. According to this, the enthalpy of fusion of PuO_2 based on the assumption presented in [Eps67], was estimated to be 75 kJ.mol^{-1} [DeB11].

In the study presented in [Gom11], the authors employ in their analysis the values recommended in [Car01].

In [Ari09], the melting temperature and the heat of fusion of UO_2 have been determined by means of Molecular Dynamics calculations. In [Boy12], the melting point of UO_2 nanocrystals has been investigated by means of the Molecular Dynamics approach. The authors apply 10 different interatomic potentials noting a general underestimation of the heat of fusion. Compared to the value of 70 ± 4 kJ.mol^{-1} recommended in [Fin00], the results of simulations are underestimated by 25–30 kJ.mol^{-1}.

Similar outcomes are reported in [Gho16]. The authors employ classical Molecular Dynamics to calculate melting temperature, enthalpy increments, and density for solid and liquid UO_2 and PuO_2. The heats of fusion of UO_2 and PuO_2 are generally underestimated in comparison with the experimental measurements, however, melting temperatures are in reasonable good agreement [Gho16].

Kim et al. calculate the heat of fusion of UO_2 using a many-body interatomic potential [Kim17]. In agreement with the melting temperature predicted by the model (between 3000 and 3100K) their results are close to the recommendation published in [Car01].

This project has received funding from the Euratom research and training programme 2019-2020 under grant agreement No 945022.

Table 6.1: Comparison of melting temperatures and heats of fusion of UO_2, PuO_2, MOX.

Reference	UO_2		PuO_2		MOX
	$T_{melting}$ (K)	Heat of fusion (kJ mol^{-1})	$T_{melting}$ (K)	Heat of fusion (kJ mol^{-1})	Heat of fusion (kJ mol^{-1})
Epstein, 1967	3113	88.8	2663	70.3	
Epstein, 1967	3113	77.9	2663	66.6	
Hein and Flagella, 1968	3120	76.2			
Ogard et al., 1969					81.2
Leibowitz et al., 1971	3120[a]	74.1			
Leibowitz et al., 1974					67[b]
Ohse et al., 1976	3133	69.1			82.5[c]
Adamson et al., 1985	3120	86.9	2701	90.5	
Komatsu et al., 1988	3138	77.9	2718	66.6	
Bakker et al., 1997	3123	78	2663	67	
Konno & Hirosawa, 1998					74.7[d]
Fink, 2000	3120	70			
Konno & Hirosawa, 2002	3138	78	2701	62	
Kato et al., 2008	3123	77.9	2843	70.9	
Arima et al., 2009[e]	3125	60			
De Bruycker et al., 2011			3017	75	
Ghosh et al., 2016	3050-3075	58.94	2800-2825	43.21	
Kim et al., 2017[f]	3000-3100	58.85			

[a] qualitative evaluation from Fig, 2 in [Lei71]
[b] MOX 20 mol.% in PuO_2
[c] MOX 20 mol.% in PuO_2 ; O/M = 1.96 ; melting temperature 3073 K
[d] MOX 30 wt.% in plutonium ; O/M = 2.00 ; melting temperature 2993 K
[e] Yakub potential (two phases 3x3x3x2)
[f] the published value is 218 $kJ.kg^{-1}$

6.2 Conclusions and recommendations

The recommendations for the enthalpy of fusion of UO_2 in [Fin00] and [Car01] are slightly under–predicting most of the values found in the open literature. However, they are in good agreement with the experimental measurements. For PuO_2, the determinations are numerical and lower than the values of UO_2 whereas the value of its melting temperature has moved from 2663 K in [Eps67] to 3017 K in [DeB11]. For MOX, few data are available and the recommendation in [Car01] is based on the measurements discussed in [Lei74]. The heats of fusion show deviations slightly higher than the uncertainties usually reported and the values found in the open literature are quite consistent and based on an ideal solution model and the entropy of fusion as presented in Eq. 6.1. Molecular Dynamics calculations could be of interest especially for MOX with high plutonium content

This project has received funding from the Euratom research and training programme 2019-2020 under grant agreement No 945022.

where the development and the re-definition of the phase diagram of the UO_2-PuO_2 system has been significant.

6.3 References

[Ada85] M.G. Adamson, E.A. Aitken and R.W. Caputi, Experimental and thermodynamic evaluation of the melting behavior of irradiated oxide fuels, J. Nucl. Mater. **130** (1985) 349.

[Ait68] Aitken E.A. and Evans S.K., A Thermodynamic Data Program Involving Plutonia and Urania at High Temperatures, General Electric Report GEAP-5672 (1968).

[Ari09] T. Arima, K. Idemitsu, Y. Inagaki, Y. Tsujita, M. Kinoshita and E. Yakub, Evaluation of melting point of UO_2 by molecular dynamics simulation, J. Nucl. Mater. **389** (2009) 149.

[Bak97] K. Bakker, E.H.P. Cordfunke, R.J.M. Konings and R.P.C. Schram, Critical evaluation of the thermal properties of ThO_2 and $Th_{1-y}U_yO_2$ and a survey of the literature data on $Th_{1-y}Pu_yO_2$, J. Nucl. Mater. **250** (1997) 1.

[Boy12] A.S. Boyarchenkov, S.I. Potashnikov, K.A. Nekrasov and A.Y. Kupryazhkin, Molecular dynamics simulation of UO_2 nanocrystals melting under isolated and periodic boundary conditions J. Nucl. Mater. **427** (2012) 311.

[Car01] J.J. Carbajo, G.L. Yoder, S.G. Popov and V.K. Ivanov, A review of the thermophysical properties of MOX and UO_2 fuels, J. Nucl. Mater. **299** (2001) 181.

[Cha74] M.G. Chasanov, L. Leibowitz and S.D. Gabelnick, High temperature physical properties of fast reactor materials, J. Nucl. Mater. **49** (1973) 129.

[DeB11] F. De Bruycker, K. Boboridis, P. Pöml, R. Eloirdi, R.J.M. Konings and D. Manara, The melting behaviour of plutonium dioxide: A laser-heating study, J. Nucl. Mater. **416** (2011) 166.

[Eps67] L.F. Epstein, Ideal solution behavior and heats of fusion from the UO_2–PuO_2 phase diagram, J. Nucl. Mater. **22** (1967) 340.

[Fin00] J.K. Fink, Thermophysical properties of uranium dioxide, J. Nucl. Mater. **279** (2000) 1.

[Fin81] J.K. Fink, M.G. Chasanov and L. Leibowitz, Thermophysical properties of uranium dioxide, J. Nucl. Mater. **102** (1981) 17.

[Gho16] P.S. Ghosh and N. Kuganathan, C.O.T. Galvin, A. Arya, G.K. Dey, B.K. Dutta and R.W. Grimes, Melting behavior of $(Th,U)O_2$ and $(Th,Pu)O_2$ mixed oxides, J. Nucl. Mater. **479** (2016) 112.

[Gom11] J.L.M.A. Gomes, C.C. Pain, M.D. Eaton, B. Tollit, A.J.H. Goddard, M.D. Piggott, K. Ziver and Y. Yamane, Coupled neutronics-fluids modelling of criticality within a MOX powder system, Prog. Nucl. Energy **53** (2011) 523.

This project has received funding from the Euratom research and training programme 2019-2020 under grant agreement No 945022.

[Hei68] R.A. Hein and P.N. Flagella, General Electric Co. (USA), Nuclear Materials and Propulsion Operation Report GEMP–578 (1968).

[Kat08] M. Kato, K. Morimoto, H. Sugata, K. Konashi, M. Kashimura and T. Abe, Solidus and liquidus temperatures in the UO_2-PuO_2 system, J. Nucl. Mater. **373** (2008) 237.

[Kim17] W.K. Kim, J.H. Shim and M. Kaviany, Thermophysical properties of liquid UO_2, ZrO_2 and corium by molecular dynamics and predictive models, J. Nucl. Mater. **491** (2017) 126.

[Kom88] J. Komatsu, T. Tachibana and K. Konashi, The melting temperature of irradiated oxide fuel, J. Nucl. Mater. **154** (1988) 38.

[Kon98] K. Konno and T. Hirosawa, Melting temperature of irradiated fast reactor mixed oxide fuels, J. Nucl. Sci. Technol. **35** (1998) 494.

[Kon02] K. Konno and T. Hirosawa, Melting temperature of mixed oxide fuels for fast reactors, J. Nucl. Sci. Technol. **39** (2002) 771.

[Lei71] L. Leibowitz, M.G. Chasanov, L.W. Mishler, D.F. Fischer, Enthalpy of liquid uranium dioxide to 3500 °K, J. Nucl. Mater. **39** (1971) 115.

[Lei74] L. Leibowitz, D.F. Fischer, M.G. Chasanov, Enthalpy of Molten Uranium-Plutonium Oxide, Report ANL-8082 (1974).

[Lyo67] W.L. Lyon and W.E. Baily, The solid–liquid phase diagram for the UO_2–PuO_2 system, J. Nucl. Mater. **22** (1967) 332.

[Oga69] A.E. Ogard, J.G. Reavis and J.A. Leary, Proc. 16th Conf. on Remote Systems Technology, Idaho Falls, Idaho, USA (1969) 265.

[Ohs76] R.W. Ohse, P.C. Berrie, H.G. Bogensberger and E.A. Fischer, Extension of vapour pressure measurements of nuclear fuels $(U,Pu)O_2$ and UO_2 to 7000 K for fast reactor safety analysis, J. Nucl. Mater. **59** (1976) 112.

This project has received funding from the Euratom research and training programme 2019-2020 under grant agreement No 945022.

7. Emissivity

This chapter was originally provided by R. Calabrese (ENEA).

7.1 Literature data

Safety analysis requires knowledge of the thermal radiation properties of nuclear fuel materials especially above their melting points. Moreover, this quantity is important for accurate measurements based on the use of laser heating [Bob80a, Ron98]. The spectral radiance of a surface is determined through the Planck's radiation law (ideal blackbody) multiplied by the normal spectral emissivity that depends on temperature and wavelength [Nun14].

The total hemispherical emittance is a quantity relevant to the accident conditions and the formation of a molten core phase. This quantity is obtained by integration over the hemispherical space of the directional spectral emissivity whose values depends on the incidence angle [Bob80a].

In [Ohs76] the values of emissivity used in their experimental study on vapour pressure through a laser heating technique, were based on the review presented in [Neu73] and the hypothesis that the emissivity of rare earth oxides shows no change when passing through the melting point [McM68].

Bober et al. measured the normal spectral emissivity of UO_2 in the temperature interval 2000 – 4100 K at a wavelength of 630 nm (visible) [Bob80a]. Their results show that the emissivity has a weak dependence on temperature up to the melting point thereafter it increases markedly. The indications presented in this study are in good agreement with previous measurements performed at low temperature and at a wavelength of 650 nm [Cab67, Hel69, Sch78]. Their findings were not in agreement with the results published in [Cla58] where the values of emissivity move from 0.85 down to 0.37 with temperature increasing from 964 K to 2220 K. According to the review of Harding et al. (1989), the evaluations in [Cla58] are rejected casting doubts on the reliability of the experimental technique employed by the author. The measurements performed in the far infrared at a wavelength of 10600 nm showed that beyond the melting point the normal spectral emissivity of UO_2 decreases with increasing temperature [Bob80a]. Authors note that the emissivity of sintered samples was slightly higher in comparison with pre-melted samples. The results obtained for a wavelength of 10600 nm show a fairly good agreement with the results published in [Cab67] and [Cla66]. The authors conclude that the emittance of sintered UO_2 shows no dependence on temperature (up to melting), surface roughness, density and stoichiometric variations [Bob80b].

Bober presented a series of emissivity measurements performed on UO_2 in the temperature interval 2000 – 4000 K for three values of wavelength (647, 514.5 and 458 nm), different incident angles, and polarization [Bob80b]. The results, while confirming previous conclusions, show a slight dependence on wavelength and proved that the total hemispherical emittance was lower than the near-normal spectral emissivity by about 5% [Bob80b]. The author notes that to obtain more

This project has received funding from the Euratom research and training programme 2019-2020 under grant agreement No 945022.

reliable information regarding the total hemispherical emittance of liquid UO_2 measurements up to the far infrared are necessary [Bob80b].

In [Sal99], the authors aim at investigating the structural modification occurring in UO_2 approaching the melting temperature. For the purpose, they measured the reflectivity in the interval 2000 – 4200 K at a wavelength of 644 nm. The experimental results confirm the existence of a pre-melting transition around $0.85*T_{melting}$. The authors measured the spectral emissivity of UO_2 confirming good agreement with the data of Bober et al. [Sal99]. The values of emissivity are increasing before reaching melting and nearly constant beyond. At 3.5 MPa the emissivity maintains its increasing trend beyond the melting temperature. The condensation of the vapor plume over the sample could explain an overall reduction of the emissivity under this experimental condition [Sal99].

In his review, Fink states that the studies in [Bob80a] are reliable and consistent with the majority of the experimental studies published at the time [Fin00]. The author, in agreement with the indications in [Har89], recommends for the total hemispherical emittance of UO_2 the value presented in Eq. 7.1.

$$\varepsilon^h = 0.85 \pm 0.05 \qquad \text{Eq. 7.1}$$

In agreement with the previous review [Fin81], Fink recommends the correlation of Bober et al. for the normal spectral emissivity of pre-melted UO_2 at 630 nm extending its validity in the visible range (400 - 700 nm). The temperature may vary in the interval 1000 – 3120 K.

$$\varepsilon^n = 0.836 + 4.321.10^{-6}(T - 3120) \qquad \text{Eq. 7.2}$$

The normal spectral emissivity of liquid UO_2 recommended by Fink in the visible range is presented in Eq. 7.3.

$$\varepsilon^n = 1 - 0.1609 \exp\left(-3.7897.10^{-4}\Delta T - 3.2718.10^{-7}\Delta T^2\right) \qquad \text{Eq. 7.3}$$

In this correlation, $\Delta T = T - 3120$ and T lies in the interval 3120 – 4200 K [Fin00].

The author notes that this relationship should not be used in the infrared and far infrared regions where the emissivity is expected to decrease from 0.85 to 0.4 with temperature increasing up to 4000 K [Fin00].

In [Ron02], a value of 0.86 ± 0.01 for the UO_2 normal spectral emissivity at 650 nm and at melting (3110 K) is reported. The experimental measurements discussed in [Man05] are in good agreement with the recommendations given in [Fin00]. The oxygen-to-metal ratio should not have a significant effect on the value of UO_2 emissivity [Man05]. These results are further confirmed in [Man08]. This study does not indicate an increase with temperature of the normal spectral emissivity of the liquid UO_2 as in the Fink's recommendations.

As aforementioned, the measurement of the normal spectral emissivity of PuO_2 and UO_2 is important for the determination of the true temperature in a laser heating technique. For the purpose, the experimental set-up presented in

This project has received funding from the Euratom research and training programme 2019-2020 under grant agreement No 945022.

[DeB11a] employs a spectro-pyrometer working in the interval 550 - 920 nm. The values of the normal spectral emissivity of PuO_2 and UO_2 determined in this study are not significantly different [DeB11a]. This statement has been confirmed by the measurements performed on MOX samples with high concentration of PuO_2 (80 and 90 mol.%) [DeB11b]. Based on these findings, the approach adopted for the analysis of the experimental measurements was to assume that the emissivity of MOX is not depending on wavelength (greybody approximation) and equal to 0.83 ± 0.05 [DeB11b].

In agreement with the results presented here a constant value is often employed in the literature. In [Mus99], the melting point of UO_2 was measured by means of a laser heating technique assuming a value of 0.85 for the normal spectral emissivity (at 650 nm). In [Sob08] the emissivity of fuel is 0.85. Constant values of emissivity, 0.8 and 0.88, are applied in [Yu12] and [Mel13], respectively. In [Wil11] a value of 0.8 is used. In [Auf13] the value employed for emissivity is 0.95.

Previously, the results of Bober et al. were employed in the study [Yag88]. Hayes and Peddicord [Hay93] adopt the hypothesis that the total hemispherical emittance of UO_2 remains higher than 0.8 up to melting. The spectral emissivity of liquid UO_2 recommended by Fink (Eq. 7.2) has been used in [Wel08].

In [Yam06] the emissivity was defined according to the MAPRO–11 model that predicts a decrease of emissivity in the interval 1000 – 2050 K while below and above this interval remains constant and equal to 0.8707 and 0.4083, respectively [Yam06]. This correlation is mostly based on the work of Claudson.

7.2 Conclusions and recommendations

The data presented here is mostly consistent and in fair agreement with the studies of Bober et al. often cited and recommended. Measurements of the directional spectral emissivity in the far infrared region are still an open issue to determine with high accuracy the total hemispherical emittance a quantity relevant to accident conditions. The behavior of the normal spectral emissivity with temperature of the liquid UO_2 has not been revised in the literature. The reported different behavior in the visible and far infrared region has not been clearly assessed. This comment is valid for PuO_2 and MOX fuel where no explicit indications have been found.

7.3 References

[Auf13] M. Aufiero, A. Cammi, C. Fiorina, L. Luzzi and A. Sartori, A multi-physics time-dependent model for the Lead Fast Reactor single-channel analysis, Nucl. Eng. Des. **256** (2013) 14.

[Bob80a] M. Bober, H.U. Karow and K. Müller, Study of the spectral reflectivity and emissivity of liquid ceramics, High Temperatures – High Pressures **12** (1980) 161.

This project has received funding from the Euratom research and training programme 2019-2020 under grant agreement No 945022.

[Bob80b] M. Bober M., Spectral reflectivity and emissivity of solid and liquid UO_2 as a function of wavelength, angle of incidence, and polarization, High Temperatures – High Pressures **12** (1980) 297.

[Cab67] F. Cabannes, J.P. Stora and J. Tsakiris, C.R. Acad. Sci. Rev. Ser. B 264 (1967) 45.

[Cla58] T.T. Claudson, Emissivity Data for Uranium Dioxide, Report AW-55414 (1958); see also pp. 196-197, in: J. Belle (Ed.), Uranium Dioxide Properties and Nuclear Applications, US AEC (1961).

[Cla66] H.E. Clark and D.G. Moore, A rotating cylinder method for measuring normal spectral emittance of ceramic oxide specimens from 1200 to 1600 °K, J. Res. Nat. Bur. Stand. Sect. A, **70A** (1966) 393.

[DeB11a] F. De Bruycker, K. Boboridis, P. Pöml, R. Eloirdi, R.J.M. Konings and D. Manara, The melting behaviour of plutonium dioxide: A laser-heating study, J. Nucl. Mater. 416 (2011) 166.

[DeB11b] F. De Bruycker, K. Boboridis, R.J.M. Konings, M. Rini, R. Eloirdi, C. Guéneau, N. Dupin and D. Manara, On the melting behaviour of uranium/plutonium mixed dioxides with high-Pu content: A laser heating study, J. Nucl. Mater. **419** (2011) 186.

[Fin81] J.K. Fink, M.G. Chasanov and L. Leibowitz, Thermophysical properties of uranium dioxide, J. Nucl. Mater. **102** (1981) 17.

[Fin00] J.K. Fink, Thermophysical properties of uranium dioxide, J. Nucl. Mater. **279** (2000) 1.

[Har89] J.H. Harding, D.G. Martin, P.E. Potter, Thermophysical and thermochemical properties of fast reactor materials, Commission of the European Communities, Report EUR 12402 (1989).

[Hay93] S.L. Hayes and K.L. Peddicord, Radiative heat transfer in porous uranium dioxide, J. Nucl. Mater. **202** (1993) 87.

[Hel69] P.C. Held, D.R. Wilder, High-Temperature Hemispherical Spectral Emittance of Uranium Oxides at 0.65 and 0.70 μm, J. Am. Ceram. Soc. **52** (1969) 182.

[Man05] D. Manara, C. Ronchi, M. Sheindlin, M. Lewis and M. Brykin, Melting of stoichiometric and hyperstoichiometric uranium dioxide, J. Nucl. Mater. **342** (2005) 148.

[Man08] D. Manara, M. Sheindlin, W. Heinz and C. Ronchi, New techniques for high-temperature melting measurements in volatile refractory materials via laser surface heating, Rev. Sci. Instrum. **79** (2008) 113901.

[McM68] W.R. Mc Mahon and D.R. Wilder, Hemispherical Spectral Emittance of Selected Rare Earth Oxides, J. Am. Ceram. Soc. **51** (1968) 186.

[Mel13] R. Mella and M.R. Wenman, Axisymmetric whole pin life modelling of advanced gas-cooled reactor nuclear fuel, J. Nucl. Mater. **437** (2013) 154.

This project has received funding from the Euratom research and training programme 2019-2020 under grant agreement No 945022.

[Mus99] M. Musella, C. Ronchi, M. Sheindlin, Dependence of the Melting Temperature on Pressure up to 2000 Bar in Uranium Dioxide, Tungsten, and Graphite, Int. J. Thermophys. **20** (1999) 1177.

[Neu73] G. Neuer, R. Brandt and G. Haufler, A literature study of the thermal conductivity and emission rate of solid UO_2, IRS Rep. SB3 (1973), in German.

[Nun14] U. Carvajal Nunez, D. Prieur, R. Bohler, D. Manara, Melting point determination of uranium nitride and uranium plutonium nitride: A laser heating study, J. Nucl. Mater. **449** (2014) 1.

[Ohs76] R.W. Ohse, P.C. Berrie, H.G. Bogensberger and E.A. Fischer, Extension of vapour pressure measurements of nuclear fuels $(U,Pu)O_2$ and UO_2 to 7000 K for fast reactor safety analysis, J. Nucl. Mater. **59** (1976) 112.

[Ron98] C. Ronchi, M. Sheindlin, M. Musella, G.J. Hyland, Thermal conductivity of uranium dioxide up to 2900 K from simultaneous measurement of the heat capacity and thermal diffusivity, J. Appl. Phys. **85** (1998) 776.

[Ron02] C. Ronchi, M. Sheindlin, Laser-Pulse Melting of Nuclear Refractory Ceramics, Int. J. Thermophys. **23** (2002) 293.

[Sal99] T.P. Salikhov, V.V. Kan and C. Ronchi, Radiative properties of uranium dioxide near its melting point, Int. J. Thermophys. **20** (1999) 1163.

[Sch78] J. Schoenes, Optical properties and electronic structure of UO_2, J. Appl. Phys. **49** (1978) 1463.

[Sob08] A. Soba and A. Denis, Simulation with DIONISIO 1.0 of thermal and mechanical pellet-cladding interaction in nuclear fuel rods, J. Nucl. Mater. **374** (2008) 32.

[Wel08] M.J. Welland, B.J. Lewis, W.T. Thompson, A comparison of Stefan and Phase Field modeling techniques for the simulation of melting nuclear fuel, J. Nucl. Mater. **376** (2008) 229.

[Wil11] R.L. Williamson, Enhancing the ABAQUS thermomechanics code to simulate multipellet steady and transient LWR fuel rod behavior, J. Nucl. Mater. **415** (2011) 74.

[Yag88] S.K. Yagnik and D.R. Olander, Surface temperature transients from pulsed laser heating of UO_2, J. Nucl. Mater. **154** (1988) 253.

[Yam06] A. Yamaji, Y. Oka, Y. Ishiwatari, J. Liu, M. Suzuki, Principle of rationalizing the criteria for abnormal transients of the Super LWR with fuel rod analyses, Ann. Nucl. Energy. **33** (2006) 984.

[Yu12] H. Yu, W. Tian, Z. Yang, G.H. Su, S. Qiu, Development of Fuel Rod Behavior Analysis code (FROBA) and its application to AP1000, Ann. Nucl. Energy. **50** (2012) 8.

This project has received funding from the Euratom research and training programme 2019-2020 under grant agreement No 945022.

8. Theoretical density

This chapter was originally provided by J-P. Ottaviani (CEA).

8.1 Literature data

The general formula for the calculation of the theoretical density of $(U_{1-y}Pu_y)O_{2-x}$ in the solid state is presented in Eq. 8.1.:

$$\rho_s = \frac{4(M_{HA} + (2-x)M_O)}{N\ a^3} \qquad \text{Eq. 8.1}$$

Where:
a is the lattice parameter,
x is the deviation from stoichiometry in oxygen,
N is the Avogadro number ($N = 6.022\ 10^{23}\ mol^{-1}$),
M_O is the atomic mass of oxygen ($M_O = 16\ g.mol^{-1}$),
M_{HA} is the average atomic mass of Heavy Atoms, calculated from the Pu content, the isotopic composition of the fuel, and the atomic mass of each isotope using Eq. 8.2:

$$M_{HA} = (1-y)\sum_i \gamma_i M(U_i) + y\sum_j \delta_j M(Pu_j) \qquad \text{Eq. 8.2}$$

Where:
y is the fractional Pu content,
U_i is uranium isotope,
γ_i is the fractional part of isotope U_i in uranium,
Pu_j is plutonium isotope,
δ_j is the fractional part of isotope Pu_j in plutonium.

If the atomic masses M_{HA} and M_O are expressed in g and the lattice parameter a in pm, the theoretical density is calculated in $g.cm^{-3}$ using the correlation recommended by Philipponneau as per Eq. 8.3:

$$\rho_s = 1.66\ 10^6 \frac{4M_{HA} + 64(2-x)}{a^3} \qquad \text{Eq. 8.3}$$

Recommendations for lattice parameter are given in chapter 2.The melting point density of liquid UO_2 recommended is 8640 $kg.m^{-3}$, calculated using the solid density given by Martin's equation for thermal expansion [Mar88] (9560 $kg.m^{-3}$ at 3120 K, assuming that the density of UO_2 is 10963 $kg.m^{-3}$ at 273 K) and the change of density on melting determined by Christensen (-9.6%, i.e. -920 $kg.m^{-3}$) [Chr63].

This project has received funding from the Euratom research and training programme 2019-2020 under grant agreement No 945022.

For MOX fuels it is assumed the same decrease in density on melting as for UO_2 (920 $kg.m^{-3}$). Between the solidus and liquidus temperatures it is suggested to obtain densities by linear interpolation.

8.1.1 Effect of addition of minor actinides

From a study of Kato and Konashi [Kat09] analyzing the effect of addition of minor actinides on the lattice parameter of stoichiometric or hypo-stoichiometric uranium-plutonium mixed oxide fuels, it becomes possible to suggest a correlation for the calculation of theoretical density at room temperature of stoichiometric or hypo-stoichiometric uranium-plutonium mixed oxide fuels doped with americium and neptunium, of type $(U_{1-y-y'-y''}Pu_yAm_{y'}Np_{y''})O_{2-x}$, using Eq. 8.3 and determining M_{HA} and lattice parameter as per Eq. 8.4 and Eq. 8.5 respectively.

$$\mathrm{M_{HA}\,(g)} = (1-\mathrm{y}-\mathrm{y}'-\mathrm{y}'')\sum_{\mathrm{i}}\gamma_{\mathrm{i}}\mathrm{M(U_i)} + \mathrm{y}\sum_{\mathrm{j}}\delta_{\mathrm{j}}\mathrm{M(Pu_j)} + \mathrm{y}'\sum_{\mathrm{k}}\mu_{\mathrm{k}}\mathrm{M(Am_k)} + \mathrm{y}''\sum_{\mathrm{l}}\nu_{\mathrm{l}}\mathrm{M(Np_l)} \qquad \text{Eq. 8.4}$$

$$\mathrm{a\,(pm)} = 547.1 - 7.6\mathrm{y} - 10.0\mathrm{y}' - 3.8\mathrm{y}'' + (25.8 - 0.9\mathrm{y} - 1.1\mathrm{y}' - 0.4\mathrm{y}'')\mathrm{x} \qquad \text{Eq. 8.5}$$

Where:

x is the deviation from stoichiometry in oxygen,
y is the fractional Pu content,
y' is the fractional Am content,
y'' is the fractional Np content,
$\mathrm{U_i}$ is uranium isotope,
γ_{i} is the fractional part of isotope $\mathrm{U_i}$ in uranium,
$\mathrm{Pu_j}$ is plutonium isotope,
δ_{j} is the fractional part of isotope $\mathrm{Pu_j}$ in plutonium,
$\mathrm{Am_k}$ is americium isotope,
μ_{k} is the fractional part of isotope $\mathrm{Am_k}$ in americium,
$\mathrm{Np_l}$ is neptunium isotope,
ν_{l} is the fractional part of isotope $\mathrm{Np_l}$ in neptunium,

This correlation could be considered as a recommendation for the calculation of theoretical density at room temperature of stoichiometric or hypo-stoichiometric uranium-plutonium-minor actinides mixed oxides within the following limits: $0 \leq Pu/M \leq 100\%$, $0 \leq Am/M \leq 2\%$, $0 \leq Np/M \leq 12\%$, $1.985 \leq O/M \leq 2$.

8.1.2 Effect of temperature

The general formula for the calculation of the theoretical density of $(U_{1-y}Pu_y)O_{2-x}$ is usable whatever the temperature as long as the fuel remains in a single phase solid state. The theoretical density at the temperature T can be calculated from the value of the lattice parameter at the same temperature using Eq. 8.6.

This project has received funding from the Euratom research and training programme 2019-2020 under grant agreement No 945022.

$$\rho_s(T) = 1.66\ 10^6 \frac{4M_{HA} + 64(2 - x)}{[a(T)]^3} \qquad \text{Eq. 8.6}$$

The dependence on temperature of the lattice parameter having yet to be assessed as the subject of future experimentation it is also conceivable to calculate the dependence on temperature of the theoretical density using thermal expansion data as per Eq. 8.7:

$$\rho_s(T) = \frac{\rho_{s_0}}{\left[\frac{L(T)}{L_0}\right]^3} = \frac{\rho_{s_0}}{[1 + \Delta L/L_0]^3} \qquad \text{Eq. 8.7}$$

Where:

ρ_{s_0} is the theoretical density at a reference temperature,
L and L_0 are lengths at temperature T and reference temperature respectively,

The quantities $L(T)/L_0$ or $\Delta L/L_0$ given for stoichiometric actinide dioxides (Cf. chapter 9) can be combined to assess the thermal expansion of stoichiometric actinides mixed dioxides using mixing rules as per Eq. 8.8 or Eq. 8.9:

$$\frac{L}{L_0}\left((U,Pu)O_{2.00}\right) = (1 - y)\frac{L}{L_0}(UO_{2.00}) + y\frac{L}{L_0}(PuO_{2.00}) \qquad \text{Eq. 8.8}$$

$$\frac{\Delta L}{L_0}\left((U,Pu)O_{2.00}\right) = (1 - y)\frac{\Delta L}{L_0}(UO_{2.00}) + y\frac{\Delta L}{L_0}(PuO_{2.00}) \qquad \text{Eq. 8.9}$$

Where y is the mass fraction of PuO_2 in the MOX [2].

However, as shown on Figure 8.1, UO_2 and PuO_2 have very similar thermal expansion [Mar88; Tok73]. Hence, it can be considered that:

$$\frac{L}{L_0}\left((U,Pu)O_{2.00}\right) \approx \frac{L}{L_0}(UO_{2.00}) \approx \frac{L}{L_0}(PuO_{2.00}) \qquad \text{Eq. 8.10}$$

or

$$\frac{\Delta L}{L_0}\left((U,Pu)O_{2.00}\right) \approx \frac{\Delta L}{L_0}(UO_{2.00}) \approx \frac{\Delta L}{L_0}(PuO_{2.00}) \qquad \text{Eq. 8.11}$$

[2] Strictly the mixing law asked that the volume fraction of the constituents is used here as a weighting factor, and not their mass fraction. However, with regard to UO_2 and PuO_2 these two quantities are relatively close to one another.

This project has received funding from the Euratom research and training programme 2019-2020 under grant agreement No 945022.

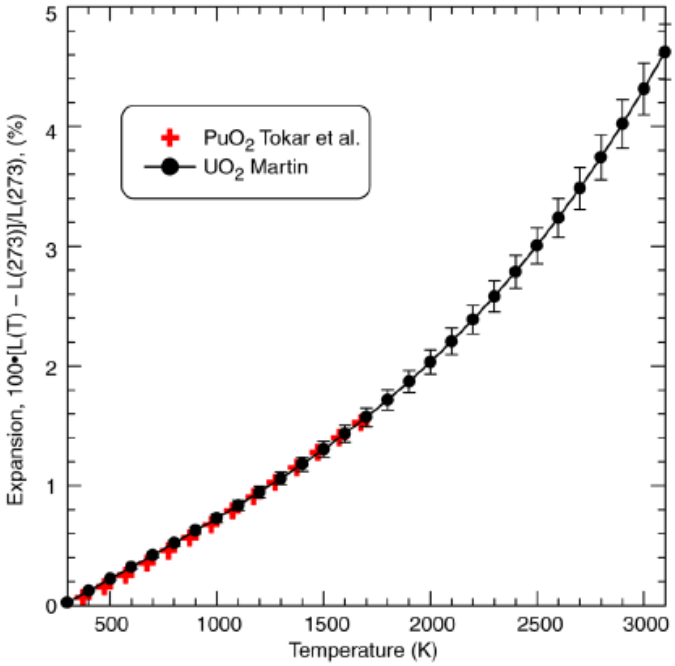

Figure 8.1: Relative thermal expansion of UO_2 and PuO_2 fuels [Mar88, Tok73].

From the equations of thermal expansion $L(T)/L_0$ developed by Martin to be used for UO_2 and MOX fuels [Mar88], Carbajo et al. recommended in 2001 the correlations hereafter to calculate the density of solid stoichiometric UO_2 and MOX fuels [Car01] as per Eq. 8.12 and Eq. 8.13:

For temperatures T from 273 K to 923 K:

$$\rho_s(\mathrm{kg.m^{-3}}) = \frac{\rho_{s_0}}{[9.9734\ 10^{-1} + 9.802\ 10^{-6}T - 2.705\ 10^{-10}T^2 + 4.391\ 10^{-13}T^3]^3} \quad \text{Eq. 8.12}$$

And for temperatures T from 923K to the UO_2 or MOX fuel melting temperature:

$$\rho_s(\mathrm{kg.m^{-3}}) = \frac{\rho_{s_0}}{[9.9672\ 10^{-1} + 1.179\ 10^{-5}T - 2.429\ 10^{-9}T^2 + 1.219\ 10^{-12}T^3]^3} \quad \text{Eq. 8.13}$$

Where ρ_{s_0} refers to density at 273 K:

$\rho_{s_0}(UO_{2,00}) = 10970\ \mathrm{kg.m^{-3}}$
$\rho_{s_0}(PuO_{2,00}) = 11460\ \mathrm{kg.m^{-3}}$
$\rho_{s_0}((U_{1-y}, Pu_y)O_{2.00}) = 10970 + 490y\ (\mathrm{kg.m^{-3}})$ for $(0 \le y \le 1)$ according to the linear law

The recommended uncertainty in the density of UO_2 and MOX fuels is 1% for the entire temperature range.

Based on a very limited amount of data analyzed by Martin [Mar88] the coefficient of thermal expansion of hypo-stoichiometric $(U,Pu)O_{2-x}$ solid MOX fuels was recommended to be calculated by the corresponding coefficient of the stoichiometric fuel, multiplying it by a factor of $(1 + 3.9x)$. Analysis of the

This project has received funding from the Euratom research and training programme 2019-2020 under grant agreement No 945022.

experimental data showed that this recommendation is valid up to 1800K. However, in the absence of high temperature data, Martin [Mar88] as well as Carbajo et al. [Car01] suggested to use it up to the melting temperature.

The corresponding effect on theoretical density has not been reported. However taking into account the equivalent formulations for the corrective factor recommended by Martin as per Eq. 8.14, Eq. 8.15 or Eq. 8.16, it can be suggested to calculate the theoretical density of hypo-stoichiometric $(U,Pu)O_{2-x}$ solid MOX fuels with the correlations given in Eq. 8.17 and Eq. 8.18:

$$\alpha\left((U,Pu)O_{2-x}\right) = (1+3{,}9x)\ \alpha\left((U,Pu)O_{2.00}\right) \approx (1+3.9x)\ \alpha(UO_{2.00}) \qquad \text{Eq. 8.14}$$

$$\frac{L}{L_0}\left((U,Pu)O_{2-x}\right) = \left[\frac{L}{L_0}\left((U,Pu)O_{2.00}\right)\right]^{(1+3.9x)} \approx \left[\frac{L}{L_0}(UO_{2.00})\right]^{(1+3.9x)} \qquad \text{Eq. 8.15}$$

$$\frac{\Delta L}{L_0}\left((U,Pu)O_{2-x}\right) \approx (1+3.9x)\ \frac{\Delta L}{L_0}\left((U,Pu)O_{2.00}\right) \approx (1+3.9x)\ \frac{\Delta L}{L_0}(UO_{2.00}) \qquad \text{Eq. 8.16}$$

For temperatures T from 273 K to 923 K:

$$\rho_s\left((U,Pu)O_{2-x}\right) = \frac{\rho_{s_0}\left((U,Pu)O_{2-x}\right)}{[9.9734\ 10^{-1} + 9.802\ 10^{-6}T - 2.705\ 10^{-10}T^2 + 4.391\ 10^{-13}T^3]^{3(1+3.9x)}} \qquad \text{Eq. 8.17}$$

And for temperatures T from 923K to the UO_2 or MOX fuel melting temperature:

$$\rho_s\left(\left((U,Pu)O_{2-x}\right)\right) = \frac{\rho_{s_0}\left((U,Pu)O_{2-x}\right)}{[9.9672\ 10^{-1} + 1.179\ 10^{-5}T - 2.429\ 10^{-9}T^2 + 1.219\ 10^{-12}T^3]^{3(1+3.9x)}} \qquad \text{Eq. 8.18}$$

At reference temperature the deviation from stoichiometry in oxygen in the hypo-stoichiometric domain causes both an increase of lattice parameter and a decrease of molar mass which lead to a decrease of the theoretical density of MOX fuels. In the range of x between 0 and 0.1 ($1.90 \leq O/M \leq 2.00$) the effect is quasi linear. It can be assessed from the general formulation of density that increasing x of 0.01 causes a decrease in theoretical density at reference temperature of about 0.22%.

A correlation for the density of liquid UO_2 was given in 1990 by Breitung and Reil [Bre90] as per Eq. 8.19:

$$\rho_l(\mathrm{kg.m^{-3}}) = 8860 - 9.285\ 10^{-1}(T - 3120) \qquad (3120 \leq T(K) \leq 7600) \qquad \text{Eq. 8.19}$$

The uncertainty of the correlation is ± 1.4% at 3120 K, +1.6% and −2% at 3500 K, +2.2% and −4% at 4500 K, + 3% and −6.3% at 5400 K, + 4.2% and −10% at 6500 K, + 6% and −15.4% at 7600 K (Cf Figure 8.2). This correlation is consistent with the equation given by the same authors for the instantaneous volumetric

This project has received funding from the Euratom research and training programme 2019-2020 under grant agreement No 945022.

thermal expansion coefficient [3] of liquid UO_2 and MOX fuels for mole fractions of Pu lower than 25% and given in Eq. 8.20:

$$\alpha_{v,l}(K^{-1}) = -\frac{1}{\rho_l}\frac{d\rho_l}{dT} = \frac{9.285\ 10^{-1}}{8860 - 9.285\ 10^{-1}(T - 3120)} \qquad \text{Eq. 8.20}$$

$$(3120 \leq T(K) \leq 7600)$$

These equations from Breitung and Reil are in good agreement with the experimental data given by Drotning for the volume expansion coefficient of liquid UO_2, and its density at the melting point $(T_m = 3120\ K)$ [Dro82]:

$$\frac{d\rho_l}{dT}(kg.m^{-3}.K^{-1}) = -(9.16 \pm 0.43)\ 10^{-1} \qquad \text{Eq. 8.21}$$

$$\rho_l(T_m) = 8860 \pm 60\ kg.m^{-3} \qquad \text{Eq. 8.22}$$

Because the measurements by Drotning are more precise than those of Christensen [Chr63] the consistent correlations suggested by Drotning for density at the melting point, and by Breitung and Reil for density and volume expansion coefficient of liquid UO_2, were recommended in 2000 by Fink [Fin00] rather than the change in density on melting of Christensen.

Same correlations from Breitung and Reil were also recommended in 2001 by Carbajo et al. to be used for both liquid UO_2 and MOX fuels in the range 3120 – 4500 K with a relative uncertainty of 4% [Car01]. Indeed, the effect of the plutonium content on the density of liquid oxide fuel seems to be negligible, compared to the remaining uncertainty in the density data. Then it appears justified to recommend the Breitung and Reil correlations for both UO_2 and $(U_{1-y}Pu_y)O_{2-x}$ mixed oxide with $y \leq 0.25$.

[3] Strictly, in the single-phase region, the volumetric thermal expansion coefficient is given by $\alpha = \frac{1}{v}\left(\frac{\partial v}{\partial T}\right)_P$. Considering here $\alpha = -\frac{1}{\rho_l}\frac{d\rho_l}{dT}$ assumes the approximation of incompressible substances.

This project has received funding from the Euratom research and training programme 2019-2020 under grant agreement No 945022.

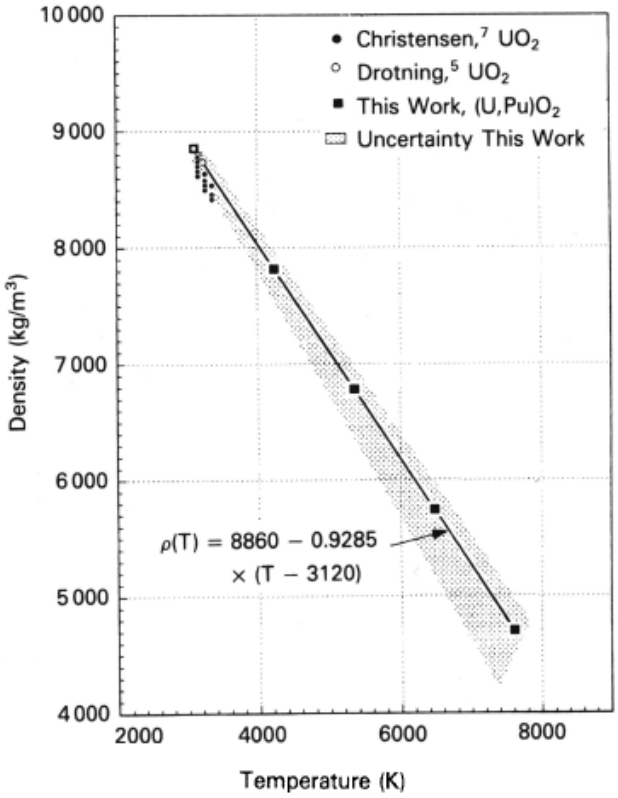

Figure 8.2: Density of liquid (U,Pu) mixed oxide as a function of temperature [Bre90], and comparison to earlier density measurements on liquid UO_2 [Chr63, Dro82].

8.2 Conclusions and recommendations

The recommendation for theoretical density is applicable only at room temperature. However, knowing the evolution of the lattice parameter as a function of temperature is of major interest for a better assessment of the theoretical density change versus temperature. The high-temperature X-ray diffractometer available at CEA could be used to extend the recommendation at high temperature performing lattice parameter measurements up to the melting point. Such measurements should be achieved on UO_2 and MOX fuels with various compositions, including Pu content up to 35%, and oxygen to metal ratio in the range 1.94 – 2.00. Further, same type of measurements should be achieved on MOX fuels containing also few percents of minor actinides Am and Np. Then, all these data could also be used for comparison with densities obtained from thermal expansion data determined by dilatometry.

Strictly speaking, the density of an oxide fuel is a function of the uranium and plutonium isotopic vector, the Pu/(U+Pu) ratio, and the O/(U+Pu) ratio. However the differences between solid uranium and solid (U,Pu) oxides are small. For instance, at 298 K the theoretical density of $^{238}UO_{2.00}$ and $(^{238}U_{0.75}{}^{239}Pu_{0.25})O_{2.00}$ differ by only 1%. Since the thermal expansion of both oxides is also identical within the quite small uncertainties up to the melting temperature, the plutonium content seems to have a small effect on the density of solid oxide fuel.

This project has received funding from the Euratom research and training programme 2019-2020 under grant agreement No 945022.

The same appears to be the case in the liquid regime. Because the experimental uncertainty should cover the relatively small effect of the plutonium content on the liquid oxide density, it seems not to be relevant to consider further experimentation in this domain, except to develop a technique very precise for measuring at high temperature.

8.3 References

[Bre90] W. Breitung, K.O. Reil, The Density and Compressibility of Liquid (U,Pu)-Mixed Oxide, Nucl. Sci. Eng. 105 (1990) 205.

[Car01] J.J. Carbajo, G.L. Yoder, S.G. Popov and V.K. Ivanov, A review of the thermophysical properties of MOX and UO_2 fuels, J. Nucl. Mater. **299** (2001) 181.

[Chr63] J.A. Christensen, Thermal Expansion and Change in Volume of Uranium Dioxide on Melting, J. Am. Ceram. Soc. **46** (1963) 607.

[Dro82] W.D. Drotning, Thermal Expansion of Molten Uranium Dioxide, Proceedings of 8th Symposium on Thermophysical Properties (ed. J V Saugers) ASME, New York (1982), Vol. II, p.245.

[Fin00] J.K. Fink, Thermophysical properties of uranium dioxide, J. Nucl. Mater. **279** (2000) 1.

[Kat09] M. Kato and K. Konashi, Lattice parameters of $(U,Pu,Am,Np)O_{2-x}$, J. Nucl. Mater. **385** (2009) 117.

[Mar88] D.G. Martin, The thermal expansion of solid UO_2 and (U,Pu) mixed oxides – A review and recommendations, J. Nucl. Mater. **152** (1988) 94.

[Tok73] M. Tokar, A.W. Nutt and T.K. Keenan, Linear Thermal Expansion of Plutonium Dioxide, Nucl. Technol. **17** (1973) 147.

This project has received funding from the Euratom research and training programme 2019-2020 under grant agreement No 945022.

9. Thermal expansion

This chapter was originally provided by N. Vér (MTA-EK).

9.1 Literature data

Available thermal expansion data obtained by dilatometry for stoichiometric $UO_{2.00}$ and for UO_{2+x} with 0 < x < 0.13 and 0.23 < x < 0.25 were critically assessed by D.G. Martin [Mar88] and led to the Eq. 9.1 and Eq. 9.2 valid for temperatures up to $UO_{2.00}$ melting point (3120 K).

- for 273 ≤ T ≤ 923 K

$$a = a_{273K}(9.9734 \times 10^{-1} + 9.802 \times 10^{-6} \times T - 2.705 \times 10^{-10} \times T^2 + 4.391 \times 10^{-13} \times T^3) \quad \text{Eq. 9.1}$$

- for 923 ≤ T ≤ 3120 K

$$a = a_{273K}(9.9672 \times 10^{-1} + 1.179 \times 10^{-5} \times T - 2.429 \times 10^{-9} \times T^2 + 1.219 \times 10^{-12} \times T^3) \quad \text{Eq. 9.2}$$

With a the lattice parameter of the sample at T of the fluorite phase (in Å) and T the temperature (in K).

These relations were later confirmed by Carbajo *et al.* [Car01] and J.K. Fink [Fin00] who revaluated the associated uncertainties. The thermal expansion for $UO_{2.00}$ calculated with Eq. 9.1 and Eq. 9.2 is plotted in Figure 9.1.

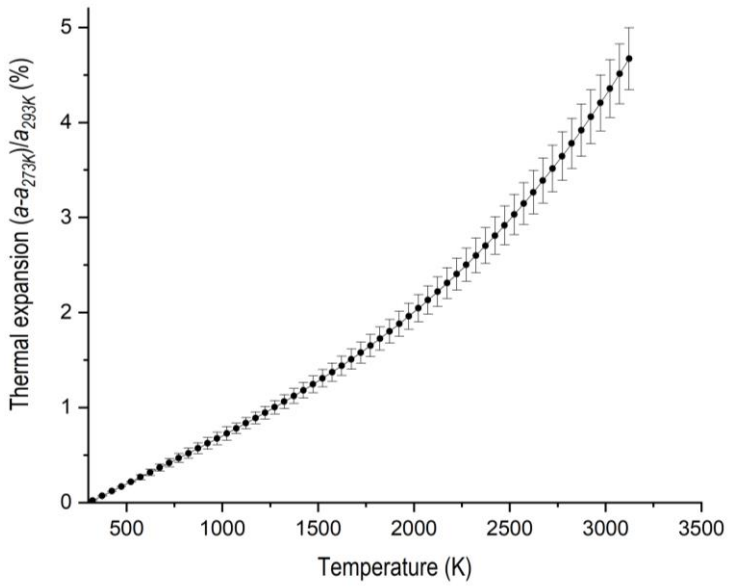

Figure 9.1: D.G. Martin [Mar88] thermal expansion recommendation for stoichiometric UO2.00 with uncertainties determined by J.K. Fink [Fin00].

This project has received funding from the Euratom research and training programme 2019-2020 under grant agreement No 945022.

Based on data available on stoichiometric $(U,Pu)O_{2.00}$ containing up to 25% Pu/(U+Pu) and $PuO_{2.00}$, D.G. Martin [Mar88] concluded that equations Eq. 9.1 and Eq. 9.2 can be also used for stoichiometric $(U,Pu)O_{2.00}$ on the whole Pu range (0-100%). Nevertheless, except one measurement at ~2300 K, no thermal expansion data for stoichiometric $(U,Pu)O_2$ and $PuO_{2.00}$ exists above 1900 K. As concluded in the previous revision of this catalogue, the range of validity of D.G. Martin recommendations for $(U,Pu)O_{2.00}$ have to be reduced to 300-1900K.

Concerning the impact of oxygen hypostoichiometry, in his review D.G. Martin recommended that the thermal expansion of $(U,Pu)O_{2-x}$ corresponded to the value for $(U,Pu)O_{2.00}$ corrected by a factor [1 + 3.9 (± 0.9) x] where x is the deviation from oxygen stoichiometry 2.00 as in $(U, Pu)O_{2-x}$. This relation would be valid for oxygen/metal (O/M) ratios ranging from 1.940 to 1.995. Nevertheless, this recommendation is based on a very limited number of experimental data and only on measurements up to 1273K. Furthermore, one major issue with this recommendation is that the presence of miscibility gaps (2 and 3 phases domains) for Pu content greater than 17% (Pu/(U+Pu)) and O/M ratios smaller than 1.97 in the U-Pu-O ternary phase diagram was not considered[Gué20].

In 2016, based on the new experimental results obtained on UO_2, $(U,Pu)O_2$ and PuO_2 and a critical review of values existing in the literature, Kato *et al.* [Kat16] published an extended study of thermal expansion of $(U,Pu)O_2$. By coupling a thermogravimetric analyser with a dilatometer, Kato *et al.* achieved a fine and accurate control of the O/M ratio (M=U+Pu) during new measurements performed on $U_{0.7}Pu_{0.3}O_{2.00\text{-}1.97}$ and $U_{0.52}Pu_{0.48}O_{2.00}$ samples up to 1950 K. The results obtained for the stoichiometric samples are compared in Figure 9.2 with results obtained on $UO_{2.00}$, $PuO_{2.00\text{-}1.92}$ by Uchida *et al.*[Uch11 ; Uch14]. Up to 1500K, in agreement with D.G. Martin recommendations, no difference is observed between $UO_{2.00}$, $PuO_{2.00}$ and $(U,Pu)O_{2.00}$. Above 1500K, an impact of the Pu content is clearly observed.

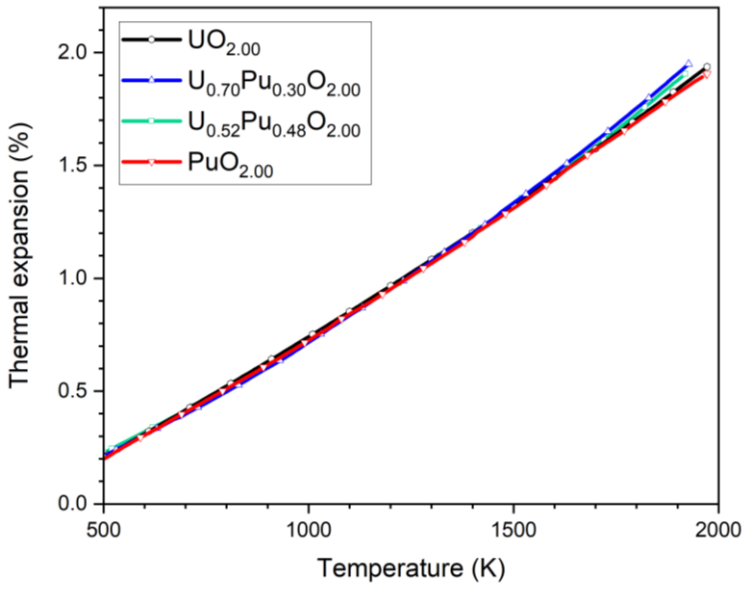

Figure 9.2: Experimental results of thermal expansion measured by Uchida et al. for $UO_{2.00}$ [Uch11] and $PuO_{2.00}$ [Uch14] and by Kato et al. on $(U,Pu)O_{2.00}$ [Kat16] (Uncertainty: ±0.002%)

This project has received funding from the Euratom research and training programme 2019-2020 under grant agreement No 945022.

Based on their results, Kato *et al.* [Kat16] proposed the following equations:

$$\frac{\Delta L}{L_0} = a_0 + a_1 T + a_2 T^2 + a_3 T^3 \qquad \text{Eq. 9.3}$$

With L and L_0 lengths at temperature T in K and 300 K, $\Delta L = (L - L_0)$ and coefficients a_0, a_1, a_2 and a_3 are defined using

$$a_i = b_0 + b_1 C_{Pu} + b_2 x + b_3 C_{Pu}^2 + b_4 x^2 + b_5 C_{Pu} x \qquad \text{Eq. 9.4}$$

With C_{Pu} the Pu content in mol. %, x the deviation from 2.00 oxygen stoichiometry, b_0, b_1, b_2, b_3, b_4 and b_5 are constants. Their values are given in Table 9.1.

Table 9.1: Coefficients b_0, b_1, b_2, b_3, b_4 and b_5 of Eq. 9.4.

	b_0	b_1	b_2	b_3	b_4	b_5
a_0 ($\times 10^{-3}$)	-2.8809	0.0301	-4.3954	0.0156	-15.1759	2.5642
a_1 ($\times 10^{-6}$)	9.5024	-0.1864	15.8173	-0.0229	7.6285	-7.5789
a_2 ($\times 10^{-10}$)	2.0894	2.9483	-19.9227	-1.0355	73.8931	11.6442
a_3 ($\times 10^{-13}$)	4.4096	-1.4263	23.5638	0.0251	-54.751	-14.418

In Figure 9.3, thermal expansion calculated using D.G. Martin (Eq. 9.1 and Eq. 9.2) and Kato *et al.* equations (Eq. 9.3 and Eq. 9.4) for $UO_{2.00}$ and $PuO_{2.00}$ are compared. The later values are within the uncertainties domain of D.G. Martin equation up to 2450K and 3000K for $PuO_{2.00}$ and $UO_{2.00}$, respectively. Nevertheless, considering the reduced uncertainties observed by Kato *et al.* (0.002 %) compared to those suggested by J.K. Fink [Fin00], the impact of plutonium content should be considered above 1500K and Kato *et al* relations should used for stoichiometric $(U,Pu)O_{2.00}$ compounds. Kato *et al* achieved to obtain rather small uncertainties which can be explained by the fact that experimental data used were generated by the same research group. Uncertainties suggested by J. K. Fink were the result of a review work of the all experimental data available in the open literature and obtained by different experimental techniques which explained larger values compared to Kato *et al*. These conclusions show that the Kato et al relations (Eq. 9.3 and Eq. 9.4) should be used for $(U,Pu)O_{2.00}$ samples.

This project has received funding from the Euratom research and training programme 2019-2020 under grant agreement No 945022.

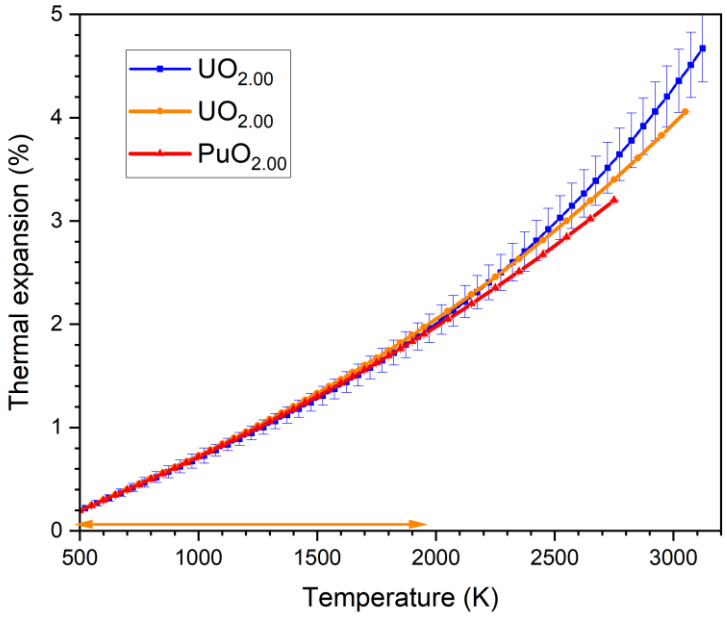

Figure 9.3: Comparison between thermal expansion using D.G. Martin recommendation [Mar88] in blue and using Kato et al. [Kat16] relations for $UO_{2.00}$ and $PuO_{2.00}$. The orange arrow represents the experimental range studied by Kato.

The results obtained by Kato *et al.* on hypostoichiometric $(U,Pu)O_2$ samples are compared to D.G. Martin equations in Figure 9.4. The Kato *et al.* experimental data are systematically lower than the values calculated using D.G. Martin relation corrected from the hypostoichiometry. Considering that Kato *et al.* equations (Eq. 9.3 and Eq. 9.4) should be used for hypo stoichiometric $(U,Pu)O_{2-x}$. The effect of hypostoichiometry for $U_{0.70}Pu_{0.30}O_{2-x}$ can be observed in Figure 9.5.

This project has received funding from the Euratom research and training programme 2019-2020 under grant agreement No 945022.

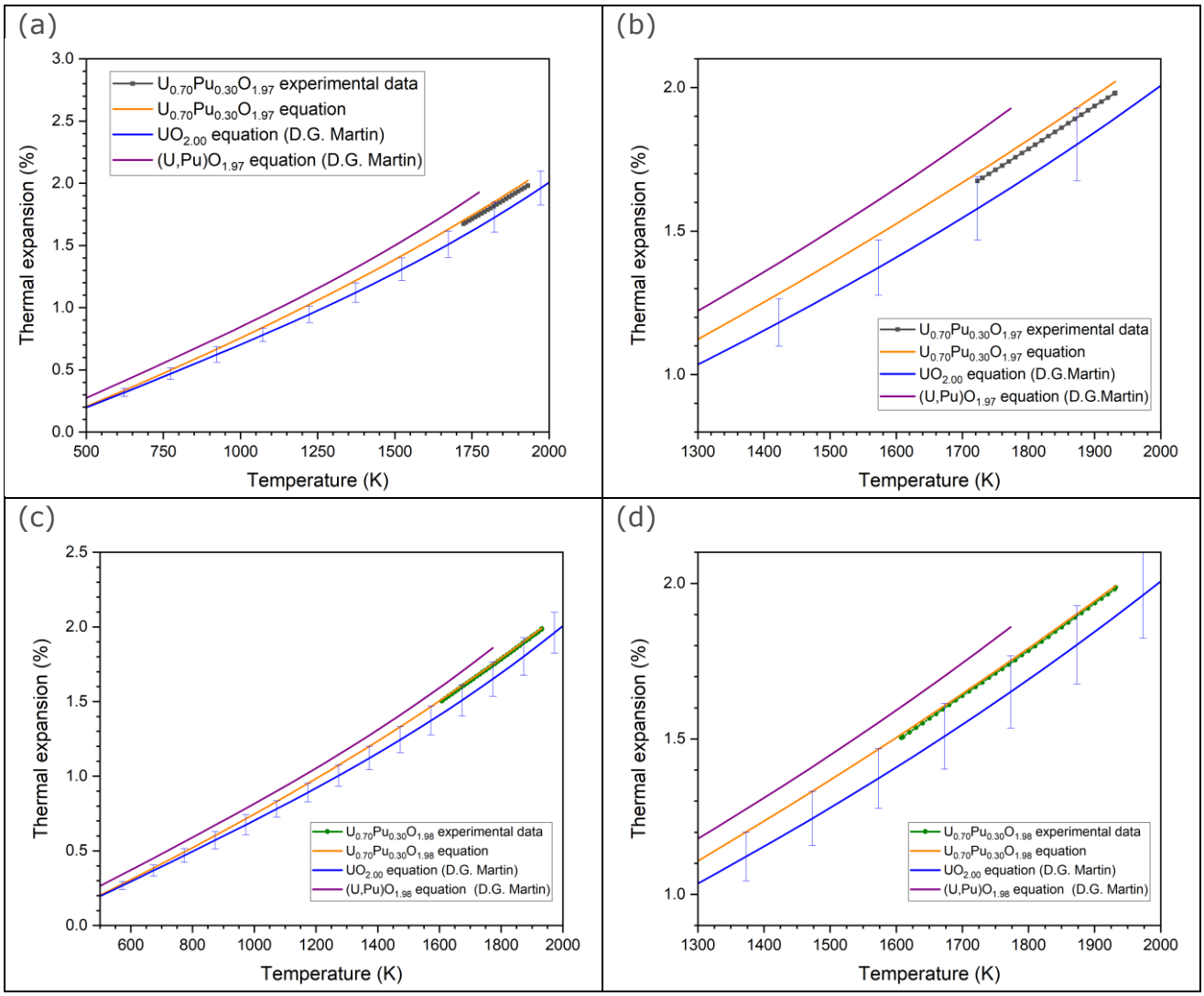

Figure 9.4: Comparison between Kato *et al* [Kat16] results (experimental and calculated) and D.G. Martin [Mar88] relations (calculated) for $U_{0.70}Pu_{0.30}O_{1.97}$ (a and b) and $U_{0.70}Pu_{0.30}O_{1.98}$ (c and d).

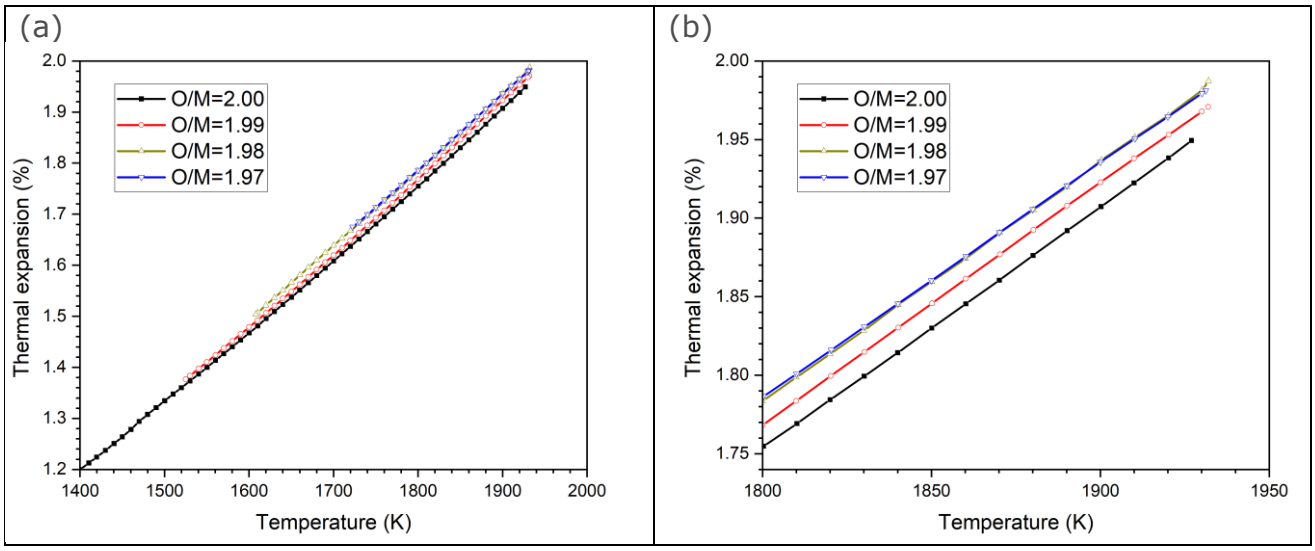

Figure 9.5: Thermal expansion calculated $U_{0.70}Pu_{0.30}O_{2-x}$ using Kato et al [Kat16] equations (uncertainty: ±0.002).

This project has received funding from the Euratom research and training programme 2019-2020 under grant agreement No 945022.

9.2 NEA recommendation

The recommended law in [NEA25] for thermal expansion is the one proposed by Kato [Kat16] and given in Eq. 9.3 and Eq. 9.4, with coefficients from Table 9.1. thermal expansion is given a dependency of the plutonium content and O/M ratio.

This correlation is also valid for MOX doped with up to 4 mol.% of minor actinide (Np and Am) up to 1050 K.

Considering the heterogeneity of irradiated fuel composition, the burn-up effect on thermal expansion cannot be correctly assessed.

The range of parameters for the validity of the recommendation is:

- Temperature from 300 to 1900 K
- O/M from 2.00 to 1.97 but can be extrapolated in a larger range when single phase is assumed
- Pu content from 0 to 48% in MOX and 100%Pu (PuO_2)

Uncertainty is constant for the whole ranges (T, O/M and Pu content) and is estimated to be ± 0.002 %.

9.3 Data obtained in the frame of the ESFR-SMART project

In the frame of the ESFR-SMART project, thermal expansion on three fresh MOX samples were measured [ESF23]. The name on chemical compositions of these samples is summarized in Table 9.2 and are extracted from P. Fouquet-Metivier thesis[Fou22]. Thermal expansion was measured using High-Temperature X-ray Diffraction in the 300-1873K range. During measurements, a reducing atmosphere of He/H_2 4% + 55 ppm H_2O (pO_2 = $1x10^{-28}$ atm) was used. The oxygen inside the experimental chamber was monitored by an oxygen gauge, resulting in an oxygen potential ranging between -489.2 $kJ.mol^{-1}$ at 1873 K and -494.7 $kJ.mol^{-1}$ at 923 K. The experimental uncertainties on the lattice parameter and temperature are ± 0.003 Å and ± 15 K respectively.

Table 9.2: Details of the three fresh $(U,Pu)O_2$ samples studied.

Name	Composition
PHENIX29	$U_{0.70}Pu_{0.29}Am_{0.01}O_{1.984}$
CAPRA4	$U_{0.70}Pu_{0.28}Am_{0.02}O_{2.004}$
TRABANT40	$U_{0.60}Pu_{0.39}Am_{0.01}O_{1.995}$

The lattice thermal expansions of the three samples are plotted in Figure 9.6. The results are compared to the recommendations of D.G. Martin [Mar88] and Kato *et al.* [Kat16] using initial O/M ratios given in Table 9.2.

This project has received funding from the Euratom research and training programme 2019-2020 under grant agreement No 945022.

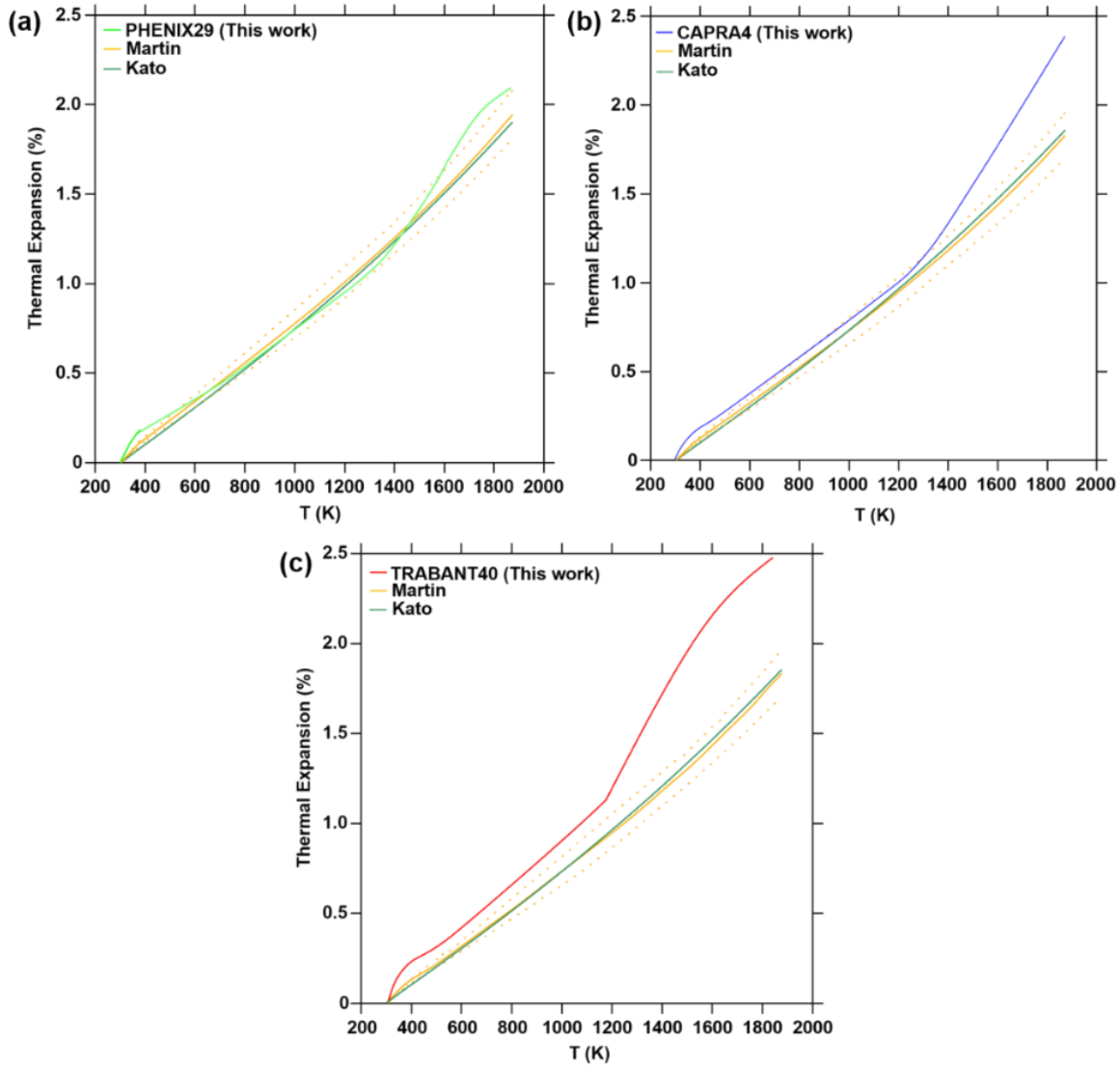

Figure 9.6: Thermal expansions of the PHENIX29, CAPRA4 and TRABANT40, from 300 to 1873 K [Fou22].

For the three compositions, a deviation from the recommendations of D.G. Martin and Kato *et al.* is observed: above 1500 K for the PHENIX29, above 1300 K for the CAPRA4 and on the whole temperature range for the TRABANT40. This observation is assumed to originate from the reduction of the samples occurring at high temperature. Indeed, in the two recommendations, the O/M ratio is supposed to be constant during the whole experiment and equal to the initial O/M ratio before thermal treatment for D.G. Martin and Kato *et al.*.

In order to better understand the difference observed recommendations, P. Fouquet-Metivier [Fou22] calculated the O/M ratio of the samples assuming the equilibrium with the gas atmosphere using the thermodynamic U-Pu-O model available in the TAF-ID database V13. The results of these calculations are plotted in Figure 9.7 illustrating that reduction of the three samples occurred during the measurements. These results clearly explained the disagreements observed in Figure 9.6.

This project has received funding from the Euratom research and training programme 2019-2020 under grant agreement No 945022.

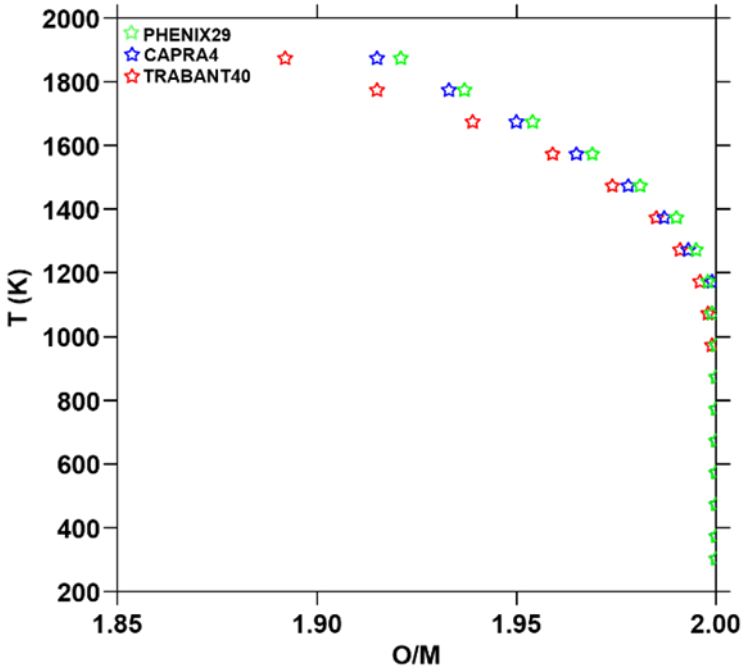

Figure 9.7: Variation in the O/M ratio of the samples with temperature (He/H_2 4% + 55 ppm H_2O) [Fou22].

In Figure 9.8, the experimental results with thermal expansion calculated with the Kato et al relations using the deviation from stoichiometry calculated (cf Figure 9.7) at each temperature. A better agreement is noticed for the PHENIX29 on the whole temperature range and from room temperature to 1400 K the CAPRA4 sample. On the contrary, for the TRABANT40, the thermal expansion calculated from Kato *et al.* still differs from the one determined here, with too low values. Indeed, in their work, Kato *et al.* performed their experiments for a minimum O/M ratio of 1.97, whereas in this study the minimum value reached was 1.89.

These results show that the equation given by Kato *et al.* cannot be used for lower O/M ratios than their experimental range of validity (1.97≤O/M≤2.00).

This project has received funding from the Euratom research and training programme 2019-2020 under grant agreement No 945022.

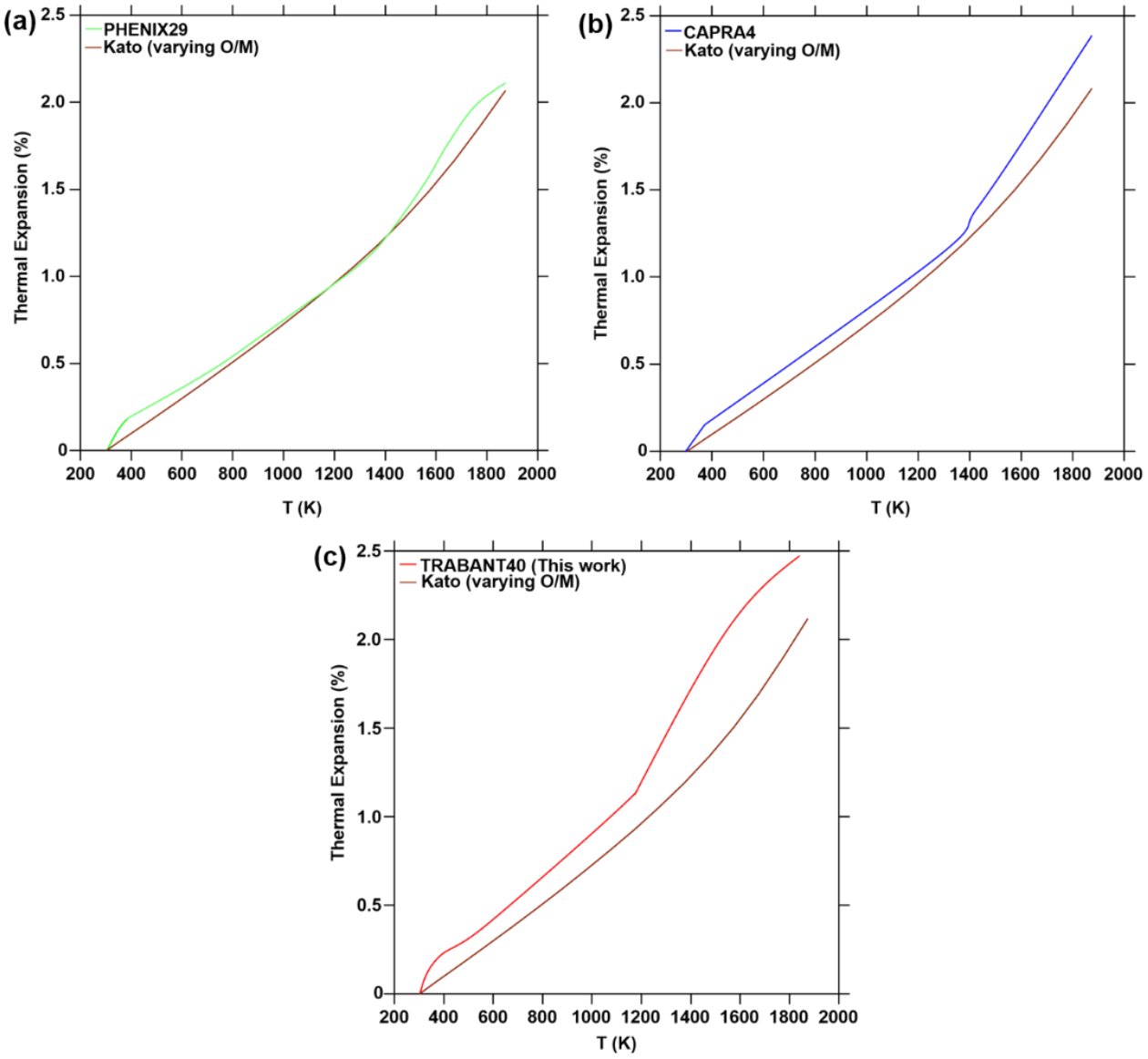

Figure 9.8: Thermal expansions of (a) PHENIX29, (b) CAPRA4 and (c) TRABANT40, compared to the recommendation of Kato *et al.* with varying O/M ratio [Fou22].

9.4 Data obtained in the frame of the PuMMA project

In the frame of the PuMMA project, thermal expansion was measured between 300 and 1800K with XRD-HT setup on one fresh MOX samples (MOX70-F), manufactured by co-milling process, with an O/M ratio of 1.99 ± 0.01 and a Pu content of 69% [PuM25]. During data acquisition, peaks of the $(U,Pu)O_2$ phase (faces centered cubic (fcc) structure) were observed over the whole temperature range and their drift toward larger 2θ angular positions as the temperature decrease highlight that the lattice parameter of this phase decrease with temperature as expected.

This project has received funding from the Euratom research and training programme 2019-2020 under grant agreement No 945022.

The lattice thermal expansion of the sample is plotted in Figure 9.9 and compared to the recommendations of D.G. Martin [Mar88] and Kato *et al.* [Kat16] using initial O/M ratios of 2.00.

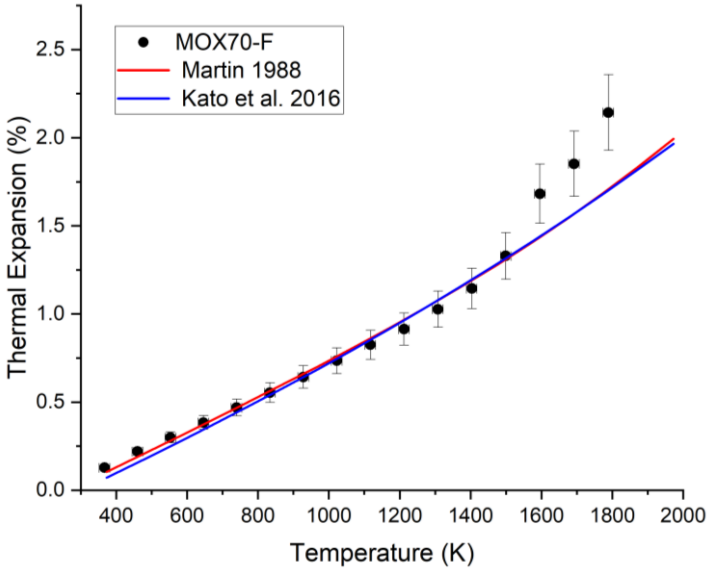

Figure 9.9: Thermal expansion for MOX70-F sample compared to empirical relations for O/M=2.00.

As one can see on Figure 9.9, the thermal expansion of the MOX70-F sample is in very good agreement with the two empirical relations up to 1500K. Above this value, the experimental values are higher. As this experiment was performed in a reducing atmosphere ($pO_2=10^{-28}$ atm), this increase can be attributed to the reduction of the sample (lower O/M values). Figure 9.10 shows the comparison with the empirical relation of Kato *et al.* for O/M=1.97 (limit of the validity range) and the calculated values, although still not close to the experimental values, are closer to the latter. This therefore validates the hypothesis of a reduction of the sample above 1500K.

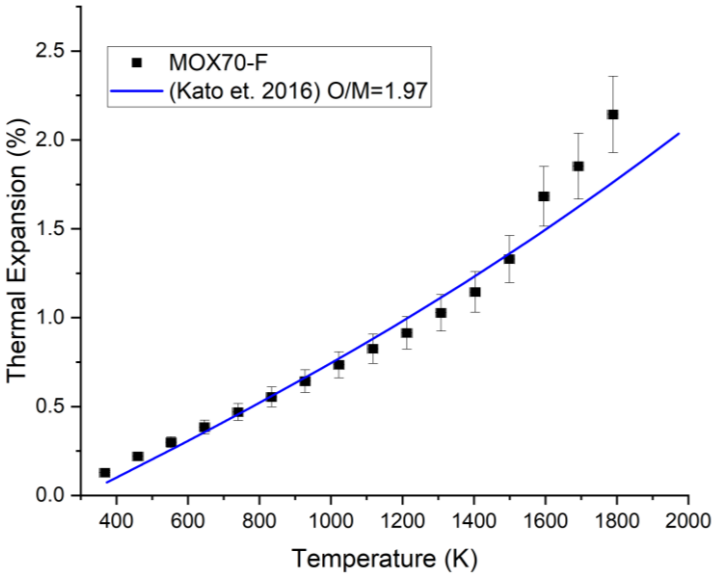

Figure 9.10: Thermal expansion for MOX70-F sample compared to empirical relations for O/M=1.97.

This project has received funding from the Euratom research and training programme 2019-2020 under grant agreement No 945022.

The results obtained on the MOX70-F sample are compared on Figure 9.11 to thermal expansion of $(U,Pu)O_2$ samples with 29 and 39 % Pu/(U+Pu), i.e. samples PHENIX29 and TRABANT40 respectively, described in §9.2.

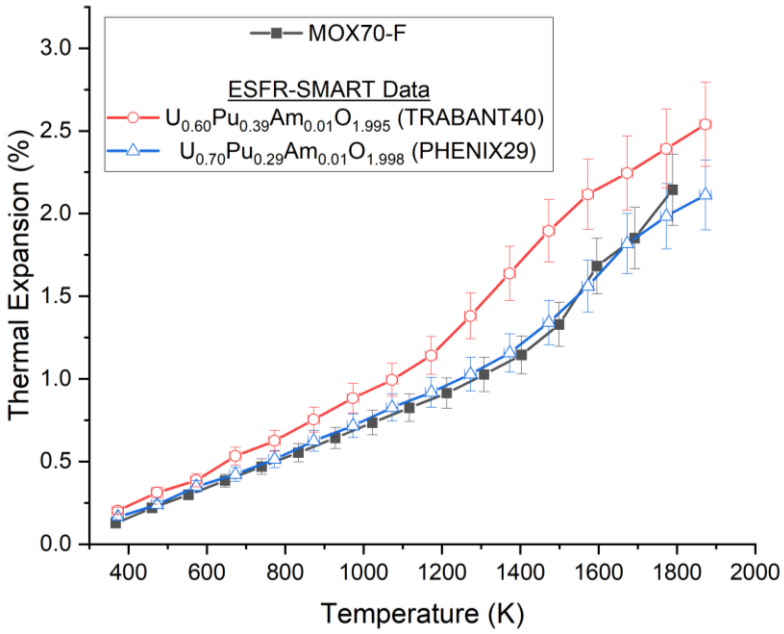

Figure 9.11: Thermal expansion for MOX70-F sample compared to empirical relations for O/M=1.97.

The three samples have the same behavior with an increase of their thermal expansion for temperature above 1200-1500 K due to the decrease of their O/M ratios. It's worth noting that the thermal expansion both in term in values and reduction are almost identical for MOX70-F and PHENIX 29 samples despite their differences in term of Pu content. For these compositions, the experimental results are in good agreement up to 1400 K, before their reduction, with both D.G. Martin and Kato *et al.* empirical laws. Meaning that the plutonium content up to 29% and for 70% does not have an impact in $(U,Pu)O_2$ thermal expansion. For 39% Pu, this not the case as the experimental results show a deviation from the two empirical law on the whole temperature range.

9.5 Conclusions and recommendations

Based on the new experimental results obtained in the framework of ESFR-SMART and PuMMA projects and the recent bibliography, the recommendation for thermal expansion of $(U,Pu)O_2$ is to use the Kato et al relations (Eq. 9.3 and Eq. 9.4) and the parameters given in Table 9.1.

The validity ranges are the following:

- Pu content: 0-100% for $(U,Pu)O_2$,
- O/M ratio: 2.00 – 1.97
- Temperature: 300-1900 K

P. Fouquet-Métivier [Fou22] has proposed a new set of parameters to replace those given in Table 9.1 in order to extend the O/M validity range down to values shown in Figure 9.7. Considering that no experimental measurements of the O/M

This project has received funding from the Euratom research and training programme 2019-2020 under grant agreement No 945022.

ratios are given in this work, these new set of parameters and the extended O/M ratio range cannot be recommended.

These perfectly illustrated the lack of experimental data, thermal expansion and O/M in the same conditions. The crucial point would perform further TGA experiments to correlate the variation of the O/M ratio with the thermal expansion beyond the validity ranges given before.

9.6 References

[Car01] J. J. Carbajo, G. L. Yoder, S. G. Popov and V. K. Ivanov, « A review of the thermophysical properties of MOX and UO_2 fuels », Journal of Nuclear Materials 299 (2001) 181-198.

[ESF23] D. Staicu, D. Robba, L. Vlahovic, P. Pöml, E. Dahms, P. Fouquet-Metivier, F. Cabezas, M.-M. Desagulier, Ph. Martin, N. Chauvin, I. Viallard and J.-C. Dumas, « New measurements of properties of MOX fuel with associated characterizations », Deliverable D2.5.5, ESFR-SMART European Project (2023).

[Fin00] J. K. Fink, « Thermophysical properties of uranium dioxide », Journal of Nuclear Materials 279 (2000) 1-18.

[Fou22] P. Fouquet-Métivier, « Study of the influence of americium on thermodynamic and structural properties of $(U,Pu)O_{2\pm x}$ mixed oxides », Thèse de doctorat, Université Paris-Saclay (2022).

[Gué20] C. Guéneau, A. Chartier, P. Fossati, L. Van Brutzel and P. Martin, « 7.03 - Thermodynamic and Thermophysical Properties of the Actinide Oxides », dans : Comprehensive Nuclear Materials (Second Edition), R. J. M. Konings, R. E. Stoller, Éd. Oxford: Elsevier, 2020, 111-154

[Kat16] M. Kato, Y. Ikusawa, T. Sunaoshi, A. T. Nelson and K. J. McClellan, « expansion measurement of $(U,Pu)O_{2-x}$ in oxygen partial pressure-controlled atmosphere », Journal of Nuclear Materials 469 (2016) 223-227.

[Mar88] D. G. Martin, « The thermal expansion of solid UO_2 and (U,Pu) mixed oxides — a review and recommendations », Journal of Nuclear Materials 152 (1988) 94-101.

[NEA25] N. Chauvin et al., Recommendations on Fuel Properties for Fuel Performance Codes, NEA/NSC/R(2024)1, July 2025

[PuM25] P. Martin, M.-M. Desagulier, J. Martinez, C. Guéneau, M. Pons, M. Duchateau, T. Barral, D. Staicu, L. Vlahovic, D. Robba and N. Clavier, « Measurements of thermal properties on fresh fuels », Deliverable D3.7, PuMMA European Project (2025).

[Uch11] T. Uchida, T. Sunaoshi, M. Kato, et K. Konashi, « Thermal Properties of UO_2 by Molecular Dynamics Simulation », *Progress in Nuclear Science and Technology* 2 (2011) 598-602.

This project has received funding from the Euratom research and training programme 2019-2020 under grant agreement No 945022.

[Uch14] T. Uchida, T. Sunaoshi, K. Konashi, et M. Kato, « Thermal expansion of PuO_2 », *Journal of Nuclear Materials* 452 (2014) 281-284.

This project has received funding from the Euratom research and training programme 2019-2020 under grant agreement No 945022.

10. Elastic constants

This chapter was originally provided by N. Vér (MTA-EK)

10.1 Literature data

The four elastic constants which are relevant to polycrystalline materials are the Young's modulus (E), the shear modulus (G), the bulk modulus (B) and Poisson's ratio (ν). Because in practice only two of these four parameters are independent variables, recommendations are given only for E and G; values of B and ν can then be derived from Eq. 10.1 and Eq. 10.2.

$$B = \frac{E\,G}{3\,(3G - E)} \qquad \text{Eq. 10.1}$$

$$\nu = \frac{E}{2G} - 1 \qquad \text{Eq. 10.2}$$

In addition, it is necessary to differentiate between adiabatic and isothermal elastic constant values. These will be distinguished below through the use of subscripts S and T, respectively. While at room temperature adiabatic and isothermal elastic constants are virtually identical, differences between the two increase with temperature so that by 2929 K, E_S, B_S and ν_S are respectively 3, 33 and 12% higher than their isothermal counterparts. (Note that at any specific temperature values of the adiabatic and isothermal shear moduli are identical.) Adiabatic elastic constants should be employed in situations when stresses vary with time by Eq. 10.3.

$$L \geq 5 \times 10^{-3}\, t^{0.5} \qquad \text{Eq. 10.3}$$

where t is the time constant of the applied stress (sec) and L is an appropriate dimension of the solid under stress (m). Otherwise isothermal elastic constant values should be employed.

Main of following recommendations are based on a review of the elastic constants of polycrystalline oxide fuels between 298 K and the melting temperature by Martin [Mar89].Post-90's experimental works have been focused mainly on two areas. In Japan a series of measurements was performed in order to characterize the high burn-up low decontamination MOX fuel [Yam97] [Yam98] [Yam01] [Kur09] [Tan12]. In France the research was aimed at the development of new investigation techniques, such as microacoustic devices and microindentation, for evaluation of the local elastic properties of irradiated nuclear fuels [Roq99] [Roq00] [Lau02] [Gat05] [Lau12] [Lau14] [Cap16] [Mar16] [Mar17] [Sta17a] [Bal18].

Table 10.1 compares the recommendations of Martin [Mar89] and MATPRO [MAT01] and the results of the recent studies.

This project has received funding from the Euratom research and training programme 2019-2020 under grant agreement No 945022.

Table 10.1: Summary of findings on the elastic properties (Young's modulus) of UO_2 presented in the literature.

Influencing parameters	Domain of variation of influencing parameters	Domain of variation of Young's modulus		
		[Mar89]	[MAT01]	Recent studies
Young's modulus at 298 K (GPa)		222	225.8	
Temperature (K)	298 → 1273	0 → - 13%	0 → - 11%	-
Porosity	0 → 0.1	0 → - 25%	0 → - 28%	0 → - 26% [Gat05] [Lau12] [Cap16]
Stoichiometry	0 → -0.05	0 → - 7%	0 → - 8%	-
	0 → +0.05	0 → - 5%	0 → - 6%	-
Grain size (µm)	5 → 35	0 → - 5%	-	no effect [Lau02]
Pu content (at.%)	0 → 20	0 → 0%	0 → 3%	0 → ~ 4% [Sta17a]
Ce content (at.%)	0 → 20	-	-	0 → - 40% [Yam97] [Yam98] [Mar17]
Gd2O3 content (wt%)	0 → 10	-	-	0 → - 15% [Mar17]
Burn-up (GWd/tM)	0 → 100	-	-	0 → - 25% [Lau12] [Lau14] 0 → - 33% [Mar17]

10.1.1 Recommendations for stoichiometric, fully dense UO_2 and $(U,Pu)O_2$

The elastic constants of stoichiometric, fully dense UO_2 as a function of temperature, T, are given by the following relationships:

- Isothermal Young's modulus:

$$E_T = 2.2693 \times 10^{2} - 1.5399 \times 10^{-2} T - 9.597 \times 10^{-6} T^{2} \quad \text{if } 273\,K \le T \le 2610\,K \qquad \text{Eq. 10.4}$$

$$E_T = -1.33445 \times 10^{3} + 1.18106\,T - 2.38803 \times 10^{-4} T^{2} \quad \text{if } 2610\,K \le T \le 2929\,K \qquad \text{Eq. 10.5}$$

This project has received funding from the Euratom research and training programme 2019-2020 under grant agreement No 945022.

- Adiabatic Young's modulus:

$$E_S = 2.2685 \times 10^{2} - 1.3428 \times 10^{-2} T - 9.746 \times 10^{-6} T^{2} \quad \text{if } 273\ K \le T \le 2610\ K \qquad \text{Eq. 10.6}$$

$$E_S = -1.48030 \times 10^{3} + 1.29473\ T - 2.60352 \times 10^{-4} T^{2} \quad \text{if } 2610\ K \le T \le 2929\ K \qquad \text{Eq. 10.7}$$

- Shear modulus:

$$G = 8.583 \times 10^{1} - 5.157 \times 10^{-3} T - 3.747 \times 10^{-6} T^{2} \quad \text{if } 273\ K \le T \le 2610\ K \qquad \text{Eq. 10.8}$$

$$G = -5.7625 \times 10^{2} + 5.02189 \times 10^{-1} T - 1.00939 \times 10^{-4} T^{2} \quad \text{if } 2610\ K \le T \le 2929\ K \qquad \text{Eq. 10.9}$$

with T in K and E_T, E_S and G in units of GPa.

Errors in the Young's modulus recommendations are about 1% at room temperature, rising to 10% at 2929 K; corresponding figures for the shear modulus are 3% and 12%. **The above recommendations apply also to stoichiometric, fully dense $(U,Pu)O_2$**; however errors in Young's modulus and shear modulus values derived from Eq. 10.4 to Eq. 10.9 are about twice the corresponding UO_2 figures. The elastic constants of fully dense $UO_{2.00}$ and $(U,Pu)O_{2.00}$ derived from equations Eq. 10.4 to Eq. 10.9 and Eq. 10.1-Eq. 10.2 are shown in Figure 10.1 and Figure 10.2.

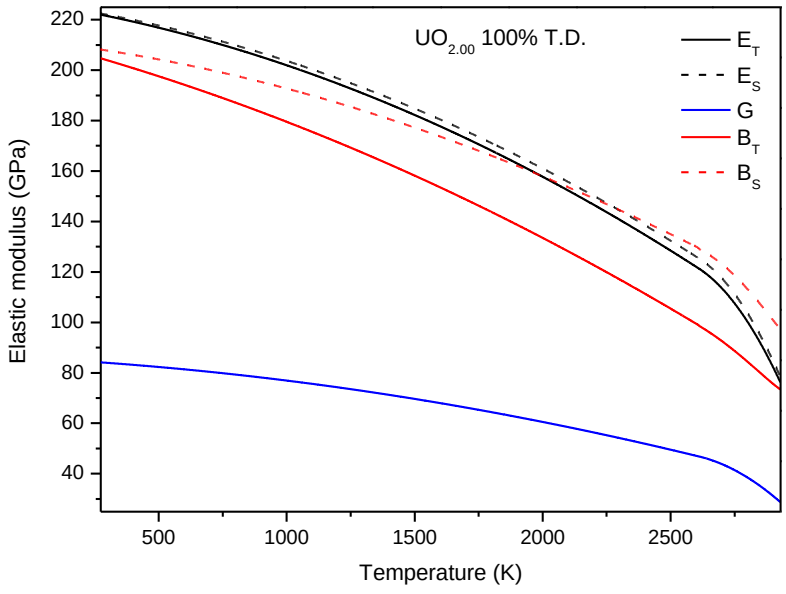

Figure 10.1: Young's modulus, shear modulus and bulk modulus of fully dense $UO_{2.00}$ and $(U,Pu)O_{2.00}$ as a function of temperature.

This project has received funding from the Euratom research and training programme 2019-2020 under grant agreement No 945022.

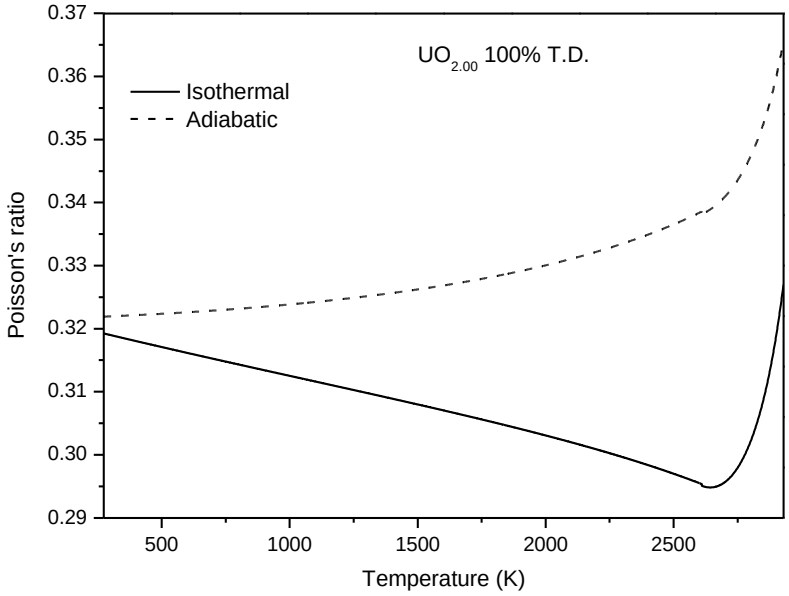

Figure 10.2: Poisson's ratio of fully dense $UO_{2.00}$ and $(U,Pu)O_{2.00}$ as a function of temperature.

No recommendations are given over the temperature range 2929-3120 K, the melting point of UO_2, because no experimental data are available. In principle, not unreasonable values of E_T, E_S and G may be obtained in this temperature range using Eq. 10.5, Eq. 10.7 and Eq. 10.9, respectively. However it should be noted that with increasing temperature the resulting bulk modulus, derived from Eq. 10.1, first decreases (as at lower temperatures), attains a minimum value at 2985 K (B_T) or 3007 K (B_S), becomes infinite at 3094 K (B_T) or 3103 K (B_S) and subsequently is negative. Values of Poisson's ratio, derived from Eq. 10.2, appear to behave more satisfactorily over this temperature range since they increase monotonically with temperature. However it should be noted that Poisson's ratio values exceed 0.50 at temperatures above 3094 K (isothermal) and 3103 K (adiabatic), i.e. when the corresponding bulk modulus becomes infinite.

10.1.2 Effect of temperature

The elastic modulus of UO_2 decreases with increasing temperature. The assumption of a linear decrease of the elastic modulus of stoichiometric UO_2 with increasing temperature (as done e.g. in [MAT01]) was not justified at temperatures above ~1773 K and there was some evidence from the experimental data of nonlinearity at lower temperatures [Mar89]. The temperature dependence of the elastic constants exhibits a discontinuity at about 2610 K where UO_2 undergoes a Bredig transition.

The MATPRO analysis did not include the only data above ~1773 K (and up to 2929 K) by Clausen et al. [Cla85], and the linear relationship based on the available UO_2 fuel data in the temperature range 450 to 1600 K was simply extrapolated to the approximate melting temperature [MAT01]. Thus, the linear expression used in the MATPRO correlation for the effect of temperature

This project has received funding from the Euratom research and training programme 2019-2020 under grant agreement No 945022.

systematically overpredicts the Young's modulus at a low (<450 °C) and high (>1600 °C) temperature.

Since the review work by Martin [Mar89], all experimental works on the elastic properties of oxide fuels have been done at room temperature. The only exception is the work by Yamada et al. [Yam98] which is discussed in Section 10.1.7.

10.1.3 Effects of porosity

In order to allow for the effects of porosity,isothermal or adiabatic Young's modulus and shear modulus values derived from Eq. 10.4 to Eq. 10.9 should be multiplied by a factor.

- if $0 \leq p < 0.30$

$$E_{S,T}(p) = E_{S,T}(p=0)(1-2.50\,p) \qquad \text{Eq. 10.10}$$

$$G(p) = G(p=0)(1-2.25\,p) \qquad \text{Eq. 10.11}$$

- if $p \geq 0.30$

$$E_{S,T}(p) = E_{S,T}(p=0)\frac{(1-p)}{(1+6\,p)} \qquad \text{Eq. 10.12}$$

$$G(p) = G(p=0)\frac{(1-p)}{(1+3.85\,p)} \qquad \text{Eq. 10.13}$$

where p is the fractional porosity. The uncertainty in the numerical value within each of these brackets is $\pm$ 0.4.

The elastic modulus of UO_2 decreases with an increasing volume fraction of porosity. Based on experimental evidence, Martin [Mar89] concluded that the linear decrease of the elastic modulus of UO_2 with increasing porosity seems to be valid up to the highest porosity values measured, namely 28% (Boocock et al. [Boo72]).

The linear expression in MATPRO [MAT01] to describe the effect of porosity on Young's modulus in the limited range of porosities of interest (between 0 and 0.1) was evaluated with the existing high temperature data (and not with the room temperature data).

Recently, Roque et al. [Roq00] investigated the effect of porosity on the elastic properties of nuclear fuel materials at room temperature by microacoustic techniques (acoustic microscopy and microechography). All of their samples had the same stoichiometric composition ($UO_{2.00}$) and the same microstructure (approximately same grain size) and the porosity (1-10%) was the only parameter whose role should be related to elastic modulus alterations. The pore size distribution was centered both on 1 µm and 10 µm.

This project has received funding from the Euratom research and training programme 2019-2020 under grant agreement No 945022.

Their experimental results showed good agreement between the elastic moduli of samples having a porosity spectrum centered on 1 µm and 10 µm which proved that elastic modulus varies as a function of the porosity ratio and not as a function of the pore size. From their measurement results they established the following linear laws of variation of elastic constants as a function of porosity:

$$E = 220\,(1 - 2.34\,p) \qquad \text{Eq. 10.14}$$

$$G = 82\,(1 - 2.03\,p) \qquad \text{Eq. 10.15}$$

Eq. 10.14 and Eq. 10.15 are in good agreement with Martin's recommendations [Mar89]. From the comparison between their experimental data and the Berryman's model [Ber80a] [Ber80b], they deduced a pore shape factor equal to 0.4 (oblate spheroidal pores with an aspect ratio c/a = 0.4) in the range of 1–10% porosity. According to Berryman's model it can be shown that the elastic constants are very sensitive to the porosity morphology/pore shape variation [Lau12].

The above results were extended by Gatt et al. [Gat05] over the porosity range from 1 to 20%. Their experimental data can be given by the following linear relationship:

$$E = 222\,(1 - 2.62\,p) \qquad \text{Eq. 10.16}$$

$$G = 84\,(1 - 2.48\,p) \qquad \text{Eq. 10.17}$$

Eq. 10.16 and Eq. 10.17 are also in good agreement with Martin's recommendations [Mar89].

From the comparison of the analytical–numerical estimates to the micro-acoustic experimental data Gatt et al. [Gat05] concluded that:

- The usual empirical fits of Martin [Mar89] performed on a wide range of bibliographic data give accurate estimates of elastic properties as a function of porosity.
- The UO_2 nuclear ceramics contain both spherical (intra-granular) cavities and ellipsoidal (inter-granular) cavities. Agreement with experimental data cannot be reached unless including a population of ellipsoidal pores (inter-granular cavities).
- Assuming that inter-granular pores have ellipsoidal shapes, their aspect ratio is lower than about 0.25 (penny shaped oblates). (For a microstructure with 10% of porosities made up only of ellipsoidal inter-granular cavities, i.e. containing 0% of spherical cavities, the experimental data could be reached with an aspect ratio of about 0.25.)

Elastic moduli E and G values of non-irradiated UO_2 measured by ultrasonic method in the porosity range of 0–20% are given in [Lau12] by Eq. 10.18 and Eq. 10.19

$$E = 223\,(1 - 2.69\,p) \qquad \text{Eq. 10.18}$$

This project has received funding from the Euratom research and training programme 2019-2020 under grant agreement No 945022.

$$G = 84\,(1 - 2.46\,p)$$ Eq. 10.19

Cappia et al. [Cap16] performed Vickers microhardness and Young's modulus measurements (by acoustic microscopy) on irradiated fuel samples at a burn-up range 60–110 GWd/tM. From the results the Young's modulus dependence on the local porosity (up to 20%) was derived and extended to the full radial profile, including the high burn-up structure. The obtained dependence could be well represented by a linear correlation and no major differences could be identified in the Young's modulus decrease with porosity between irradiated and non-irradiated UO_2 by the authors.

10.1.4 Effect of deviation from stoichiometry

In order to allow for the effect of deviations from stoichiometry, the above recommendations for the isothermal and adiabatic Young's modulus should be multiplied by a factor as per Eq. 10.20.

$$E_{S,T}((U,Pu)O_{2+x}) = E_{S,T}(UO_{2.00})(1 + a\,x)$$ Eq. 10.20

- if x > 0 (hyperstoichiometry): $a = -1.06 \pm 0.14$
- if x > 0 (hypostoichiometry) : $a = 1.37 \pm 0.19$

In like manner the shear modulus should be taken as the stoichiometric value multiplied by a factor a per Eq. 10.21.

$$G((U,Pu)O_{2+x}) = G(UO_{2.00})(1 + c\,x)$$ Eq. 10.21

- if x > 0 (hyperstoichiometry): $c = -1.09 \pm 0.14$
- if x > 0 (hypostoichiometry): $c = -1.34 \pm 0.19$

These recommendations indicate that both the Young's modulus and the shear modulus decrease when the O/M ratio is altered in either direction from that of the stoichiometric composition.

Elastic moduli are higher for stoichiometric fuel but decrease with hyper- or hypostoichiometric samples. The influence of stoichiometry is difficult to quantify, because other parameters (e.g., the fabrication route, grain size, etc.) interfere [Lau12]. In his review work Martin [Mar89] concluded that the Young's modulus of UO_{2+x} depends not only on the value of x but also on the manufacturing procedure, since this will affect the relative amount of the U_4O_{9-y} phase that is present.

The only recent study on the effect of O/M ratio on the mechanical properties of hyper-stoichiometric uranium dioxide was performed by Laux et al. [Lau12]. The results obtained by acoustic microscopy and extrapolated to 0% of porosity are in

This project has received funding from the Euratom research and training programme 2019-2020 under grant agreement No 945022.

good agreement with all the previous measurements (see Figure 10.3) but they cover a relative limited range of stoichiometry from 2 to 2.015.

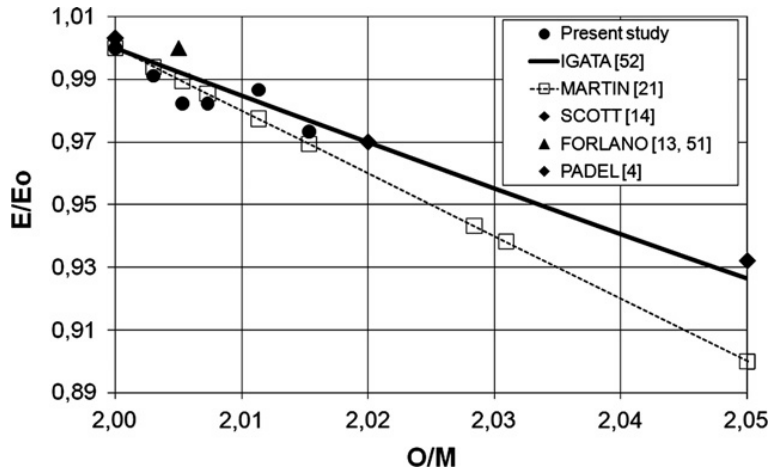

Figure 10.3: Young's modulus for UO_{2+x} at room temperature, expressed as a ratio of the stoichiometric value, as a function of O/M = 2+x [Lau12].

10.1.5 Effect of grain size

The only study on the effect of grain size on the elastic constants reported by Martin [Mar89] was the work of Igata and Domoto [Iga73]. They observed a decrease of 5% in the room temperature Young's modulus of UO_2 when the grain size was increased from 5 to 35 μm, so the effect was regarded by Martin as fairly small.

Recently, Laux et al. [Lau02] studied the effect of grain size on the elastic moduli of UO_2 by acoustic microscopy and microechography. In their measurements the size of the grains (10-90 μm) had no influence on the intrinsic (extrapolated to 0% of porosity) elastic moduli.

10.1.6 Effect of PuO_2 content

Although the published $(U,Pu)O_2$ mixed oxide data are very limited and scattered, several authors indicate that the addition of PuO_2 to UO_2 causes a moderate increase in Young's modulus:

- Boocock et al.'s [Boo72] values for UO_2 and $(U,Pu)O_2$ are very similar.
- De Novion et al.'s [Nov70] results indicate that the Young's modulus increases by 4% when the plutonium content is raised from 0 to 15%.
- Nutt et al. [Nut70] found an only 11% higher modulus value for a mixed $(U,Pu)O_2$ containing 70% plutonium than the corresponding UO_2 figure.

Based on these scarce data on mixed oxides, Matthews [Mat74] and Martin [Mar89] concluded that the elastic constants of stoichiometric $(U,Pu)O_2$ should be taken to be identical to those of UO_2. However, in MATPRO [MAT01] a 3% increase in Young's modulus due to an addition of 20% PuO_2 to UO_2 was regarded as the most reliable estimate, based on [Boo72, Mat74, Nut70, Nov70].

This project has received funding from the Euratom research and training programme 2019-2020 under grant agreement No 945022.

Again, given the inadequate data (only one measurement on the elastic constants of $(U,Pu)O_2$ above room temperature by Padel and de Novion [Pad69]), Martin was forced to assume that the temperature dependence of the corresponding elastic moduli relating respectively to stoichiometric mixed oxide and UO_2 are the same [Mar89].

The effect of local heterogeneities in the U/Pu composition ratio, which may occur when solid mixed-oxide bodies are manufactured by initially blending together UO_2 and PuO_2 powders, has been investigated by Nutt et al. [Nut70]. Decreases in the Young's modulus of ~10% and 25% were observed when heterogeneities occur in the solid on scales of ~50 μm and 200 μm respectively [Mar89].

New results might be obtained with molecular dynamic simulation: Balboa López indicates a small increase of the Young's modulus of about 5% between 0% and 100% of Pu [Bal18]. This variation of the Young's modulus is consistent with the above reported experimental results where an increase of 4% and 11% is observed for Pu content of 15% and 70% respectively. However, Young's modulus and Poisson ratio of the poly-crystal are not a direct result of the molecular dynamic simulation and are deduced from the computed single crystal elastic constants.

10.1.7 Effect of additives and fission products

Because UO_2 and $(U,Pu)O_2$ are used as fuel in nuclear reactors, the effect of irradiation on the elastic constants is of interest. The main effects are expected to arise from the introduction of fission products into the material. Gaseous fission products will largely precipitate into bubbles, which may be treated as additional voidage. The effects of the solid fission products have been simulated by doping the material with appropriate simulants [Mar89].

Several authors have reported on the influence of fission products/additives (to simulate burn-up or to study low fission gas release fuel and integrated burnable absorbers fuel) on the elastic properties.

Marlowe and Kaznoff [Mar69] found that the addition of 6% fission product simulants or 1% gadolinium oxide to UO_2 did not significantly alter the elastic moduli. Boocock et al. [Boo72] also reported that the addition of 6 wt.% of fission products, comprising transition metals and lanthanides, to a mixed oxide reduced both the Young's modulus and the shear modulus by less than 10%. Based on these results, Martin [Mar89] concluded that the effect of solid fission products on the elastic constants is not large.

Recently, in Japan a series of measurements was performed on $(U,Ce)O_2$ in order to understand the behavior of uranium dioxide fuel under irradiation in connection with the changes in the phase relations and in the thermodynamic and mechanical properties caused by accumulated fission products [Yam97] [Yam98] [Yam01] [Kur09]. On the other hand, the studies of the physico-chemical properties of $(U,Ce)O_2$ are considered to help to understand the properties of $(U,Pu)O_2$ in some degree, because of the similar chemical and/or thermodynamic behavior of cerium and plutonium.

This project has received funding from the Euratom research and training programme 2019-2020 under grant agreement No 945022.

Yamada et al. [Yam97] [Yam98] performed high-temperature X-ray diffraction analysis from room temperature to 1273 K and ultrasonic pulse-echo measurements up to 673 K on $(U,Ce)O_2$ pellets with CeO_2 contents ranging from 0 to 20 mol.% of CeO_2 to estimate the change in the lattice parameter and mechanical properties of $(U,Ce)O_2$ with the CeO_2 content. Although the lattice parameter decreased with CeO_2 content, the intrinsic (corrected for porosity) elastic moduli of $(U,Ce)O_2$ were found to decrease with increasing CeO_2 content at room temperature. The decrease was about 35-40% and 30-35% in the Young's and shear modulus, respectively, and about 25% in the Poisson's ratio with 20 mol.% CeO_2 content compared to UO_2.

The elastic moduli of all $(U,Ce)O_2$ were found to decrease with rising temperature [Yam98], as a result of the increase of the bond length accompanied by the thermal expansion. The changes in the Young's and shear moduli of $(U,Ce)O_2$ with temperature were smaller than the change of UO_2 (see Figure 10.4 and Figure 10.5). This was consistent with the result that the linear thermal expansion coefficient of $(U,Ce)O_2$ decreased with increasing CeO_2 content.

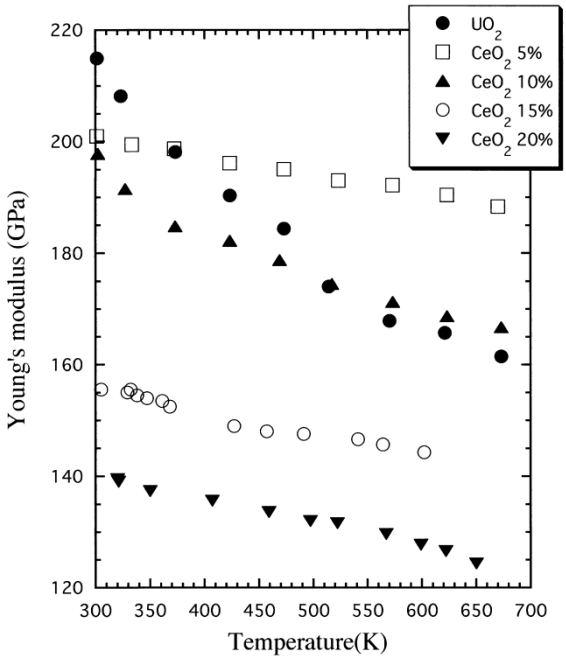

Figure 10.4: Change in the Young's modulus of fully dense $(U,Ce)O_2$ with temperature [Yam98].

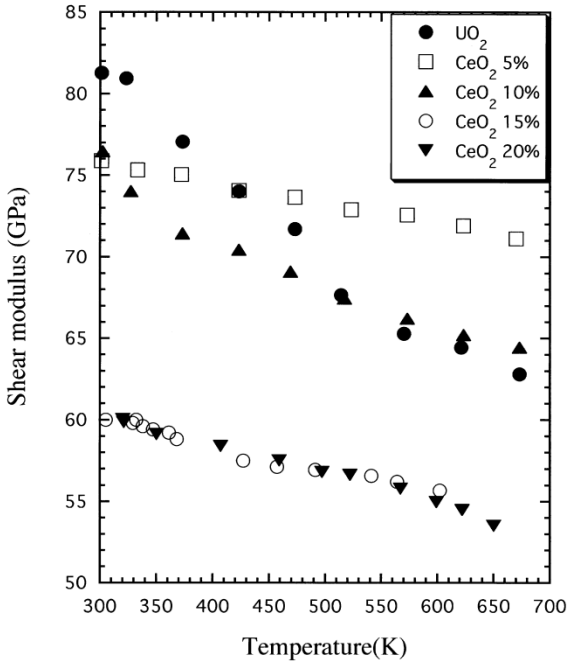

Figure 10.5: Change in the shear modulus of fully dense $(U,Ce)O_2$ with temperature [Yam98].

In order to evaluate the safety of high burn-up MOX fuel, Yamanaka et al. [Yam01] studied the mechanical properties of simulated 50 – 250 GWd/tM burn-up fuel: $(U_{0.8-x}Ce_{0.2}M_x)O_2$ [M: Nd ($0 \leq x \leq 0.13$) or Zr ($0 \leq x \leq 0.06$)]. The elastic moduli of $(U_{0.8-x}Ce_{0.2}M_x)O_2$ were found to decrease with increasing M content. The reduction rate in the elastic moduli of $(U_{0.8-x}Ce_{0.2}Zr_x)O_2$ is much greater than that of $(U_{0.8-x}Ce_{0.2}Nd_x)O_2$, which indicates that the dissolution of ZrO_2 to the fuel matrix have greater effect on the elastic moduli than the case of Nd_2O_3 dissolution.

Kurosaki et al. [Kur09] investigated the effect of Nd and Pr addition on the mechanical properties of $(U,Ce)O_2$ with the aim to assess the performance of high

This project has received funding from the Euratom research and training programme 2019-2020 under grant agreement No 945022.

burn-up low decontamination MOX fuel with large quantities of fission products and minor actinides. They also experienced decreasing Young's modulus for $(U_{0.65-x}Ce_{0.3}Pr_{0.05}Nd_x)O_2$ with increasing Nd content (x = 0.01 – 0.12, corresponding to 0 – 250 GWd/tM). However, they derived 21% higher Young's modulus value for $(U_{0.65-x}Ce_{0.3}Pr_{0.05})O_2$ from their indentation test results than that recommended by Martin [Mar89] for stoichiometric, fully dense UO_2, which does not seem to be in agreement with the previous findings.

Tanaka et al. [Tan12] prepared MOX fuels with Am and 26 different fission products, simulating low decontamination MOX fuel and high burn-up to 250 GWd/tM in order to examine the effect of both Am and a large amount of fission products addition on the thermophysical properties of MOX fuel. The elastic moduli of the fabricated pellets with a pore fraction of about 20% and O/M ratio of 2.00 were determined by an ultrasonic pulse-echo method at room temperature and corrected to 100% of the theoretical density by using the empirical relations between the moduli and density given by Nutt et al. [Nut70]. The elastic moduli of 3%Am-MOX fuel ($(U_{0.67}Pu_{0.3}Am_{0.03})O_2$) and the simulated low decontamination MOX fuel with 0 GWd/tM burn-up (MOX fuel containing 3 at.% Am and 1.5 at.% fission products) were almost the same values and about 5% lower than the recommended value for stoichiometric, fully dense UO_2 by Martin [Mar89]. The elastic moduli decreased slightly with increasing simulated burn-up: with about 10% and 20% at 150 and 250 GWd/tM, respectively, compared to the figures of the low decontamination MOX fuel with 0 GWd/tM burn-up. Because the measured elastic modulus values of the low decontamination MOX fuels simulating different burn-ups were the same level as literature data at the burn-up of about 60 GWd/tM [Boo72], Tanaka et al. concluded that the effect of addition of small amount (3 at.%) of Am on the elastic moduli of irradiated MOX fuel was almost negligible.

On the contrary, the results by Pujol et al. [Puj04] using synchrotron diffraction under high pressure and Knoop indentation on simulated UO_2 spent fuels have given a very different evolution of elastic moduli than those reported above; the elastic constants of the simulated fuels are increased with burn-up.

Yamanaka et al. [Yam09] performed a characterization work on erbium (slow burnable poison) doped UO_2 fuel pellets. The Young's modulus (determined by an ultrasonic pulse-echo method at room temperature in air) of $(U_{1-x}Er_x)O_2$ was found to decrease with the Er content ($0 \leq x \leq 0.1$), with about 10% for $(U_{0.9}Er_{0.1})O_2$ compared to UO_2. The same trend was reported for gadolinia-containing UO_2.

10.1.8 Effect of irradiation/burn-up

In-reactor measurements of Young's modulus as a function of neutron fluence [Bar76] have indicated that irradiation increases Young's modulus by about 2% at saturation. Since the effect is small and could be explained by in-reactor densification of the fuel, in [MAT01] no separate model for such burn-up related changes as fission product accumulation and fuel lattice damage was formulated.

Elastic moduli measurements executed on irradiated fuel were reported by the same expert group [Roq99] [Lau12] [Lau14] [Cap16] [Mar16] [Mar17]. During approximately twenty years of experimental campaigns, several measurements

This project has received funding from the Euratom research and training programme 2019-2020 under grant agreement No 945022.

have been performed on SIMFUEL (unirradiated chemical analogue of irradiated UO_2 fuel) samples, on commercial fuels (UO_2) irradiated in PWRs and on special irradiation discs (UO_2, UO_2 doped with Gd_2O_3, CeO_2, Cr_2O_3, kaolinite and MOX) irradiated in the Halden reactor, by high frequency acoustic microscopy and microindentation techniques.

Laux et al. [Lau12] [Lau14] measured the elastic constants of simulated spent fuel (SIMFUEL) and irradiated fuel (HBRP, N118 and MOX) samples by acoustic microscopy. From the measurement results (see Figure 10.6) they concluded that the global trend is a decrease of the elastic moduli by about 25% from 0 to 100 GWd/tM and then a stabilization beyond this limit when the solubility threshold is reached. Although only a few samples have been studied at low simulated burn-up, the elastic properties were considered to start decreasing from around 30 GWd/tM. The consistency of the data acquired on irradiated UO_2 samples and on SIMFUEL samples show that the amount of fission products in solution plays an important role in the evolution of the elastic properties and that irradiation defects have a smaller effect on the elastic properties. The broad scatter of the data is due to the influence of other parameters such as the average porosity volume, pore shape and pore size but also to the location of fission products, strongly related to the local temperature history. Some of the SIMFUEL samples contained 4, 7 or 11 additives for the same simulated burn-up, but no significant impact on the number of fission products on the elastic moduli was observed. Some of the HBRP samples (special UO_2 irradiation discs manufactured for the High Burn-up Rim Project) contained a small amount (3%) of Gd. The distinction between pure UO_2 samples and the Gd doped one was not made in Figure 10.6. But it can be noticed that a small decrease was observed for doped samples (around 10 GPa), which is in agreement with the literature.

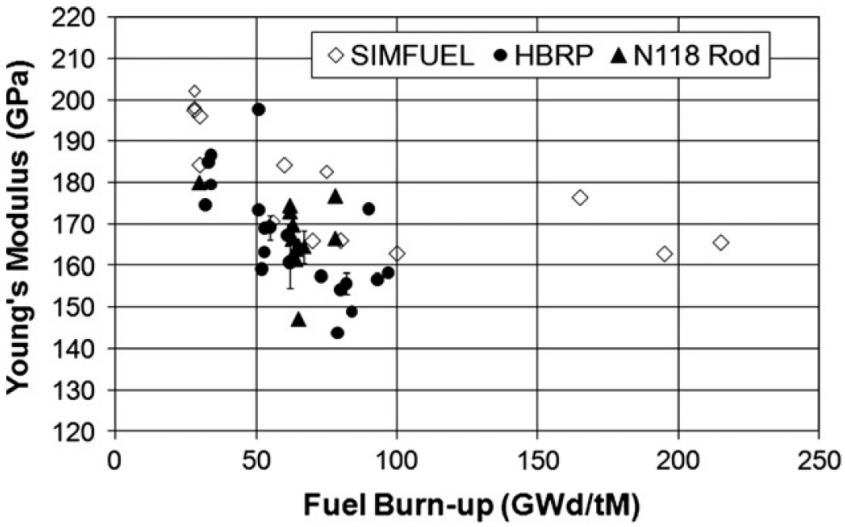

Figure 10.6: Young's modulus versus burn-up – Measurements conducted on irradiated fuel (HBRP and N118 Rod) samples and on simulated spent fuel (SIMFUEL) samples with acoustic microscopy [Lau12].

Recently, Marchetti et al. [Mar17] performed new acoustic microscopy measurements on irradiated fuel. Based on their new results and the analysis of data from the open literature they proposed an empirical relation describing the

This project has received funding from the Euratom research and training programme 2019-2020 under grant agreement No 945022.

variation of Young's modulus (GPa) with the burn-up (GWd/tM) in the burn-up range 0 – 100 GWd/tM as per Eq. 10.22.

$$E = -3.63 \cdot 10^{-10} \cdot burnup^{4.5} + 9.13 \cdot 10^{-6} \cdot burnup^{3} - 7.62 \cdot 10^{-2} \cdot burnup^{1.5} + 214 \quad \text{Eq. 10.22}$$

Before fitting, Marchetti et al. corrected the Young's modulus data for gadolinium- or cerium-doped UO_2 samples for the gadolinium or cerium content in solid solution using Eq. 10.23 and Eq. 10.24.

$$E((U,Gd)O_2) = E(UO_2) - 3.3(\%\,Gd) \quad \text{Eq. 10.23}$$

$$E((U,Ce)O_2) = E(UO_2) - 2.88(mol\%\,Ce) - 0.074(mol\%\,Ce)^2 \quad \text{Eq. 10.24}$$

The graph in Figure 10.7 illustrates the fitting of Eq. 10.22 to the data, the 95% confidence level and its corresponding prediction band. The experimental results from special irradiation and commercial PWR nuclear fuels show an overall Young's modulus reduction of ~33% in the burn-up range 0 – 100 GWd/tM. The data estimated in the low burn-up range indicates that variations in Young's modulus values due to the initial densification do not exceed ~20 GPa. The Young's modulus values determined in the different measurement campaigns are fairly scattered especially in the burn-up range 60 – 95 GWd/tM. Marchetti et al. could not establish unequivocal links between irradiation conditions such as temperature and the presence of high burn-up structure and the datapoints falling at or outside the limits of the prediction band. They concluded that the data scattering most likely related to the heterogeneity in terms of microstructure, chemical composition, measured samples conditions and irradiation history of the samples investigated. They also concluded that the validity of the relations found in the very low burn-up range and beyond 100 GWd/tM is still uncertain.

This project has received funding from the Euratom research and training programme 2019-2020 under grant agreement No 945022.

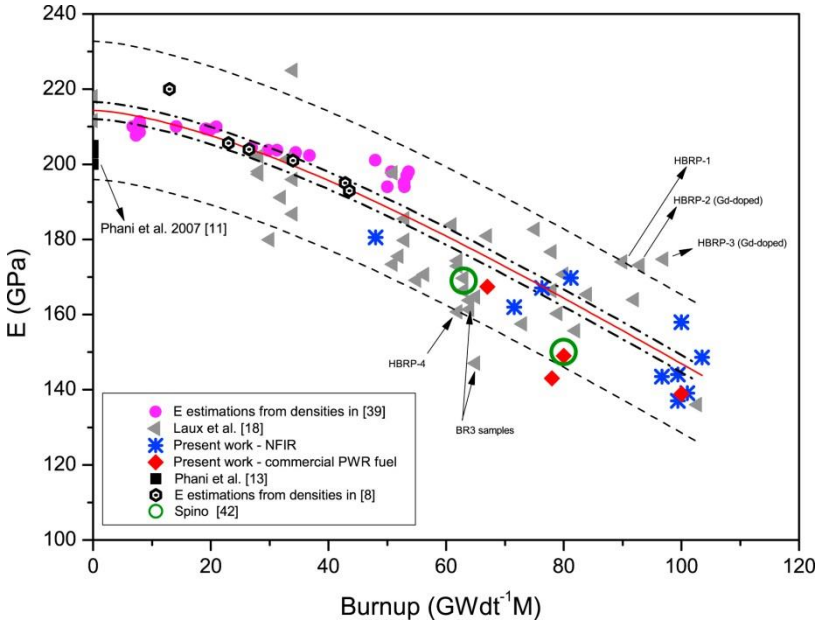

Figure 10.7: Young's modulus of the investigated samples as a function of burn-up [Mar17].

The full circles correspond to the Young's modulus estimated by Marchetti et al from the density reported in [Har98] for the standard grain UO_2.

The triangles represent the results by Laux et al. [Lau14]: HBRP samples (special irradiation discs of UO_2, $(U,Ce)O_2$ and $(U,Gd)O_2$ manufactured for the High Burn-up Rim Project and irradiated in the Halden reactor), N118 samples (commercial UO_2 fuel irradiated in the Belgian Reactor 3 (BR-3) core), and a MOX sample with a burn-up of 102.7 GWd/tM irradiated in the Halden reactor.

The asterisks and the rhombi refer to data measured by Marchetti et al. on NFIR samples (special irradiation discs of UO_2 and UO_2 doped with Gd_2O_3, Cr_2O_3, kaolinite belonging to the Nuclear Fuel Industry Research program and irradiated in the Halden reactor) and on UO_2 samples from commercial PWR fuel, respectively.

The black squares are relative to the Young's moduli of unirradiated UO_2 samples determined by Phani et al. [Pha07].

The empty small circles correspond to the estimations from densities published in [Ass77] for the standard UO_2 fuel by Marchetti et al.

The empty large circles are the Knoop indentation results obtained by Spino in [Spi05].

The dot-dashed lines represent 95% of confidence level, whilst the external dashed lines indicate 95% prediction band.

It has to be noted that Young's modulus values for simulated fuels determined by Pujol et al. [Puj04] from Knoop indentation tests do not agree with data from acoustic microscopy [Lau12] [Lau14] [Cap16] [Mar16] [Mar17]. The results of a new Knoop indentation campaign performed on irradiated fuel samples by Spino [Spi05] however fit perfectly with data from acoustic microscopy (see Figure 10.7). Although the new results from Knoop indentation tests alleviated the problem of discrepancies in the elastic moduli measured on irradiated fuels, differences observed in simulated fuel remained.

10.1.9 Effect of long-term storage on unirradiated fuel

In the framework of ESNII+ Project, the Young's modulus of un-irradiated stoichiometric samples was determined at room temperature by high frequency acoustic microscopy:

This project has received funding from the Euratom research and training programme 2019-2020 under grant agreement No 945022.

- PHENIX MOX fuel (containing 23.5% Pu) both after storage (i.e. having accumulated alpha self-irradiation point defects after approx. 17 years of storage) and after annealing at 1500 K [Sta17a].
- TRABANT MOX fuel (containing 45% Pu) as stored (i.e. having accumulated alpha self-irradiation point defects) [Sta17b].

No porosity correction was applied.For PHENIX fuel samples, the Young's modulus for the sample damaged by alpha self-irradiation is about 5% lower (195.2 ± 1.5 GPa) than for the annealed sample (204.6 ± 1.9 GPa). The results obtained for the PHENIX fuel are in reasonably good agreement with the recommendations of Martin [Mar89] and MATPRO [MAT01] by taking into account the 5% porosity and the ~20% PuO_2 content of the sample (194 and 200 GPa, respectively, see Table 10.1).

The value obtained for the TRABANT fuel damaged by alpha self-irradiation (190 ± 8 GPa) is ~3% lower than the value measured for the non-annealed PHENIX fuel. Applying the recommendations of Martin [Mar89] with 7% porosity [Sta17b], a young's modulus value equal to 183 GPa is calculated which is included within the uncertainty of the measured value. In MATPRO [MAT01], a 3% increase in Young's modulus due to an addition of 20% PuO_2 to UO_2 is recommended, which leads to a value of 187 GPa very close to the experimental value (190.0 ± 8 GPa). Nevertheless, no recommendation exists for a 45% Pu content. Therefore, considering the experimental uncertainty, the measured value is in good agreement with the recommendations of Martin [Mar89] and MATPRO [MAT01].

10.2 NEA recommendation

The recommended laws in [NEA25] for elastic constants are given in Eq. 10.25 to Eq. 10.28 for Young's modulus, Shear modulus, Bulk modulus and Poisson's ratio.

$$E(Pu,p,x,T) = [217.99 \cdot (1-Pu) + 249.54 \cdot Pu] \cdot \left[\frac{(1-p)^2}{1+1.124330 \cdot p}\right] \cdot [1.0 - 2.72739 \cdot x + 13.84392 \cdot x^2] \cdot [1.012527 - 2.282\ 10^{-5} \cdot T - 6.312\ 10^{-8} \cdot T^2] \quad \text{Eq. 10.25}$$

$$G(Pu,p,x,T) = [82.52 \cdot (1-Pu) + 94.91 \cdot Pu] \cdot \left[\frac{(1-p)^2}{1+0.95275 \cdot p}\right] \cdot [1.0 - 2.88078 \cdot x + 15.49419 \cdot x^2] \cdot [1.009549 - 1.182\ 10^{-5} \cdot T - 6.671\ 10^{-8} \cdot T^2] \quad \text{Eq. 10.26}$$

$$B(Pu,p,x,T) = [203.66 \cdot (1-Pu) + 225.63 \cdot Pu] \cdot \left[\frac{(1-p)^2}{1+3.43192 \cdot p}\right] \cdot [1.0 - 1.57715 \cdot x + 1.48101 \cdot x^2] \cdot [1.036438 - 1.099\ 10^{-4} \cdot T - 3.851\ 10^{-8} \cdot T^2] \quad \text{Eq. 10.27}$$

$$\nu(Pu,p,x,T) = [0.32051 \cdot (1-Pu) + 0.31882 \cdot Pu] \cdot [1 - 1.03223 \cdot p] \cdot [1.0 + 0.69962 \cdot x - 7.52905 \cdot x^2] \cdot [1.017906 - 6.420\ 10^{-5} \cdot T + 1.506\ 10^{-8} \cdot T^2] \quad \text{Eq. 10.28}$$

Where: Pu is Pu/(Pu+U) weight fraction, p is porosity fractional volume, x is the deviation from stoichiometry (2.00 – O/M ratio) and T is the temperature (in K).

The presence of pores induces a degradation of the mechanical properties of MOX fuel.

Du to the lack of experimental data on the effect of minor actinides on the elastic properties of MOX in the open literature, no recommendation can be done.

This project has received funding from the Euratom research and training programme 2019-2020 under grant agreement No 945022.

Local quantities such as temperature, porosity, plutonium and minor actinides concentration, and O/M ratio change under irradiation with an effect on the elastic properties of MOX fuel. The determination of these quantities allows considering the effect of burn-up.

The range of parameters for the validity of the recommendation is:

- Temperature from 300 to 2930 K (or up to melting if melting occurs at T < 2930 K)
- O/M from 2.00 to 1.90
- Pu content from 0 to 100%
- Porosity from 0 to 20%

It can be assumed that uncertainties at low temperature are between 6% and 8% increasing to about 15% at high temperature.

10.3 Conclusions and recommendations

Based on the elastic moduli measurements performed on oxide fuels since the review work by Martin [Mar89], the Young's modulus of an oxide fuel can be expressed as per Eq. 10.29.

$$E = E_0.f(T).g(p).h(x).i(Pu).j(dop).k(BU) \qquad \text{Eq. 10.29}$$

Where :

E_0 (GPa) Young's modulus of the non-irradiated, fully dense, stoichiometric UO_2 fuel at room temperature,
T (K) temperature,
p (-) fractional porosity,
x (-) deviation from stoichiometry,
Pu (-) Pu content,
dop (-) dopant content,
BU (GWd/tM) burn-up.

Since the review work by Martin, no experimental work was dedicated to investigate the temperature dependence of elastic properties of oxide fuels, thus Eq. 10.4 to Eq. 10.9 recommended by Martin can be used to calculate the elastic moduli of an oxide fuel as a function of temperature. Because of technical problems, the ultrasonic velocity technique has only been used at around room temperature; also the resonant frequency method is unsuitable at temperatures above ~1773 K because of the monotonic increase in the damping of the excited wave with temperature [Mar89]. The only results above ~1773 K (and up to 2929 K) [Cla85] have been obtained from neutron inelastic scattering measurements on single crystals, with the use of the derived phonon dispersion relationships at low wavevectors to evaluate elastic moduli. Also only one measurement exists on the elastic constants of $(U,Pu)O_2$ above room temperature [Pad69].

The effect of porosity on the elastic properties of nuclear fuel materials was thoroughly investigated in the last twenty years, and the obtained dependences, both on irradiated and non-irradiated fuel, agreed well with Martin's

This project has received funding from the Euratom research and training programme 2019-2020 under grant agreement No 945022.

recommendations. Eq. 10.16-Eq. 10.17 and Eq. 10.18-Eq. 10.19, published in [Gat05] and in [Lau12] respectively, can be recommended to calculate the elastic moduli dependence on the fractional porosity.

The agreement between the three sets of available data [Nov70] [Pad69] [Nut70] relating to the Young's modulus as a function of O/M ratio is poor. Therefore, Martin [Mar89] considered only the selfconsistent and most comprehensive data due to de Novion et al. [Nov70] to formulate his recommendation. Moreover, the data available to describe the effect of variations in the O/M ratio on Young's modulus are difficult to interpret because it is possible that the fabrication history of the fuel is more significant than the O/M ratio in determining the Young's modulus [Mar89] [MAT01]. The only recent study by Laux et al. [Lau12] cover a very limited range of stoichiometry from 2 to 2.015, so the influence of stoichiometry on the elastic constants is still not well quantified.

The addition of PuO_2 to UO_2 causes a moderate (at ~25 at.% Pu content about 5%) or even negligible increase in Young's modulus. However as in case of the effect of non-stoichiometry, the effect of PuO_2 addition is based on limited data and is therefore uncertain. More experimental measurements especially for higher Pu content (up to 45 at.% Pu) are needed in order to validate or to correct the current recommendations.

As reported in [Mar17], a 10 wt% Gd_2O_3 content decreases the Young's modulus of oxide fuel by ~15% as compared to UO_2. Marchetti et al. [Mar17] also pointed out that the effect of fuel additives on Young's modulus at different burn-up needs further systematic investigation, as the corrections for dopant content are mainly based on measurements performed on unirradiated uranium dioxide samples.

To calculate the variation of Young's modulus with the burn-up, the empirical relation determined by Marchetti et al. [Mar17] can be used in the burn-up range 0–100 GWd/tM. Because the validity of Eq. 10.22 is still uncertain in the very low burn-up range and beyond 100 GWd/tM, here more experimental measurements are needed in order to validate or to correct the present relation.

10.4 References

[Ass77] H. Assmann and R. Manzel, The matrix swelling rate of UO_2, J. Nucl. Mater. **68** (1977) 360.

[Bal18] H.E. Balboa López, Simulation of thermos-mechanical properties of $(U,Pu)O_2$ nuclear fuel under irradiation using atomistic simulations, PhD thesis, 2018

[Bar76] V. M. Baranov, Yu. K. Bibilashvili, I. S. Golovnin, V. N. Kakurin, T. S. Men'shikova, Yu. V. Miloserdin and A. V. Rimashevskii, In-reactor measurements of the modulus of elasticity of uranium dioxide, Sov. Atom. Energ. **40** (1976) 37.

[Ber80a] J. G. Berryman, Long-wavelength propagation in composite elastic media I. Spherical inclusions, J. Acoust. Soc. Am. **68** (1980) 1809.

This project has received funding from the Euratom research and training programme 2019-2020 under grant agreement No 945022.

[Ber80b] J. G. Berryman, Long-wavelength propagation in composite elastic media II. Ellipsoidal inclusions, J. Acoust. Soc. Am. **68** (1980) 1820.

[Boo72] J. Boocock, A. S. Furzer and J. R. Matthews, The Effect of Porosity on the Elastic Moduli of UO_2 as Measured by an Ultrasonic Technique, AERE-M 2565, September 1972.

[Cap16] F. Cappia, D. Pizzocri, M. Marchetti, A. Schubert, P. Van Uffelen, L. Luzzi, D. Papaioannou, R. Macián-Juan and V. V. Rondinella, Microhardness and Young's modulus of high burn-up UO_2 fuel, J. Nucl. Mater. **479** (2016) 447.

[Cla85] K. Clausen, W. Hayes, M. T. Hutchings, J. K. Kjems, J. E. MacDonald and R. Osborn, High Temp. Sci. **19** (1985) 189.

[Gat05] J.-M. Gatt, Y. Monerie, D. Laux and D. Baron, Elastic behavior of porous ceramics: application to nuclear fuel materials, J. Nucl. Mater. **336** (2005) 145.

[Har98] Y. Harada and S. Doi, Irradiation Behavior of Large Grain UO_2 Fuel Rod by Active Powder, J. Nucl. Sci. Technol. **35** (1998) 411.

[Iga73] N. Igata and K. Domoto, Fracture Stress and Elastic Modulus of Uranium Dioxide Including Excess Oxygen, J. Nucl. Mater. **45** (1972/73) 317.

[Kur09] K. Kurosaki, K. Tanaka, M. Osaka, H. Muta, M. Uno and S. Yamanaka, Effect of Nd and Pr addition on the thermal and mechanical properties of (U, Ce)O_2, J. Nucl. Mater. **389** (2009) 85.

[Lau02] D. Laux, B. Cros, G. Despaux and D. Baron, Ultrasonic study of UO_2: effects of porosity and grain size on ultrasonic attenuation and velocities, J. Nucl. Mater. **300** (2002) 192.

[Lau12] D. Laux, D. Baron, G. Despaux, A. I. Kellerbauer and M. Kinoshita, Determination of high burn-up nuclear fuel elastic properties with acoustic microscopy, J. Nucl. Mater. **420** (2012) 94.

[Lau14] D. Laux, W. de Weerd, D. Papaioannou, S. Kitajima, V. V. Rondinella and G. Despaux, Scanning acoustic microscope for mechanical characterization and density estimation of irradiated nuclear fuel, Progr. Nucl. Energ. **72** (2014) 63.

[Mar69] M. O. Marlowe and A. I. Kaznoff, Elastic Behavior of Uranium Dioxide, In Proceedings of the International Symposium on Nuclear Fuels. Ceramic Nuclear Fuels Eds. O. L. Kruger, A. I. Kaznoff, pp. 90-99, American Ceramic Society, Columbus, Ohio (1969).

[Mar89] D. G. Martin, The elastic constants of polycrystalline UO_2 and (U, Pu) mixed oxides: a review and recommendations, High Temperatures – High Pressures **21** (1989) 13.

[Mar16] M. Marchetti, D. Laux, F. Cappia, M. Laurie, P. Van Uffelen, V. V. Rondinella, T. Wiss and G. Despaux, High Frequency Acoustic Microscopy for the Determination of Porosity and Young's Modulus in High Burnup Uranium Dioxide Nuclear Fuel, IEEE T. Nucl. Sci. **63** (2016) 1520.

This project has received funding from the Euratom research and training programme 2019-2020 under grant agreement No 945022.

[Mar17] M. Marchetti, D. Laux, L. Fongaro, T. Wiss, P. Van Uffelen, G. Despaux and V. V. Rondinella, Physical and mechanical characterization of irradiated uranium dioxide with a broad burnup range and different dopants using acoustic microscopy, J. Nucl. Mater. **494** (2017) 322.

[MAT01] L. J. Siefken, E. W. Coryell, E. A. Harvego, J. K. Hohorst, SCDAP/RELAP5/MOD 3.3 Code Manual, MATPRO - A Library of Materials Properties for Light-Water-Reactor Accident Analysis, U.S. Nuclear Regulatory Commission Report NUREG/CR-6150 Vol. 4 (INEL-96/0422), Rev. 2, January 2001.

[Mat74] J. R. Matthews, Mechanical Properties and Diffusion Data for Carbide and Oxide Fuels, Ceramics Data Manual Contribution, AERE-M2643, 1974.

[NEA25] N. Chauvin et al., Recommendations on Fuel Properties for Fuel Performance Codes, NEA/NSC/R(2024)1, July 2025

[Nov70] C. H. de Novion, B. Amice, A. Groff, Y. Guerin and A. Padel, Mechanical Properties of Uranium Plutonium Based Ceramics, Nucl. Metall. **17** (1970) 509.

[Nut70] A. W. Nutt Jr., A. W. Allen and J. H. Handwerk, Elastic and Anelastic Response of Polycrystalline UO_2-PuO_2, J. Am. Ceram. Soc. **53** (1970) 205.

[Pad69] A. Padel and Ch. de Novion, Constantes élastiques des carbures, nitrures et oxydes d'uranium et de plutonium, J. Nucl. Mater. **33** (1969) 40.

[Pha07] K. K. Phani, D. Sanyal and A. K. Sengupta, Estimation of elastic properties of nuclear fuel material using longitudinal ultrasonic velocity – A new approach, J. Nucl. Mater. **366** (2007) 129.

[Puj04] M. C. Pujol, M. Idiri, L. Havela, S. Heathman and J. Spino, Bulk and Young's modulus of doped UO_2 by synchrotron diffraction under high pressure and Knoop indentation, J. Nucl. Mater. **324** (2004) 189.

[Roq00] V. Roque, B. Cros, D. Baron and P. Dehaudt, Effects of the porosity in uranium dioxide on microacoustic and elastic properties, J. Nucl. Mater. **277** (2000) 211.

[Roq99] V. Roque, D. Baron, J. Bourgoin and J. M. Saurel, Study by acoustic microscopy of irradiated and non-irradiated uranium dioxide, J. Nucl. Mater. **275** (1999) 305.

[Spi05] J. Spino, Determination of the Young's Modulus of Irradiated Fuels by Knoop Indentation, European Commission, Joint Research Centre, Institute for Transuranium Elements, 2005. Annual Activity Report.

[Sta17a] D. Staicu, E. Dahms, D. Manara, J.-Y. Colle, O. Benes, M. Marchetti, D. Robba, N. Chauvin, P. M. Martin, Measurement of properties of fresh PHENIX fuel, European Commission, ESNII+ Project, Deliverable D.7.4.1 (2017).

[Sta17b] D. Staicu, E. Dahms, D. Manara, M. Marchetti, D. Robba, T. Wiss, B. Cremer, O. Dieste-Blanco, N. Chauvin, Ph. M. Martin, Characterisation and measurement of properties of fresh TRABANT fuel, European Commission, ESNII+ Project, Deliverable D.7.3.4 (2017).

This project has received funding from the Euratom research and training programme 2019-2020 under grant agreement No 945022.

[Tan12] K. Tanaka, M. Osaka, S. Miwa, T. Hirosawa, K. Kurosaki, H. Muta, M. Uno and S. Yamanaka, Preparation and characterization of the simulated burnup americium-containing uranium–plutonium mixed oxide fuel, J. Nucl. Mater. 420 (2012) 207.

[Yam01] S. Yamanaka, S. Yoshida, K. Kurosaki, M. Uno, K. Yamamoto, T. Namekawa, Mechanical properties of (U, Ce)O_2 with and without Nd or Zr, J. Alloy. Comp. **327** (2001) 281.

[Yam09] S. Yamanaka, K. Kurosaki, M. Katayama, J. Adachi, M. Uno, T. Kuroishi, M. Yamasaki, Thermal and mechanical properties of (U, Er)O_2, J. Nucl. Mater. **389** (2009) 115.

[Yam97] K. Yamada, S. Yamanaka, T. Nakagawa, M. Uno, M. Katsura, Study of the thermodynamic properties of (U, Ce)O_2, J. Nucl. Mater. **247** (1997) 289.

[Yam98] K. Yamada, S. Yamanaka, M. Katsura, Physico-chemical properties of (U, Ce)O_2, J. Alloy. Comp. **275–277** (1998) 725.

[Wac65] J. B. Wachtman Jr., M. L. Wheat, H. J. Anderson, J. L. Bates, Elastic constants of single crystal UO_2 at 25 °C, J. Nucl. Mater. **16** (1965) 39.

This project has received funding from the Euratom research and training programme 2019-2020 under grant agreement No 945022.

11. Brittle-to-ductile transition temperature

This chapter was originally provided by G. Trillon (Framatome).

11.1 Literature data

In the publications reviewed, the brittle-to-ductile transition for nuclear ceramic is defined, for a given strain rate, as the temperature where yield stress and ultimate stress are not the same anymore. Below this temperature, the fuel displays a brittle mechanical behavior. Above, plasticity occurs.

In case of UO_2, it has been determined [Led92] that two transitions occurred as temperature increases (Figure 11.1).

- A low temperature transition at T_C :
  - Below T_C fuel behavior is brittle.
  - Above T_C fuel behavior is pseudo-brittle, with some plastic features.
- A high temperature transition at T_t above which the fuel is fully plastic.

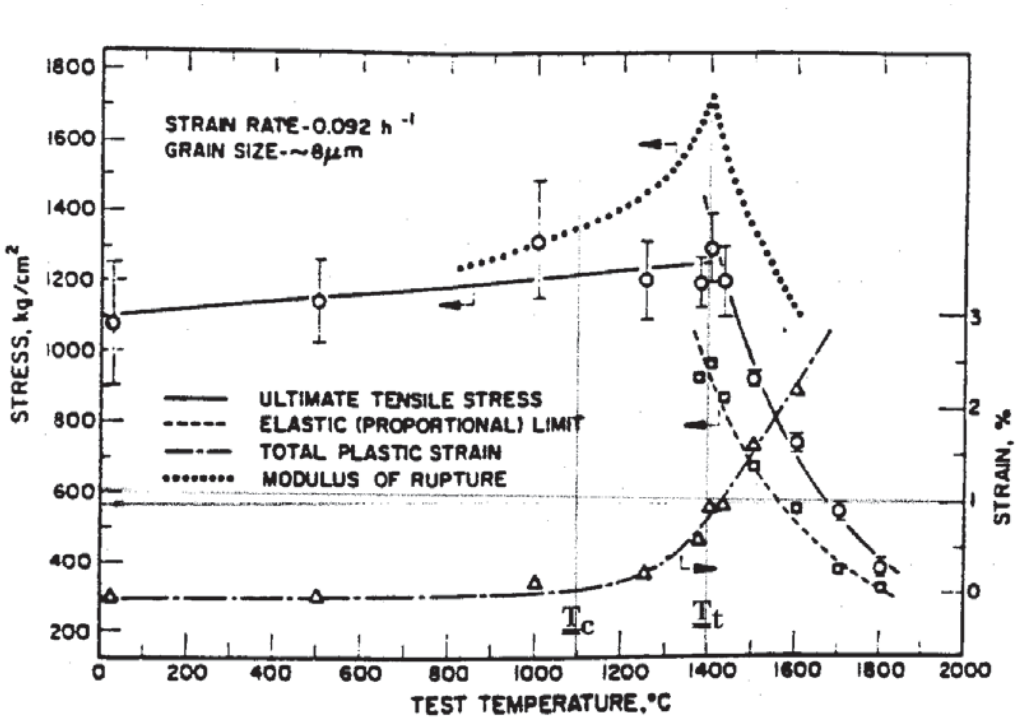

Figure 11.1: UO_2 typical plastic strain test versus temperature as per [Can71]

The reference method for investigating the brittle-to-ductile transition is bending tests. However some data has also been found about uniaxial compressive testing.

This project has received funding from the Euratom research and training programme 2019-2020 under grant agreement No 945022.

11.1.1 Compressive load

Under compressive load, [Pet77] has found out that pre-cracked PuO_2 pellets – supposedly stoichiometric with grain size ≈ 13 µm and ≈ 92% of Theoretical Density (T.D.) – exhibit brittle behavior up to 1400°C under relatively modest strain rate (≈ 10^{-3} s^{-1}). Because of the presence of inner cracks before testing, this result is highly doubtful. For instance, crack-free PuO_2 pellets (grain size ≈ 15 µm, O/M = 1.88 and ≈ 87% T.D.) have demonstrated a plastic behavior above 1000°C. This latter result is consistent with [Sto94] experiment of compressive load of pure UO_2 (strain rate of $2.5 \cdot 10^{-4}$ s^{-1}), where transgranular (=brittle) fracture is observed below 1100°C and largely intergranular (=ductile) cracks above 1200°C.

11.1.2 Four-point bending

Using a four-point bend test, [Rob71] has investigated the brittle-to-ductile transition temperature of a 20 wt% PuO_2 MOX fuel. Characteristics of fuels samples investigated are reported in Table 11.1.

Table 11.1: Four-point bend test measurements [Rob71] – Samples characteristics.

Sample		1	2	3	4	5	6	7
PuO_2 content (%wt.)		20±0.2						
Blending		Mechanical co-blending (ball milling)						
Sintering	Duration	2 h 15 min	3 h	4 h				
	T (°C)	1625	1700	1575		1625	1575	
	Atmosphere	He-6%H_2						
Porosity (%T.D.)		3.4±0.5	4.0±0.5	4.3±0.2	7.3±0.9	8.8±0.6	10.5±0.8	12.0±1.0
O/M		1.970±0.005						
Grain size (µm)		2.5 ± 0.5				0.7 ± 0.5		
Sample dimensions (cm)		4.6 x 0.6 x 0.3						

Results show that $T_C \approx T_t$ (no pseudo-brittle domain) and that this single transition lays around half the melting temperature, for low strain rate: 1445-1460°C at $2.4 \cdot 10^{-5}$ s^{-1} for a 96%T.D. sample. As a matter of comparison, the first transition T_C in a 97%T.D. UO_2 sample has been measured to be of 1100°C (at $2.6 \cdot 10^{-5}$ s^{-1}), and the second one T_t of 1400°C. However, the MOX and UO_2 samples were quite different in terms of microstructure (for instance grains sizes of 2.5 µm for MOX and 8 µm for UO_2).

This project has received funding from the Euratom research and training programme 2019-2020 under grant agreement No 945022.

The transition temperature measurements were demonstrating sensitivity to both strain rate and sample porosity: the brittle-to-ductile transition temperature increases with increasing strain rate and decreases with increasing porosity [Rob71], [Rob73]. This behaviour is consistent with UO_2 [Led92].

11.2 Conclusions and recommendations

The reference test for brittle-to-ductile transition temperature $T_c(°C)$ determination being the four-point bending test, we propose to keep the recommendations from [Rob71] for 20 wt.% PuO_2 MOX fuel, which are:

- As a function of $\dot{\varepsilon}$ the strain rate (h^{-1}) : $T_c(°C) = \frac{5.510^4}{28.6 - \ln \dot{\varepsilon}} - 273$
  for $0.085 \leq \dot{\varepsilon} \leq 0.73$, and for high density fuels (96-97% T.D.).
- As a function of the porosity volume fraction P : $T_c(°C) = 1487 - 1588P$
  for $0.03 \leq P \leq 0.12$ at a strain rate of 0.085 h^{-1}.

11.3 References

[ASTM] Standard test method for flexural strength of advanced ceramics at ambient temperature. ASTM C 1161-90, 1991.

[Can71] R.F. Canon et al., J. Am. Cer. Soc. 54 (1971) 105.

[Led92] A. Ledac, Private communication (1992)

[Pet77] J.J. Petrovic, S.S. Hecker, C.C. Land and D.L. Rohr, Mechanical properties of $^{238}PuO2$, Los Alamos National Laboratory report LA-6529 (April 1977).

[Rob71] J.T.A. Roberts and B.J. Wrona, Nature of brittle-to-ductile transition in UO2 – 20 wt% PuO_2 nuclear fuel, J. Nucl. Mater. 41 (1971) 23.

[Rob73] J.T.A. Roberts, Brittle fracture of oxide nuclear fuel, J. Nucl. Mater. 47 (1973) 125.

[Sto94] M.G. Stout, R.W. Ellis, and R.A. Pereyra., Mechanical behavior of $^{238}UO_2$, $^{238}PuO_2$ and $^{239}PuO_2$ as a function of strain rate and temperature, Los Alamos National Laboratory report LA-12811-MS (August 1994).

This project has received funding from the Euratom research and training programme 2019-2020 under grant agreement No 945022.

12. Yield stress

This chapter was originally provided by G. Trillon (Framatome).

12.1 Literature data

Yield stress is the limit over which strain relationship with stress is not linear anymore (Cf Figure 12.1). In other words, yield stress defines the boundary in between elastic, reversible strain, and plastic, irreversible deformation. At temperatures well below the brittle-to-ductile transition, yield stress in ceramic such as a nuclear fuel pellet is equivalent to the ultimate stress. Thus, we are going to look only for yield stress data when plasticity may occur in the fuel, whether due to sufficient high temperature, sufficient low strain rate or a combination of both. For brittle behavior information, where yield stress and ultimate stress are the same, data reported in chapter 13 should be considered.

Elastic moduli of fuel do not seem to be significantly affected by PuO_2 content [Mar90]. Thus MOX fuel behavior under compressive and tensile stress should remain similar to UO_2 in the elastic domain. Consistently, the yield stress of MOX fuel is expected to be close to UO_2.

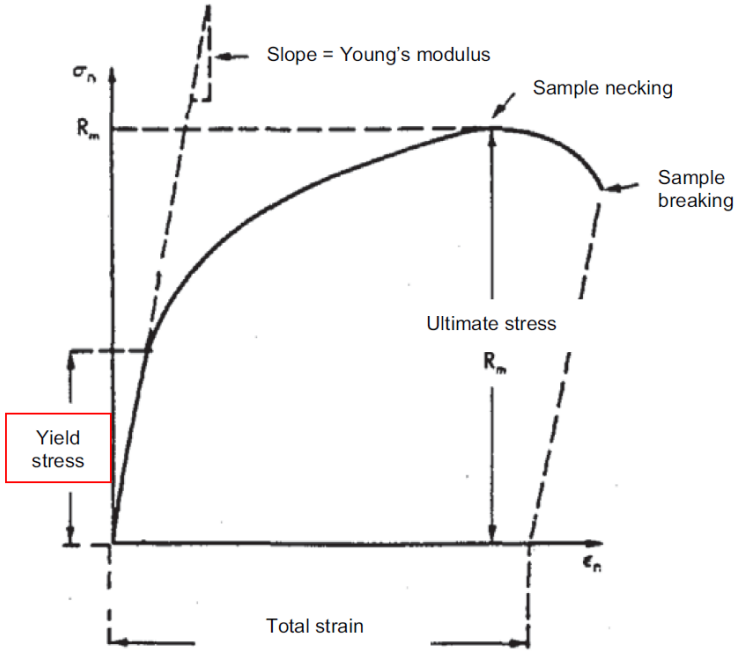

Figure 12.1: Example of a nominal stress versus strain tensile test [Led92] – Definition of yield stress.

12.1.1 Uniaxial compressive yield stress

While no compressive (neither tensile) loading curves have been found in the literature for MOX fuel, such data exist for pure UO_2 and PuO_2 pellets ([Pet77] & [Sto94]). In these studies, the yield stress under compressive loads of both

This project has received funding from the Euratom research and training programme 2019-2020 under grant agreement No 945022.

materials has been found to be very similar below 1200°C at a strain rate of 10^{-3} s^{-1} (Figure 12.2).

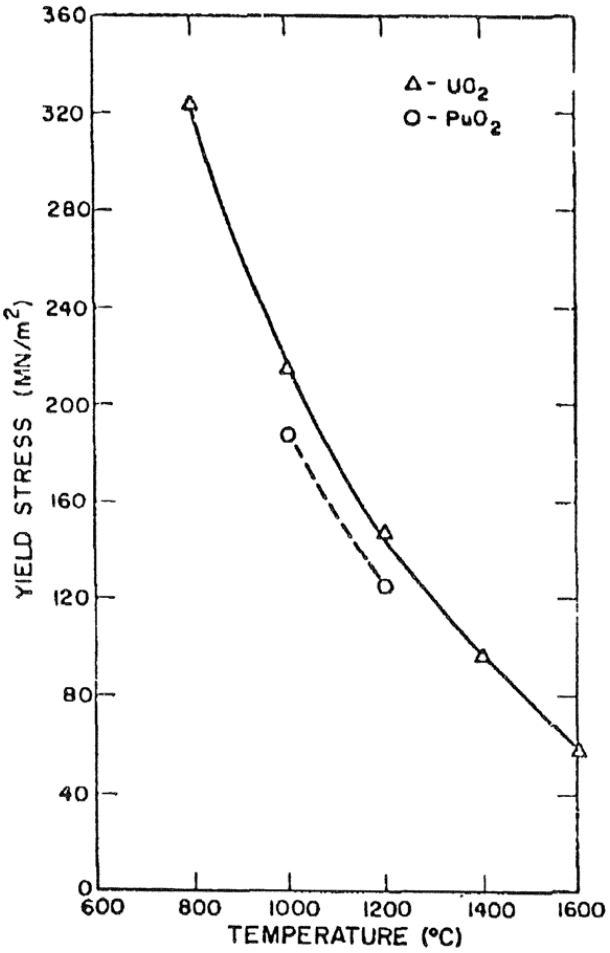

Figure 12.2: UO_2 and $^{239}PuO_2$ compressive yield stress values versus temperature ([Pet77]).

Effect of temperature

The temperature sensitivity of compressive yield stress appears to be similar for both pure UO_2 and pure PuO_2 (crack-free pellets, [Pet77]), at least below 1200°C. Therefore, it should also be the same for MOX fuel, i.e. a decrease versus temperature.

12.1.2 Flexural yield stress

The yield stress of 20%wt. PuO_2 MOX fuel has been determined by Roberts & Wrona [Rob71] using a four-point bend apparatus. Samples characteristics are reported in Table 12.1.

This project has received funding from the Euratom research and training programme 2019-2020 under grant agreement No 945022.

Table 12.1: Four-point bend test measurements [Rob71] – Samples characteristics.

Sample		1	2	3	4	5	6	7
PuO_2 content (%wt.)		20±0.2						
Blending		Mechanical co-blending (ball milling)						
Sintering	Duration	2 h 15 min	3 h	4 h				
	T (°C)	1625	1700	1575		1625	1575	
	Atmosphere	He-6%H_2						
Porosity (%T.D.)		3.4±0.5	4.0±0.5	4.3±0.2	7.3±0.9	8.8±0.6	10.5±0.8	12.0±1.0
O/M		1.970±0.005						
Grain size (µm)		2.5 ± 0.5				0.7 ± 0.5		
Sample dimensions (cm)		4.6 x 0.6 x 0.3						

Samples average grain sizes are low (0.65 to 2.5 µm) leading to a specific microstructure named "ultra-fine" grain structure. Instability of such microstructure under thermal treatment (and therefore potentially during test routines) is reported by [Rob71].

Effects of temperature, strain rate and initial porosity were benchmarked by [Rob71].

Effect of temperature and strain rate

As per Figure 12.3 and Figure 12.4, above the brittle to ductile transition T_c , the yield stress σ_y decrease with increasing temperature and increase with increasing strain rate.

[Rob71] has proposed a relationship in between the plastic strain rate $\dot{\varepsilon}$ (0.15 to 0.73 h^{-1}), the yield stress σ_y and the temperature as given by Eq. 12.1:

$$\dot{\varepsilon} = A\sigma_y^n e^{-\frac{\Delta H}{RT}} \qquad \text{Eq. 12.1}$$

With:

A a structure-sensitive constant

$n = 2$ the stress exponent, characteristic of the deformation mechanism

$\Delta H = 121.5$ (kcal/mole) the activation enthalpy

R the gas constant

T the temperature (in K) with 1600 ≤ T ≤ 2000

This project has received funding from the Euratom research and training programme 2019-2020 under grant agreement No 945022.

[Rob71] explains the plastic behavior under low stress of the MOX samples by a grain-sliding mechanism, here enhanced by the ultra-fine grain structure. The values obtained for n and ΔH are typical of such a mechanism. For instance, standard UO_2 at 8 µm gain size measured under the same conditions gives values typical of large grains ceramics deformation behavior ($n = 4.23$ and $\Delta H = 82$). However, results from [Boh70] on a large grain 20 wt% PuO_2 MOX hints values of $n = 1$ and $\Delta H = 110$ at low stress, very similar to the small grain samples of [Rob71]. Therefore, it is not clear whether the difference in plastic behavior in between MOX and UO_2 samples is due to the ultra-fine grain structure, to grain boundaries embrittlement because of Pu addition, or to another parameter such as oxygen stoichiometry.

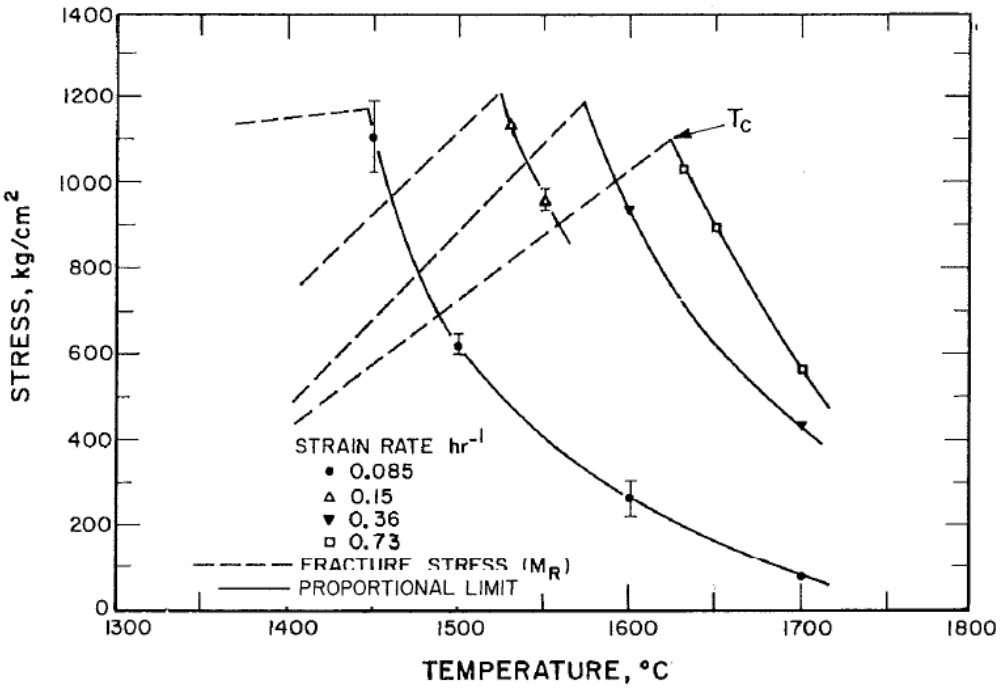

Figure 12.3: Effects of temperature and strain rate on the yield stress (proportional limit) for high density samples (samples 1 & 2 from [Rob71]).

Effect of porosity

As per Figure 12.4, the yield stress decrease with increasing porosity. According to [Rob71], pores behavior under stress may be described through the combination of the following antagonist mechanisms:

- Production of dislocation sources under conditions of localized yielding
- Creation of shear stress, further enhancing the grain sliding process
- Stress relaxation by pores equal or larger than the typical grain size

This project has received funding from the Euratom research and training programme 2019-2020 under grant agreement No 945022.

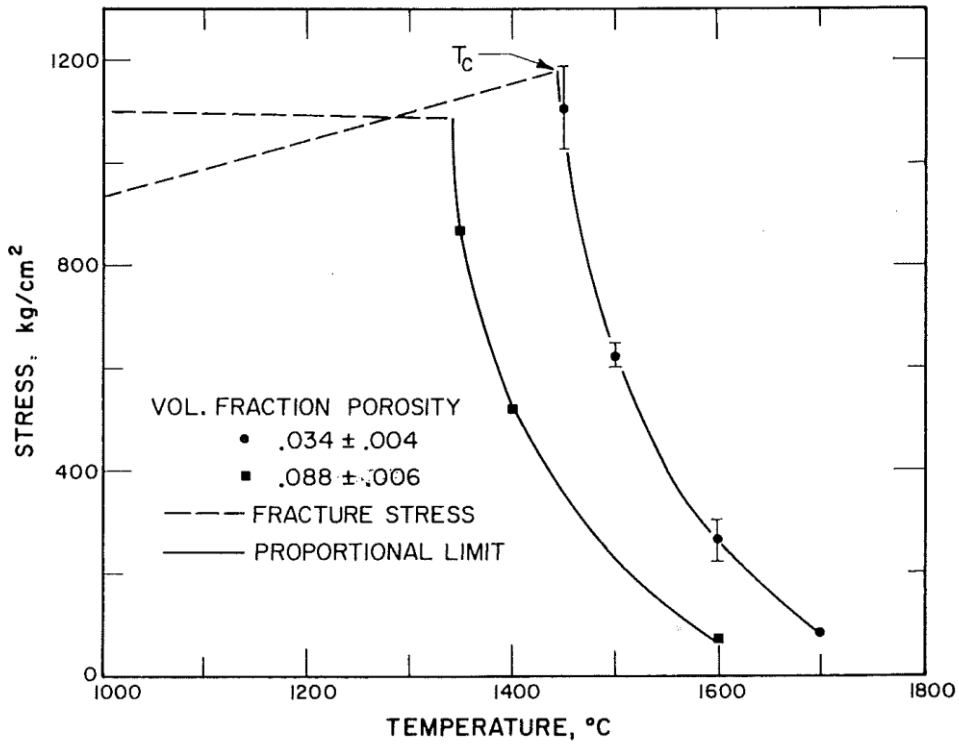

Figure 12.4: Effects of temperature and porosity on the yield stress (proportional limit), at a strain rate of $2.4 \cdot 10^{-5}$ s^{-1} ([Rob71]).

12.2 Conclusion and recommendation

- **Uniaxial compressive yield stress**

Based on a comparison of pure UO_2 and PuO_2, MOX fuel uniaxial compressive yield stress is on a precautionary basis the same as UO_2, whatever the Pu content, and up to 1200°C.

- **Flexural yield stress**

Weakening fuel grain boundaries due to Pu has already been noticed in the case of the tensile tests achieved by [Sto94] (see section 13.2.1.1 from chapter 13). It is believed that [Rob71] has evidenced such an effect on his MOX samples rather than "ultra-fine grains" microstructure effect. Therefore, the following relationship is of application for a 20 wt% PuO_2 MOX fuel in the ductile domain:

$$\dot{\varepsilon} = A\sigma_y^n e^{-\frac{\Delta H}{RT}}$$

With:

σ_y the yield stress (in MN/m^2)

$\dot{\varepsilon}$ the plastic strain rate (in h^{-1}) with $0.15 \leq \dot{\varepsilon} \leq 0.73$

A a structure-sensitive constant, to be further determined for a typical, fast reactor MOX fuel microstructure.

This project has received funding from the Euratom research and training programme 2019-2020 under grant agreement No 945022.

$n = 2$ the stress exponent, characteristic of the deformation mechanism, to be further confirmed for a typical, fast reactor MOX fuel microstructure

$\Delta H = 121.5$ the activation enthalpy (in kcal/mole), to be further confirmed for a typical, fast reactor MOX fuel microstructure

R the gas constant

T the temperature (in K) with 1600 ≤ T ≤ 2000

12.3 References

[Boh70] P.E. Bohaboy and S.K. Evans, Plutonium and other actinides (Proc. 4th Intern. Conf., 1970), part 1, p.478.

[Led92] A. Ledac, Private communication (1992).

[Mar90] D.G. Martin (AEA Harwell), Recommendations for the elastic constants of UO_2 and (U,Pu) mixed oxides – Fast Reactor Data Manual – Novembre 1990.

[Pet77] J.J. Petrovic, S.S. Hecker, C.C. Land and D.L. Rohr, Mechanical properties of $^{238}PuO_2$, Los Alamos National Laboratory report LA-6529 (April 1977).

[Rob71] J.T.A. Roberts and B.J. Wrona, Nature of brittle-to-ductile transition in UO_2 – 20 wt% PuO_2 nuclear fuel – J. Nucl. Mater. 41 (1971) 23.

[Sto94] M.G. Stout, R.W. Ellis, and R.A. Pereyra., Mechanical behavior of $^{238}UO_2$, $^{238}PuO_2$ and $^{239}PuO_2$ as a function of strain rate and temperature, Los Alamos National Laboratory report LA-12811-MS (August 1994).

This project has received funding from the Euratom research and training programme 2019-2020 under grant agreement No 945022.

13. Ultimate stress

This chapter was originally provided by G. Trillon (Framatome).

13.1 Literature data

The ultimate stress, also named ultimate strength, is the maximal stress a pellet can withstand before breaking (Cf Figure 13.1). In ceramic nuclear fuels, at temperatures well below the brittle-to-ductile transition, the break results from brittle failure without plastic deformation and the ultimate stress is easily measured (catastrophic fracture). At higher temperature, plastic deformation occurs and the ultimate stress should be considered as the highest stress measured without significant stretching/creeping of the sample (if no breaking prior to that). In the articles found however, it is the fracture stress that is investigated, no matter what sample plastic deformation occurred (up to 17% for [Pet77]). In case of no breaking of the sample, the maximum stress applied is given as the ultimate stress [Rob71].

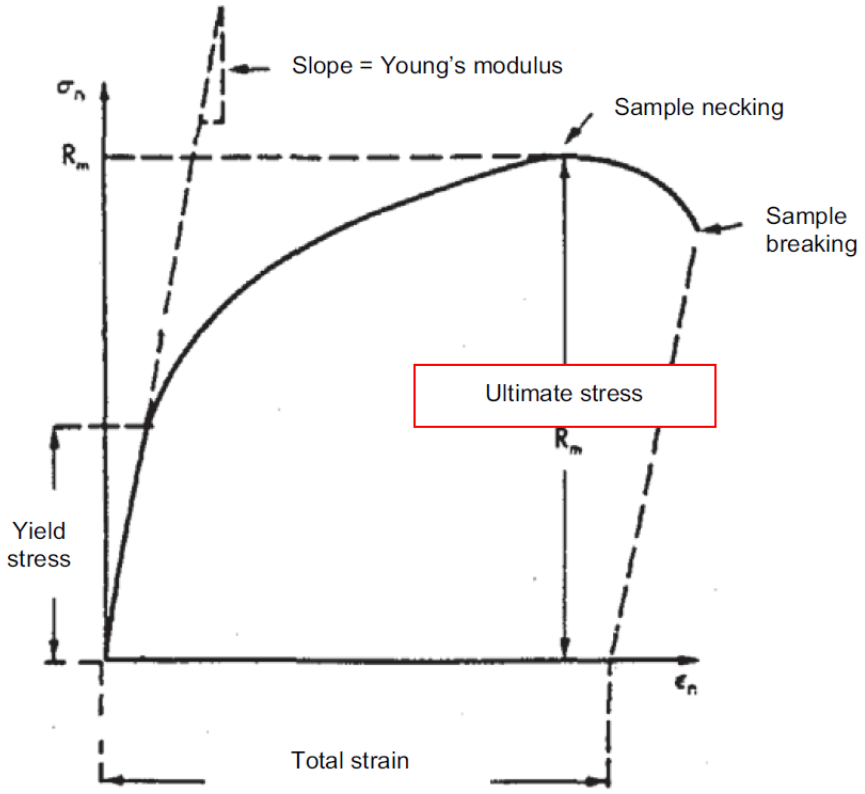

Figure 13.1: Example of a nominal stress versus strain tensile test [Led92] – Definition of ultimate stress.

This project has received funding from the Euratom research and training programme 2019-2020 under grant agreement No 945022.

13.1.1 Uniaxial compressive and tensile ultimate stress

While no uniaxial compressive neither tensile loading curves has been found in the literature for MOX fuel, such data exist for pure UO_2 and PuO_2 pellets ([Pet77] & [Sto94]). In the study of [Pet77] however, most of the PuO_2 pellets were pre-fractured during the fabrication process. High uncertainties are associated to these data. Hence a comparative analysis is achieved hereby from a qualitative point of view only.

In these studies the compressive ultimate stress of both materials has been found to be very similar below 1200°C at a strain rate of about 10^{-3} s^{-1}. Over 1400°C, the ultimate strength (i.e. the fracture stress here) of PuO_2 becomes significantly lower than the one of UO_2.

Tensile behaviors on the other hand do not seem to match in between UO_2 and PuO_2 [Sto94], PuO_2 being much more brittle than UO_2 under tensile load (here simulated using diametral compression load). This poor mechanical resistance of PuO_2 under tensile stress is attributed to weaker grain boundaries than UO_2 [Sto94].

Effects on compressive ultimate stress (and partially on tensile ultimate stress also) of temperature, strain rate, porosity, grain size and of storage have been investigated by [Pet77].

13.1.1.1 Effect of temperature

Below 1200°C, where ultimate and yield stresses of UO_2 are usually not experimentally distinguishable, compressive test results of [Pet77] for pure PuO_2 pellets are very close to UO_2 values (see Figure 13.2). In between 1200°C and 1400°C, the ultimate stress of PuO_2 pellets becomes lower than that of UO_2. Above 1400°C, in the plastic domain, this difference becomes significant, the ultimate stress of UO_2 being reported to be twice the one of PuO_2.

Regarding tensile ultimate stress, PuO_2 samples broke at 28 MPa at 800° C and 16 MPa at 1400°C ([Sto94], from [Pet77]). In the brittle domain, this is much lower than the compressive ultimate stress results. In the ductile domain however, results seems to be similar.

The mechanism proposed for explaining sample breaking in the brittle domain is transgranular fracture propagation. In the plastic domain, fracture is explained through grain sliding and intergranular fracture propagation. The weaker grain boundaries in PuO_2 should therefore be the cause of the lower ultimate stresses reported above 1200°C.

This project has received funding from the Euratom research and training programme 2019-2020 under grant agreement No 945022.

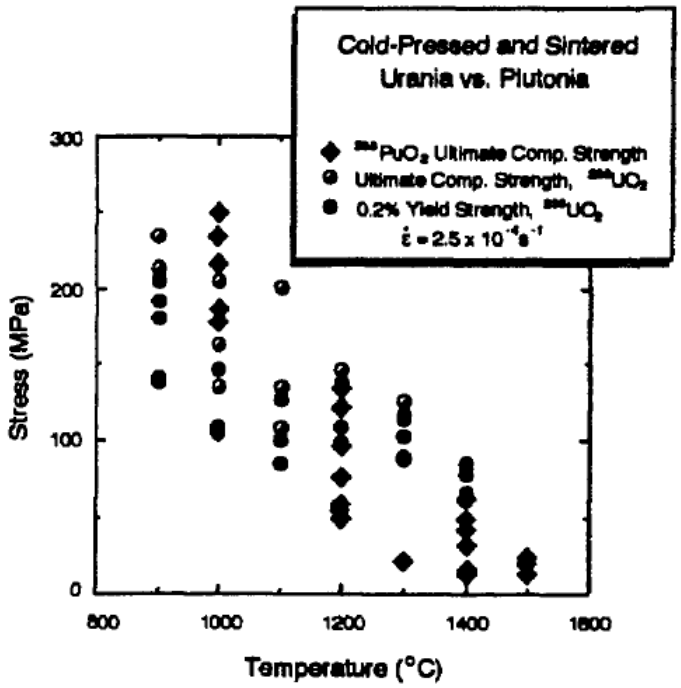

Figure 13.2: UO_2 and $^{238}PuO_2$ compressive ultimate (fracture) stress versus temperature ([Pet77] & [Sto94]).

13.1.1.2 Effect of strain rate

[Pet77] found out that increasing the strain rate drastically improves the compressive ultimate stress of pure PuO_2 pellets, at least in the high temperature domain (temperatures above 1200°C, see Figure 13.3). [Pet77] suggests that such an effect should not be visible in the brittle domain, since this dependence to strain rate is typical of a grain sliding mechanism (=plastic deformation). Since it is the modulus of rupture which is in practice reported by [Pet77], this dependence of the fracture stress to strain rate may also be explained by a shift of the brittle-to-ductile transition towards higher temperatures with increasing strain rate (see Figure 11.1 from chapter 11).

This project has received funding from the Euratom research and training programme 2019-2020 under grant agreement No 945022.

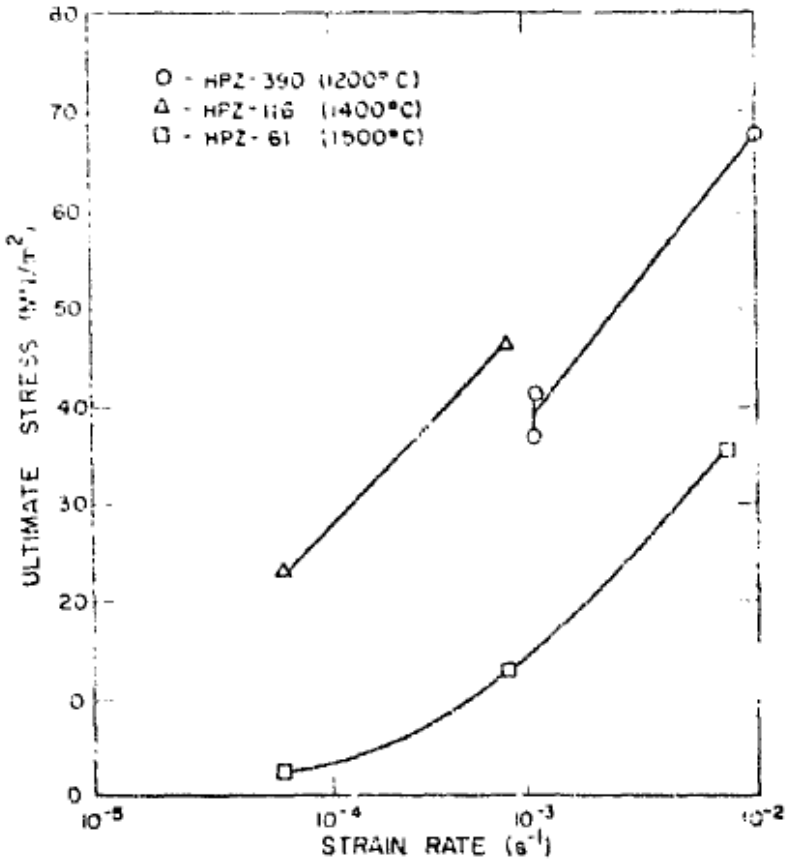

Figure 13.3: $^{238}PuO_2$ compressive ultimate (fracture) stress versus strain at various temperatures ([Pet77] & [Sto94]).

13.1.1.3 Effect of grain size

No marked effect of the grain size on the compressive ultimate (fracture) stress was found by [Pet77] (see Figure 13.4). The results remain in the statistical data scatter for 12 μm and 16 μm samples, even if a decreasing trend is noticeable in the ductile domain. As per [Pet77], grain size effect on ultimate stress may have been concealed by the pre-existent cracks in samples, since it is usually observed on UO_2 samples. It is likely, however, that the increment in grain size was too small to evidence such an effect on compressive strength.

This project has received funding from the Euratom research and training programme 2019-2020 under grant agreement No 945022.

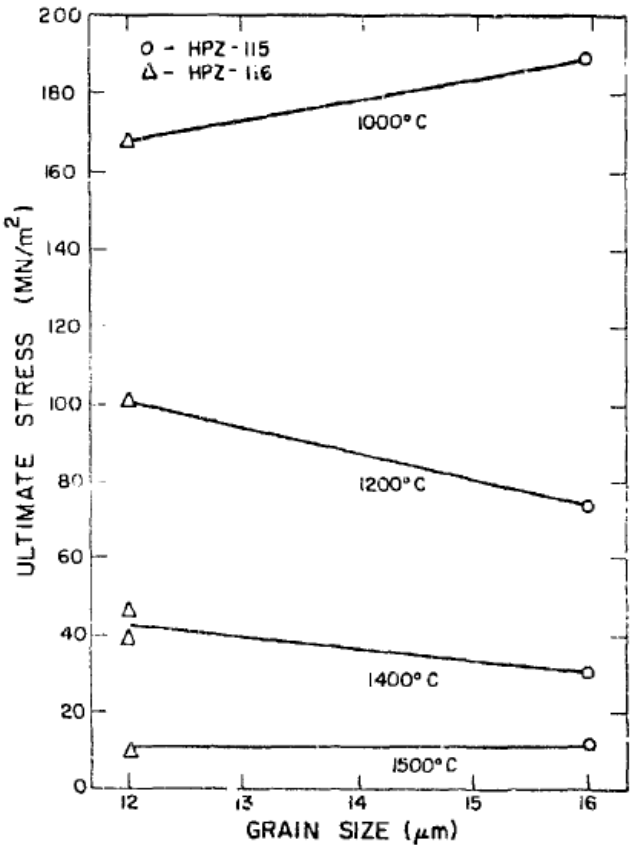

Figure 13.4: $^{238}PuO_2$ compressive ultimate (fracture) stress versus grain size at various temperatures ([Pet77] & [Sto94]).

13.1.1.4 Effect of porosity

A decrease in sample porosity (i.e. an increase of its density) leads as usual for ceramics to an increase of its fracture strength [Pet77] (see Figure 13.5), in both the brittle and the plastic domain.

This project has received funding from the Euratom research and training programme 2019-2020 under grant agreement No 945022.

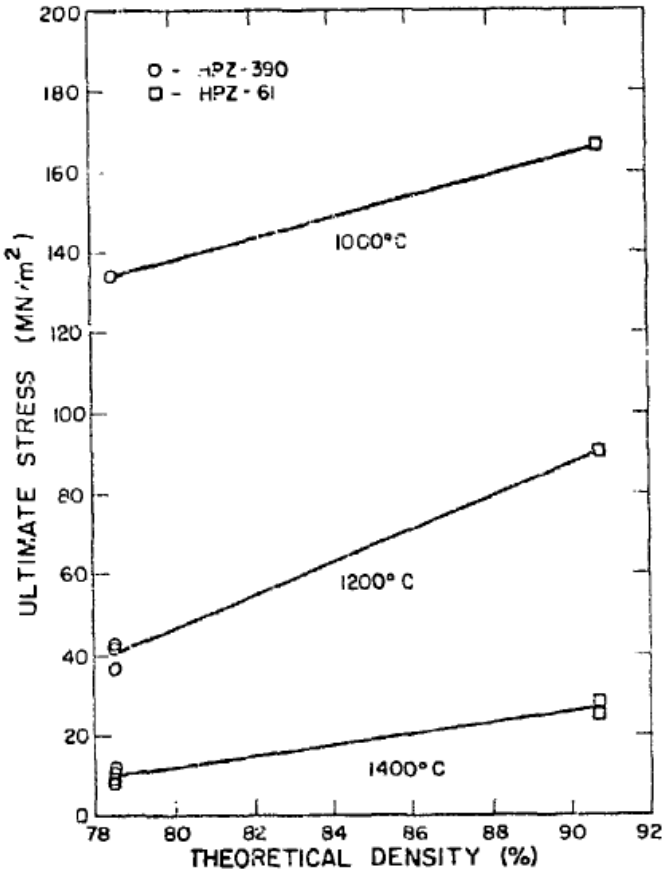

Figure 13.5: $^{238}PuO_2$ compressive ultimate (fracture) stress versus sample density at various temperatures ([Pet77] & [Sto94]).

13.1.1.5 Effect of storage

Due to microstructural damage through alpha-decay and helium generation [Lan80], storage duration may have an impact on compressive ultimate stress, at least at test temperatures high enough to promote He bubbles nucleation. [Pet77] results (see Figure 13.6) do not clearly evidence such an impact. At low temperature, (below 1400°C), effect of microstructural damage and He bubbles nucleation may have been hindered by the pre-existent cracks in samples. For 1400°C compressive tests an effect is clearly observed, still. At higher temperature (1500°C), it is supposed that fast He diffusion towards grain boundaries has occurred, without any impact on the plastic behavior.

This project has received funding from the Euratom research and training programme 2019-2020 under grant agreement No 945022.

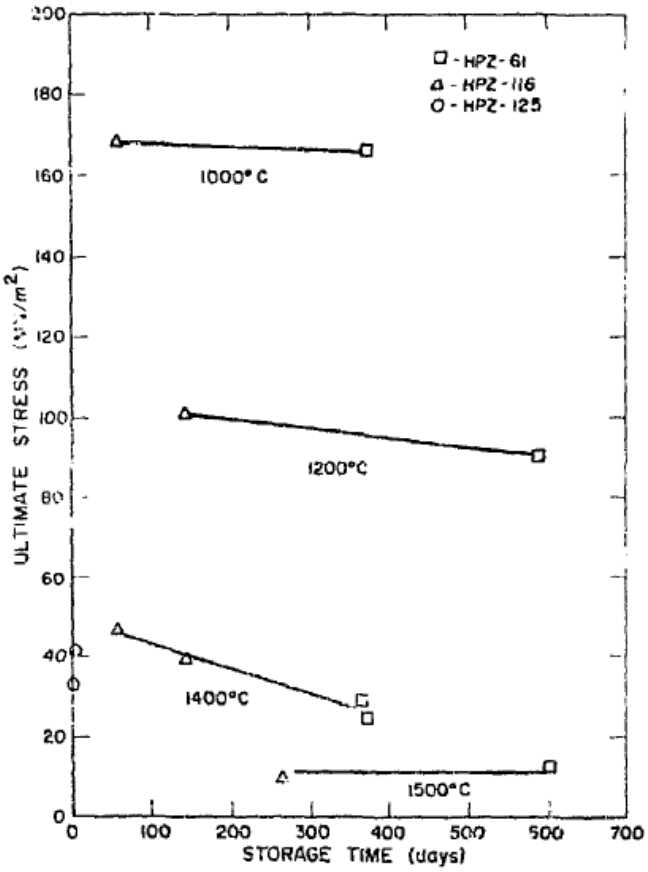

Figure 13.6: $^{238}PuO_2$ compressive ultimate (fracture) stress versus storage time at various temperatures ([Pet77] & [Sto94]).

13.1.2 Flexural ultimate stress

The ultimate (fracture) stress of 20%wt. PuO_2 MOX fuel has been determined by Roberts & Wrona ([Rob71] & [Rob73]) using a four-point bend apparatus. Samples characteristics are reported in Table 13.1 and Table 13.2.

This project has received funding from the Euratom research and training programme 2019-2020 under grant agreement No 945022.

Table 13.1: Four-point bend test measurements [Rob71] – Samples characteristics.

Sample		1	2	3	4	5	6	7
PuO_2 content (%wt.)		20±0.2						
Blending		Mechanical co-blending (ball milling)						
Sintering	Duration	2 h 15 min	3 h	4 h				
	T (°C)	1625	1700	1575		1625	1575	
	Atmosphere	He-6%H_2						
Porosity (%T.D.)		3.4±0.5	4.0±0.5	4.3±0.2	7.3±0.9	8.8±0.6	10.5±0.8	12.0±1.0
O/M		1.970±0.005						
Grain size (µm)		2.5 ± 0.5				0.7 ± 0.5		
Sample dimensions (cm)		4.6 x 0.6 x 0.3						

Table 13.2: Four-point bend test measurements [Rob73] – Samples characteristics.

PuO_2 content (%wt.)	20±0.2
Blending	Mechanical co-blending (ball milling)
Porosity (%T.D.)	6.5±0.5
O/M	1.97
Grain size (µm)	5
Sample dimensions (cm)	4.6 x 0.6 x 0.3

Samples from [Rob71] have an "ultra-fine" grain microstructure with grain sizes of 0.65 µm and 2.5 µm. Instability of such microstructure under thermal treatment (and therefore potentially during test routines) is reported. [Rob73] makes report of samples with larger grain size (5 µm to 30 µm), which should be better representative of a standard fuel.

Effects of temperature, strain rate, and initial porosity were benchmarked by [Rob71] & [Rob73]. Fracture in the ductile domain was not specifically measured by [Rob71] and [Rob73]. Only data in the brittle domain and in the neighborhood of the transition temperature were collected by these authors. The main conclusions are:

- The ultimate (fracture) stress increases with increasing temperature.
- Other parameters such as strain rate, porosity, grain size, O/M or impurities are negligible when compared to temperature.

This project has received funding from the Euratom research and training programme 2019-2020 under grant agreement No 945022.

13.1.2.1 Effect of temperature

[Rob73] has fitted the relationship given by Eq. 13.1 on all available experimental data on 20%wt. PuO_2 MOX (see Figure 13.7):

$$\sigma_F = 43.5 + 0.058\,T \qquad \text{Eq. 13.1}$$

With:

σ_F the flexural ultimate (fracture) stress (in MN/m^2);

T the temperature (in °C) with $20 \leq T \leq 1900$.

The standard deviation associated to this adjustment is ±15.8 MN/m^2.

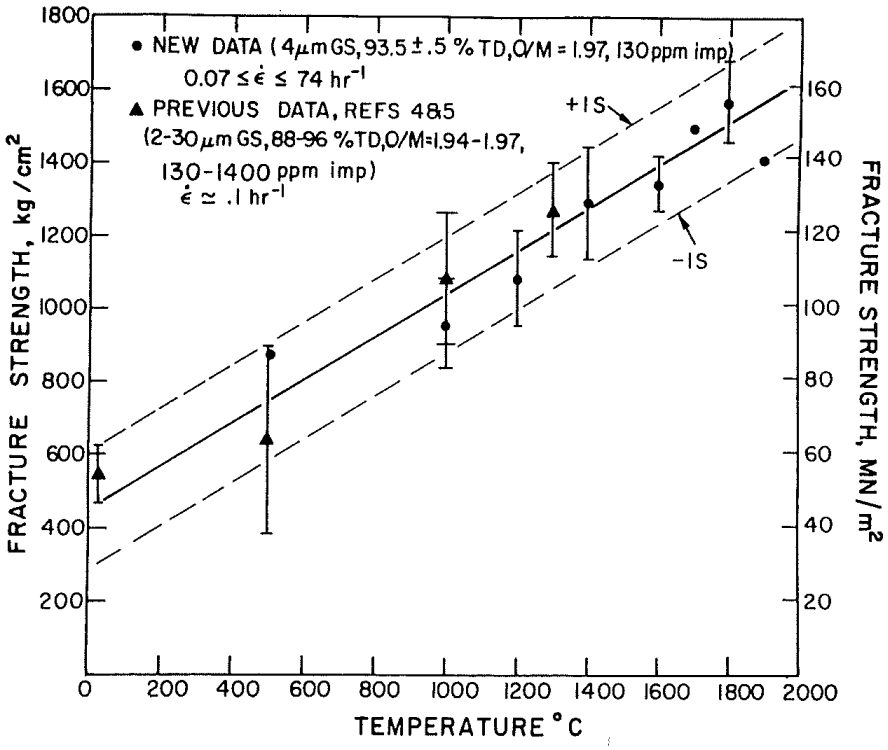

Figure 13.7: Effect of temperature on the ultimate stress (fracture strength) [Rob73].

13.1.2.2 Effect of strain rate

In contradiction with [Rob71], [Rob73] reports no significant effect of strain rate on the ultimate stress of 20%wt. PuO_2, at least in the brittle domain (see Figure 13.8). Wrong results from [Rob71] are explained by defective samples.

This project has received funding from the Euratom research and training programme 2019-2020 under grant agreement No 945022.

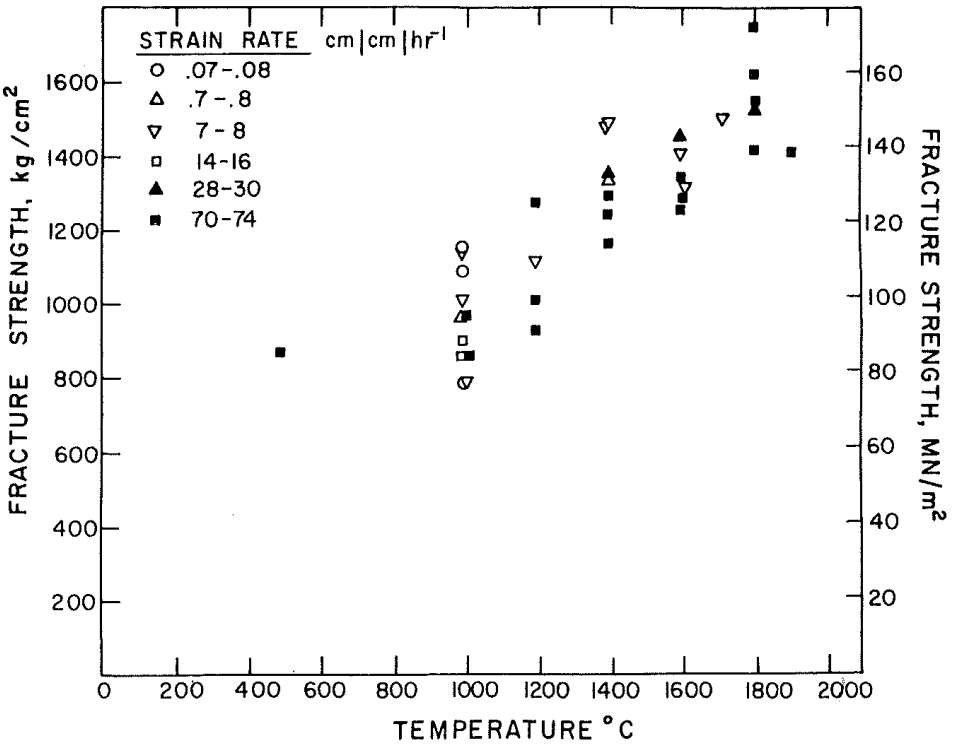

Figure 13.8: Effects of strain rate and temperature on the ultimate stress (fracture strength) [Rob73].

13.1.2.3 Effect of porosity

[Rob71] results outline a decrease of the ultimate (fracture) stress in the brittle domain with increasing porosity (i.e. decreasing sample density, see Figure 13.9). This conclusion is somewhat dimmed by different grain sizes in [Rob71] samples.

At temperatures near the brittle-to-ductile transition, the ultimate (fracture) stress becomes even more sensitive to porosity, according to [Rob71].

This project has received funding from the Euratom research and training programme 2019-2020 under grant agreement No 945022.

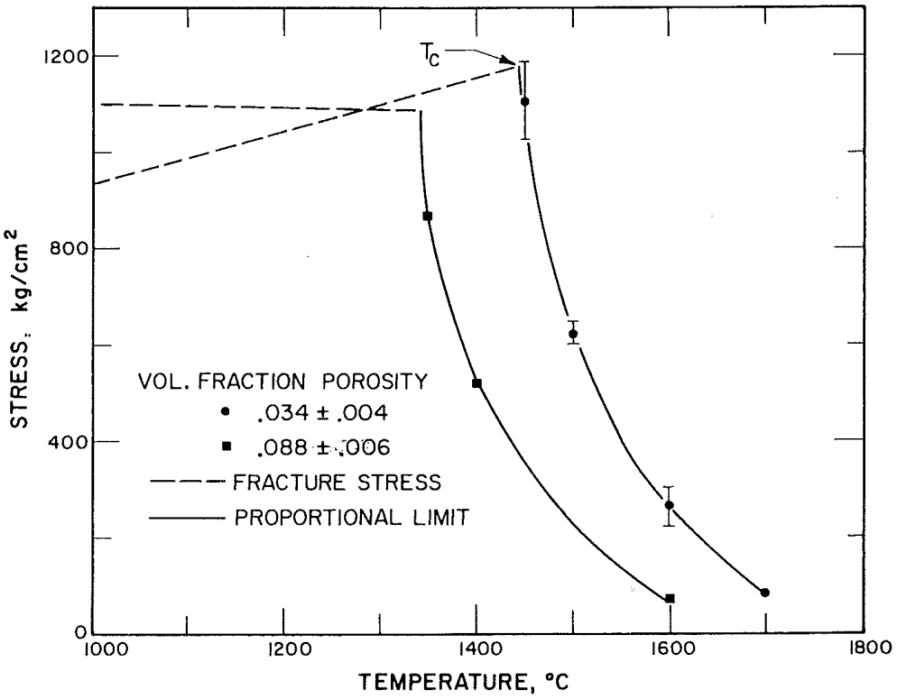

Figure 13.9: Effects of temperature and porosity on the ultimate (fracture) stress at a strain rate of 2.4 10^{-5} s^{-1}

13.2 Conclusion and recommendation

- **Uniaxial compressive and tensile ultimate stress**

In the brittle domain, based on a comparison of pure UO_2 and PuO_2 compressive behavior, MOX fuel uniaxial compressive ultimate (fracture) stress is on a precautionary basis the same as UO_2 whatever the Pu content. Below the brittle-to-ductile transition temperature, effects on MOX fuel compressive ultimate stress of temperature, strain rate, grain size and porosity should be very similar to UO_2 (see [Rad79] for instance). A specificity of MOX fuel however is an additional possible effect of storage duration that does not exist in UO_2.

In the ductile domain however, MOX uniaxial compressive ultimate (fracture) stress should be lower than UO_2, due to the addition of Pu which likely weakens grain boundaries. This conclusion being drawn from a qualitative comparison of pure PuO_2 and UO_2 behavior, it is not possible to provide here quantitative evaluation of effects such as temperature, strain rate, grain size, and porosity. Storage duration on the other hand seems to have a lesser, if any, impact at higher temperature (>1500°C).

Concerning uniaxial tensile ultimate (fracture) stress, existing data permit only to outline its nonequivalence to compressive ultimate stress, as usual in ceramics.

However there is no experimental data acquired on MOX fuel to support these recommendations.

This project has received funding from the Euratom research and training programme 2019-2020 under grant agreement No 945022.

- **Flexural ultimate stress**

In the brittle domain, [Rob73] concludes that flexural ultimate stress is not sensitive to strain rate neither to microstructural effects (i.e. pores, grain size a.s.o). Exceptions are flaws that are larger than the average microstructure grain size and pores diameter (i.e. large pores, large impurity particles or surface defects). The main parameter of influence remains the temperature. From [Rob73], the recommended relationship for temperature dependence of ultimate flexural stress of 20%wt. PuO_2 MOX is given by Eq. 13.1 :

$\sigma_F = 43.5 + 0.058\,T$ with:

σ_F the flexural ultimate (fracture) stress (in MN/m^2);

T the temperature (in °C) with 20 ≤ T ≤ 1900.

The standard deviation associated to this adjustment is ±15.8 MN/m^2. This relationship is valid only for brittle fracture.

13.3 References

[Lan80] C.C. Land, Microstructural damage produced by helium in aged $^{238}PuO_2$ fuels, Los Alamos National Laboratory report LA- 8083 (February 1980).

[Led92] A. Ledac, Private communication (1992).

[Pet77] J.J. Petrovic, S.S. Hecker, C.C. Land and D.L. Rohr, Mechanical properties of $^{238}PuO_2$, Los Alamos National Laboratory report LA-6529 (April 1977).

[Rad79] K.C. Radford, "Effect of fabrication parameters and microstructure on the mechanical strength of UO_2 fuel pellets", J. Nucl. Mater. **84** (1979) 222.

[Rob71] J.T.A. Roberts and B.J. Wrona, Nature of brittle-to-ductile transition in UO_2 – 20 wt% PuO_2 nuclear fuel, J. Nucl. Mater **41** (1971) 23.

[Rob73] J.T.A. Roberts, Brittle fracture of oxide nuclear fuel, J. Nucl. Mater. **47** (1973) 125.

[Sto94] M.G. Stout, R.W. Ellis, and R.A. Pereyra, Mechanical behavior of $^{238}UO_2$, $^{238}PuO_2$ and $^{239}PuO_2$ as a function of strain rate and temperature Los Alamos National Laboratory report LA-12811-MS (August 1994).

This project has received funding from the Euratom research and training programme 2019-2020 under grant agreement No 945022.

14. Thermal creep

This chapter was originally provided by J. Klousal (UJV).

14.1 Literature data

The most common empirical form of the creep rate equation ($\frac{d\varepsilon}{dt}$) of UO_2 or MOX is given by Eq. 14.1:

$$\frac{d\varepsilon}{dt} = \left(A_1 F + \frac{A_2}{d_g^2}\exp\left(-\frac{Q_1}{RT}\right)\right)\sigma + A_3\sigma^{4.5}\exp\left(-\frac{Q_2}{RT}\right) \qquad \text{Eq. 14.1}$$

Where *F* denotes local fission rate, σ the stress (majority of experimental data was obtained with uniaxial loading, Von Misses stress is generally used in application) and d_g is the fuel grain size. Some older works use slightly different exponent in the power creep part, e.g.4.4 in [Rou72]. Parameters *A* and activation energies *Q* incorporate the effect of porosity, stoichiometry and Pu content. The formula represents combination of three mechanisms – radiation induced creep, the viscous creep with some grain boundary sliding occurring at low stresses and the dislocation-climb process, which operates at stresses greater than a transition stress that is governed by the grain size.

The recommended formula for combined thermal and irradiation induced creep based on the review by Matthews et Martin, which in turn originated in the work by Dumbill [Dum87] and Hough [Hou88] is given in Eq. 14.2:

$$\frac{d\varepsilon}{dt} = f(p)\left\{\sigma\left[A_1 F + \frac{(A_2 + A_2^F F)}{d_g^2}\exp\left(-\frac{Q_1}{RT}\right)\right] + A_3\sigma^{4.5}\exp\left(-\frac{Q_2}{RT}\right)\right\} \qquad \text{Eq. 14.2}$$

With :
$A_1 = 2.26.10^{-30}$ $m^3.MPa^{-1}$
$A_2 = 1.11.10^{-6}$ $s^{-1}.m^2.MPa^{-1}$
$A_2^F = 6.62.10^{-26}$ $m^5.MPa^{-1}$
$A_3 = 5.20.10^4$ $s^{-1}.MPa^{-4.5}$
$Q_1 / R = 48000$ K, $Q_1 = 3.99.10^5$ $J.mol^{-1}$
$Q_2 / R = 75000$ K, $Q_2 = 6.24.10^5$ $J.mol^{-1}$
The effect of porosity *p* is approximated by $f(p) = \exp(25p)$.

The full version of Dumbill's formula for thermal creep includes also the primary creep component ε_p as well as the dependence on the Pu content and deviation from the stoichiometry *x*. The expression is given in Eq. 14.3 (given values of parameters reproduce creep rate in s^{-1} when σ is input in MPa):

$$\frac{d\varepsilon}{dt} = \left[f_1(p)\frac{\sigma}{d_g^2} + 4.8.10^{10} f_2(p)\left(K - M\varepsilon_p\right)\exp\left(-\frac{27000}{T}\right)\sigma^{4.5}\right]F(x,T)G(Pu) \qquad \text{Eq. 14.3}$$

This project has received funding from the Euratom research and training programme 2019-2020 under grant agreement No 945022.

It should be noted that the porosity enhancement factors are different in linear and power terms:

$f_1(p) = \exp(3.0 * p)$ and $f_2(p) = \exp(2.2 * p)$

The creep rate grows with the PuO_2 weight fraction (*Pu)* up to 0.15:

$G(Pu) = 0.2 + (16/3)Pu$ if Pu < 0.15 and $G(Pu) = 1$ otherwise.

The impact of the deviation from stoichiometry is expressed as temperature dependent function as per Eq. 14.4.

$$F(x,T) = 1.07.10^{-9}\exp\left(-\frac{21000}{T}\right)\left(\sqrt{x^2 + 2000\exp\left(-\frac{27000}{T}\right)} + x\right)^2 + 4.03.10^{-7}|x|\exp\left(-\frac{40000}{T}\right) \quad \text{Eq. 14.4}$$

Strain hardening law is used to model the non-stationary (primary) creep. The enhancement factor applied to the power term is $(K - M\varepsilon_p)$ where *K* and *M* are model parameters and ε_p the primary creep strain:

$$\frac{d\varepsilon_p}{dt} = \left[4.8.10^{10} f_2(p)\left(K - 1 - M\varepsilon_p\right)\exp\left(-\frac{27000}{T}\right)\sigma^{4.5}\right]F(x,T)G(Pu) \quad \text{Eq. 14.5}$$

With K = 6 and M =50

The description of the application of the strain hardening (and softening) law in the fast reactor fuel performance code may be found for example in [Rit93].

There has been only very limited amount of new information published in the open literature since 1990, especially related to the FBR MOX. In fact, even the very recent codes used to model the FBR MOX behavior employ the models dating in 1970s, for example the FEAST-OXIDE [Kar10] with the Roubort's model [Rou72]. The other often cited source from 1970s are works of Bohaboy [Boh70]. Therefore it is of interest to focus also on the recent results related to the LWR MOX and UO_2 fuels.

Recently, a less empirical approach to the UO_2 creep has been adopted by Malygin et al. ([Mal09] and [Mal10]) with the resulting formula given in Eq. 14.6:

$$\frac{d\varepsilon}{dt} = \alpha\frac{\Omega D_V}{kTd_g^2}\sigma + \beta\frac{D_V}{kT\mu^{3.5}\sqrt{bN}}\sigma^{4.5} \quad \text{Eq. 14.6}$$

Where α and β are constants that depend on the degree of relaxation of the tangential stresses at the boundary of a grain, Ω is the atomic volume, D_V is the volume diffusion coefficient, k is Boltzmann's constant, b is the Burgers vector, N is the density of mobile dislocations, and μ is the shear modulus. These parameters are distinctive for MOX fuel, however α and β still must be tuned by

This project has received funding from the Euratom research and training programme 2019-2020 under grant agreement No 945022.

comparison with experimental data. The porosity enhancement factor assumed in the work based on the fitting of LWR UO_2 is given by Eq. 14.7

$$f(p) = 1 + 1234.1\, p^{1.8} \qquad \text{Eq. 14.7}$$

Golovin et al [Gol00] have studied the thermal creep rate of PuO_2 as well as the MOX fuels in thermal spectrum. The high temperature component is again expressed as the combination of grain boundary sliding term linear in stress and disclocation climb term with typical power law behavior. The activation energies are reported to be 3.6 – 4.0 $.10^5$ J.mol^{-1} and 5.6 – 5.9 $.10^5$ J.mol^{-1} respectively, which is consistent with the recommendation given in Eq. 14.2. They also note that "at temperatures above 1400–1450°C the creep rate of UO_2 approaches that of $(U,Pu)O_2$".

Some information concerning the French MOX test programme (albeit for LWR) was published by Caillot et al. at the PCI seminar in Aix in 2004 [Cai04]. The out-of pile creep test reported was performed in the LEFCA facility of CEA Cadarache and involved MIMAS MOX pellets with different Pu content (0, 6 and 10%). The secondary creep rates were of the same order of magnitude as soon as the stress exceeded 60 MPa, below 60 MPa the MOX creep was greater compared to UO_2 despite smaller grain size.

There was no systematic difference between 6 and 10% Pu MOX. The activation energies were $4.0.10^5$ J.mol^{-1} in UO_2 and $5.0.10^5$ J.mol^{-1} in MOX. Most importantly, the paper shows marked difference in the primary creep rate measured. At the temperature about 1550°C and 40 MPa load the creep strain is greater by a factor of 2 in MOX sample in spite of lower temperature and grain compared to UO_2.

Calabrese et al. [Cal25] give an interesting review of the different models proposed for thermal creep of FBR MOX. They compared the correlations employed to account for the impact of porosity, the effects of plutonium content and stoichiometry, leading to a new correlation for steady-state creep based on the work of Routbort et al. [Rou72]. In particular, this new correlation addresses the impact of stoichiometry deviation as illustrated per example on Figure 14.1 for a temperature of 1823 K.

This project has received funding from the Euratom research and training programme 2019-2020 under grant agreement No 945022.

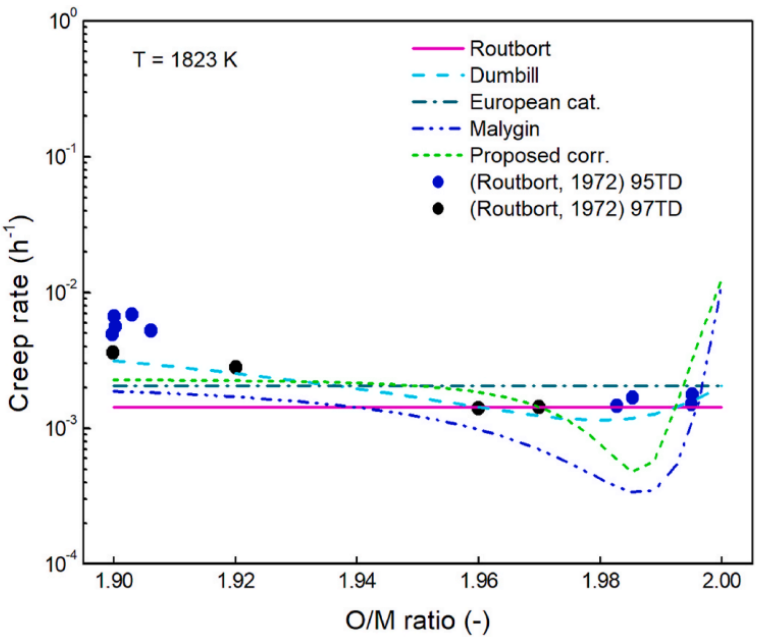

Figure 14.1: Creep rates as a function of stoichiometry for different models (T = 1823 K) compared to measurements from [Rou72]– from [Cal25]

14.2 Conclusion and recommendations

There are no publicly published new data on the FBR MOX thermal creep which would require change of the recommendation given in Eq. 14.2, although it would be worthwhile to exploit the work of Malygin and derive the creep rate using his formula and the fundamental physical properties of MOX fuel in question. Impact of stoichiometry deviation shall also be further assessed.

For the detailed calculation of the pellet-cladding interaction the primary creep given by Eq. 14.5 should be considered as well.

14.3 References

[Boh70] P.E. Bohaboy and S.K. Evans, Compressive Creep Properties of UO_2-PuO_2 Compounds, Proceedings of the 4th International Conference on Plutonium and Other Actinides, Santa Fe, New Mexico, 1970.

[Cai04] L. Caillot, C. Nonon and V. Basini, Out-of-pile and In-pile Viscoplastic Behaviour of Mixed-oxide Fuel, Pellet-clad Interaction in Water Reactor Fuels, Seminar Proceedings, Aix-en-Provence, France, 9-11 March 2004.

[Cal25] R. Calabrese and S. Hirooka, Comparison of correlations for thermal creep of FBR MOX, Progress in Nuclear Energy 178 (2025) 105516

[Dum87] S. Dumbill, C.A. English, J. Harding , D.G. Martin, J.R. Matthews, J.M. Perks and T.M. Williams, Final progress report on data collection and

This project has received funding from the Euratom research and training programme 2019-2020 under grant agreement No 945022.

evaluation for fast reactor fuel and cladding thermo mechanical properties, Report AERE-G 4455 (1987).

[Gol00] I.S. Golovnin, Propeties of Plutonium Dioxide As Nuclear Fuel, Atomic Energy Vol. 89, No. 2, 2000.

[Hou88] A. Hough, Compressive creep in nuclear oxides, Report AERE-R 13232, AGT 010101/P7 (1988).

[Kar10] A. Karahan and J. Buongiorno, Modeling of thermo-mechanical and irradiation behavior of mixed oxide fuel for sodium fast reactors, J. Nucl. Mater. **396** (2010) 272.

[Mal09] V.B. Malygin, K.V. Naboichenko, A.S. Shapovalov, Y.K. Bibilashvili, Recommendations for calculating the thermal creep properties of uranium dioxide when analyzing fuel-element serviceability, At. Energy **107** (2009) 381.

[Mal10] V. B. Malygin, K. V. Naboichenko, A. S. Shapovalov, Y. K. Bibilashvili, Recommendations for calculating the rate of irradiation-induced creep of oxide fuel when analyzing fuel-element serviceability, At. Energy **108** (2010) 121.

[Rit93] H.J. Ritzhaupt-Kleissl, M. Heck: SATURN FS-1, A Computer Code for Thermo-Mechanical Fuel Rod Analysis, Report KfK 5203, September 1993

[Rou72] J.L. Routbort, N.A. Javed, J.C. Voglewede, Compressive creep of mixed-oxide fuel pellets, J. Nucl. Mater. **44** (1972) 247.

This project has received funding from the Euratom research and training programme 2019-2020 under grant agreement No 945022.

15. Diffusion/migration of pores and fission gas bubbles

This chapter was originally provided by A. Fedorov (NRG).

15.1 Literature data

In UO_2 and $(U,Pu)O_2$ fuels the fission gasses xenon and krypton as well as helium are produced as a result of direct fission reactions and transmutation decay chains. At the operation temperatures, fission gases are insoluble in the fuel matrix and mobile. For the gas atoms rejected from the matrix the following routes are possible:

- direct gas release from the fuel.
- filling the pre-existing as-fabricated porosity.
- precipitation within the fuel in the form of bubbles. The precipitation of bubbles takes place within fuel grains, at dislocations or other lattice irregularities, or at grain boundaries.

All three routes are detrimental for fuel performance. Direct gas release causes pressure build-up in the fuel pin plenum and, as a consequence, excess pressure on the fuel cladding. The two other options lead to fuel swelling, and consequently to fuel cladding mechanical interaction, jeopardizing mechanical integrity of both. Moreover, formation of bubbles decreases thermal conductivity of the fuel, which implies higher central temperature, which in turn promotes further bubble growth.

Bubbles grow by diffusion limited processes of accumulation of mobile gas atoms and vacancies, and via coalescence if they come in contact. The bubbles shrink by capture of self-interstitials, thermal resolution or dissociation at high temperatures (> 1500 °C), or disintegrate by passage of fission fragments or neutrons (recoil resolution). As a counter play of these processes, bubble size typically saturates at a few nanometers.

Newly formed bubbles should be distinguished from fabricated porosity because their shape, sizes, gas pressure, mobility and general behavior are quite different. Thus the fabricated porosity relatively fast evolves into lenticular pores bigger than 1 micrometer in size which under typical irradiation conditions move to the fuel pellet center in the existing temperature gradient resulting into formation of the central void and fuel densification at periphery. The gas filled bubbles are much smaller, under micrometer size and have a spherical shape inside the gains and lenticular and triangulated shapes at grain boundaries and junctions.

Fission gas accumulated in the bubbles and pores can be released back to the fuel matrix, (via thermal or recoil resolution) and be re-trapped by other sinks, or transported to the grain boundary with further release to the fuel plenum.

In another mechanism, which does not require resolution of bubbles, the bubbles/pores form an interconnected or tunnel network of open porosity

This project has received funding from the Euratom research and training programme 2019-2020 under grant agreement No 945022.

(coalescence). Typically such a network of lenticular pores is formed along the grain boundaries. As the network becomes interconnected the gas is vented resulting in a so-called burst release. The interconnection of the bubble network comes along with micro-cracking along the same grain boundaries. This mechanism is held responsible for onset of (high) fission gas release.

Alternatively, bubbles and pores can move as an entity thus providing a different mechanism for fission gas transport.

Mobility of bubbles was in the focus of many publications in the past. This chapter is based on the monograph of Olander [Ola76], extended reviews made by Nichols [Nic69; Nic79], works of Van Uffelen [Uff02], Cottrell [Cot02], Evans [Eva95; Eva96], Geguzin [Geg73], and references therein.

15.1.1 Brownian motion

In the absence of gradient, the atoms of the material matrix randomly hop over the inner surface of the bubble resulting in a form of Brownian motion of the latter. The resulting motion of bubbles is also random.

On microscopic level three mechanisms of Brownian bubble motion are considered: *surface diffusion, volume diffusion and vaporization.*

In case of the **surface diffusion** the atoms (ions) move along the surface of the bubble with the rate characterized by the surface diffusion coefficient. From geometrical considerations the overall bubble diffusion is obtained as per Eq. 15.1.

$$D_b = \frac{3\,\lambda\,\Omega}{2\,\pi\,R^4} D_s \qquad \text{Eq. 15.1}$$

Where :
D_s is the surface diffusion coefficient,
λ is the lattice constant,
Ω is the atomic elementary volume,
R is the bubble radius.

In oxide fuel, preservation of stoichiometry implies that ions of both sub-lattices should be transported along the bubble surface congruently, therefore the slowest species (in UO_2 the uranium cation) defines the overall diffusion rate.

In case of the **volume diffusion** the motion of the species is normal to the bubble surface and takes place via the matrix of the fuel. Similar to the surface diffusion, the slowest species defines the overall diffusion rate. The bubble diffusion coefficient is defined as per Eq. 15.2.

$$D_b = \frac{3\,\Omega}{4\,\pi\,R^3} D_v \qquad \text{Eq. 15.2}$$

where D_v is the volume diffusion coefficient.

In case of **vaporization** or vapor diffusion the diffusing species also move normal to the bubble surface, but via the bubble volume. This mechanism includes the

This project has received funding from the Euratom research and training programme 2019-2020 under grant agreement No 945022.

following steps: evaporation, diffusion through the vapor or bubble gas, and condensation. The evaporation step is considered rate limiting. Preservation of stoichiometry requires congruent vaporization, therefore the least volatile species controls the overall rate. The bubble diffusion coefficient for vapor diffusion is given by Eq. 15.3.

$$D_b = \frac{3\,\Omega^2\,\alpha_v\,p_v}{4\,\pi\,k\,T\,R^3} D_g \qquad \text{Eq. 15.3}$$

where:
D_g is the diffusion coefficient in the gas,
p_v is the equilibrium vapor pressure of the rate controlling species,
α (≤1) measures the departure from equilibrium.

For all considered mechanisms the Brownian motion is effective only for small bubbles: $D_b \sim R^{-4}$ for surface diffusion and $D_b \sim R^{-3}$ for volume diffusion and vaporization (under condition that D_g is constant).

15.1.2 Drift in field gradients

Under typical fuel operation, bubbles and pores present in the fuel matrix are subjected to extreme gradients of various fields. The most important are the thermal gradient (> 10^5 K/m), vacancy concentration gradient, stress field gradient, and electric potential gradient. Different from the random Brownian motion, bubble motion is directional within a field gradient.

Nichols has developed a generic approach to describe drift of bubbles in a field gradient of general nature [Nic69; Nic79]. The drift velocity is calculated as a product of bubble mobility M_b and force F_b applied to the bubble as per Eq. 15.4.

$$v_b = M_b\,F_b \qquad \text{Eq. 15.4}$$

The mobility is related to the bubble diffusion coefficient D_b via the Nernst-Einstein equation (Eq. 15.5).

$$M_b = \frac{D_b}{k\,T} \qquad \text{Eq. 15.5}$$

There is a relation between the microscopic force f acting on individual atomic species and F_b as given per Eq. 15.6.

$$F_b = -\left(\frac{4\,\pi\,R^3}{3\,a_0^3}\right) f \qquad \text{Eq. 15.6}$$

where R is the bubble radius, and a_0 is the lattice parameter.

This project has received funding from the Euratom research and training programme 2019-2020 under grant agreement No 945022.

15.1.2.1 Thermal gradient

The thermal gradient presents the strongest driving force for bubble motion in fuels. Under typical operation conditions the thermal gradients can be as high as 4000 K/cm. In case of surface thermal diffusion the effective force per atom *f* is given by Eq. 15.7 [Nic69; Nic79].

$$f = -\frac{Q_s}{T}\left(\frac{dT}{dx}\right) \qquad \text{Eq. 15.7}$$

Where Q_s is the heat of transport for the surface thermal self-diffusion mechanism. The Q_s measures a net heat flow per unit matter flow.

For the same three atomistic transport mechanisms drift velocities are:

- Surface diffusion mechanism:

$$v_b = \frac{2\,D_s\,\nu_s\,\Omega\,Q_s}{k\,T^2\,R}\left(\frac{3K}{2K+K'}\right)\nabla T_\infty \qquad \text{Eq. 15.8}$$

- Volume diffusion mechanism:

$$v_b = \frac{D_v\,Q_s}{k\,T^2}\left(\frac{2(K-K')}{2K+K'}\right)\nabla T_\infty \qquad \text{Eq. 15.9}$$

- Vaporization mechanism:

$$v_b = \frac{2\,D_g\,\Omega\,\alpha_v\,p_v\,\Delta H_v}{k^2\,T^3}\left(\frac{3K}{2K+K'}\right)\nabla T_\infty \qquad \text{Eq. 15.10}$$

Where:
$\nu_s = \lambda/\Omega$ is a number of rate controlling species per unit surface area
Ω is the atomic volume
The expression inside the brackets presents the numerical factor connecting the local thermal gradient inside the bubble/pore and macroscopic bulk thermal gradient ∇T_∞.
The *K* and *K'* are the thermal conductivities of the matrix and bubble, respectively (for pores and bubbles $K >> K'$).
ΔH_v is the activation energy for evaporation of the rate limiting species.

Using typical fuel operation parameters from Table 15.1 [Ola76], the drift velocity of a 200 Å bubble at 2000 K in a gradient of 4000 K/cm is estimated as 2.3×10^{-6} cm/sec.

In case of bubble/cavity drift in thermal gradient the drift velocity is inversely proportional to the bubble size for the surface diffusion mechanism and independent of *R* for the volume diffusion mechanism. The drift velocity via the vaporization mechanism is also independent of *R* under condition that D_g is constant. It the fission gas pressure inside the bubble is at equilibrium with the

This project has received funding from the Euratom research and training programme 2019-2020 under grant agreement No 945022.

surface tension, $p = 2\gamma/R$, and $D_g \sim 1/p,$ the drift velocity is proportional to *R*, and , hence, larger pores/bubbles move rapidly than the small ones.

The surface diffusion mechanism is dominant for sub-micron size, while volume diffusion and vapor transport are dominant in the region of a few to ten micrometers.

Since normally $\Delta H_v > Q_v > Q_s$, where Q_v and Q_s are the activation energies for volume and surface diffusion, as the temperature increases, the dominant mechanism shifts from surface to volume diffusion, and then to vapor transport.

The pores and bubbles always move up the thermal gradient (under a trivial condition, K > K'). Because of the difference in the thermal gradient along the pore size the leading end of the pore moves faster than the trailing end. Therefore the elongation of the pore increases. This effect is limited by arising gradient in the chemical potential (Gibbs–Thomson Effect) which eventually stabilizes the elongated shape of the pore. Small pores, where the difference in temperature across the pore is much smaller than the average temperature, preserve their shape and migrate without distortion.

Lenticular pores apparently originate from non-spherical flat shapes (fabricated porosity), rather than formed during drift. The pores move up the thermal gradient, to the center of fuel pellet, leaving densified matrix behind. This motion takes place before the onset of gas release.

Note that for bubble motion one requires both, high temperature for activation of transport mechanism (surface/volume diffusion or vaporization) and temperature gradient. A typical temperature profile in fuel pellet has a quadratic dependency on radius, with high temperature but small gradient at the center, and relatively low temperature but steep gradient at periphery. Thus under typical fuel operation the optimum conditions for bubble migration are not realized.

15.1.2.2 Vacancy concentration gradient

Vacancy gradient is another driving force for bubble/pore motion. Grain boundaries present a source of thermal vacancies, causing drift of bubbles from the grain interior towards the grain boundaries.

The bubble drift velocity in a vacancy gradient does not depend on the bubble radius and is described by Eq. 15.11 [Geg73; Eva96].

$$v_b = 2\, D_V\, \Omega \left(\frac{dC_V}{dx}\right) \qquad \text{Eq. 15.11}$$

where D_V is the vacancy diffusivity.

Strong temperature gradients also introduce gradients in concentration of thermal vacancies, therefore both effects are correlated.

This project has received funding from the Euratom research and training programme 2019-2020 under grant agreement No 945022.

15.1.2.3 Stress field gradient

In a varying elastic stress field, a bubble moves in the direction down the stress gradient, i.e. away from compressive stress. The driving force for such motion is reduction of the Gibbs free energy of the system which comprises two main contributions accounting for the bubble surface (interfaces with the matrix) and gas inside the bubble. Assuming that the gas inside the bubble obeys the ideal law and is in mechanical equilibrium with the matrix at the local hydrostatic stress, two approximations for the driving force F_b are found (Eq. 15.12 for small bubbles and Eq. 15.13 for the large ones) [Ola76].

- For small bubbles, $3\sigma R \ll 4\gamma$:

$$F_b = -\frac{\pi R^4 \sigma}{\gamma}\left(\frac{d\sigma}{dx}\right) \qquad \text{Eq. 15.12}$$

- For large bubbles, $3\sigma R \gg 4\gamma$:

$$F_b = -\frac{4 \pi R^3}{3}\left(\frac{d\sigma}{dx}\right) \qquad \text{Eq. 15.13}$$

Under typical operation conditions the stress gradient provides a much smaller driving force than the temperature gradient (Eq. 15.14) [Ola76] (see also Table 15.1).

$$\frac{(F_b)_{stress}}{(F_b)_{temp}} = \frac{R \sigma^2 a_0^3}{2 \gamma k T (Q_s/kT)} \frac{(1/\sigma)}{(1/T)} \frac{(d\sigma/dx)}{(dT/dx)} \approx 0.03\% \qquad \text{Eq. 15.14}$$

Local stress fields can be introduced by moving dislocations and grain boundaries, thus the dislocations and grain boundaries can drag bubbles along their motion. On the other hand, if mobility of bubbles due to other causes is higher (for example, due to temperature gradient), the same stress fields can pin the bubbles reducing their mobility.

15.1.2.4 Electric field gradient

UO_2 and $(U,Pu)O_2$ present ionic crystals where diffusion of cations (uranium/plutonium ions) and anions (oxygen ions) takes place within a separate sub-lattice. Transport of bubbles and cavities requires movement of both types of species. Non-congruent diffusion or vaporization leads to deviations from stoichiometry, which creates not only concentration gradients but also electric potential.

Such electric potential gradient works against further deviations from stoichiometry, by slowing down or suppressing the diffusion of a faster species, and/or providing additional driving force for diffusion of the slower species.

In practice, this mechanism is not implemented explicitly in models, but rather accounted by natural requirement of congruent diffusion or vaporization fluxes,

This project has received funding from the Euratom research and training programme 2019-2020 under grant agreement No 945022.

and by implying that that the transport of the slowest species is the rate limiting process for the overall bubble motion

15.1.3 Practical examples

To get a feeling on the efficiency of different bubble/pore transport mechanisms a number of calculations were carried out using the equations presented above. The parameters used in the calculations are given in Table 15.1.

The Brownian bubble diffusion coefficients as a function of bubble radius are calculated for two temperatures, 1000 and 2000 K. All three mechanisms for atomic transport are included, surface diffusion, volume diffusion, and vaporization. The results are presented in Figure 15.1 and Figure 15.2. The bubble diffusion coefficients are compared to the atomic Xe diffusion coefficient as defined by Matzke [Mat80]. It is seen that the bubble diffusion only for surface diffusion mechanism and for small bubbles, less than 1 μm for 1000 K, and less than 10 nm for 2000 K, is more efficient than the atomic xenon diffusion. Figure 15.3 and Figure 15.4 demonstrate the diffusion coefficients for bubble diffusion and xenon atomic diffusion as a function of reciprocal temperature. The slope of each curve is defined by the corresponding activation energy. It is expected that vaporization mechanism would dominate at higher temperatures, however using the literature data for U vapor pressure from [Ack69] does not provide the expected steepness of the slope.

Figure 15.3 and Figure 15.4 demonstrate the bubble drift velocity in a temperature gradient of 4000 K/cm and stress gradient 10^{10} Pa/m at a stress 10^4 kN/m^2, both at T= 2000 K. The values for the gradients chosen for the calculations are the same as those used examples in [Ola76]. The bubble radius is 10 nm. Figure 15.3 presents the bubble velocity as a function of bubble radius, and Figure 15.4 presents the bubble velocity as a function of reciprocal temperature. It is seen that for the field gradients used in the calculations the drift velocity due to the thermal gradient is more than 100 times bigger than that for the stress gradient.

In Figure 15.3 (left) it is demonstrated that the drift velocity for surface diffusion is $\propto 1/R$, for volume diffusion is independent from R, and for vaporization $\propto R$, under condition that the fission gas pressure inside a bubble is in equilibrium with the surface tension.

This project has received funding from the Euratom research and training programme 2019-2020 under grant agreement No 945022.

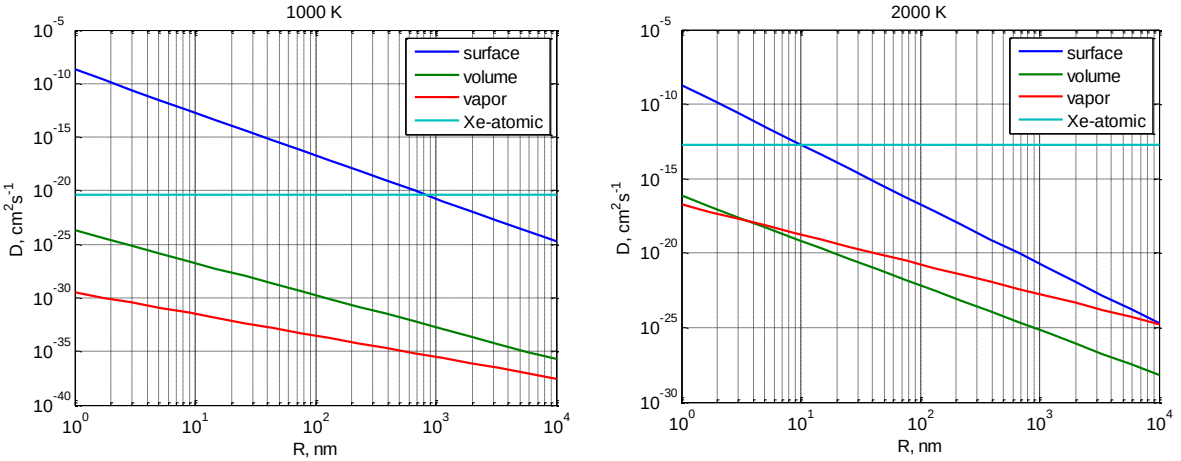

Figure 15.1: Brownian bubble diffusion coefficients as a function of bubble radius.

Calculated for three transport mechanisms and compared to the atomic xenon diffusion coefficient at 1000 K (left) and 2000 K (right). Parameters used in calculation are given in Table 15.1.

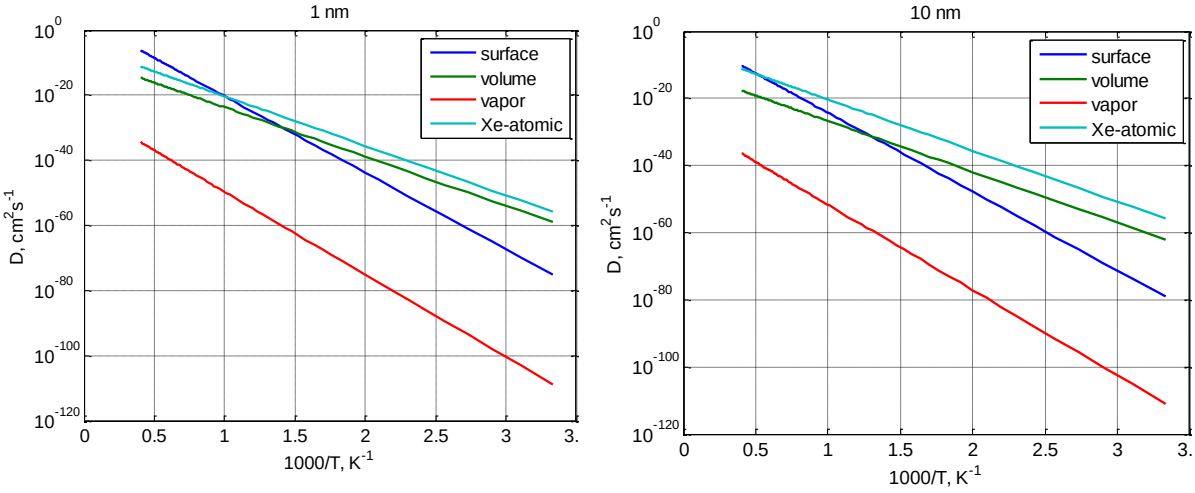

Figure 15.2: Brownian bubble diffusion coefficients as a function of reciprocal temperature.

Calculated for three transport mechanisms and compared to atomic xenon diffusion coefficient. Bubble radius is 1 nm (left) and 10 nm (right). Parameters used in calculation are given in Table 15.1.

This project has received funding from the Euratom research and training programme 2019-2020 under grant agreement No 945022.

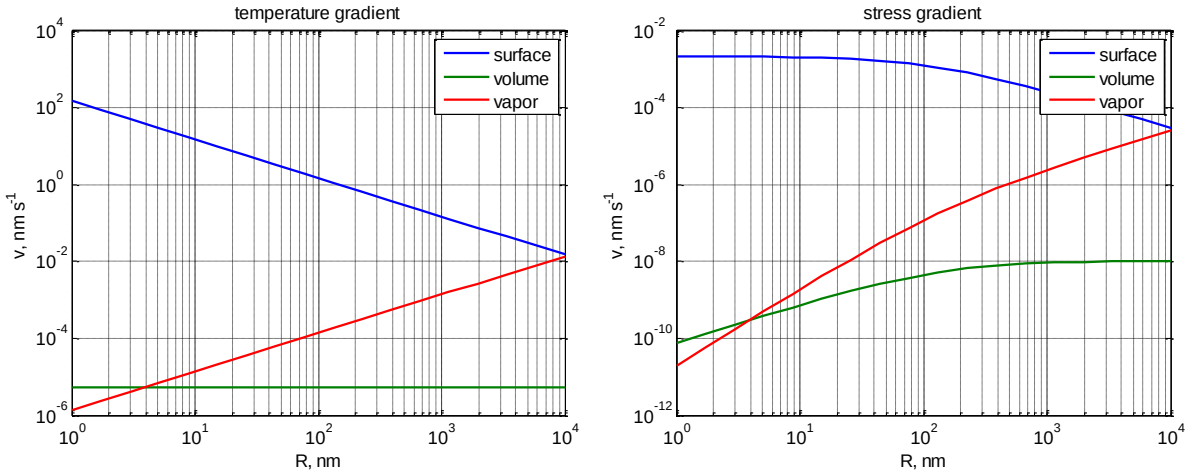

Figure 15.3: Drift bubble velocity in temperature gradient (left) and stress gradient (right) as a function of bubble radius.
The temperature used in the calculations is 2000 K. Other parameters involved are given in Table 15.1.

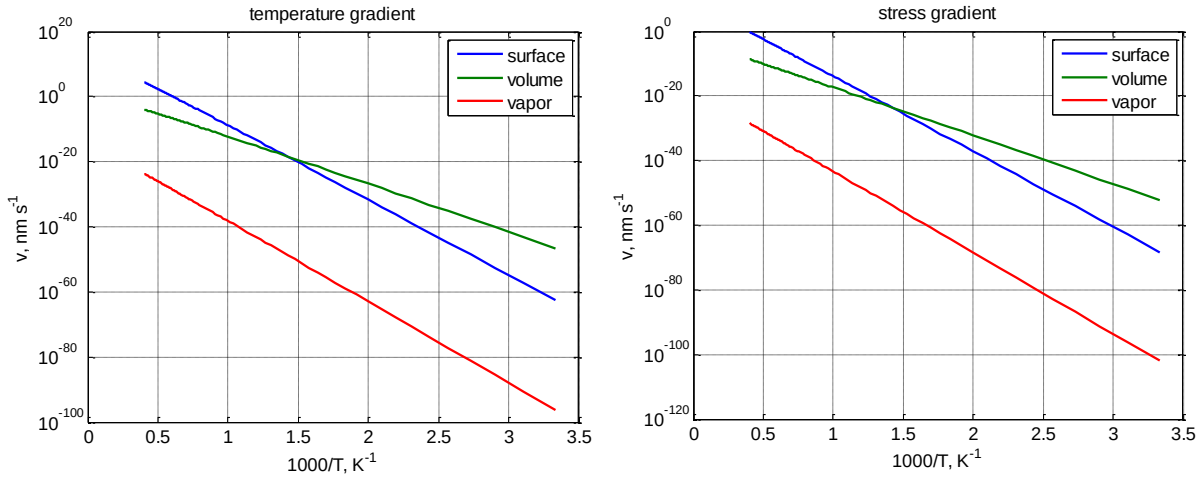

Figure 15.4: Drift bubble velocity in temperature gradient (left) and stress gradient (right) as a function of reciprocal temperature.
The bubble radius used in the calculations is 1 nm. Other parameters involved are given in Table 15.1.

This project has received funding from the Euratom research and training programme 2019-2020 under grant agreement No 945022.

Table 15.1: Parameters used in the calculations, if not specified are taken from [Ola76].

Parameter	Units	Value/expression
R, bubble radius	m	$2\ 10^{-8}$
$a_0^3=\Omega$, atomic volume	m^3	$4\ 10^{-29}$
σ, hydrostatic stress	N/m^2	10^7
$d\sigma/dx$, stress gradient	Pa/m	10^{10}
T, absolute temperature	K	2000
dT/dx, thermal gradient	K/m	$4\ 10^5$
Q_s, heat of transport	kJ/mol	415
D_s, cation surface diffusion at 2000 K	m^2/s	$5\ 10^{-11}$
D_s, cation surface diffusion	m^2/s	$D_s = 4.10^5 \exp\left(-\frac{450000}{RT}\right)$
D_v, cation volume diffusion	m^2/s	$D_s = 4.10^{-11} \exp\left(-\frac{290000}{RT}\right)$
D_{Xe}, Xe atomistic diffusion [Mat89]	m^2/s	$D_{Xe} = 7.6.10^{-10} \exp\left(-\frac{290000}{RT}\right)$
γ, surface tension	N/m	1
U vapor pressure, [Ack69]	Pa	$1.013 \times 10^5 \times 10^{5.71-\frac{25230}{T}}$
P_{Xe}, fission gas pressure inside bubble	Pa	$P_{Xe} = 2\gamma/R$
$D_{Xe,b}$, fission gas diffusion inside bubble	m^2/s	$D_{Xe,b} = 1/3\bar{v}\lambda$
$\bar{v}$, average Xe velocity in gas phase in bubble	m/s	$\bar{v} = \sqrt{\frac{8RT}{\pi\mu}}$
λ, scattering length in gas phase (r – Xe atomic radius)	m	$\lambda = \frac{1}{\sqrt{2}(\pi r^2)n}$
n, fission gas density in bubble	m^{-3}	$n = \frac{N}{V} = \frac{P_{Xe}}{kT}$

15.1.4 Experimental observation

Mobility of pores and bubbles have been observed experimentally and reported in the literature [Ola76; Nic79; Eva96]. It is well accepted that drift of lenticular pores towards the pellet center in the temperature gradient is an important phenomenon, which leads to formation of the central hole and densification of the rest of the fuel. Example of such bubble motion is demonstrated in Figure 15.5. Figure 15.6 shows the velocities of lenticular voids in a temperature gradient created in a laboratory out-of pile experiment. The enthalpy derived in this experiment, 480 $kJ.mol^{-1}$, is close to the value of the heat of vaporization.

This project has received funding from the Euratom research and training programme 2019-2020 under grant agreement No 945022.

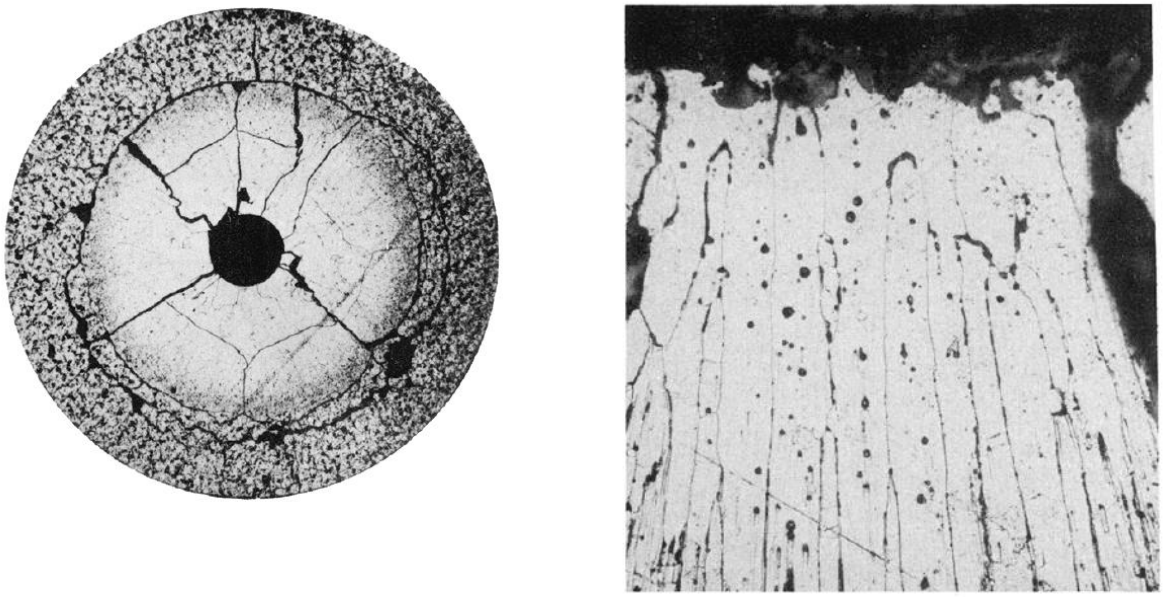

Figure 15.5: Cross-section of ThO_2 + 5 wt% UO_2 fuel rod after irradiation (Ref. 1 in [Nic79]) ; Migration of fission gas bubbles and metallic fission product particles up the thermal gradient in $(Pu_{0.2}U_{0.8})O_2$ fuel rod (Ref. 121 in [Nic79]).

The edge of the central void, toward which they are migrating, is at the top of the figure.

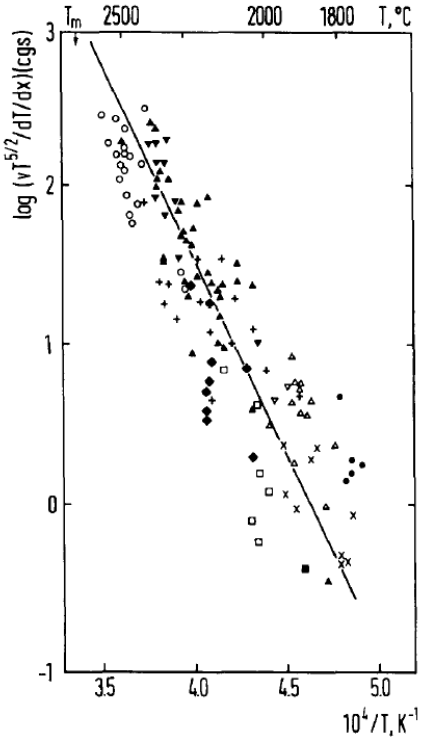

Figure 15.6: Experimentally determined velocities of lenticular voids during the first restructuring of UO_2 in an out-of-pile thermal gradient (Ref. 17 in [Mat89]).

This project has received funding from the Euratom research and training programme 2019-2020 under grant agreement No 945022.

Example of helium bubble migration in temperature gradient UC fuel is demonstrated in Figure 15.7. The observed inverse dependency of the displacement (= velocity) on the bubble radius suggests that the bubble mobility is controlled by the surface diffusion mechanism.

In Figure 15.8 experimental values of bubble diffusivities are compared to a typical effective diffusion coefficient obtained from the out-of pile fission gas release data. It is argued if the bubble diffusion can provide a sufficiently fast gas transport mechanism to explain the gas release experimental results.

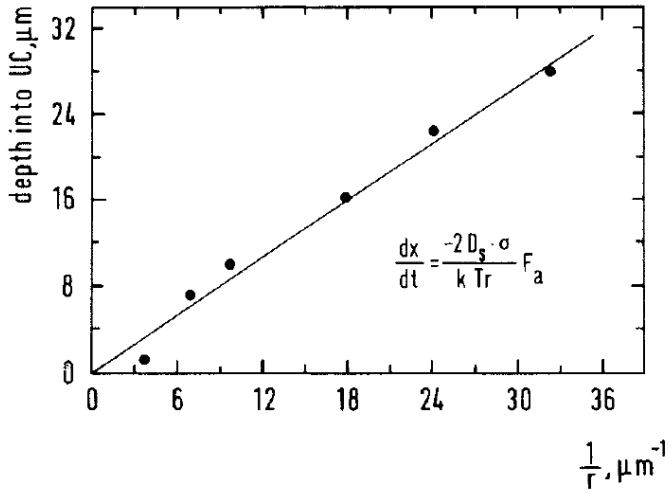

Figure 15.7: Drift of He bubbles in temperature gradient in UC as a function of bubble radius (Ref 95 in [Mat80]).

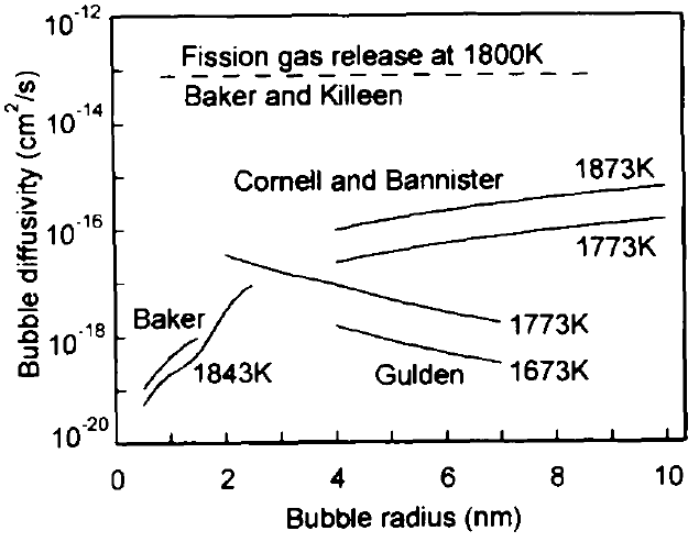

Figure 15.8: Bubble diffusivity in UO_2 as a function of bubble radius compared with an effective diffusion coefficient calculated from gas release measurements. ([Eva95] and references therein).

This project has received funding from the Euratom research and training programme 2019-2020 under grant agreement No 945022.

15.2 Conclusion and recommendations

Transport mechanisms of pores and bubbles in UO_2 and (U, Pu)O_2 fuels are reviewed. On the microscopic level three mechanisms are considered: surface diffusion, volume diffusion and vaporization. In absence of field gradients these mechanisms result in random Brownian motion of bubbles, with mobility strongly reduced with increase of bubble radius. In ionic crystals, such as UO_2 and (U, Pu)O_2, preservation of stoichiometry requires that transport of ions via diffusion or vaporization mechanisms is congruent, therefore mobility of the slowest species defines the rate of the overall bubble transport.

In the presence of field gradients, bubble motion is directional and is characterized by drift velocity. The same three atomistic mechanisms were considered. In case of a thermal gradient, which is the most prominent driving force under typical fuel operation conditions, the bubbles and pores move up the thermal gradient. The surface diffusion mechanism yields a drift velocity which is inversely proportional to the bubble size, and therefore is more applicable for small, sub-micrometer bubbles. For the volume diffusion mechanism, the drift velocity is independent from bubble radius. In case of vaporization mechanisms, the drift velocity is proportional to the bubble radius, and therefore, this mechanism is effective in the region of a few to ten micrometers pores.

As the temperature increases the dominant mechanism shifts from the surface diffusion to volume diffusion, and then to vapor transport.

Other considered field gradients which provide driving forces for bubble motion are thermal vacancy concentration gradients (correlated to the temperature gradient), stress field gradients, and electrostatic potential gradients.

Fission gas bubbles produced during fuel operation should be distinguished from fabricated (pre-existing) porosity because of their shape, sizes, gas pressure, mobility and general behavior are quite different.

Drift of lenticular pre-existing pores towards the fuel pellet center up the temperature gradient is an important phenomenon which results in formation of a central void and fuel densification.

Motion of gas filled bubbles in the temperature or vacancy gradients has been observed experimentally, but it is questioned if this mechanism can dominate over other fission gas transport mechanism: atomic gas diffusion, bubble coalescence and interconnection at grain boundaries.

15.3 References

[Ack69] R. J. Ackermann, E. G. Rauh, J. Phys. Chem., **73 (4)**, 1969, pp 769–778

[Cot02] G. A. Cottrel, J. Nucl. Mater. **302** (2002) 220.

[Eva95] J.H. Evans, J. Nucl. Mater. **225** (1995) 302.

This project has received funding from the Euratom research and training programme 2019-2020 under grant agreement No 945022.

[Eva96] J. H. Evans, J. Nucl. Mater. **238** (1996) 175.

[Geg73] Y. E. Geguzin, Migration of Macroscopic Inclusions in Solids, Springer; 1973, ISBN-13: 978-1475758443.

[Mat80] Hj. Matzke, Radiation Effects, 1980, Vol. 53, pp. 219-242.

[Mat89] Hj. Matzke and H. Blank, J. Nucl. Mater. **166** (1989) 120.

[Nic69] F. A. Nichols, J. Nucl. Mater. **30** (1969) 143.

[Nic79] F. A. Nichols, J. Nucl. Mater. **84** (1979) 1.

[Ola76] D. R. Olander, Fundamental Aspects of Nuclear Reactor Fuel Elements, 1976, ISBN 0-87079-031-5

[Uff02] P. van Uffelen, Contribution to the Modelling of Fission Gas Release in Light Water Reactor Fuel, Thesis, 2002.

This project has received funding from the Euratom research and training programme 2019-2020 under grant agreement No 945022.

16. Diffusion/migration of fission gas

This chapter was originally provided by A. Fedorov (NRG).

16.1 Literature data

In UO_2 and $(U,Pu)O_2$ fuels fission gasses (FG), xenon and krypton, and helium are produced as results of direct fission reactions and transmutation decay chains. At the operation temperatures these inert gases are insoluble in the fuel matrix and mobile. Both factors provide a driving force and necessary conditions for segregation of gas atoms at grain boundaries or dislocations in a form of gas bubbles, and their further growth.

Depending on many factors, such as grain size and diffusion length, the bubbles are formed inside the fuel grains and at the grain boundaries. Further, via various transport mechanisms a considerable fraction of the produced FG is released in the fuel plenum.

Presence of the FG and helium, both in the fuel and in the fuel plenum, affects in great deal operation conditions of the fuel, and limits the fuel lifetime. The formation and growth of the FG bubbles results in fuel swelling, which promotes pellet-cladding gap closure followed by pellet-cladding mechanical interaction (PCMI). Bubbles reduce thermal conductivity of fuel in the same manner as fabricated porosity, leading to higher central temperature.

The fission gas release (FGR) to the fuel rod free volume, on the other hand, causes pressure build-up in the fuel rod plenum and degradation of thermal conductivity of the filling gas. Consequently, the fuel temperature increases, which in turn leads to higher FGR (thermal feedback) until the rod fails due to cladding ballooning and cladding burst.

Swelling and FG release in the plenum are considered as two complementary phenomena.

It is clear that diffusion of fission gasses is central in all process related to behaviour of FG in fuels. This chapter presents an overview of the diffusion parameters in use for transport of FG in MOX and UO_2 fuels.

16.1.1 Definitions and Formulations of FG Diffusion

Various transport mechanisms affecting the fission gas behaviour in nuclear fuel are extensively discussed in the literature [Ola76; Mat80; Mat86; Bal90; Uff02]. The transport mechanisms typically involve the following processes:

- Lattice diffusion of single fission gas atoms and helium
- Trapping at pre-existing defects (impurities, precipitates, dislocations, closed pores) and radiation induced defects (vacancy and vacancy-gas atoms clusters, dislocation loops, fission gas and helium bubbles, fission product precipitates, etc).

This project has received funding from the Euratom research and training programme 2019-2020 under grant agreement No 945022.

- Athermal recoil resolution of fission gas and helium bubbles by energetic fission products and neutrons
- Grain boundary diffusion
- Sweeping of bubbles and gas from the matrix by moving grain boundaries
- Bubble migration
- Bubble interconnection (typically at grain boundary)

Most of the transport mechanisms are implemented in different dedicated FGR models and Fuel Performance Codes (FPC), although not always using the same formulation of equations and parameters. Considering that such complex transport mechanisms as bubble diffusion and grain boundary sweeping are subject of FPC development, this report will rather focus on elementary lattice diffusion of a single (fission) gas atom, which presents the basic process controlling many other transport phenomena.

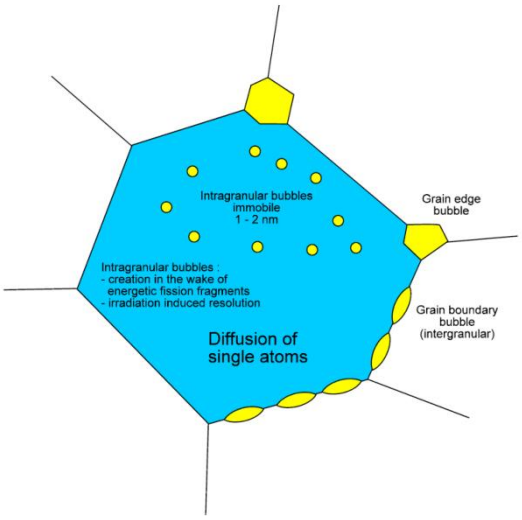

Figure 16.1: Basic mechanisms of fission gas release [Uff02].

Even limiting this discussion to the lattice diffusion of a single fission gas atom some unambiguity in the definitions of the diffusion coefficient has to be resolved first. According to Matzke [Mat80] the following definitions of the bulk diffusion coefficients are considered:

This project has received funding from the Euratom research and training programme 2019-2020 under grant agreement No 945022.

Table 16.1: Definitions of the FG bulk diffusion coefficient's proposed by Matzke [Mat80].

D_{int}	Intrinsic diffusion of a single gas atom in the undamaged fuel lattice. D is affected by deviation from stoichiometry, oxygen potential, and Pu concentration.
D_{trap}^{lab}	Diffusion in the presence of traps, but in the absence of radiation. Measured in laboratory, out-of pile experiments. The traps can be pre-existing and/or irradiation induced (post irradiation examination)
$D_{trap}^{in-pile}$	Diffusion in the presence of both, traps and irradiation, describing gas mobility between fission gas bubbles. Measured in in-pile irradiation experiments.
D_{eff}	$D_{trap}^{in-pile} b/(g+b)$ describing effective mobility including precipitation in bubbles. b – resolution probability; g – capture probability (formulation of Speight).

The D_{trap}^{lab} accounts for detrimental effect of traps (different from bubbles) present within the fuel grains on mobility of the FG. Traps can be both pre-existing and irradiation induced. There is however, no clear reference to the kind of the traps, neither to specific mechanism of trapping and de-trapping mechanisms involved.

The $D_{trap}^{in-pile}$ accounts in addition to enhancement of FG mobility via vacancy assistant diffusion due to introduction of irradiation induced vacancies. Generally $D > D_{trap}^{in-pile} > D_{trap}^{lab}$.

Effect of presence of FG bubbles on the FG mobility is accounted by introducing the effective diffusion coefficient D_{eff} using Speight model:

$$D_{eff} = \frac{b}{g+b} D_{trap}^{in-pile}$$

where b – resolution probability and g – capture probability. The $D_{trap}^{in-pile}$ is FG diffusion coefficient in the fuel matrix between the bubbles. The diffusion controlled capture to the bubbles is:

$$g = 4\pi D_{trap}^{in-pile} R_b N_b$$

where R_b is the average bubbles radius and N_b is the bubbles density. Note that in this approach all bubbles have the same size and gas pressure.

The recoil resolution rate is:

$$b = 3.03 F \pi l_f (R_b + Z_0)^2$$

This project has received funding from the Euratom research and training programme 2019-2020 under grant agreement No 945022.

where *F* represents the fission rate, Z_0 is the radius of the bubble distraction area around the fission fragment track. In a different formulation

$$b = 3 \times 10^{-23} \times F.$$

Turnbull *et al* proposed to describe the single atom gas diffusion in UO_2 grain by considering three diffusion mechanisms dominant in different temperature regimes:

$$D = D_a + D_b + D_c = 7.6 \times 10^{-10} exp(-\frac{3.02}{kT}) + 5.64 \times 10^{-25} \sqrt{\dot{F}}\, exp(-\frac{1.19}{kT}) + 8 \times 10^{-40} \dot{F}$$

D_a is thermally activated intrinsic diffusion dominant above 1400 °C with the Arrhenius type of dependency on the fuel temperature *T*:

$$D_a = D_0 exp(-\Delta H/kT)$$

where D_0 is the pre-exponent factor, ΔH is the activation enthalpy, *T* is the absolute temperature and *k* is the Boltzmann constant $k = 8.62 \times 10^{-5}$ eV/K. Similar to D_{int} in definition of Matzke, D_a describes the intrinsic atomic diffusion in absence of traps and radiation.

Two other terms account for increase in mobility due to radiation. D_b is cation vacancy assisted diffusion, which depends both on the fuel temperature (thermal vacancies) and fission rate density (irradiation induced vacancies).

D_c is the athermal term, which dominates below 250 °C and depends only on the fission rate density.

The retarding effect of trapping on fission gas mobility is not directly included in the Turnbull formulation. The effective diffusion is defined using the same Speight model or similar formulation:

$$D_{eff} = \frac{b}{g + b} D$$

where $D = D_a + D_b + D_c$.

It has been reported in the literature that using the effective diffusion coefficient as introduced above leads to systematic underestimation of the FGR fraction at high temperatures and transients. Therefore, additional transport mechanisms meant to increase FG mobility were considered:

- Grain boundary swiping
- Thermal resolution of bubbles
- Bubble migration, random Brownian or direct drift in thermal gradient

Establishing a relation between the intrinsic diffusion coefficient and measured fission gas release fraction is not trivial, even for laboratory experiments, where the lattice bulk diffusion can be reasonably isolated from other processes. In the reactor in-pile and post irradiation experiments the measured gas released fraction is a results of a whole spectrum of transport phenomena, and for interpretation of such experimental data application of FPC is required.

This project has received funding from the Euratom research and training programme 2019-2020 under grant agreement No 945022.

In a very simple form by interpretation of FGR data two regimes are usually considered:

- FGR fraction < 1%

FG transport inside the fuel grains is described by standard diffusion model with the matrix diffusion coefficient as proposed by Turnbull. The fission gases expelled from the fuel matrix are accommodated within the intra- and intergranular bubbles and pre-existing porosity. FGR from the fuel is moderate (<1%) and mainly due to athermal mechanisms.

- FGR fraction > 1%

Grain boundaries have limited capability to accommodate FG in the form of intergranular bubbles. Eventually the bubbles get interconnected, and the gas accumulated inside the intergranular bubbles is vented to the plenum which results in the onset of the FGR. There is an empirical criterion for the onset of the FGR, which is a function of burn-up and temperature. The widely used Vitanza or Halden burnup threshold criteria for the onset of FGR in UO_2 fuel is formulated as follows:

$BUP\ (MWd/tUO_2) = 5.0 \times \exp\left(\frac{9800}{T_{cl}(℃)}\right)$.

16.1.2 Intrinsic Diffusion Parameters

For the thermally activated diffusion of Xe in UO_2 and $UO_{2\pm x}$, D_a , the following parameters are proposed (all pre-exponent factors are in m^2/s, activation enthalpy in eV, and absolute temperature in K):

- *Near stoichiometric:*

$D_a = 6.7 \times 10^{-10} exp(-3.09(eV)/kT)$, for UO_2 (Turnbull, [Tur82; And12])

$D_a = 0.5 \times 10^{-4} \times exp(-3.9(eV)/kT)$, for UO_2 (Matzke, [Mat86])

- *Non stoichiometric:*

$D_a = 0.5 \times 10^{-4} \times exp(-6.0(eV)/kT)$, for UO_{2-x} (Matzke, [Mat86])

$D_a = 0.5 \times 10^{-4} \times exp(-1.7(eV)/kT)$, for UO_{2+x} (Matzke, [Mat86])

The activation energies for the intrinsic diffusion found in the literature and adopted in various FPC's vary between the values proposed by Turnbull and Matzke. In case of non-stoichiometric fuel the diffusion coefficient decreases with x for UO_{2-x} (sub- stoichiometric) and increases with x for UO_{2+x}, (hyper-stoichiometric), see Figure 16.4. The observed enhancement of the Xe diffusion coefficient for hyper-stoichiometric fuel is correlated with the cation vacancy concentration and mobility, and oxygen interstitial concentration, all increase with *x*. For small deviations from stoichiometry the enhancement is proportional to x^2. At higher deviations because of the cation vacancy clustering saturation will occur [Uff02].

This project has received funding from the Euratom research and training programme 2019-2020 under grant agreement No 945022.

The mixed $(U,Pu)O_{2+x}$ fuel is normally sub-stoichiometric, typically the starting O/(U+Pu) = 1.98, therefore one would expect lower fission gas mobility for MOX fuel [Mat80]. Lower O/M (M=U+Pu) ratio occur in the centre of the pellet and the ratio increases with burn-up. The burn-up, however, does not lead to increase of gas mobility. On the contrary, the gas mobility decrease with the burn-up with further saturation (above 10^{24} f/m^3), because of the build-up of the irradiation induced defects [Mat80].

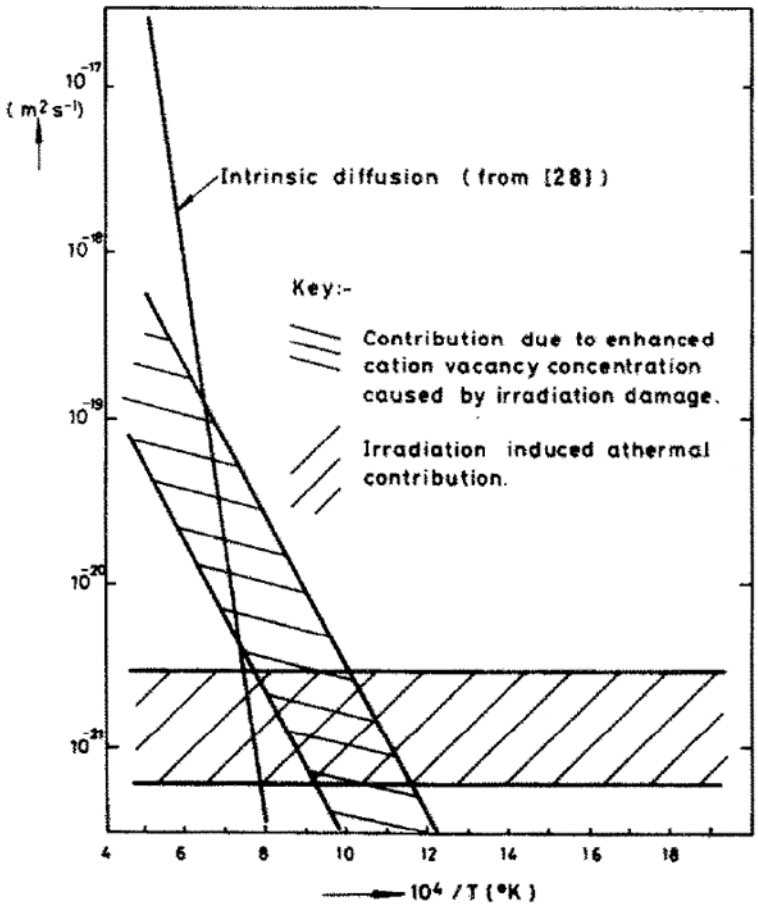

Figure 16.2: Possible components of the in-pile rare gas diffusion coefficient [Tur82].

According to Matzke, the equilibrium site for Xe in stoichiometric UO_2 is neutral trivacancy (Schottky trio) [Mat89]. Equilibrium site for Xe in UO_{2+x} can be charged trivacancy or a single cation vacancy.

Ab initio calculations support that preferred solution site for Xe is V_U-V_O divacancy or V_U-$2V_O$ neutral trivacancy, depending on the oxygen chemical potential. Xe migration requires involvement of another cation vacancy [Bal90; Gov08]. Thus self-diffusion of V_U is rate determining for Xe diffusion.

In [And12] Andersson attempted to compare the experimental enthalpy values proposed by Turnbull and Matzke to the DFT calculations, and to find physical mechanisms responsible for the observed diffusivities. It was argued that depending on stoichiometry, xenon atom occupies different trap sites: V_{UO} (U-O divacancy) for near-stoichiometric UO_2, V_{O2} (O-O divacancy) for UO_{2-x}, and V_U (U-vacancy) for UO_{2+x}. The elementary jump occurs via arrival of a cation vacancy,

This project has received funding from the Euratom research and training programme 2019-2020 under grant agreement No 945022.

V_U. The DFT calculated enthalpy parameters obtained in [And12] are compared with the experimental values in Table 16.2.

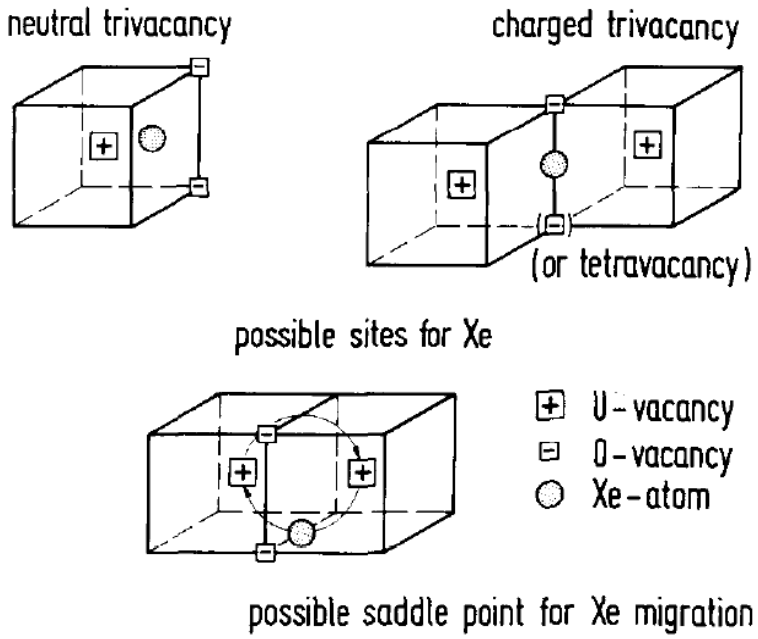

Figure 16.3: Equilibrium lattice site of Xe in UO, and possible migration path [Mat89].

Table 16.2: Calculated and measured Xe and Kr activation energies. All units are in eV [And12].

	UO_{2-x}	UO_2	UO_{2+x}
Xe calculated	5.70	3.86	1.52
Xe experimental	6.0	3.9	1.7
Kr calculated	6.37	4.04	1.61

This project has received funding from the Euratom research and training programme 2019-2020 under grant agreement No 945022.

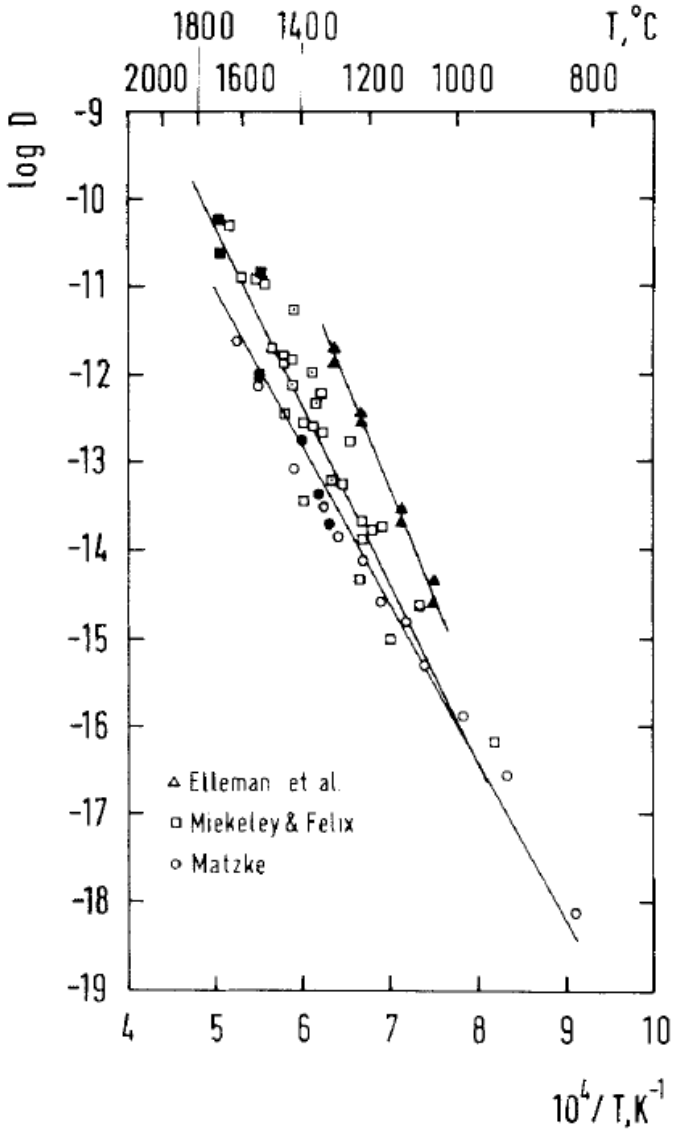

Figure 16.4: Arrhenius diagram for the diffusion of Xe in UO_2. The data are thought to represent largely unperturbed diffusion of single gas atoms [Mat80].

16.1.3 Formulations of FG Diffusion in FPC

A revised expression for the atomic diffusion coefficient was proposed by Turnbull in [Tur00] where in the third term a slight temperature dependence is introduced:

$$D = D_a + D_b + D_c$$
$$= 7.6 \times 10^{-10} exp\left(-\frac{3.02}{kT}\right) + 1.38 \times 10^{-16}\sqrt{R}\exp\left(-\frac{1.19}{kT}\right)$$
$$+ \ 7 \times 67^{-22} R exp(-\frac{0.24}{kT})$$

This project has received funding from the Euratom research and training programme 2019-2020 under grant agreement No 945022.

The formulation for the single atom diffusion coefficient proposed by Turnbull, only with somewhat different parameters is adopted in the FPC TRANSURANUS, model FGRM09 [Las09]:

$$D = D_a + D_b + D_c = 7.6 \times 10^{-10} exp(-\frac{3.02}{kT}) + 3.22 \times 10^{-16} \sqrt{R}\, exp(-\frac{1.19}{kT}) + 6 \times 10^{-23} R,$$

where R is the rating in W/gU. The D_c affects release only from the surface layer typically to a depth of 20 nm. Accordingly, D_c is not used in the stable fission gas release calculations.

A very similar formulation for the atomic diffusion coefficient is adopted in the FPC BISON development at the Idaho National Laboratory (INL) [Pas13]:

$$D = D_a + D_b = 7.6 \times 10^{-10} exp(-\frac{3.03}{kT}) + 1.41 \times 10^{-25} \sqrt{\dot{F}}\, exp(-\frac{1.19}{kT})$$

Note, that the pre-exponent factor for D_b is different, and no athermal contribution is considered.

Also in the SPHERE FPC which was used to model FGR in sphere pack fuel only two first terms were employed:

$$D = D_a + D_b = 7.6 \times 10^{-10} exp(-\frac{3.03}{kT}) + 4.84 \times 10^{-22} \sqrt{\dot{F}}\, exp(-\frac{1.19}{kT})$$

A different formulation for the effective volume diffusion coefficient, D_{eff}, was used by Lemehov et al., (MACROS FPC) to model fission gas release in MOX with high content of Pu:

$$D_{eff} = D_F + D_R + \frac{b_f}{b_f + 4\pi R_b N_b D_T} D_T$$

where

$$D_F = 1.35 \times 10^{-39} \dot{F}$$

$$D_R = 2.0 \times 10^{-7} \sqrt{\dot{F}}\, exp(-\frac{5.155(eV)}{kT})$$

$$D_T = 2.4 \times 10^{-16} exp(-\frac{0.7(eV)}{kT}) + 1.5 \times 10^{-22} \sqrt{\dot{F}}\, exp(-\frac{1.95(eV)}{kT})$$

where D_F is the a-thermal diffusion constant caused by the ion explosion and primary collisions in fission tracks; D_R represents the diffusion mechanisms acting during the quenching phase of primary track zone; D_T is the diffusion coefficient caused by the annealing stage of fission fragment tracks; b_f is the probability of resolution of fission gases accumulated in the intragranular bubbles, R_b is the average radius of intragranular bubbles; and N_b is the volume density of intragranular bubbles.

In FRAPCON3 (FGR model Ans-5.4, MASSIH, based on Forsberg and Massih model) the following formulation for intragranular fission gas diffusion is adopted [Ber97; Lan97]:

This project has received funding from the Euratom research and training programme 2019-2020 under grant agreement No 945022.

$$D_{low} = 2.11 \times 10^{-16} \times exp(-9508/T)$$

$$D_{high} = 3.00 \times 10^{-12} \times exp(-26316/T) \times 100^{(BU-21)/35}$$

$$D = max(D_{low}, D_{high})$$

The model is employed on MOX fuel without modification [Tve07].

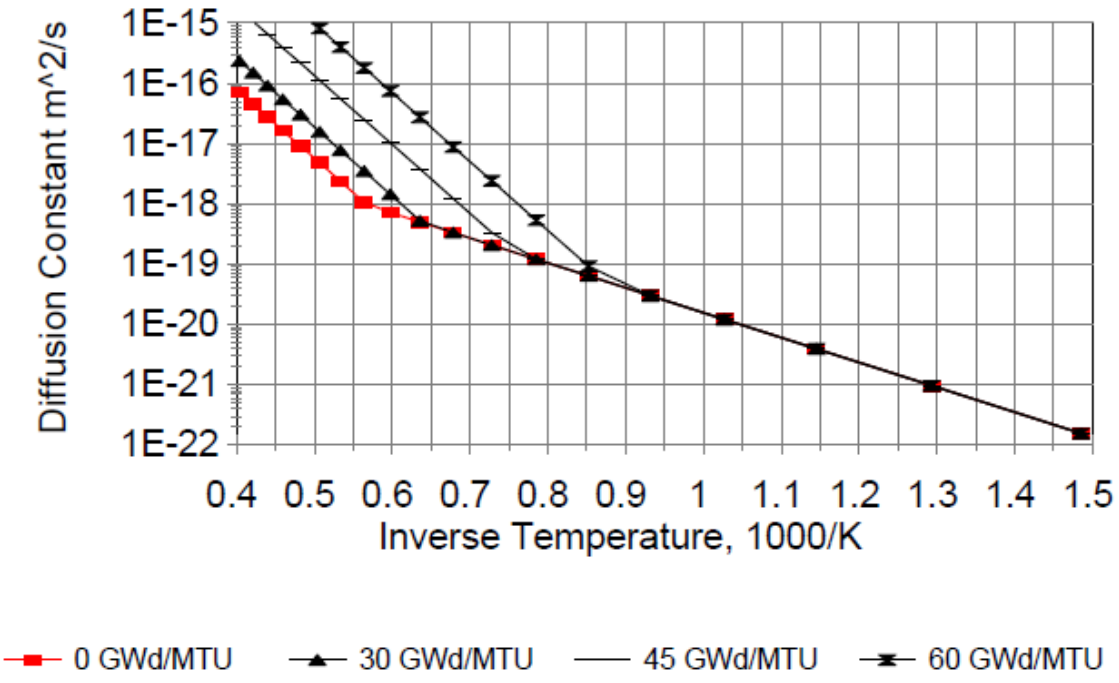

Figure 16.5: FRAPCON-3 (Modified MASSIH Model) Diffusion Constant as a Function of Temperature and Burnup [Lan97].

In Figure 16.6 FG diffusion coefficients adopted in various FPC's to calculate FGR in UO_2 are compared. In this plot a fission rate of $F = 10^{19}$ m^{-3} sec^{-1} is used. Clearly, the spread in the diffusion coefficients in use is substantial.

This project has received funding from the Euratom research and training programme 2019-2020 under grant agreement No 945022.

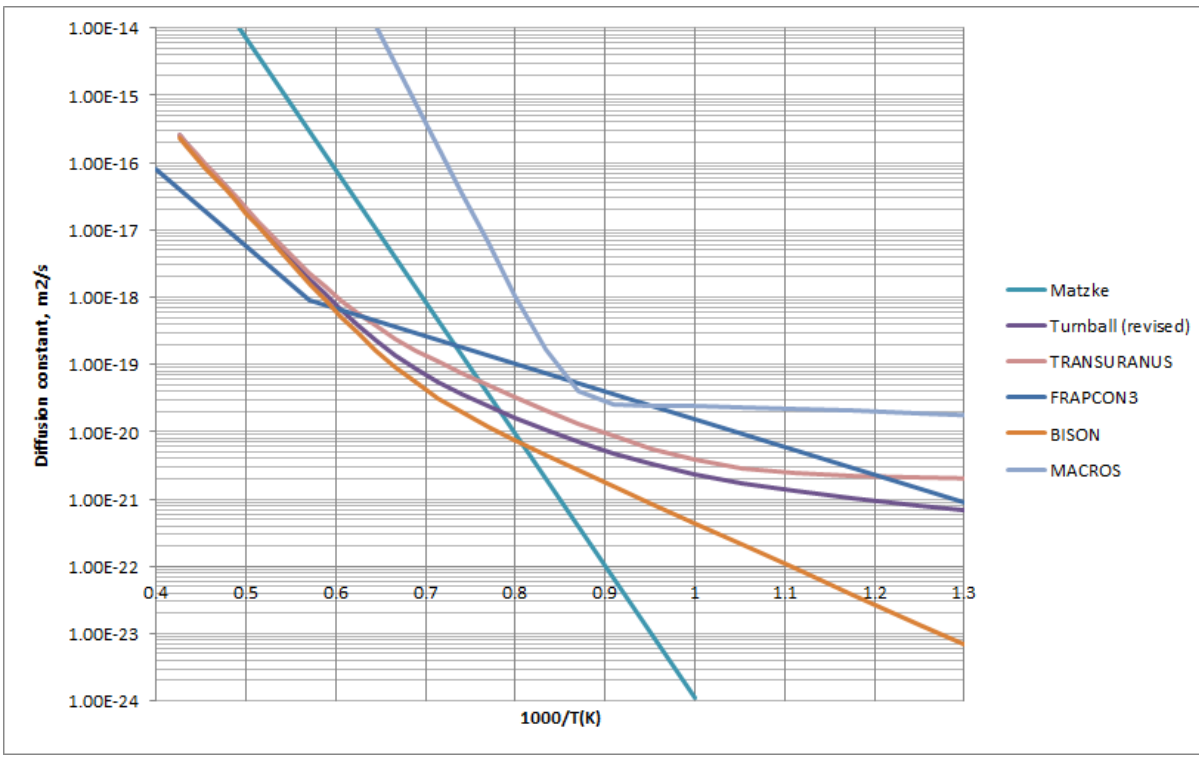

Figure 16.6: FG atomic diffusion coefficient in fuel grain used in different FPC. (In calculations the fission rate $F = 10^{19}$ $m^{-3}sec^{-1}$ is used).

It should be mentioned that inert gases Kr and Xe are practically not formed directly by fission, but rather produced via β-decay from the precursor: Se and Br in the case of Kr, Te and I in the case of Xe. Many of such precursors are mobile and have a half-life long enough to contribute in the final distribution of the inert gases. The precursor mobility can even exceed the inert gas mobility. For example, I and Te diffuse faster than Xe, and Br diffuses faster than Kr. The precursor enhancement of the fission gas mobility for most isotopes is less than 30%, and in some FPC is incorporated in the effective diffusion coefficient [Ola76; Uff02].

16.1.4 Fission gas release in MOX fuel

Production and release of fission gases and helium both in MOX and UO_2 fuel have critical impact on the fuel operation and life time.

Although production of xenon and krypton is slightly lower in MOX, helium is produced in much bigger quantities (4-10 times higher than in UO_2). Moreover, helium production takes place both during fuel operation and after discharge from the reactor. The latter is relevant for fuel storage.

In most of the reported data, for both steady-state and power ramps, MOX fuels show larger FGR than UO_2 for the same burn-up. This is mainly attributed to lower thermal conductivity of MOX, stronger degradation rate of the thermal conductivity with burnup, and higher linear powers at EOL.

Implementation of the MOX thermal conductivity alone in FPC's and using the same unmodified UO_2 models for FG transport typically lead to under-prediction of FGR in MOX.

This project has received funding from the Euratom research and training programme 2019-2020 under grant agreement No 945022.

Other important feature of MOX fuel which is hold responsible for high FGR is microstructural non-homogeneity. MOX fuel contains Pu-rich agglomerates which during operation reach extremely high local burnup and attain a microstructure similar to HBS in rim UO_2. Fission gases produced in these Pu-rich grains are accumulated inside the pores of the HBS and in bubbles at grain boundaries. A practical approach to account for this effect is to reduce the threshold burnup for the fission gas release onset (applied in FPC COPERNIC).

Most FPC's employed to model FGR in MOX use Booth-Speight models for grain diffusion with the unmodified diffusion coefficient in Turnbull formulation validated for UO_2:

$$D = C_1 exp(-\frac{Q_1}{kT}) + C_2\sqrt{\dot{F}}\, exp(-\frac{Q_2}{kT}) + C_3\dot{F}$$

Here the first term is the thermally activated intrinsic diffusion which is dominant above 1400 °C, the second term is irradiation induced enhancement of the cation vacancy assisted diffusion, and the third term represents athermal mobility present below 250 °C. $\dot{F}$ is the fission rate in fissions.m^{-3}.sec^{-1}, T is the absolute temperature in K and k is the Boltzmann constant.

Even for UO_2 the coefficients used in different FPC have a substantial spread:

		pre-exponent	activation energy, in eV (K)
1	thermally activated	7.6×10^{-10} [m^2/s]	3.02(35000)-3.09(35858)
2	irradiation induced vacancy assisted	4.84×10^{-18} – 5.64×10^{-25} [m$^{7/2}$ s$^{-1/2}$]	1.19(13800)
3	athermal	0-8 $\times10^{-40}$ [m^7]	

In order to improve agreement with experimental data in FRAPCON3, for example, the diffusion coefficient was increased by factor 1.7. On the other hand, the diffusion coefficients used in various FPC and validated on UO_2 already vary by decades.

Involvement and adjustment of other transport mechanisms in FPC's which potentially can enhance FGR in MOX, grain boundary swiping, bubble migration, etc, has not been reported.

16.2 Conclusions and recommendations

Direct use of the diffusion parameters for Fission Gas in UO_2 to model Fission Gas Release (FGR) in MOX fuel generally would lead to underprediction of FGR. To obtain higher values of FGR some models use practical empiric corrections: simple multiplication factor or reduction of the threshold burn-up for FGR onset.

Considering clear demand in reliable prediction of FGR in MOX fuel more physically based adaptation of present FPC's is required.

This project has received funding from the Euratom research and training programme 2019-2020 under grant agreement No 945022.

16.3 References

[And12] D. Andersson, Bulk and surface controlled diffusion of fission gas atoms, Los Alamos National Laboratory report, LA-UR-12-24002.

[Bal90] R.G.J. Ball and R.W. Grimes. Diffusion of Xe in UO_2. J. Chem. Soc. Faraday Trans., **86** (1990) 1257.

[Ber97] G.A. Berna, C.E. Beyer, K.L. Davis, D.D. Lanning, FRAPCON-3: A Computer Code for the Calculation of Steady-State, Thermal-Mechanical Behavior of Oxide Fuel Rods for High Burnup, December 1997, NUREG/CR-6534, Volume 2, PNNL-11513

[Gov08] K. Govers, Atomic scale simulations of noble gases behaviour in uranium dioxide, Thesis, Université Libre de Bruxelles, 2008

[Lan97] D.D. Lanning, C.E. Beyer, C.L. Painter, FRAPCON-3: Modifications to Fuel Rod Material Properties and Performance Models for High-Burnup Application, October 1997, NUREG/CR-6534, Volume 1,PNNL-11513.

[Las09] K. Lassmann, A. Schubert, P. Van Uffelen, Cs. Győri, J. van de Laar, TRANSURANUS HANDBOOK, version 'V1M1J09', January 2009, D-76125 Karlsruhe.

[Mat80] Hj. Matzke, Radiation Effects **53** (1980) 219.

[Mat86] Hj. Matzke, J. Less-Common Metals **121** (1986) 537.

[Mat89] Hj. Matzke and H. Blank, J. Nucl. Mater. **166** (1989) 120.

[Ola76] D.R. Olander, Fundamental Aspects of Nuclear Reactor Fuel Elements, 1976, ISBN 0-87079-031-5

[Pas13] G. Pastore, J.D. Hales, S.R. Novascone, D.M. Perez, B.W. Spencer, R.L. Williamson, Analysis of Fission Gas Release in LWR Fuel Using the BISON Code, LWR Fuel Performance Meeting/Top Fuel 2013, INL/CON-13-28389, September 2013

[Tur82] J.A. Turnbull, C.A. Friskney, J.R. Findlay, F.A. Johnson and A.J. Walter, J. Nucl. Mater. **107** (1982) 168.

[Tur00] J.A. Turnbull and E. Kolstad, Investigations On Radioactive And Stable Fission Gas Release Behaviour At The HALDEN Reactor, in Proceedings of the Fission Gas Behaviour In Water Reactor Fuels Seminar, Cadarache, France, 26-29 September 2000, p 369.

[Tve07] T. Tverberg, Mixed-oxide (MOX) Fuel Performance Benchmark, OECD Halden Reactor Project, NEA/NSC/DOC(2007)6 No. 4450, 2007

[Uff02] P. van Uffelen, Contribution to the Modelling of Fission Gas Realease in Light Water Reactor Fuel, Thesis, 2002.

This project has received funding from the Euratom research and training programme 2019-2020 under grant agreement No 945022.

17. Diffusion/migration of U and Pu

This chapter was originally provided by M.A. Mignanelli (NNL).

17.1 Literature data

The large radial temperature gradient in a mixed oxide fuel pin during irradiation in a fast reactor causes a redistribution of the actinide cations due to diffusion (more specifically, thermal diffusion) and/or migration of certain species.

After many months of irradiation, the net result is a Pu/U molar ratio which is higher in the hot, inner region of the fuel pellets than in the cold, outer region. Modelling this change in relative Pu concentration is necessary since this has an effect on in-reactor fuel performance and potentially also on the ability to reprocess the fuel (since solubility in nitric acid decreases with increasing Pu content). With respect to in-reactor fuel performance: heat generation by fission becomes higher in the inner region, leading to increases in fuel centreline temperature; and the local thermal conductivity, creep rate and solidus/liquidus temperatures along the fuel radius are altered, although it is important to note that these are also strongly affected by changes in local stoichiometry (that is, in oxygen-to-metal molar ratio). The change in Pu/U molar ratio is difficult to measure, but has been observed in high burn-up fuel irradiated with high centreline temperatures (e.g. by electron probe microanalysis (EPMA) of radial fuel sections during post-irradiation examination).

For solid fuel, the processes by which uranium and plutonium can diffuse or migrate in the radial temperature gradient have been discussed by Clement and Finnis [Cle78a]. Three possible mechanisms were identified:

- (a) Pore migration,
- (b) Migration along cracks,
- (c) Diffusion in the solid (which can be volume, surface, or grain boundary diffusion).

For molten fuel, an additional solidus-liquidus separation process may occur [Bob73a], but this is not considered further in this review.

A pore migrating towards the centre of the fuel by evaporation-condensation provides an opportunity for redistribution of the heavy metal atoms to occur (mechanism (a)). Since the vapour pressure of uranium-bearing species (UO_2, UO_3) exceeds that of the plutonium-bearing species (primarily PuO and PuO_2), the uranium oxides will evaporate faster from the hotter side of the pore, and a Pu-rich region will therefore build up at the section of the pore surface that is closest to the fuel centreline. This local plutonium excess can then diffuse towards the centre of the fuel.

Clement and Finnis [Cle78b] developed a model for pore migration where pores are idealised as thin discs. The Pu current (that is, the relative concentration of Pu

This project has received funding from the Euratom research and training programme 2019-2020 under grant agreement No 945022.

being transported per unit area per unit time) due to pore migration, J_P, is given by Eq. 17.1:

$$J_P = \frac{pD^e}{d}.\delta c.\exp\left(-\frac{D^e}{lv}\right) \qquad \text{Eq. 17.1}$$

where D^e is the mean value of the Pu diffusion coefficient in the Pu-rich layer in front of the migrating pore, p is the volume fraction of the coarse porosity, v is the pore velocity, l is the pore diameter, d is the pore thickness, and

$$\delta c = \frac{lc}{20}\nabla T \qquad \text{Eq. 17.2}$$

where c is the relative plutonium concentration (i.e. Pu/(U+Pu)) and T is the temperature.

The exponential term in Eq. 17.1 is to allow for the fact that if pore velocities are too low, the excess plutonium will have time to migrate around the pores to their colder side, thereby tending to negate the plutonium current towards the centre of the fuel.

Preferential evaporation/condensation of the more volatile uranium oxides along cracks is another possible mechanism whereby plutonium concentrations could be enhanced in the central regions of pellets (mechanism (b)). However, Clement and Finnis [Cle78a] have shown that, in practice, the concentration of cracks is too low for such a process to have a significant effect. Accordingly, this particular mechanism is not considered any further.

The third mechanism is solid-state diffusion in a temperature gradient (mechanism (c)). The plutonium current due to solid-state diffusion, J_S, is represented by Bober *et al* [Bob73a], and by Bober and Schumacher [Bob73b], as given by Eq. 17.3.

$$J_S = -D\left[\nabla c + c(1-c).\frac{Q^*\nabla T}{RT^2}\right] \qquad \text{Eq. 17.3}$$

where D is the diffusion coefficient of Pu, Q^* is the heat of transport, and R is the gas constant (strictly, D is the chemical interdiffusion coefficient of U and Pu, but this is equal to the self-diffusion coefficient of Pu to a good approximation). Calculations by Clement and Finnis [Cle78a] suggest that, in general, this particular mechanism should be the most significant in determining the redistribution of uranium and plutonium. In addition, Thetford [The91] has shown that, compared with the plutonium current due to solid-state diffusion, the current due to pore migration is only significant in the case of fresh fuel, or fuel which has experienced very low burn-up (since as irradiation proceeds, the porosity migrates to the central void, so that the value of *p*, and therefore the relative importance of this mechanism, drops). Hence, transport by solid-state diffusion should be regarded as the most significant mechanism, since it is known that uranium/plutonium transport is a fairly slow process that takes place over the course of months, if not years.

This project has received funding from the Euratom research and training programme 2019-2020 under grant agreement No 945022.

17.1.1 Volume diffusion coefficient

Recommendation is given here after for the cation diffusion coefficient in $(U,Pu)O_{2+x}$ fuel (which is also applicable to UO_{2+x}), where x can be either negative (hypostoichiometric fuel) or positive (hyperstoichiometric fuel). The recommendation is strictly only applicable out-of-pile, since it is fitted to out-of-pile data.

Using the law of mass action and an assumption of local electroneutrality, the relative anion vacancy concentration (molar fraction of vacancies), V, is given by Eq. 17.4a [Lid66].

$$2V = -x + \sqrt{x^2 + 4K_F} \qquad \text{Eq. 17.4a}$$

where K_F is the law of mass action equilibrium constant for the formation of Frenkel defects on the anion sub-lattice. Using the expression for K_F from the derivation of the catalogue recommendation for the anion diffusion coefficient then leads to Eq. 17.4b.

$$2V = -x + \sqrt{x^2 + 6.792.10^5 \exp\left(-\frac{45937}{T}\right)} \qquad \text{Eq. 17.4b}$$

The cation diffusion coefficient is expressed as the sum of three terms for diffusion via divacancies (anion-cation vacancy pairs), single cation vacancies, and cation interstitials, respectively. The dependence of each of these three terms on the relative anion vacancy concentration, V (inverse dependence, inverse square dependence, and square dependence, respectively) is consistent with a direct proportionality to the relative concentrations of divacancies, single cation vacancies, and cation interstitials, as shown by Lidiard [Lid66]. The activation energies and pre-exponential factors in the three terms were fitted to a variety of tracer diffusion coefficient measurements and their associated activation energies for both U in UO_2 and Pu in mixed oxide fuel. In addition, activation energies obtained from creep measurements were included in the fitting exercise.

The resulting expression for the cation diffusion coefficient, D_c ($m^2.s^{-1}$), is given by Eq. 17.5:

$$\mathrm{D_c} = \frac{2.38.10^{-3}}{\mathrm{V}} \exp\left(-\frac{85547}{\mathrm{T}}\right) + \frac{32.18}{\mathrm{V}^2} \exp\left(-\frac{115119}{\mathrm{T}}\right) + 1.97.10^{-2}\mathrm{V}^2 \exp\left(-\frac{70423}{\mathrm{T}}\right) \qquad \text{Eq. 17.5}$$

Sample values of the cation diffusion coefficient derived from Eq. 17.5 for the hypostoichiometric, stoichiometric and hyperstoichiometric oxides are shown in Table 17.1(a) and (b).

Diffusion coefficients calculated using Eq. 17.5 are compared with the tracer diffusion results in Figure 17.1 to Figure 17.3 – the open symbols denote Pu tracer diffusion and the closed symbols U tracer diffusion. Figure 17.4 compares the

This project has received funding from the Euratom research and training programme 2019-2020 under grant agreement No 945022.

activation energy predicted by the model with that measured from creep experiments. The minimum diffusion coefficients and the maximum activation energy occur for very slightly hypostoichiometric material. Table 17.2 relates the references shown in these figures with the references at the end of this chapter.

Table 17.1: Recommended cation diffusion coefficients for mixed oxide fuel.

Temp (K)	Deviation to stoichiometry				
	-0.10	**-0.08**	**-0.06**	**-0.04**	**-0.02**
1000	-34.29	-34.48	-34.73	-35.09	-35.69
1250	-28.17	-28.37	-28.62	-28.96	-29.54
1500	-24.09	-24.28	-24.53	-24.86	-25.28
1750	-21.17	-21.36	-21.58	-21.85	-22.01
2000	-18.97	-19.14	-19.32	-19.47	-19.38
2250	-17.21	-17.34	-17.44	-17.44	-17.26
2500	-15.69	-15.75	-15.78	-15.76	-15.68
2750	-14.29	-14.33	-14.36	-14.37	-14.37
3000	-13.03	-13.05	-13.08	-13.11	-13.13

(a) $\log_{10}D$ (m^2s^{-1}) for hypostoichiometric oxide.

Temp (K)	Deviation to stoichiometry						
	0.0	**0.02**	**0.04**	**0.06**	**0.08**	**0.10**	**0.20**
1000	-32.40	-22.45	-21.84	-21.49	-21.24	-21.05	-20.45
1250	-26.91	-20.43	-19.82	-19.47	-19.22	-19.03	-18.43
1500	-23.21	-19.08	-18.48	-18.12	-17.88	-17.68	-17.08
1750	-20.52	-18.09	-17.50	-17.16	-16.91	-16.72	-16.12
2000	-18.48	-17.29	-16.75	-16.41	-16.17	-15.98	-15.39
2250	-16.88	-16.42	-16.05	-15.78	-15.56	-15.38	-14.81
2500	-15.55	-15.40	-15.23	-15.08	-14.93	-14.80	-14.32
2750	-14.36	-14.32	-14.28	-14.23	-14.17	-14.11	-13.80
3000	-13.15	-13.16	-13.17	-13.18	-13.18	-13.18	-13.12

(b) $\log_{10}D$ (m^2s^{-1}) for stoichiometric and hyperstoichiometric oxide.

This project has received funding from the Euratom research and training programme 2019-2020 under grant agreement No 945022.

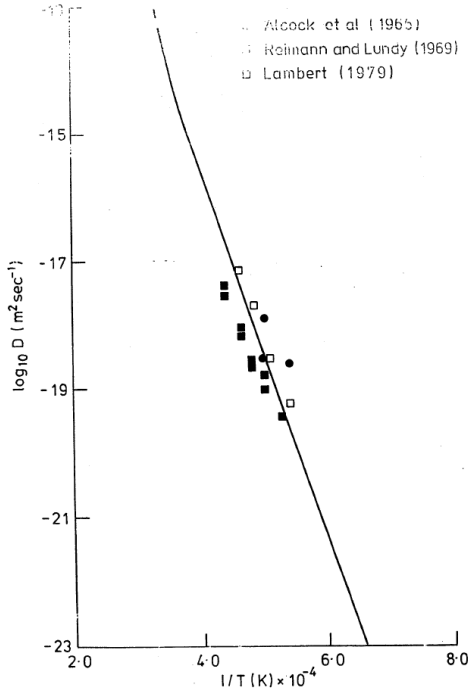

Figure 17.1: Comparison of recommendation with experiments for MO2.

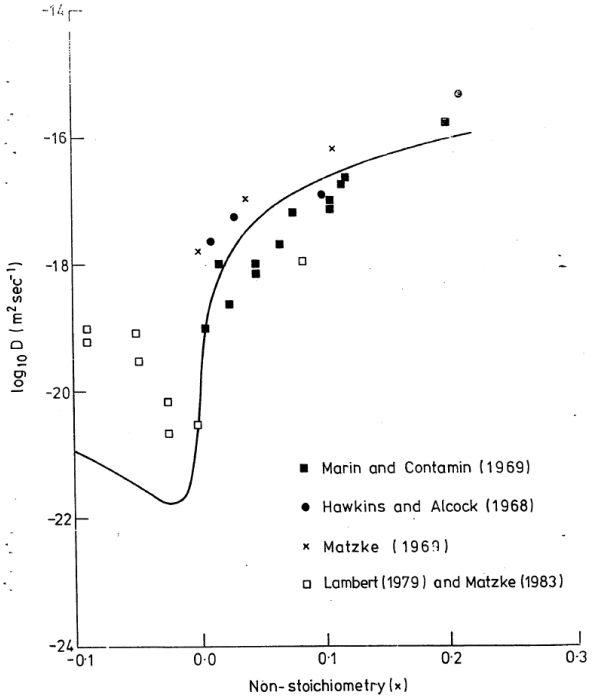

Figure 17.2: Comparison of recommendation with experiments at 1773K.

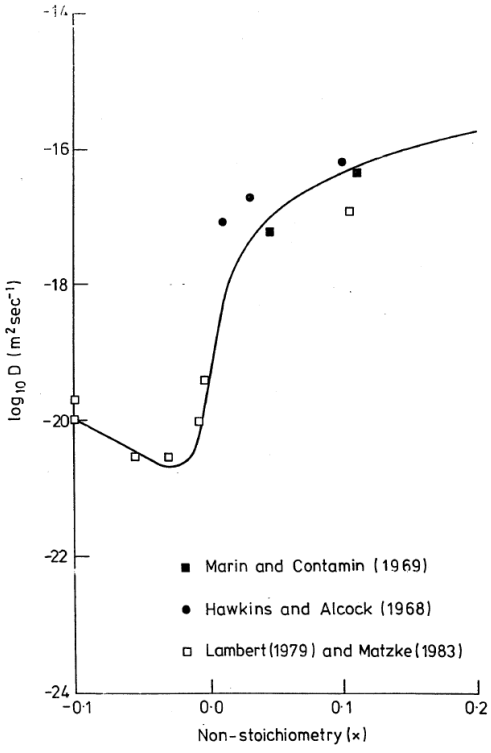

Figure 17.3: Comparison of recommendation with experiments at 1873K.

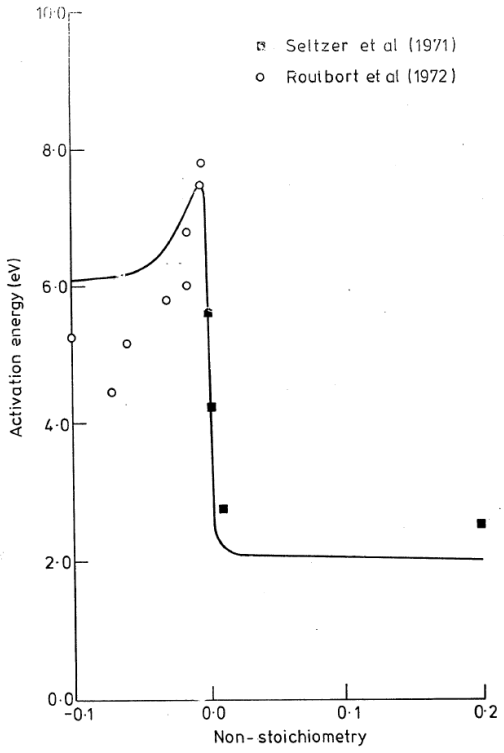

Figure 17.4: Comparison of recommendation with the activation energy from creep data.

This project has received funding from the Euratom research and training programme 2019-2020 under grant agreement No 945022.

Table 17.2: Related references for Figure 17.1 to Figure 17.4.

Ref on Figure 17.1 to Figure 17.4.	Associated reference
Alcock et al (1965)	[Alc65]
Reimann and Lundy (1969)	[Rei69]
Lambert (1979) and Matzke (1983)	[Mat83b]
Marin and Contamin (1969)	[Mar69]
Hawkins and Alcock (1968)	[Haw68]
Matzke (1969)	[Mat69]
Seltzer et al (1971)	[Sel71]
Routbort et al (1972)	[Rou72]

17.1.2 Surface and grain boundary diffusion coefficients

The recommended equation for calculating the surface cation self-diffusion coefficient (which was derived for UO_2) is given by [Mat83b] as per Eq. 17.6.

$$D_c(surf) = 50.\exp\left(-\frac{54152}{T}\right) \qquad [m^2.s^{-1}] \qquad \text{Eq. 17.6}$$

However, Matzke [Mat83b] places no great confidence in this expression due to the significant uncertainty. (It should be noted that there is a typographical error in this reference [Mat83b] for the pre-exponential factor, which was incorrectly derived from a previous survey [Mat76].)

Lambert [Lam78, Mat83b] has used his measured volume diffusion coefficients to re-analyse the UO_2 data of Yajima *et al* [Yaj66] and obtained the following expression for the grain boundary diffusion coefficient:

$$D_c(gb) = 2.62.10^{-3}\exp\left(-\frac{39587}{T}\right) \qquad [m^2.s^{-1}] \qquad \text{Eq. 17.7}$$

A grain boundary diffusion coefficient has also been deduced by Reynolds and Burton from UO_2 creep and sintering measurements [Rey79] and is given in Eq. 17.8.

$$D_c(gb) = 1.38.10^{-6}\exp\left(-\frac{28760}{T}\right) \qquad [m^2.s^{-1}] \qquad \text{Eq. 17.8}$$

Eq. 17.8 gives values about an order of magnitude lower than Eq. 17.7 in the temperature region where Eq. 17.7 was obtained (2173 – 2423 K), and is broadly consistent with the values deduced by Olander [Ola87] in mixed $(U,Th)O_2$. However, it is recommended that Eq. 17.7 should be used to calculate the grain

This project has received funding from the Euratom research and training programme 2019-2020 under grant agreement No 945022.

boundary diffusion coefficient, although it was noted that no great confidence should be placed in the values obtained.

Neither of the recommendations above take account of the effects of deviations from stoichiometry. This is because there were said to be no reliable data available on these effects for either surface or grain boundary diffusion coefficients. Marin [Mar69] has shown that the grain boundary diffusion coefficient is much larger in hyperstoichiometric UO_2 than stoichiometric material (activation energy falls from 2.95 eV to 1.99 eV) but the data were judged to be too scattered to be used as the basis for a recommendation which is dependent on deviation from stoichiometry.

Studies on actinide redistribution mechanisms in mixed oxide fuel have been reported by Di Marcello *et al* [Mar14]. Models for the solid-state thermal diffusion and vapour transport of plutonium and americium were incorporated into the TRANSURANUS fuel performance code [Las92]; the effect of fuel non-stoichiometry on both diffusion coefficient and pore velocity was taken into account. The actinide redistribution occurring by thermal diffusion was determined using the approach derived by Bober *et al* [Bob73a] (as previously described). The Pu diffusion coefficient was that proposed by Bober and Schumacher [Bob73b] (for fuel with an O/M ratio of 1.98) adjusted by a function F(O/M) to take account of the dependence on deviation from stoichiometry as given in Eq. 17.9.

$$D_c = 3.4.10^{-5}\exp\left(-\frac{55891}{\mathrm{T}}\right)\frac{F(\frac{O}{M})}{F(1.98)} \qquad [m^2.s^{-1}] \qquad \text{Eq. 17.9}$$

The function F(O/M) was developed based on the available experimental data [Mar12]. The actinide redistribution occurring by pore migration was modelled by the approach of Clement and Finnis [Cle78a] (as previously described).

The TRANSURANUS plutonium and americium transport models were validated against post-irradiation examination data from two short-term irradiation experiments – B11 and B14 – performed in the JOYO experimental fast reactor [Mae09, Mae11]. The fuel tested was MOX with minor actinide additions. The calculated actinide distribution is in good agreement with the experimental data, although it was noted that more accurate measurements of pore velocity and Pu diffusion coefficient as a function of O/M ratio and temperature are required to improve predictions of Pu transport; the results for pin PTM0001 containing $U_{0.666}Pu_{0.31}Am_{0.024}O_{1.98}$ are shown in Figure 17.5. These results, together with those from simulated irradiations to higher burn-ups, confirm that under normal operation conditions with a decreasing fuel power, redistribution via pore migration is important only during the central hole formation at the beginning of life, whereas thermal diffusion represents the dominant effect for long-term irradiation.

This project has received funding from the Euratom research and training programme 2019-2020 under grant agreement No 945022.

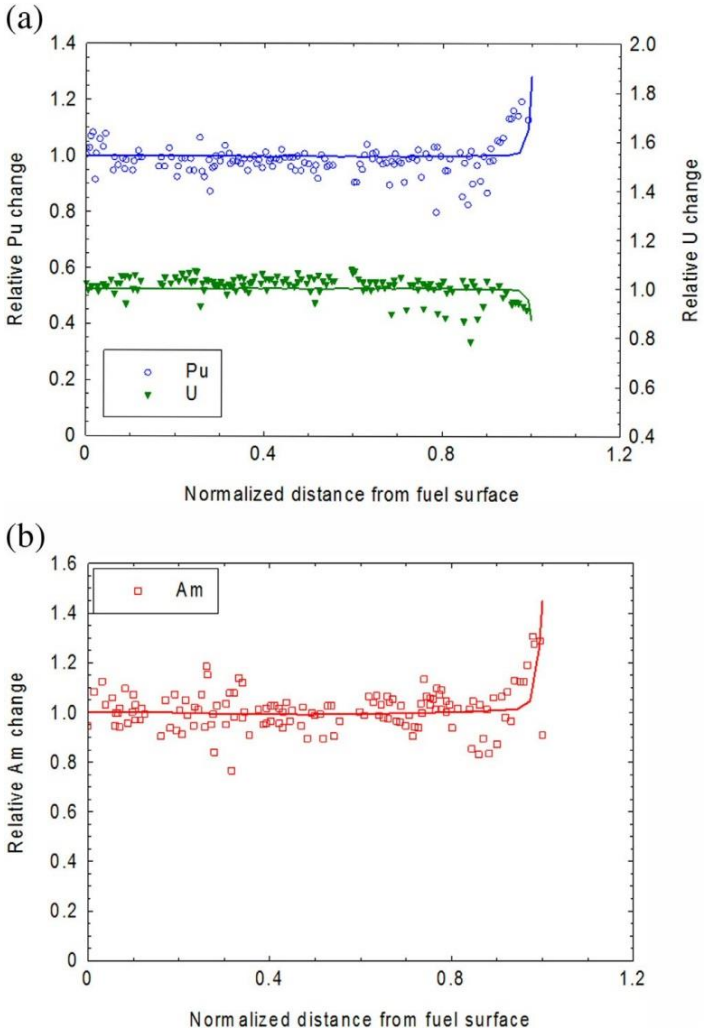

Figure 17.5: Calculated and measured normalised radial profiles of U, Pu (a) and Am (b) for the PTM0001 fuel pin from the JOYO B14 experiment [Mar14].

The computer code FEAST-OXIDE has been developed to predict the steady-state and transient behavior of mixed oxide fuel in sodium-cooled fast reactors [Kar10]. Pu transport is simulated using Bober et al's model for solid-state diffusion [Bob73a], with the same Pu diffusion coefficient. The FEAST-OXIDE code was benchmarked against the available FFTF, EBR-II and JOYO database for steady-state and transient irradiations. The agreement for all these benchmarks was satisfactory.

Both the TRANSURANUS and FEAST-OXIDE Pu transport models described above were based on equivalent models in the CEDAR code [Ish01]. The CEDAR predictions were validated against experimental data from various irradiations (up to burn-ups of 110 GWd/t) of JNC MOX fuel with O/M ratios of 1.95 to 1.99 and Pu contents of 27 to 30 wt%. Measured radial Pu profiles have been published for two specimens – XD0992 and XD1071 – both of which were irradiated for 560 effective full power days to a burn-up of ~ 110 GWd/t. XD0992 had an O/M ratio of 1.99 and a Pu content of 27 wt%, while XD1071 had an O/M ratio of 1.955 and a Pu content of 30 wt%.

This project has received funding from the Euratom research and training programme 2019-2020 under grant agreement No 945022.

Using single crystal and polycrystalline UO_2 specimens, measurements of uranium volume and grain boundary diffusion coefficients have been made by Sabioni *et al* [Sab98, Sab00] using a ^{235}U tracer and depth profiling by secondary ion mass spectrometry (SIMS). The measured volume and grain boundary diffusion coefficients are both orders of magnitude lower than those obtained by other researchers, and those predicted by this catalogue recommendations. This was ascribed to a deficiency in measured volume diffusion coefficients (which in turn are used to determine measured grain boundary diffusion coefficients) from earlier work – that is, that the coefficients from earlier work incorrectly included the effects of grain boundary diffusion. However, this is inconsistent with the data analysis used in developing the recommendations for this catalogue, and so the data of Sabioni *et al* are not considered further here.

The Reynolds and Burton cation grain boundary diffusion coefficient expression [Rey79] was modified by Kogai [Kog97] and adopted as a fission gas atom grain boundary diffusion coefficient in his light water reactor fission gas release and swelling model. The same diffusion coefficient was implemented in the fission gas release model of Van Uffelen [Uff02]. The modification by Kogai gives diffusion coefficients which are in good agreement with Lambert's correlation [Lam78]. Thus, the work of Kogai and Van Uffelen provides indirect support to thiscatalogue recommendation for the cation grain boundary diffusion coefficient.

17.2 Conclusions and recommendations

The results from the recent investigations on cation diffusion/migration do not necessitate any changes of the recommendations for Pu diffusion coefficients (that is, volume, surface and grain boundary diffusion coefficients). However, the recommended volume diffusion coefficient is strictly only applicable out-of-pile. In-pile, solid-state diffusion is enhanced by an irradiation-induced contribution, D_{irr}. This contribution is generally taken to be that derived by Matzke [Mat83a], namely

$$\mathrm{D_{irr}} = 1.2.10^{-39}\dot{\mathrm{F}} \qquad [m^2.s^{-1}] \qquad \text{Eq. 17.10}$$

where $\dot{\mathrm{F}}$ is the fission rate (fissions.m^{-3}.s^{-1}).

It should be noted that a value for grain boundary width is required in any application of the recommended grain boundary diffusion coefficient. The value used should be consistent with that assumed in the derivation of the grain boundary diffusion coefficient. Hence, Lambert's value [Lam78] should be used.

With respect to the heat of transport for Pu thermal diffusion, a value was not originally recommended in this catalogue. However, Bober and Schumacher's value of -146.5 kJ.mol^{-1} [Bob73b] is used in TRANSURANUS [Mar14], FEAST-OXIDE [Kar10] and CEDAR [Ish01], and can therefore be recommended here.

New (post-1990) experimental data obtained from the post-irradiation examination of irradiated MOX fuel should be assessed to validate the Pu transport models currently used in fuel performance codes. Data of interest are on the evolution of the Pu concentration radial profile as a function of the radial

This project has received funding from the Euratom research and training programme 2019-2020 under grant agreement No 945022.

temperature profile, burn-up, O/M ratio and Pu content. The published data used to validate the TRANSURANUS, FEAST-OXIDE and CEDAR codes would be a good starting point.

17.3 References

[Alc65] C.B. Alcock, R.J. Hawkins, A.W.D. Hills and P. McNamara, A study of cation diffusion in stoichiometric UO_2 using α–ray spectrometry, Proc. Symp. on Thermodynamics with Emphasis on Nuclear Materials and Atomic Transport in Solids, Vol. II, IAEA, 1966.

[Bob73a] M. Bober, G. Schumacher and D. Geithoff, Plutonium redistribution in fast reactor mixed oxide fuel pins, J. Nucl. Mater. **47** (1973) 187.

[Bob73b] M. Bober and G. Schumacher, Material transport in the temperature gradient of fast reactor fuels, Adv. Nucl. Sci. and Technol. **7** (1973) 121.

[Cle78a] C.F. Clement and M.W. Finnis, Plutonium redistribution in mixed oxide $(U,Pu)O_2$ nuclear fuel elements, J. Nucl. Mater. **75** (1978) 193.

[Cle78b] C.F. Clement and M.W. Finnis, The movement of lenticular pores in mixed oxide $(U,Pu)O_2$ nuclear fuel elements, J. Nucl. Mater. **75** (1978) 115.

[Haw68] R.J. Hawkins and C.B. Alcock, A study of cation diffusion in UO_{2+x} and ThO_2 using α–ray spectrometry, J. Nucl. Mater. **26** (1968) 112.

[Ish01] T. Ishii and T. Asaga, An investigation of the Pu migration phenomena during irradiation in fast reactor, J. Nucl. Mater. **294** (2001) 13.

[Kar10] A. Karahan and J. Buongiorno, Modeling of thermo-mechanical and irradiation behavior of mixed oxide fuel for sodium fast reactors, J. Nucl. Mater. **396** (2010) 272.

[Kog97] T. Kogai, Modelling of fission gas release and gaseous swelling of light water reactor fuels, J. Nucl. Mater. **244** (1997) 131.

[Lam78] R.A. Lambert, PhD Thesis, University of Surrey, 1978 (see also [Mat83b]).

[Las92] K. Lassmann, TRANSURANUS: a fuel rod analysis code ready for use, J. Nucl. Mater., **188** (1992) 295.

[Lid66] A.B. Lidiard, Self-diffusion of uranium in UO_2, J. Nucl. Mater., **19** (1966) 106.

[Mae09] K. Maeda, S. Sasaki, M. Kato and Y. Kihara, Radial redistribution of actinides in irradiated FR-MOX fuels, J. Nucl. Mater. **389** (2009) 78.

[Mae11] K. Maeda, K. Katsuyama, Y. Ikusawa and S. Maeda, Short-term irradiation behaviour of low-density americium-doped uranium-plutonium mixed oxide fuels irradiated in a fast reactor. J. Nucl. Mater. **416** (2011) 158.

This project has received funding from the Euratom research and training programme 2019-2020 under grant agreement No 945022.

[Mar12] V. Di Marcello, A. Schubert, J. van de Laar and P. van Uffelen, Extension of the TRANURANUS plutonium redistribution model for fast reactor performance analysis, Nucl. Eng. Des. **248** (2012) 149.

[Mar14] V. Di Marcello, V. Rondinella, A. Schubert, J. van de Laar and P. van Uffelen, Modelling actinide redistribution in mixed oxide fuel for sodium fast reactors, Progress in Nuclear Energy **72** (2014) 83.

[Mar69] J.F. Marin and P. Contamin, Uranium and oxygen self-diffusion in UO_2, J. Nucl. Mater. **30** (1969) 16.

[Mat69] Hj. Matzke, On uranium self-diffusion in UO_2 and UO_{2+x}, J. Nucl. Mater. **30** (1969) 26.

[Mat76] Hj. Matzke, Lattice defects and irradiation damage in ThO_2, UO_2 and $(U,Pu)O_2$, in Plutonium 1975 and Other Actinides, North Holland/Elsevier, p. 801.

[Mat83a] Hj. Matzke, Radiation enhanced diffusion in UO_2 and $(U,Pu)O_2$, Radiation Effects **75** (1983) 317.

[Mat83b] Hj. Matzke. Diffusion processes and surface effects in non-stoichiometric nuclear fuel oxides UO_{2+x} and $(U,Pu)O_{2\pm x}$, J. Nucl. Mater. **114** (1983) 121.

[Ola87] D.R. Olander, Lattice and grain boundary diffusion in polycrystalline thoria-urania, J. Nucl. Mater. **144** (1987) 105.

[Rei69] D.K. Reimann and T.S. Lundy, Cation self-diffusion in UO_2, J. Nucl. Mater., **28** (1968) 218; also Diffusion of ^{233}U in UO_2, J. Amer. Ceram. Soc. **52** (1969) 511.

[Rey79] G.L. Reynolds and B. Burton, Grain-boundary diffusion in uranium dioxide: the correlation between sintering and creep and a reinterpretation of creep mechanism, J. Nucl. Mater. **82** (1979) 22.

[Rou72] J.L. Routbort, N.A. Javed and J.C. Voglewede, Compressive creep of mixed oxide fuel pellets, J. Nucl. Mater. **44** (1972) 247.

[Sab98] A.C.S. Sabioni, W.B. Ferraz and F. Millot, First study of uranium self-diffusion in UO_2 by SIMS, J. Nucl. Mater. **257** (1998) 180.

[Sab00] A.C.S. Sabioni, W.B. Ferraz and F. Millot, Effect of grain-boundaries on uranium and oxygen diffusion in polycrystalline UO_2, J. Nucl. Mater. **278** (2000) 364.

[Sel71] M.S. Seltzer, J.S. Perrin, A.H. Clauer and B.A. Wilcox, A review of creep behavior of ceramic nuclear fuels, Reactor Tech. **14** (1971) 99.

[The91] R. Thetford, Segregation in oxide fast reactor fuel, in Mathematica/Mechanical Modelling of Reactor Fuel Elements, CEC Report EUR-13660, p. 35, 1991.

[Uff02] P. Van Uffelen, Contribution to the modelling of fission gas release in light water reactor fuel, PhD thesis, Université de Liège, 2002.

[Yaj66] S. Yajima, H. Faruya and T. Hirai, Lattice and grain boundary diffusion of uranium in UO_2, J. Nucl. Mater. **20** (1966) 162.

This project has received funding from the Euratom research and training programme 2019-2020 under grant agreement No 945022.

18. Diffusion/migration of oxygen

This chapter was originally provided by M.A. Mignanelli (NNL).

18.1 Literature data

The large radial temperature gradient in a mixed oxide fuel pin during irradiation in a fast reactor causes a redistribution of oxygen due to diffusion and/or migration of certain species [Sar74]. The diffusion of anions (O^{2-}) in MO_2 ($M=U_{1-x}Pu_x$) is very much faster than that of cations [Mat86a] (Pu^{3+}, Pu^{4+}, U^{4+}) with the ratio D^O/D^M typically $\sim 10^7$ at a typical fuel operating temperature of 0.6 T_{melt} (~ 1800 K, taking the melting temperature, T_{melt}, as the liquidus point of $U_{0.8}Pu_{0.2}O_{1.99}$, which is ~3055 K). This factor contributes to the rapid redistribution of oxygen in mixed oxide fuel in the early stages of irradiation (that is, during the first few hours). Modelling the resultant changes in O/M ratio is necessary since this has an effect on fuel performance. In particular, the local creep rate, thermal conductivity, fission gas diffusion coefficient, and solidus/liquidus temperatures along the fuel radius are altered, and the extent of clad corrosion is impacted.

Fast reactor oxide fuel is initially hypostoichiometric, with an as-manufactured O/M ratio which is typically in the range 1.97 to 1.99. As irradiation proceeds and the radial temperature gradient is rapidly established, oxygen transport towards the cooler peripheral regions occurs, but these peripheral regions do not become hyperstoichiometric due to the buffering effect of the internal surface of the clad (for example, the formation of Cr_2O_3). The buffering effect is in turn due to the oxygen potential (that is, the partial pressure of oxygen in equilibrium with the fuel) increasing significantly as the stoichiometric composition is approached, such that any excess oxygen reacts with the clad.

Further redistribution of oxygen occurs during the course of the irradiation as more oxygen is made available due to the production of fission products which are not oxidised (that is, inert gases, Cs, Te, I and noble metals).

18.1.1 Chemical diffusion and self-diffusion

Matzke gives a good description of chemical diffusion and self-diffusion of oxygen. Quoting from his 1986 paper [Mat86b]:

"For oxidation and reduction, chemical diffusion of oxygen is rate-determining. The corresponding diffusion coefficients $\tilde{D}$ are deduced from measurements of the rate at which thermodynamic equilibrium conditions are achieved by diffusion of point defects (oxygen vacancies for MO_{2-x}, oxygen interstitials for MO_{2+x}) within the chemical gradient set-up [sic] when the oxygen pressure of the gas atmosphere or the temperature are suddenly changed. A prerequisite is that oxygen transport across the gas-solid interface is fast and not rate-limiting. Most frequently, weight changes are measured to determine $\tilde{D}$.

If equilibrium is achieved, self-diffusion coefficients D describe oxygen transport. Since no suitable radioactive tracers exist for oxygen [...] either mass

This project has received funding from the Euratom research and training programme 2019-2020 under grant agreement No 945022.

spectrometry with ^{18}O, or different suitable nuclear techniques must be used to measure diffusion profiles of the naturally occurring inactive ^{18}O isotope [...]

A somewhat simplified relation [Matzke's references omitted] between $\tilde{D}$ and D for oxygen diffusion in e.g. UO_{2+x} is given by

$$\tilde{D}^O = FD = D^O \frac{(2+x)}{2RT} \frac{d\{\Delta\bar{G}(O_2)\}}{dx}$$ *[where FD should read FD^O]*

[...] the thermodynamic factor F (and hence essentially the oxygen potential $\Delta\bar{G}(O_2)$), varies equally strongly with x as does D^O in UO_{2+x} [...] but has the opposite trend. The product of D^O and F, and hence $\tilde{D}^O$, are nearly constant and thus fairly independent of x [...]. The $\tilde{D}^O$ values are very high indeed, thus explaining the high rates of oxidation and reduction of the oxides $MO_{2\pm x}$."

18.1.2 Diffusion in temperature gradient (thermal diffusion)

During an anneal in a radial temperature gradient, the oxygen distribution evolves until it reaches a steady state whereby the composition variation with temperature along the gradient is unchanging. Two possible mechanisms have been proposed for the movement of oxygen in a temperature gradient: the migration of oxygen-bearing species in the gas phase in equilibrium with the fuel surface; and the solid-state diffusion of oxygen ions in the bulk of the fuel.

Gas phase diffusion

The gas phase mechanism involves the transport of oxygen from the hotter to the colder regions of the fuel as a result of the higher equilibrium pressure at the more elevated temperatures for a given O/M ratio. Various gases can provide transport routes for oxygen via cyclic reactions in the gas phase (e.g. CO/CO_2, H_2/H_2O) [Ran67]. Transport is also possible via vaporised metal oxides (e.g. PuO_2, UO_3, Cs_2MoO_4) [Ola76].

Gas diffusion mechanisms require continuous gas phase pathways, such as those due to radial cracks or interconnected pores. Therefore in the central regions of pellets where these are absent, solid-state diffusion is the operative mechanism [Bob73].

As emphasised by Olander [Ola76], there are difficulties in explaining oxygen transport via gaseous cyclic reactions in hypostoichiometric mixed oxide fuel because of the extremely low oxygen potential, and therefore extremely low partial pressures of the oxygen-bearing species (e.g. CO/CO_2) at low O/M ratios; the slow reaction kinetics [Nor79] of oxygen equilibration between gas mixtures and the solid could limit the effectiveness of the gaseous diffusion mechanism. In addition, migration of oxygen by any gas diffusion mechanism will be reduced by the slow transfer between the gas phase and the solid surface, and by back-diffusion within the solid [Ait69].

This project has received funding from the Euratom research and training programme 2019-2020 under grant agreement No 945022.

Solid-state diffusion

The oxygen vacancy current (that is, the atomic fraction of oxygen vacancies in the anion sub-lattice being transported per unit area per unit time) due to solid-state diffusion, J, for fuel with composition $(U,Pu)O_{2-x}$ is given by [Sar76] and shown in Eq. 18.1.

$$J = -D\left[\frac{\nabla x}{2} + \frac{x}{2}\left(1 - \frac{x}{2}\right).\frac{Q^*\nabla T}{RT^2}\right] \qquad \text{Eq. 18.1}$$

where D is the oxygen bulk diffusion coefficient, Q^* is the heat of transport, T the absolute temperature and R the gas constant. The heat of transport is an irreversible thermodynamic quantity and relates the flow of heat associated with material transport in an isothermal system [Nor79, How64]. However, since the appropriate value that is used in the equation is derived from experimental data and differs from this particular definition, Q^* is in practice replaced by the experimentally-derived value Q to avoid confusion, and is referred to as the Arrhenius slope.

When steady state is attained, i.e. J=0,

$$ln\, x = \frac{Q}{RT} + A \qquad \text{Eq. 18.2}$$

where x is the stoichiometry deviation, A is a constant and Q the Arrhenius slope. For a given initial fuel composition, Q and A can therefore be determined by fitting to experimental curves of $ln\, x$ versus $1/T$. For fuel modelling purposes, Q as a function of x can be derived from fits to multiple experiments with different fuel compositions, with A fixed at each axial elevation to give the required pellet cross-section averaged x value (taking into account any axial migration of oxygen and any loss of oxygen from the pellet).

18.1.3 Recommended equations for anion self-diffusion

In the case of stoichiometric oxide, MO_2, the recommended equation for the anion self-diffusion coefficient is given by Eq. 18.3 [Mat87]

$$D^O_{(stoi)} = 2.6.10^{-5}\exp\left(\frac{-29876}{T}\right) \qquad [m^2.s^{-1}] \qquad \text{Eq. 18.3}$$

where T = absolute temperature.

In the case of hypostoichiometric oxide (MO_{2+x}, with x negative), the recommended equation for the anion self-diffusion coefficient is given by Eq. 18.4 [Kim81]

This project has received funding from the Euratom research and training programme 2019-2020 under grant agreement No 945022.

$$D^O_{(hypo)} = 2.2.10^{-8}|x| \exp\left(\frac{-5884}{T}\right) \qquad [m^2.s^{-1}] \qquad \text{Eq. 18.4}$$

Assuming oxygen diffusion in hypostoichiometric material is via a vacancy mechanism, the vacancy diffusion coefficient, $D_y = D^O_{(hypo)}/|x|$. (Arguably, the right-hand side should be multiplied by a factor of two [Sar76], but this can probably be ignored given the uncertainty in the diffusion coefficients.)

In the case of hyperstoichiometric oxide (MO_{2+x}, with x positive), the recommended equation for the anion self-diffusion coefficient is given by Eq. 18.5 [Con72, Mur87].

$$D^O_{(hyper)} = 2.5.10^{-7} x \exp\left(\frac{-10590}{T}\right) \qquad [m^2.s^{-1}] \qquad \text{Eq. 18.5}$$

Assuming oxygen diffusion in hyperstoichiometric material is via an interstitial mechanism, the interstitial diffusion coefficient, $D_i = D^O_{(hyper)}/x$.

Due to the limited amount of data on mixed oxide fuel available in 1990, all equations above are fitted to uranium oxide data; it is assumed that the anion self-diffusion coefficient is unaffected by the partial replacement of uranium by plutonium at a particular temperature and O/M ratio.

In terms of a general equation for D^O that can be used for any stoichiometry, it is recommended that the expression $D^O = D_i\, i + D_v\, v$ is employed, where i is the molar fraction of interstitials, and v is the molar fraction of vacancies. Using the defect model of Lidiard [Lid66] to derive expressions for i and v as a function of x, the formula for D^O becomes :

$$D^O = D_i\left[\frac{(x^2 + 4K_F)^{1/2} + x}{2}\right] + D_v\left[\frac{(x^2 + 4K_F)^{1/2} - x}{2}\right] \qquad \text{Eq. 18.6}$$

where K_F is the law of mass action equilibrium constant for the formation of Frenkel defects on the anion sub-lattice.

Since $i^2 = K_F$ for stoichiometric material (for which $i = v$ is assumed), $K_F = \left(D^0_{(stoi)}/(D_i + D_v)\right)^2$ using the formulae above for $D^0_{(stoi)}$, D_i and D_v and fitting to the resulting predictions of $\ln K_F$ as a function of $1/T$ gives

$$K_F = 1.698.10^5 \exp\left(\frac{-45937}{T}\right) \qquad \text{Eq. 18.7}$$

This implies a Frenkel defect formation energy of 3.96 eV, which is consistent with the other determinations (see discussion in [Mur87] and [Mat87]). The pre-exponential factor is much more liable to error; however, it is probably correct to within an order of magnitude. The value obtained by Hyland [Hyl84] from oxygen potential data is qualitatively different and should probably be rejected.

This project has received funding from the Euratom research and training programme 2019-2020 under grant agreement No 945022.

Eq. 18.6 may be used at all temperatures up to the melting point. However, at temperatures above the fast-ion transition (2670K) it may overestimate the self-diffusion coefficient. At high non-stoichiometries, above about x = 0.15, this expression significantly overestimates the self-diffusion coefficient. Recommended values of the anion self-diffusion coefficient for hypostoichiometric, stoichiometric and hyperstoichiometric mixed oxide fuel (as derived from Eq. 18.6 and Eq. 18.7) are shown in Table 18.1.

Table 18.1: Recommended anion self-diffusion coefficients for mixed oxide fuel.

Temp (K)	Deviation to stoichiometry					
	-0.10	**-0.08**	**-0.06**	**-0.04**	**-0.02**	**0.00**
500	-13.77	-13.87	-13.99	-14.17	-14.47	-30.10
750	-12.06	-12.16	-12.29	-12.46	-12.76	-21.74
1000	-11.21	-11.31	-11.43	-11.61	-11.91	-17.53
1250	-10.70	-10.80	-10.92	-11.10	-11.40	-14.97
1500	-10.36	-10.46	-10.58	-10.76	-11.06	-13.22
1750	-10.12	-10.21	-10.34	-10.52	-10.82	-11.95
2000	-9.93	-10.03	-10.15	-10.32	-10.60	-10.99
2250	-9.77	-9.86	-9.96	-10.07	-10.19	-10.23
2500	-9.53	-9.57	-9.60	-9.63	-9.63	-9.62
2750	-9.14	-9.14	-9.14	-9.14	-9.13	-9.11
3000	-8.72	-8.72	-8.71	-8.71	-8.70	-8.69

(a) $\log_{10}D$ (m^2s^{-1}) for hypostoichiometric and stoichiometric oxide.

Temp (K)	Deviation to stoichiometry					
	0.02	**0.04**	**0.06**	**0.08**	**0.10**	**0.20**
500	-17.50	-17.20	-17.02	-16.90	-16.80	-16.50
750	-14.43	-14.13	-13.96	-13.83	-13.73	-13.43
1000	-12.90	-12.60	-12.42	-12.30	-12.20	-11.90
1250	-11.98	-11.68	-11.50	-11.38	-11.28	-10.98
1500	-11.37	-11.07	-10.89	-10.77	-10.67	-10.37
1750	-10.93	-10.63	-10.45	-10.33	-10.23	-9.93
2000	-10.57	-10.29	-10.12	-10.00	-9.90	-9.60
2250	-10.11	-9.96	-9.83	-9.72	-9.63	-9.34
2500	-9.58	-9.53	-9.47	-9.41	-9.35	-9.11
2750	-9.10	-9.08	-9.05	-9.03	-9.00	-8.86
3000	-8.68	-8.67	-8.66	-8.65	-8.64	-8.57

(b) $\log_{10}D$ (m^2s^{-1}) for hyperstoichiometric oxide.

Figure 18.1 shows oxygen self-diffusion coefficient values as a function of the O/M ratio at four different temperatures as predicted by Eq. 18.6.

This project has received funding from the Euratom research and training programme 2019-2020 under grant agreement No 945022.

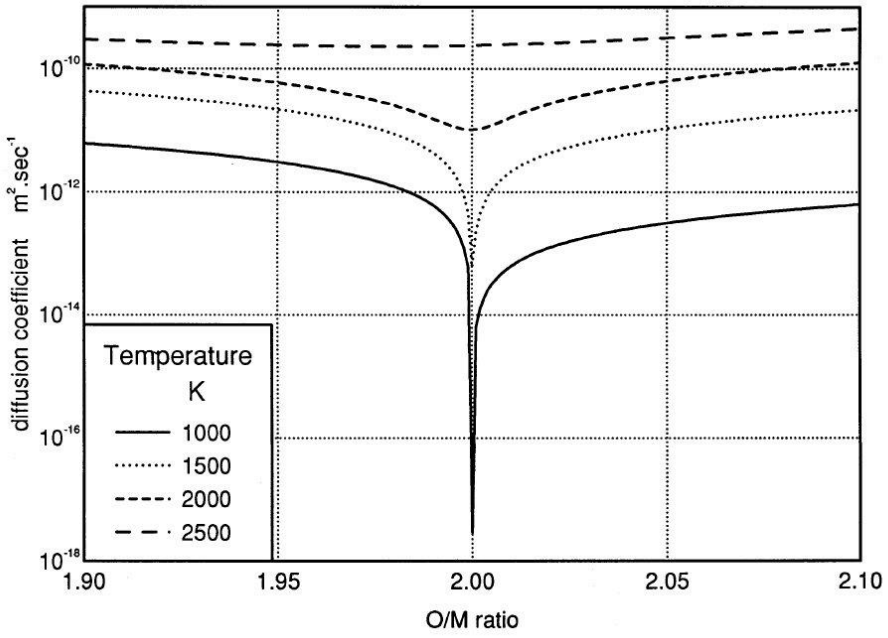

Figure 18.1: Oxygen self-diffusion coefficient values (Eq. 18.6)

There has been very limited new open literature information on anion diffusion in mixed oxide fast reactor fuel published since 1990. In fact, the only new experimental data that could be found were those published by Kato *et al* [Kat09]. They measured the kinetics of the reduction and oxidation of $(U_{0.8}Pu_{0.2})O_{2-x}$ and $(U_{0.7}Pu_{0.3})O_{2-x}$ in $Ar/H_2/H_2O$ using thermo-gravimetry. The O/M ratios in the reduction process exhibited an inverse exponential dependence with time. In addition, the time to reach equilibrium was dependent on Pu content, but almost independent of the initial O/M ratio. On the other hand, the O/M ratios in the oxidation process varied linearly with time, and the time to reach equilibrium was dependent on initial O/M ratio, but independent of Pu content. These measurement results showed that the mechanisms of the O/M ratio changes in the reduction process and the oxidation process were distinctly different. Therefore, the oxygen chemical diffusion coefficients $\widetilde{D}$ were estimated from the reduction curves only. The oxygen chemical diffusion coefficients were expressed by Eq. 18.8 and Eq. 18.9 and are plotted in Figure 18.2 as a function of reciprocal temperature, together with data from other studies.

$$ln\widetilde{D} = \left(-\frac{60000}{RT}\right) + \ln(3.03.10^{-4}) \qquad [cm^2.s^{-1}] \qquad (U_{0.8}Pu_{0.2})O_{2-x} \qquad \text{Eq. 18.8}$$

$$ln\widetilde{D} = \left(-\frac{88000}{RT}\right) + \ln(1.57.10^{-3}) \qquad [cm^2.s^{-1}] \qquad (U_{0.7}Pu_{0.3})O_{2-x} \qquad \text{Eq. 18.9}$$

Eq. 18.8 and Eq. 18.9 give activation energies of 60 and 88 $kJ.mol^{-1}$ for $(U_{0.8}Pu_{0.2})O_{2-x}$ and $(U_{0.7}Pu_{0.3})O_{2-x}$, respectively. It was concluded that the oxygen chemical diffusion coefficient in $(U_{0.7}Pu_{0.3})O_{2-x}$ was smaller than that of $(U_{0.8}Pu_{0.2})O_{2-x}$. The diffusion coefficient did not depend strongly on the O/M variation of samples.

This project has received funding from the Euratom research and training programme 2019-2020 under grant agreement No 945022.

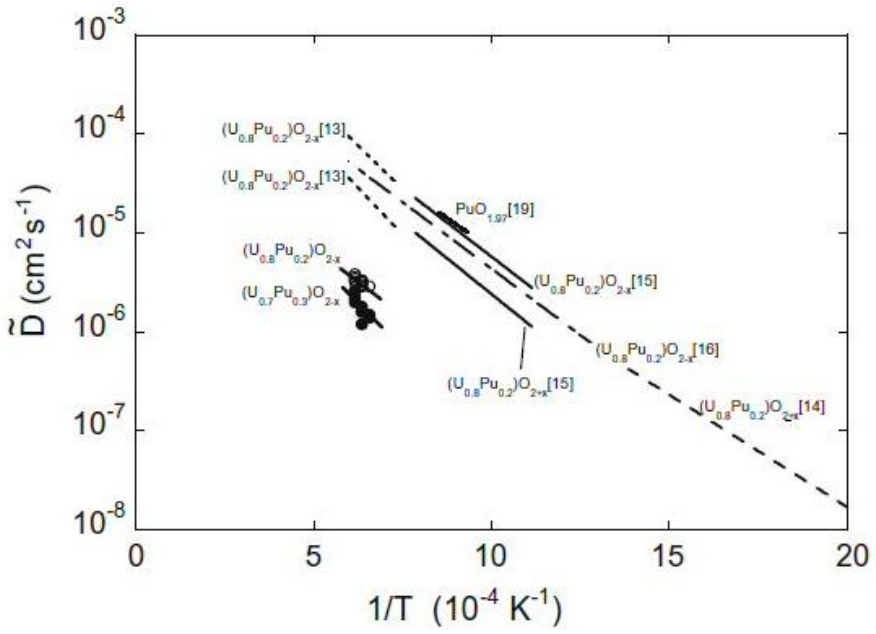

Fig.ref	Rep. ref
(13)	[Bay84]
(14)	[Dan77]
(15)	[Sar78]
(16)	[Bay79b]
(19)	[Bay79a]

Figure 18.2: Comparison of literature oxygen chemical diffusion coefficients and values obtained in the work of Kato et al [Kat09].

The data from the other works indicate larger coefficients. In these studies, the oxygen chemical diffusion coefficients were determined from kinetics of the oxidation process observed by placing samples in an atmosphere of CO_2/CO heated to the test temperatures. Kato *et al* argue that such experimental conditions are difficult to control and that this may affect the experimental results.

The "defect diffusion coefficients" D* of $(U_{1-y}Pu_y)O_{2-x}$ were estimated from the oxygen chemical diffusion coefficients measured in this work, but it is unclear whether these are actually defect (i.e. vacancy) diffusion coefficients, or anion self-diffusion coefficients.

18.2 Conclusions and recommendations

The results from the recent investigations on anion diffusion/migration do not necessitate any changes of the recommendation for the oxygen self-diffusion coefficient. With respect to the effective heat of transport (Arrhenius slope, Q) for oxygen solid-state diffusion, the oxygen chemical diffusion coefficient, and parameters associated with gas phase diffusion, no recommendations were made. An analysis of the available data – including the post-1990 data of Kato *et al* for the chemical diffusion coefficient – would be required to allow recommendations to be made; this would then enable the requirements for future experiments on oxygen transport (if any) to be determined (the work of Kato *et al* suggests that new experimental data on the oxidation/reduction kinetics of mixed oxide fuel as a function of gas atmosphere, grain size and sample density could provide a better understanding of oxygen chemical diffusion in this fuel type). However, it should be noted that: (a) the combined effects of solid-state diffusion and gas phase

This project has received funding from the Euratom research and training programme 2019-2020 under grant agreement No 945022.

diffusion on oxygen transport are generally modelled using either Eq. 18.1 (transient) or Eq. 18.2 (steady state), with the effective heat of transport implicitly covering the effects of both phenomena; (b) the usual assumption made in oxygen transport calculations for hypostoichiometric MOX fuel (as relevant here) is that the chemical diffusion coefficient is approximately equal to the self-diffusion coefficient (since the fuel can be considered to be a dilute solution of vacancies in the oxygen sub-lattice).

18.3 References

[Ait69] E.A. Aitken, Thermal diffusion in closed oxide fuel systems, J. Nucl. Mater. **30** (1969) 62.

[Bay79a] A.S. Bayoglu and R. Lorenzelli, Study of the chemical diffusion of oxygen in PuO_{2-x} by dilatometry and thermogravimetry, J. Nucl. Mater. **82** (1979) 403.

[Bay79b] A.S. Bayoglu and R. Lorenzelli, Diffusion chimique de l'oxygene dans $(U,Pu)O_{2-x}$, J. Nucl. Mater. **79** (1979) 437.

[Bay84] A.S. Bayoglu, Oxygen diffusion in fcc fluorite type nonstoichiometric nuclear oxides $MO_{2\pm x}$, Solid, State Ionics **12** (1984) 53.

[Bob73] M. Bober and G. Schumacher, Material transport in the temperature gradient of fast reactor fuels, Adv. Nucl. Sci. and Technol. **7** (1973) 121.

[Con72] P. Contamin, J.J. Bacmann and J.F. Marin, Self-diffusion of oxygen in hypostoichiometric uranium dioxide, J. Nucl. Mater. **42** (1972) 54.

[Dan77] F. D'annucci and C. Sari, Oxygen diffusion in uranium-plutonium oxide fuels at low temperatures, J. Nucl. Mater. **68** (1977) 357.

[How64] R.E. Howard and A.B. Lidiard, Matter transport in solids, Rep. Prog. Phys. **27** (1964) 161.

[Hyl84] G.J. Hyland, Oxygen potential model for stoichiometric and non-stoichiometric uranium dioxide, EEC Commission Report EUR 9410 EN, 1984.

[Kat09] M. Kato, K. Morimoto, T. Tamura, T. Sunaoshi, K. Konashi, S. Aono and M. Kashimura, Oxygen chemical diffusion in hypo-stoichiometric MOX, J. Nucl. Mater. **389** (2009) 416.

[Kim81] K.C. Kim and D.R. Olander, Oxygen diffusion in UO_{2-x}, J. Nucl. Mater., **102** (1981) 192.

[Lid66] A.B. Lidiard, Self-diffusion of uranium in UO_2, J. Nucl. Mater. **19** (1966) 106.

[Mat86a] Hj. Matzke, Advances in Ceramics, Vol. 17 Fission Product Behaviour in Ceramic Oxide Fuel, Westerville, Columbus, Ohio: Am. Ceram. Soc., pp.1-54, 1986.

[Mat86b] Hj. Matzke, Diffusional processes in nuclear fuels, J. Less-Common Metals **121** (1986) 537.

This project has received funding from the Euratom research and training programme 2019-2020 under grant agreement No 945022.

[Mat87] Hj. Matzke, Atomic transport properties in UO_2 and mixed oxides $(U,Pu)O_2$, J. Chem. Soc. (Faraday II), **83** (1987) 1121.

[Mur87] G.E. Murch and C.R.A. Catlow, Oxygen diffusion in UO_2, ThO_2 and PuO_2: A review, J. Chem. Soc. (Faraday II) **83** (1987) 1157.

[Nor79] D.I.R. Norris, Solid state transport as a mechanism of oxygen thermomigration in $(U,Pu)O_2$, J. Nucl. Mater. **79** (1979) 118.

[Ola76] D.R. Olander, Fundamental aspects of nuclear reactor fuel elements, TID-26711-P1, (ERDA, 1976), pp. 163.

[Ran67] M.H. Rand and T.L. Markin, Some thermodynamic aspects of $(U,Pu)O_2$ solid solutions, Thermodynamics of nuclear materials, IAEA Vienna, 1967, pp. 637.

[Sar74] C. Sari and G. Schumacher, Radial transport of oxygen in mixed-oxide fuel pins, Proc. Symp. on Thermodynamics of Nuclear Materials, IAEA Vienna, October 1974, pp. 73.

[Sar76] C. Sari and G. Schumacher, Oxygen redistribution in fast reactor oxide fuel, J. Nucl. Mater. **61** (1976) 192.

[Sar78] C. Sari, Oxygen chemical diffusion coefficient of uranium-plutonium oxides, J. Nucl. Mater. **78** (1978) 425.

This project has received funding from the Euratom research and training programme 2019-2020 under grant agreement No 945022.

19. Oxygen potential

This chapter was originally provided by S. Portier (PSI).

19.1 Literature data

In 1990, R.G.J. Ball recommended a model developed by Lindemer and Besmann [Lin85, Bes85]. The experimental data base used for development of the model can be found in the R.G.J. Ball review [Bal89] on the subject. As noticed by Ball, the proposed model is a mathematical solution providing the oxygen potential of fresh mixed oxide fuel as a function of the plutonium enrichment Pu/(U+Pu), the temperature T in Kelvin and the oxygen to metal ratio (O/M) and does not describe any physical mechanism. Moreover, this model fits experimental results for O/M between 1.9 and 2.07 and should not be extended out of this range without previous experimental validation. In the other hand, by using this model, the calculation of the oxygen potential is possible for all temperatures, compositions and O/M ratios (within the range of validation).

Several models, based on a large amount of experimental data and taking into account various physical descriptions have been developed since 1990. 4 models in particular are interesting:

- The defect theory model aims to assess the concentration of different kind of defects, such as oxygen vacancies, inserted oxygen atoms, but also cluster defects, Frenkel defects or intrinsic ionization [Nak86, Kar06, Sas99, Kat05, Kat09, Kat11] to deduce the oxygen potential. In practical, the model has been elaborated from measurements data of oxygen potentials as functions of temperature and p_{O2} (oxygen partial pressure) to estimate the concentrations of the point defects in fresh MOX. The model has been validated using set of experimental data, but only for few given composition and temperature. The temperature dependency has been implemented in the model but no development has been performed to enable the calculation for varying composition. A comparison with the previous used model is shown in Figure 19.1.

- The valence model is based on the work of Blackburn, started on UO_2 oxygen potential calculation from concentration of uranium atoms with various valences (2+ and 4+) [Bla73]. Fujino et al. extended the model to calculate the oxygen potential of irradiated MOX (intra-cations complex model) [Fuj93]. In this model, the different fission products are taken into account as a function of their valence (3+ for Y, La, Pr, Nd, Pm and Sm ; 4+ for Ce and Zr). This allows assessing the oxygen potential as a function of the original Pu enrichment, the burn-up, the temperature and the O/M ratio. Therefore this model has been validated only for existent experimental data on simulated fuels [Woo78] and irradiated fuels [Mat88], i.e. only for given original Pu content and given burn-up, implying that an effort is required for extending and validating it for larger range of enrichment and burn-up. For irradiated fuels, the amount of different fission products of interest was computed with the ORIGEN2 program [Cro81, Nak90]. A comparison with the previous used model is shown in Figure 19.2.

This project has received funding from the Euratom research and training programme 2019-2020 under grant agreement No 945022.

- The thermochemical approach [Lin85, Kri84] has been applied to MOX by S. Vana Varamban et al. [Van09]. The idea is to consider the MOX fuel as a pseudo-quaternary solid solution of UO_2-U_cO_d-PuO_2-Pu_aO_b, with b = 1.5 a and d = 2.25 c. In this approach, the U_cO_d is U_4O_9-type and Pu_aO_b is Pu_2O_3-type. The model has been validated using the experimental data from Woodley [Woo79] for 25 % Pu at 1073 K and 1273 K.

- Using the CALPHAD method, which enables to describe both the phase diagram and all the thermodynamic properties of the phases, thermochemical models have been developed by Chevalier et al. [Che98, Che02] and Guéneau et al. [Gué02] for U-O and by Kinoshita et al. [Kin03] and Guéneau et al. [Gué08] for Pu-O. The oxygen potentials of MOX with different Pu content and O/(U+Pu) have been calculated combining the previous three binary systems, and then adjusted with a few ternary interactions parameters to fit available experimental data [Gué11]. A very good agreement is obtained with all the available experimental data, as shown in Figure 19.3.

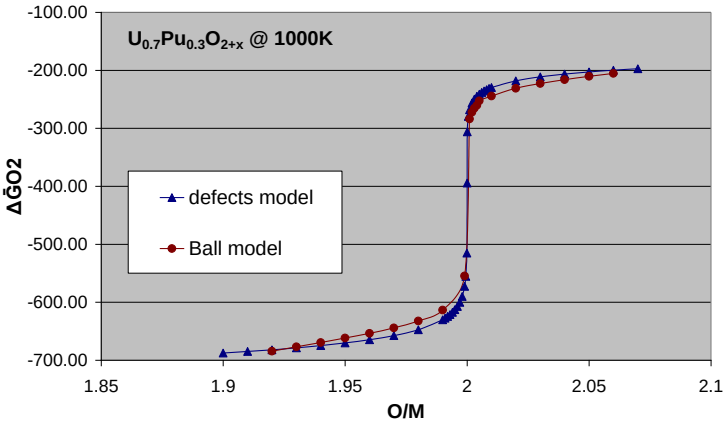

Figure 19.1: Comparison between the current model (Ball model) and the defects model [Kat11] for $U_{0.7}Pu_{0.3}O_{2\pm x}$ at 1000K.

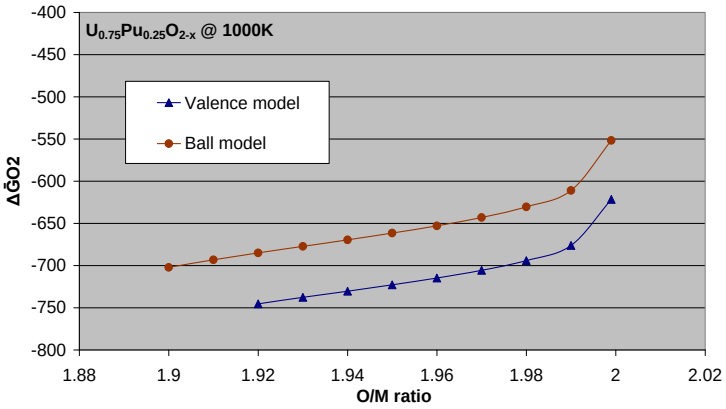

Figure 19.2: Comparison between the current model (Ball model) and the valence model [Fuj93] for $U_{0.75}Pu_{0.25}O_{2-x}$ at 1000K.

This project has received funding from the Euratom research and training programme 2019-2020 under grant agreement No 945022.

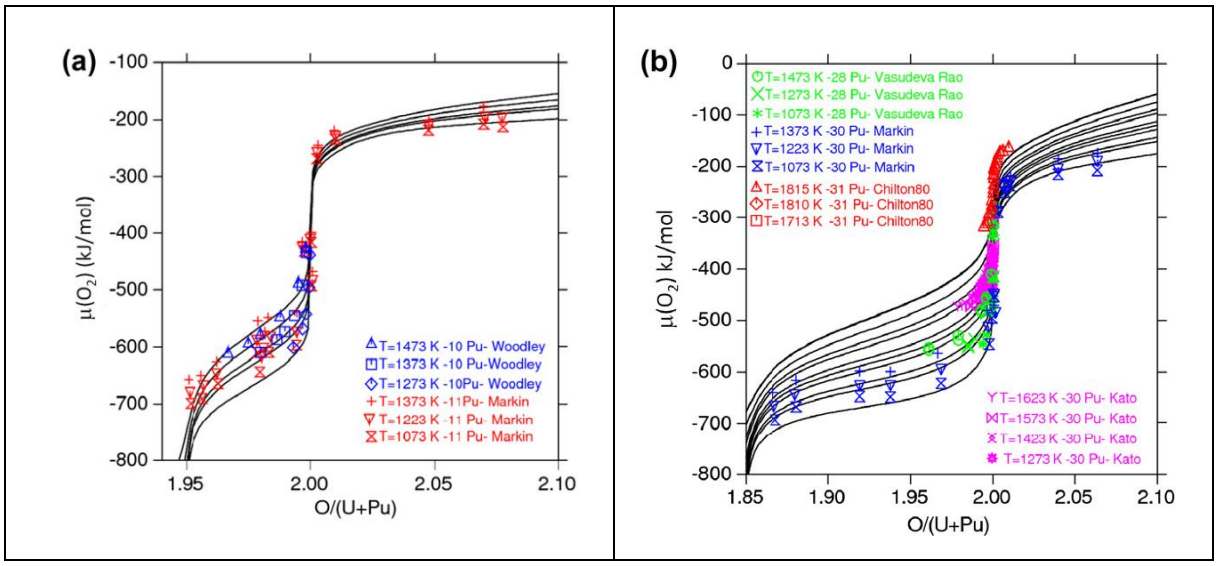

Figure 19.3: Calculated oxygen potential of MOX as a function of O/(U + Pu) ratio: (a) with 10% Pu at 1073, 1223, 1273, 1373 and 1473 K; (b) with 30% Pu at 1073, 1223, 1273, 1373, 1423, 1473, 1573, 1623, 1713, 1810, 1815 K (figures and references for experimental data can be found in [Gué11]).

19.2 NEA recommendation

The recommended law in [NEA25] for oxygen potential is the one proposed by Kato [Kat17] expressing O/M ratio as functions of Pu content, P_{O2} and temperature and given in Eq. 19.1.

$$
\begin{aligned}
&O/M \\
&= 2 - \left\{ \left(\exp\left(\frac{44.0 + 55.8 \cdot C_{Pu}}{R} \right) \cdot \exp\left(-\frac{376000}{RT} \right) \cdot {P_{O_2}}^{-1/2} \right)^{-5} + \left(\left(\exp\left(\frac{68.8 + 131.3 \cdot C_{Pu}}{R} \right) \cdot \exp\left(-\frac{515000}{RT} \right) \right)^{1/2} \cdot {P_{O_2}}^{-1/4} \right)^{-5} \right. \\
&+ \left(\left(2 \cdot \exp\left(\frac{153.5 - 96.5 \cdot C_{Pu} + 331.0 \cdot {C_{Pu}}^2}{R} \right) \cdot \exp\left(-\frac{891000}{RT} \right) \right)^{1/3} {P_{O_2}}^{-1/3} \right)^{-5} \\
&\left. + \left(\frac{1}{2} C_{Pu} \right)^{-5} \right\}^{-1/5} + \left\{ \exp\left(\frac{-22.8 - 84.5 \cdot C_{Pu}}{R} \right) \cdot \exp\left(\frac{105000}{RT} \right) \cdot {P_{O_2}}^{1/2} \right\}
\end{aligned}
\qquad \text{Eq. 19.1}
$$

Where R is gas constant (8.3145 J/mol.K), T is absolute temperature, C_{Pu} is Pu concentration Pu/(Pu + U) and P_{O2} is oxygen partial pressure (in 0.101 MPa).

Eq. 19.1 fits the available data very well for PuO_2 contents of 40-68%.

At lower Pu contents (≤ 40%), Eq. 19.1 should be used with an adjustment to the input value used for the temperature term as per Eq. 19.2.

$$T_{adjusted} = T_{actual} + 0.16 * S * (1773 - T_{actual}) \qquad \text{Eq. 19.2}$$

$$S = 1/(1 + \exp^{(-3)*(100*(0.335 - C_{Pu}))}) \qquad \text{Eq. 19.3}$$

This project has received funding from the Euratom research and training programme 2019-2020 under grant agreement No 945022.

While the effects of temperature, Pu content and O/M in the hypostoichiometric and hyperstoichiometric regions result in a gradual increase in oxygen potential, there is a point of inflection in the stoichiometric transition region (O/M of approximately 1.99 to 2.01), which shows a dramatic increase. The need to avoid reaching this inflection and triggering excess clad corrosion is the reason why fast reactor MOX fuels are designed to be hypostoichiometric, typically with O/M of ~1.97.

Effect of minor actinide could be considered using the recommendation of Hirooka [Hir20] which consists in using an adjustment to the input value used for the Pu content in Eq. 19.1 as per Eq. 19.4.

$$C_{PuMA} = C_{Pu} + 2.5 * C_{Am} + 0.5 * C_{Np} \qquad \text{Eq. 19.4}$$

Regarding, effect of burn-up, the unirradiated temperature adjusted/unadjusted versions of Kato's Equation can still be recommended to calculate the radial changes in oxygen potential in irradiated material by inputting values of O/M for different radii, calculated separately using the preferred model for differential Pu-O transport.

For both the unadjusted and adjusted temperature versions of Kato's Equation, uncertainties in oxygen potential of ±50 kJ/mol and O/M of ±0.0025 are recommended.

19.3 Conclusion and recommendations

From the bibliographic review, it appears clearly that the new models developed are based on real phenomena to describe the oxygen potentials variations as a function of the original Pu fraction in the fuel, the temperature and the stoichiometry (O/M ratio). The model developed by Guéneau et al [Gué11] exhibits the best agreement with all the data found in the literature and allows to calculate the oxygen potential for a wide range of temperature, composition and stoichiometry. It appears to be the current best model to calculate oxygen potentials in MOX.

19.4 References

[Bal89] R.G.J. Ball, 1989, AERE-R13395, AGT 010101/P15.

[Bes85] T.M. Besmann, T.B. Lindemer, J. Nucl. Mater. **130** (1985) 489.

[Bla73] P.E. Blackburn, J. Nucl. Mater. **46** (1973) 244.

[Che98] P.Y. Chevalier, E. Fischer, J. Nucl. Mater. **257** (1998) 213.

[Che02] P.Y. Chevalier, E. Fischer, B. Cheynet, J. Nucl. Mater. **303** (2002) 1.

[Cro81] A. G. Croff, J. W. McAdoo, M. J. Bjerke, ORNL-TM-7176 (1981).

This project has received funding from the Euratom research and training programme 2019-2020 under grant agreement No 945022.

[Fuj93] T. Fujino, N. Sato, T. Yamashita, K. Ouchi, J. Nucl. Mater. 201 (1993) 70.

[Gué02] C. Guéneau, M. Baichi, D. Labroche, C. Chatillon, B. Sundman, J. Nucl. Mater. **304** (2002) 161.

[Gué08] C. Guéneau, C. Chatillon, B. Sundman, J. Nucl. Mater. **378** (2008) 257.

[Gué11] C. Guéneau, N. Dupin, B. Sundman, C. Martial, J.C. Dumas, S. Gossé, S. Chatain, F. De Bruycker, D. Manara, R.J.M. Konings, J. Nucl. Mater. **419** (2011) 145.

[Hir20] S. Hirooka, T. Matsumoto, M. Kato, T. Sunaoshi, H. Uno and T. Yamada, Oxygen potential measurement of (U,Pu,Am)O2±x and (U,Pu,Am,Np)$O_{2\pm x}$, Journal of Nuclear Materials, 542 (2020)

[Kar06] P. Karen, J. Solid, State Chem. **179** (2006) 3167.

[Kat05] M. Kato, T. Tamura, K. Konashi, S. Aono, J. Nucl. Mater. **344** (2005) 235.

[Kat09] M. Kato, K. Konashi, N. Nakae, J. Nucl. Mater. **389** (2009) 164.

[Kat11] M. Kato, K. Takeushi, T. Uchida, T. Sunaoshi, K. Konashi, J. Nucl. Mater. **414** (2011) 120.

[Kat17] M. Kato, M. Watanabe, T. Matsumoto, S. Hirooka and M. Akashi, Oxygen potential, oxygen diffusion coefficients and defect equilibria of nonstoichiometric (U,Pu)$O_{2\pm x}$, *J. of Nuclear Materials,* 487, (2017), pp. 424-432

[Kin03] H. Kinoshita, M. Uno, S. Yamanaka, J. Alloys Comp. **354** (2003) 129.

[Kri84] M.V. Krishnaiah, P. Sriramamurti, J. Am. Ceram.Soc. **67** (1984) 568.

[Lin85] T.B. Lindemer, T.M. Besmann, J. Nucl. Mater. **130** (1985) 473.

[Mat88] Hj. Matzke, J. Ottaviani, D. Pellotiero, J. Rouault, J. Nucl. Mater. **160** (1988) 142.

[Nak86] A. Nakamura, T. Fujino, J. Nucl. Mater. **140** (1986) 113.

[Nak90] Y. Nakahara, T. Suzuki, K. Gunji, N. Kohno, H. Takano, Z. Yoshida, T. Adachi, Radiochim. Acta **50** (1990) 141.

[NEA25] N. Chauvin et al., Recommendations on Fuel Properties for Fuel Performance Codes, NEA/NSC/R(2024)1, July 2025

[Sas99] K. Sasaki, J. Maeir, J. Appl. Phys. **86** (1999) 5422.

[Van09] S. Vana Varamban, V. Ganesan, P.R. Vasudeva Rao, J. Nucl. Mater. **389** (2009) 72.

[Woo78] R. E. Woodley, J. Nucl. Mater. **74** (1978) 290.

[Woo79] R. E. Woodley, M. G. Adamsom, J. Nucl. Mater. **82** (1979) 65.

This project has received funding from the Euratom research and training programme 2019-2020 under grant agreement No 945022.

20. Grain growth in MOX

This chapter was originally provided by M. Verwerft (SCK-CEN).

20.1 Literature data

Grain growth of polycrystalline materials is closely studied in the processing of both ceramics and metals. The sintering process of UO_2 and $(U,Pu)O_2$ is controlled by the interplay of densification (pore mobility) and grain growth (coarsening). In the context of in-reactor grain growth, one is interested in the processes that are more generally referred to as "late stage sintering", where non-densifying coarsening of both grains and pores occur. Grain growth continues to be driven by energy minimization through reduction of free surface and grain boundary surface and the dominating microscopic processes in the late stage of sintering are volume diffusion and grain boundary diffusion. In the intermediate stage of sintering, the pores are still cylindrically shaped and form an interconnected, open network. When entering the late sintering stage, the remaining porosity is in majority closed. Isolated, lenticular pores are found on the boundaries between grains and multi-coordinated pores are found at the contact point between many grains (e.g. tetrahedrally shaped at the contact point between three grains). The total surface area is minimal when pores are located on grain boundaries, which results in a binding energy between a pore and a grain boundary: the pores tend to remain attached to the moving grain boundaries. Generally, the mobility of grain boundaries is much higher than that of pores and the pores cause the so-called "grain boundary drag". Pore mobility is driven by both surface diffusion (a densifying mechanism) and evaporation-condensation (a non-densifying mechanism), but for sizeable pores, typically µm-size and above, surface diffusion is negligible compared to evaporation-condensation. The various mechanisms are detailed in textbooks on the sintering mechanisms (see e.g. [Ger96]). At sufficiently elevated temperatures, the coarsening of both grains and pores continues during in-reactor stay.

Proposed theoretical approach for grain growth is based on the modelling of vapor pressures of UO_2, UO_3 and PuO, and taking into account the local temperature, pressure and grain boundary porosity fraction. The recommendation refers to two publications on experimental observations of MOX grain growth [Sar86, Bai90].

In its most simple form, normal grain growth, i.e. grain growth with approximate conservation of a uniform grain size distribution is analyzed in terms of the shrinkage rate of smaller grains in favor of the larger ones. The driving force is the decrease of total energy by decreasing the total grain boundary area and is expressed in terms of the radius of curvature. The radius of curvature is inversely proportional to the grain diameter, which led to the simple formulation given in Eq. 20.1 [Bur49] :

$$\frac{dD}{dt} = k(T).\frac{1}{D} \qquad \text{Eq. 20.1}$$

This project has received funding from the Euratom research and training programme 2019-2020 under grant agreement No 945022.

Herein, *k(T)* takes an Arrhenius form: $k(T) = k_0 \exp(\frac{-Q}{R.T})$, with k_0 a constant, Q the activation energy, R the universal gas constant and T the absolute temperature.

Eq. 20.1 can be readily integrated and yields to Eq. 20.2:

$$D^2 - D_0^2 = k(T).t = k_0 \exp(\frac{-Q}{R.T}).t \quad \text{Eq. 20.2}$$

Herein, D_0 is the initial grain diameter at $t = 0$. Apart from very pure systems at elevated temperatures, the kinetics of grain growth do not follow the quadratic relation of Eq. 20.2. Grain growth in real materials is analyzed according to the more general empiric formulation given in Eq. 20.3:

$$D^n - D_0^n = k_0 \exp(\frac{-Q}{R.T}) . t \quad \text{Eq. 20.3}$$

Nichols [Nic66] discussed the relation between the exponent, n, and the different rate determining transport mechanisms of pore mobility, and for evaporation-condensation where the vapor is in equilibrium with the surface tension inside the pore ($p = 2\gamma/r$), the exponent $n = 3$. The activation energy, Q, is to be interpreted as the apparent activation energy of the mechanism that is rate determining for the grain boundary movement. When surface diffusion is dominant, $n = 5$ and both for volume diffusion and evaporation-condensation with constant pressure, $n = 4$.

Grain growth in the presence of a retardation force on grain boundary motion has also been expressed as per Eq. 20.4 [Bur49]:

$$\frac{dD}{dt} = k(T).\frac{1}{D} - C \quad \text{Eq. 20.4}$$

Herein, C is a constant independent from the grain diameter and accounts for the drag forces on grain boundary movement due to interactions with pores and/or inclusions. Obviously, the drag force implicitly defines an upper limit of the grain boundaries, since $\frac{dD}{dt} = 0$ when $C = k(T).\frac{1}{D}$. Eq. 20.4 may thus be rewritten as per Eq. 20.5:

$$\frac{dD}{dt} = k(T).\left(\frac{1}{D} - \frac{1}{D_m}\right) \quad \text{Eq. 20.5}$$

With D_m the limiting grain size.

Experimental observations of grain growth in UO_2 are sometimes interpreted with a cubic rate law (Eq. 20.3, with n = 3) [Nic66, Bou01], sometimes with a quartic rate law (Eq. 20.3, with n = 4) [Sol86, Glo87, Kog89, Van13] or in terms of the formulation involving a limiting grain size (Eq. 20.5) [Ain73].

In $(U_{1-x}Pu_x)O_{2-y}$ mixed oxide fuels, less experimental results have been published. An extensive study annealing periods ranging from 7 minutes to 120 hours on stoichiometric and sub-stoichiometric MOX with composition $(U_{0.80}Pu_{0.20})O_{2.00}$ and

This project has received funding from the Euratom research and training programme 2019-2020 under grant agreement No 945022.

$(U_{0.80}Pu_{0.20})O_{1.97}$ was conducted by Sari [Sar86]. The results of an in-pile experiment on $(U_{0.68}Pu_{0.32})O_{1.97}$ was reported by Bainbridge et al. [Bai90]. Both studies interpreted their results in terms of a cubic rate law (Eq. 20.3, with n = 3). Recently, a complementary study involving stoichiometric MOX fuels of different production routes and enrichments was published by Van Uffelen et al. [Van13]. The latter study interprets data for both UO_2 and MOX fuels and concludes that the total data set is best represented by a quartic rate law (Eq. 20.3, with n = 4). In the margin of a study on thermal conductivity MOX fuels, grain growth data were obtained by Duriez et al. [Dur00], but the latter data were not interpreted in terms of grain growth kinetics by the authors.

The original data published in references [Sar86, Bai90, Dur00, Van13] have been collected for this study and interpreted assuming a cubic rate law (Eq. 20.3, with n = 3). Figure 20.1 represents the grain growth coefficient *k(T)*. The observations by Sari (Figure 20.1, top) clearly show an Arrhenius-type behavior for *k(T)*, with activation energies Q = 319 ± 30 kJ/mol and Q = 446 ± 30 kJ/mol and pre-exponential factor $k_0 = 2.55\ 10^9$ μm³/min and $k_0 = 1.11\ 10^{12}$ μm³/min for stoichiometric and sub-stoichiometric MOX, respectively. The experiments by Sari [Sar86] were made on homogeneous MOX fuels produced by a Sol-Gel method and the results clearly demonstrate an effect of stoichiometry on the grain growth rate, with markedly higher growth rates for stoichiometric than for sub-stoichiometric MOX. On the same figure, the uncertainty margins as reported by Sari for both correlations are also shown. Sari also limits the use of the derived correlations to D < 60 μm (beyond which the columnar grain growth sets in, which is a non-normal grain growth regime).

In Figure 20.1 bottom the data published by other authors are represented. Since Sari derived his correlation for the kinetic coefficient using the mean linear intercept (MLI, see ASTM-E 112) as measure for the grain diameter, the data of the other authors were converted where necessary (Duriez et al. [Dur00] also reported MLI, Bainbridge et al. [Bai90] and Van Uffelen et al. [Van13] converted their direct MLI measurements to true grain size values by multiplying with a constant factor of $\sqrt{\frac{3}{2}}$ and 1.5, respectively). One observes that the stoichiometric Sol-Gel fuels with 9% and 25% Pu/U + Pu (both reported in [Van13]) are consistent with the correlation by Sari. The Micronized Master blend fuel with 25% Pu/(U + Pu) in [Van13] and the co-milled fuels with 3% - 15% Pu/(U + Pu) in [Dur00] present slightly lower grain growth kinetics and approach the lower bound of the Sari correlation for sub-stoichiometric MOX. The low-enriched Short Binderless Route (SBR) fuel reported by [Van13] shows also low grain growth kinetics, which is attributed to the use of pore forming agents (not reported) to be used in any of the other productions.

The in-pile results by Bainbridge et al. [Bai90], although derived from sub-stoichiometric fuel, show a slightly higher grain growth rate at lower temperatures and a slightly lower grain growth rate at elevated temperatures than the correlation by Sari [Sar86]. Considering the in-pile oxygen redistribution of sub-stoichiometric MOX with nominal O/M = 1.97, one expects that in the peripheral area, the O/M ratio approaches 2.00, while in the central zone, the oxygen-to-metal ratio is much lower (see e.g. Olander [Ola76]).

This project has received funding from the Euratom research and training programme 2019-2020 under grant agreement No 945022.

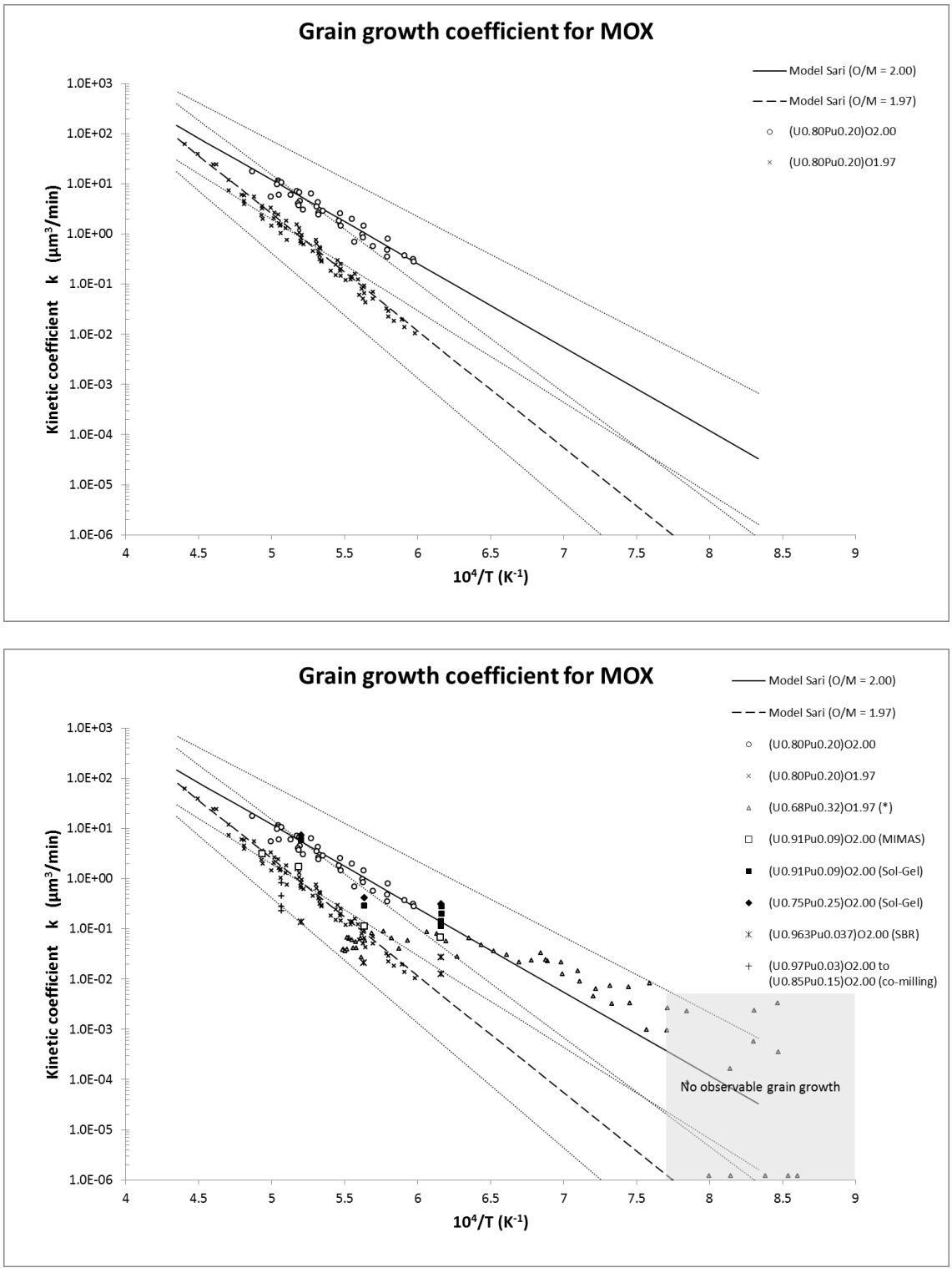

Figure 20.1: Kinetic coefficient *k(T)* derived from grain growth observations in MOX.

Top: the data set and associated model for the kinetic coefficient k(T) for stoichiometric and sub-stoichiometric MOX published by Sari [Sar86].
Bottom: the data published by Bainbridge et al. [Bai90], Van Uffelen et al. [Van13] and Duriez et al. [Dur00] are represented together with the model derived by Sari [Sar86]. The shaded area corresponds to temperatures lower than 1300 K, where no observable grain growth occurs. Data points which correspond to grain shrinkage are set at kinetic coefficient 1.0 E^{-06} rather than deleting them from the representation.

This project has received funding from the Euratom research and training programme 2019-2020 under grant agreement No 945022.

20.2 Conclusions and recommendations

The recommendation develops a mechanistic model for grain growth based on the evaporation-condensation mechanism for pore mobility. The uncertainties of the experimental data, however, may not entirely justify a modeling approach and the correlation originally proposed by Sari for two data sets, one with low grain growth kinetics (O/M = 1.97) and the other with high growth kinetics (O/M = 2.00) appears to present the upper and lower grain growth kinetics for the data sets published since then.

Within the experimental uncertainties, it is advised to calculate grain growth in MOX assuming a cubic rate law (Eq. 20.3, n = 3) and using the upper and lower boundaries for the kinetic parameters derived by Sari [Sar86], and limiting the maximum grain size to D < 60 µm (using the mean linear intercept concept). By doing so, one will obtain a scatter band with the expected upper and lower grain growth limits.

- Upper: k_0 = 2.55 10^9 µm^3.min^{-1} and activation energy Q = 319 - 30 kJ.mol^{-1} = 289 kJ.mol^{-1}
- Lower: k_0 = 1.11 10^{12} µm^3.min^{-1} and activation energy Q = 446 + 30 kJ.mol^{-1} = 476 kJ.mol^{-1}

In full writing, the proposed correlations thus read as:

- Upper limit: $D^3 = D_0^3 + 2.55 . 10^9 \, \mu m . min^{-1} \exp(\frac{-289 \, kJ/mol}{R.T}) \, . \, t$
- Lower limit: $D^3 = D_0^3 + 1.11 . 10^{12} \, \mu m . min^{-1} \exp(\frac{-476 \, kJ/mol}{R.T}) \, . \, t$

With maximum diameter (MLI): D_{max} = 60 µm.

20.3 References

[Ain73] J.B. Ainscough, B.W. Oldfield and J.O. Ware, Isothermal grain growth kinetics in sintered UO_2 pellets, J. Nucl. Mater. **49** (1973) 117.

[Bai90] J.E. Bainbridge, C.B.A. Forty and D.G. Martin, The grain growth of mixed oxide fuel during irradiation, J. Nucl. Mater. **171** (1990) 230.

[Bou01] L. Bourgeois, P. Dehaudt, C. Lemaignan and J.P. Fredric, Pore migration in UO_2 and grain growth kinetics, J. Nucl. Mater. **295(1)** (2001) 73.

[Bur49] J.E. Burke, Some factors affecting the rate of grain growth in metals in Transactions of the Metallurgical Society AIME **180** (1949) 73.

[Dur00] C. Duriez, J.P. Alessandri, T. Gervais and Y. Philipponeau, Thermal conductivity of hypo-stoichiometric low Pu content (U,Pu)O_{2-x} mixed oxide, J. Nucl. Mater. **277** (2000) 143.

[Ger96] R. German, Sintering Theory and Practice. 1996, New York: John Wiley & Sons, Inc.

This project has received funding from the Euratom research and training programme 2019-2020 under grant agreement No 945022.

[Glo87] F. Glodeanu, I. Furtuna, A. Paraschiv and M. Paraschiv, Grain growth in high density UO_2, J. Nucl. Mater. **148** (1987) 351

[Kog89] T. Kogai, R. Iwasaki and M. Hirai, In-pile and out-of-pile grain growth behavior of sintered UO_2 and $(U,Gd)O_2$ pellets, J. Nucl. Sci. Technology **26(8**) (1989) 744

[Nic66] F.A. Nichols, Theory of grain growth in porous compacts, J. Appl. Phys. **37(13)** (1966) 4599.

[Ola76] D. Olander, Fundamental aspects of nuclear reactor fuel elements. 1976, Virginia: Energy Research and Development Administration

[Sar86] C. Sari, Grain growth kinetics in uranium-plutonium mixed oxides, J. Nucl. Mater. **137** (1986) 100

[Sol86] S.E. Soliman, N. Hansen, I. Misfeldt, J.G. Rasmussen and O. Toft Sørensen. Isothermal grain growth kinetics in UO_2. in Annealing processes - Recovery, recrystallization and grain growth. (1986).Risø National Laboratory. p. 553

[Van13] P. Van Uffelen, P. Botazzoli, L. Luzzi, S. Bremier, A. Schubert, P. Raison, R. Eloirdi and M.A. Barker, An experimental study of grain growth in mixed oxide samples with various microstructures and plutonium concentrations, J. Nucl. Mater. **434** (2013) 287

This project has received funding from the Euratom research and training programme 2019-2020 under grant agreement No 945022.